Magneto-Optical Oxide Thin Films and Integrated Nonreciprocal Photonic Devices

by

Lei Bi

B.S., Materials Science and Engineering, 2004
M.S., Materials Science and Engineering, 2006
Tsinghua University, Beijing, China

Submitted to the DEPARTMENT OF MATERIALS SCIENCE AND ENGINEERING
In Partial Fulfillment of the Requirements for the Degree of

DOCTOR OF PHILOSOPHY IN MATERIALS SCIENCE AND ENGINEERING
at the
MASSACHUSETTS INSTITUTE OF TECHNOLOGY
June 2011

Signature of Author: _____
Department of Materials Science and Engineering
March 18th, 2011

Certified by : _____
Caroline A. Ross
Toyota Professor of Materials Science and Engineering
Thesis Advisor

Accepted by : _____
Christophoer Schuh
Chair, Departmental Committee on Graduate Students

This thesis is dedicated to my parents and my grandmother

谨以此论文献给我的父亲母亲和外婆

祝你们健康快乐

Magneto-Optical Oxide Thin Films and Integrated Nonreciprocal Photonic Devices

By Lei Bi

Submitted to the Department of Materials Science and Engineering on March 18, 2011 in Partial Fulfillment of the Requirements for the Degree of Doctor of Philosophy in Materials Science and Engineering

Abstract

Nonreciprocal photonic devices including optical isolators and optical circulators are indispensible components in present day optical communication systems. Although highly desired by the fast development of silicon photonics, monolithically integrating such devices on a semiconductor platform has been challenging for decades both due to material incompatibility and device designs. In this thesis, we focus on developing material and device candidates for monolithically integrated nonreciprocal photonic devices on silicon. Several magneto-optical oxide thin films including epitaxial magnetically doped perovskites and polycrystalline garnets were demonstrated with high figure of merit at communication wavelengths, while epitaxial orthoferrite films were understood to have challenges in achieving either thermodynamically limited cation ordering or kinetically limited single crystal orientations. High figure of merits of 3~4 deg/dB and 20 deg/dB were achieved in epitaxial $Sr(Ti_{0.2}Ga_{0.4}Fe_{0.4})O_3$ films and in polycrystalline $(CeY_2)Fe_5O_{12}$ films stabilized by a thin $Y_3Fe_5O_{12}$ polycrystalline layer on oxidized silicon respectively. Based on these materials, novel photonic devices including nonreciprocal strip-loaded waveguides and resonators were simulated and experimentally demonstrated. Strong nonreciprocal phase shift (NRPS) has been demonstrated in chalcogenide glass/magnetic oxide and magnetic oxide/silicon strip-loaded waveguides by numerical simulations. A nonreciprocal optical racetrack resonator based on polycrystalline garnet/silicon strip-loaded waveguides was experimentally demonstrated. This monolithically integrated device showed ~10 times footprint reduction compared to conventional nonreciprocal photonic device designs, which may serve as a fundamental structure in a variety of ultra compact photonic devices such as optical isolators, circulators, switches and modulators in the future.

Thesis Supervisor: Caroline A. Ross
Title: Toyota Professor of Materials Science and Engineering

Table of Contents

List of Tables

List of Figures

Acknowledgement

At this another quiet night of MIT, I am sitting alone in my office and writing the last part of my Ph.D. thesis. Memories bring me back to the days and nights of the past five years. I cannot stop being amazed at how far I have gone through from a fresh man to a scientific researcher, and I also cannot thank so many people enough for being part of my life all the way along in this great journey. There is not many five years in one's life, and this is surely one of the most important for me. No doubt without everyone's help I cannot get this far, not only to a Ph.D. of MIT, but also to whom I am now and whom I am going to be in the future. Thank you everyone who shared high and lows, excitements and frustrations, determinations and confusions, joys and tears with me in the past unforgettable five years. You are the most important part of my life in MIT.

I would like to express my deep gratitude and respect first to my advisor, Prof. Caroline Ross. It is because of your support that I can fulfill my dream of studying in MIT, and it is because of your guidance, encouragement and charismas that I can grow up from a green hand to a scientific researcher and engineer. I never forgot the evening in June 2006 of Beijing that you offered me a RA position in your group. It changed my life and allowed me to work with you in this great group for the most challenging problems in the world. I always appreciated this to be a great honor and probably the only chance to do the greatest research works that I have in my life. Together we have carried out a challenging project from scratch to successful results now and prosperous research topics in the future. I always benefited from your critical thinking, your clear minds and your scientific intuitions, which guided me to the correct ways of scientific research. Your encouragement and kindness on my own ideas not only helped me to work independently but also taught me how to be a great mentor. Thank you Caroline, your guidance will be precious in my whole life. I wish we can work together again in the future.

I would like to thank Dr. Gerald Dionne, a great mentor, a good friend and the best theorist I have met so far and probably to be in my whole life. I am always respecting you as my co-advisor during my Ph.D. study. Your determination of exploring scientific truth has set a good example for my research. Your inspiring tutorial on magnetism theory has shaped the cornerstones of my understanding on experimental observations. Your optimistic attitudes and humor on challenges have offered me vivid lessons of how to be a fearless scientist. I enjoyed the talks with you every time you come to MIT. Thank you Gerry, for sharing your stories both on research and life, and for always offering me invaluable suggestions standing on my situation. I hope we can keep in contact and talk about science and life in the future.

I would like to thank Prof. Tuller and Prof. Kimerling in my thesis committee, for your

suggestions on my research work and for your generous offer of sharing equipments in your groups. I have benefited a lot from your guidance. Part of my research work in this thesis such as Ce or Ga doped STF films and nonreciprocal resonator theories are inspired by your suggestions. I also enjoyed your lectures very much. I learnt my first semiconductor device physics course of 3.42 and also my first photonic material and device course of 3.46. They both offered me fundamental knowledge for my current research work and my future careers.

I would like to thank everyone in the magnetic materials and devices group for offering me this home like team in MIT. I received lots of help from Dr. Fernando Castaño, Dr. Wonjoon Jung, Dr. Vikram Sivakumar, Dr. Fillip illievski, Dr. Peng-Wei Chuang, Dr. Yeon Sik Jung, Dr. Chung Hee Nam, Dr. Carlos Garcia, Dr. David Navas Otero, Prof. Hayato Miyagawa, Dr. Jeong Gon Song, Mr. Brian Ng, Mr. Mark Mascaro, Mr. Kevin Gotrik, Mr. Adam Floyd Hannon, Mr. Nicolas Aimon, Dr. Youngman Jang, Ms. Jean Anne Currivan, Mr. Mehmet Cengiz Onbasli and Ms. Gabrielle Joseph. Thank you for the scientific discussions, training on equipments, traveling together to conferences and everyday chatting and more.

I would like to thank my close collaborators, Prof. Juejun Hu (JJ), Dr. Hyun Suk Kim, Mr. Alex Taussig, Dr. Dong Hun Kim, Mr. Peng Jiang and Dr. Lei Wang. I always felt lucky to have JJ as my classmate and collaborator since about 11 years ago. I learnt a lot from him on theories and experiment techniques of photonic devices. He is sharp in scientific problems and always kind and helpful to my questions. I am glad that we collaborated to invent the first monolithic integrated optical isolator on silicon. Dr. Hyun Suk Kim, Mr. Alex Taussig, Dr. Dong Hun Kim and Mr. Peng Jiang have been fighting side by side with me for the challenging quest of exploring novel magneto-optical materials. I have been impressed by Hyun Suk's self motivation, Alex's confidence and optimisms, and Dong Hun and Peng's diligence in our collaborations. I enjoyed working with you guys and I owe you a lot on everyday help of the experiments and life. Dr. Lei Wang and I worked together on first principle simulation of our oxide materials. He taught me from the very basics of first principle simulations and patiently answered my questions in the whole process. It was really great to see our co-authored paper published on physical review journals.

I would like to thank everyone who offered help with trainings and experiments during my Ph. D. study. I owe Mr. David Bono a lot for repairing Faraday rotation machines, VSM, PLD pumps and chambers and helping with machinery works. I received help from Dr. Scott Litzelman, Dr. Woo Chul Jung and Mr. Di Chen for using furnaces and the sputter machine in Prof. Tuller's group. I am also indebt to experts in MIT CMSE facility including Dr. Scott Speakman, Dr. Yong Zhang, Dr. Shaoyan Chu, Dr. Shiahn Chen, Dr. Elisabeth L. Shaw for their training and assistance on the characterization equipments. I thank Prof. Karl Berggren

for allowing me to use the NanoStructures Laboratory, and Mr. Jim Daley, Mr. Mark Mondol and Mr. Tim Savas for their help on the NSL facilities. I am grateful to Mr. Jie Sun and Mr. Corey Fucetola for their help on silicon resonator fabrications. I appreciate the trainings from Dr. Jiangdong Deng and Dr. Ling Xie in Center for Nanoscale Systems in Harvard for characterization and device fabrications. I also thank Dr. Kurt Broderick for training me in the Microsystem Technology Laboratory. Also, Ms. Yinlin Xie and Mr. Lenny Rigione helped my many times on the ceramic target fabrications in CMSE and Prof. Cima's group in MIT.

I would like to thank my friends in MIT and Harvard, Mr. Zibo Jiang, Miss Xiaoting Jia, Miss Chia-hua Lee, Mr. Xing Sheng, Dr. Jianfei Wang, Mr. Shiyun Lin, Dr. Jifeng Liu, Dr. Rong Sun, Dr. Jing Cheng, Mr. Yaoqi Li, Mr. Fuxian Song Dr. Bo Gong, Mr. Jianxiang Huang, Dr. Wen Feng and everyone else in the MIT Chinese Students and Scholars Association (CSSA). You made my life colorful here. Thank you for all the parties, Karaokes, hang-outs and cultural events. I will miss every one of you after I leave MIT.

I would like to specially thank everyone using the PLD machine and room 8-140. Thank you for your assistance to keep the PLD machine and the lab a safe and productive place.

Finally, I would like to express my deepest love and thanks to my dearest parents. Thank you for every day's breakfast when I was in high school, for your prayers at night when I was sick before the university entrance exam, for your joyful tears when I was admitted by Tsinghua University, for your anxiety when the fear of SARS shadowed Beijing and for every week's phone calls when we are now thousands of miles away. Thank you for nothing in particular, but for everything in general, because you offered me the two most important things: life and love. I love you, forever.

Feb. 24, 2011
Lei Bi

Chapter 1
Introduction

1.0 Overview and layout of the thesis

Perhaps one of the most important innovations of information technology in the past century is the discovery and application of electronic diodes. Usually recognized as semiconductor p-n junctions and widely used in present day electronic transistors, photodetectors, LEDs and lasers, electronic diodes act as the fundamental building blocks for modern information technologies. The functionality of an electronic diode is based on the nonreciprocal transmission of free carriers, namely the rectifying effect, in which the current passing through the device in the forward and backward directions are not equivalent. Similar nonreciprocal effects also exist for propagating light waves. As a counterpart of electric diodes in photonics, optical diodes or usually named as optical isolators are also widely applied in optical fiber communication systems. Nonreciprocal photonic devices including optical isolators and circulators are indispensible components in optical communication systems which provide high laser stability, long laser lifetime and high system efficiency.

Unlike electrons or holes, photons do not carry charge. The only physical observable which tells apart a forward propagating photon from a backward propagating one is the momentum associated with the photon. In fact, several nonreciprocal photonic devices proposed on semiconductor substrates including conventional magneto-optical devices [1] and recent proposed nonreciprocal photonic transition [2], nonreciprocal Raman amplification [3] and nonreciprocal optical cavity [4] devices all utilize this difference in photon momentums between forward and backward propagating lights to achieve nonreciprocity. Among these nonreciprocal photonic effects, the magneto-optical (MO) effect is the most studied and best understood over the past several decades. Different from electronic diodes where nonreciprocity is achieved by field and charge interactions, magneto-optical nonreciprocity is achieved by photons with different momenta interacting with electronic transitions between

different quantum electronic states of the MO material obeying the selection rule, whereas the degeneracy of the electronic states is lifted by an applied magnetic field or a remanent magnetization in the MO material. In the mid to late 1980's, strong Faraday rotation and high optical transparency at optical communication wavelengths were discovered in Bi doped iron garnets, which promoted the wide application of such materials in discrete optical isolators and circulators. Until now, iron garnet single crystals and epitaxial films are still the most widely used materials in commercial nonreciprocal photonic devices.

With the development of silicon photonics in the past 2 decades, integration of photonic devices on a semiconductor platform has become increasingly urgent. So far, optical isolators and circulators are almost the only missing planar photonic devices for monolithically integrated photonic systems on a semiconductor platform. The challenges lie in both integrating high quality magneto-optical materials and developing novel integrated nonreciprocal photonic devices on semiconductors. There are several general criteria for a practical magneto-optical material and device integrated on a semiconductor substrate.

Materials:

- Strong room temperature Faraday rotation and high optical transparency (i.e. high figure of merit) at communication wavelengths.
- Compatibility with monolithic integration processes on a semiconductor substrate.
- High temperature stability of magneto-optical effects.

Devices

- Monolithic integration for high fabrication throughput.
- Small device footprint and compatible with other planar photonic devices.
- High temperature stability of device performance
- Low cost

Until today, neither suitable materials nor devices have been developed on silicon based on the criteria above. In this thesis, we focus on monolithically integrating magneto-optical materials and devices for nonreciprocal photonic applications. We demonstrate high figure of

merit of several magneto-optical oxide thin films at 1550 nm wavelength. Based on these materials, we also simulated and experimentally demonstrated compact nonreciprocal photonic waveguides and resonators on silicon.

Chapter 1 introduces the motivation of integrating nonreciprocal photonic devices on silicon. The basic theory of magneto-optical effects is reviewed. Both material and device challenges for integrating nonreciprocal photonic devices on silicon are summarized. Chapter 2 describes the experimental methods used in this study. Chapter 3 summarizes the study of the structure, magnetic, magneto-optical and optical properties of orthoferrite thin films including $BiFeO_3$, Bi_2FeMnO_6 and $LaFeO_3$ epitaxial films. First-principles simulations were carried out to understand the magnetic and optical properties of Bi_2FeMnO_6 films, which explain the thermodynamic limit of cation ordering in this material as well as the low optical transparency in the communication wavelengths. Multiple crystal orientations were observed and controlled by experimental conditions in epitaxial $LaFeO_3$ films which are demonstrations of kinetically limited crystal growth process in such films. Chapter 4 is dedicated to understanding the structure and properties of a new class of room temperature ferromagnetic perovskites, the Fe and Co doped $SrTiO_3$ films. Room temperature ferromagnetism, high Faraday rotation and high optical transparency were observed in these films at 1550 nm wavelength. The ferromagnetism associated with strong magnetoelastic anisotropy in such films is understood as strain induced spin alignment. Defect chemistry design of such materials changes the magnetic and optical properties systematically. A high figure of merit of 3~4 dB/cm is experimentally demonstrated in $Sr(Ti_{0.2}Ga_{0.4}Fe_{0.4})O_{3-\delta}$ films. $As_2S_3/Sr(Ti_{0.6}Fe_{0.4})O_{3-\delta}$ and $Sr(Ti_{0.2}Ga_{0.4}Fe_{0.4})O_{3-\delta}$ strip-loaded waveguides were fabricated and characterized. The nonreciprocal phase shift properties of these devices are simulated using numerical methods. Chapter 5 demonstrates monolithic integration of $Y_3Fe_5O_{12}$ and Bi or Ce doped polycrystalline iron garnet films on silicon. Bi or Ce doped $Y_3Fe_5O_{12}$ polycrystalline phases were stabilized by a two-step growth method. The structure and magneto-optical properties of polycrystalline garnet films are found to be highly related to the film fabrication process. Chalcogenide Glass/garnet waveguides and resonators were fabricated and proposed for nonreciprocal phase shift device applications. Chapter 6 focuses

on planar nonreciprocal photonic devices based on magneto-optical oxide thin films. We experimentally demonstrated a monolithically integrated ultra-compact nonreciprocal photonic resonator using magnetic oxide/SOI strip-loaded waveguides. The optical nonreciprocity of this device is simulated and experimentally demonstrated. Possible improvements of device structures and material properties for on-chip nonreciprocal photonic device applications are also discussed. Finally, chapter 7 draws the conclusion and provides suggestions for future work.

1.1 Silicon photonics and integrated nonreciprocal photonic devices

About 3 decades ago, the innovation of fiber optical communication significantly changed the information technologies and people's everyday life. Serving as interconnections between information processed and stored in electronic systems over hundreds of kilometers away, fiber optical communication system provides huge information carrying capacity, and high energy efficiency due to little heat dissipation in optical fibers. [5] With the aggressive scaling of device footprint in present day VLSI (very-large-scale integration) electronic circuits following Moore's Law, the boundary between optical and electronic interconnection has been driven continuously toward shorter distances. There are mainly two driving forces for this process to take place. The first is the heat dissipation in electronic interconnects due to wire resistance. As transistor and interconnect electric wire density increase exponentially, the power density also exponentially increases, and heat dissipation is becoming the most challenging issue in microprocessors. The second is the interconnection "bottle-neck" effect, which describes an exponential increase of electronic interconnection time as devices scale down to sub 100 nm scale due to RC delay. [6] The low power dissipation and high bandwidth of optical communication provides a natural solution to replace certain levels of electronic interconnections. Therefore, integrating optical components in a semiconductor platform has becoming increasingly urgent in recent years. As a counterpart of microelectronics in integrated circuits, silicon photonics offers a possible solution to integrate photonic components by using standard electronic semiconductor integration processes and

silicon based materials. Several major semiconductor companies including Intel and IBM are actively developing integrated optical components and systems for the next decade semiconductor systems. Recently, a 50 Gbps silicon photonic link [7] and various silicon photonic devices [8][9] have been developed by Intel and IBM respectively.

In an optical communication system, the major processes of light are the generation, modulation, propagation and detection of photons, which are realized by lasers, modulators, fibers (waveguides) and detectors respectively. Other important devices support these major functions and enter the system at various positions. For instance, optical isolators enter between the laser and other optical components to stabilize the laser performance; optical amplifiers exist in optical fibers to amplify the signal after long distance propagation and attenuation; optical multiplexers and demultiplexers may be present in front and at the end of the fibers or waveguides, which combines or separates light with different wavelengths into or out of the propagation channel for high bandwidth data transmission. To integrate on a silicon platform from discrete devices, each of these devices has its specific material and integration issues. So far, most of these issues have been solved for different devices. Commercial or prototype integrated photonic devices have been successfully developed such as Ge photodetectors [10], Si waveguides [11], Si_3N_4 waveguides [12], Si modulators [13], Ge lasers [14], Er doped SiO_2 optical amplifiers [15], ring resonator optical multiplexers [16] and Si/Si_3N_4 optical resonator filters [17]. However, nonreciprocal photonic devices including optical isolators and circulators are still lack, which limits the application of a high performance integrated optical system.

The importance of nonreciprocal photonic devices has been acknowledged in fiber optical systems. Almost every laser there is an optical isolator associated with it. An optical isolator works as a one-way valve for light. Or simply put it, this device looks transparent from one way, but dark from the other side. (Of course this is in the near-IR communication wavelengths.) Such devices are important because lasers are sensitive to reflected light, which acts as undesired feedback to the laser cavity. This optical feedback can disturb the photon and free carrier populations in the cavity and also cause carrier induced index change

in the gain medium. It has been observed that a variety of laser instabilities take place when there is injection of reflected light, such as amplitude noise (RIN) [18], fluctuation in intensity [19], spectral shift [19] and frequency hopping [20]. These issues are resolved with the presence of an optical isolator. Commercial optical isolators can offer an isolation ratio up to -30~-65 dB with insertion loss less than 3 dB. [21] Figure 1-1 (a) and (b) shows typical commercial optical isolators and a schematic plot of the device structure. The device consists of two polarizers, one permanent magnet and one Faraday rotator iron garnet single crystal. When propagating forward, light is initially linearly polarized, then the plane of polarization plane rotate by 45° after passing through the garnet crystal, and finally passes through the analyzer whose polarization direction is 45° tilted with respect to the initial polarizer; when propagating backward, the polarization plane of the light continues to rotate another 45° due to the nonreciprocity of the garnet crystal and become orthogonal to the polarization direction of the polarizer, therefore optical isolation is achieved. A polarization independent optical isolator is also commercially available as shown in figure 1-1 (c) [22]. By combining birefringent crystals and Faraday rotators, the light propagates in a way that it couples into the output fiber after passing through the device in the forward propagation direction, but spatially there is "walk-off" preventing coupling back to the input fiber in the backward propagation direction. When propagating forward, light is spatially separated in to "E-ray" and "O-ray" by the birefringent crystal depending on the polarization directions. Then both components rotate their polarization by passing through the Faraday rotator and half-wave plate and recombines in the birefringent crystal at the output side. When propaging backwards, due to the nonreciprocity of the Faraday crystal, the two components further "walk-off" in space at the initial birefringent crystal and do not couple back to the input fiber. Due to the polarization independent properties of such devices, they are highly desirable in fiber optical systems. On the other hand, optical circulators are widely used in WDM type optical add-drop modules (OADM). Figure 1-2 shows a commercial 4 port optical circulator and a schematic plot of its operation principles [23]. An optical circulator has at least 3 ports. Light passes through this device in a way that it always exits from the next port of where it enters the device. For instance, light propagating in a four port optical circulator follows the trajectory of 1→2→3→4→1. In the language of transfer matrix, the device characteristics is

simply described by the following matrices,

$$S = \begin{pmatrix} 0 & 0 & 0 & 1 \\ 1 & 0 & 0 & 0 \\ 0 & 1 & 0 & 0 \\ 0 & 0 & 1 & 0 \end{pmatrix} \text{ and } SS^{*T} = \begin{pmatrix} 1 & 0 & 0 & 0 \\ 0 & 1 & 0 & 0 \\ 0 & 0 & 1 & 0 \\ 0 & 0 & 0 & 1 \end{pmatrix}$$

where the second matrix describes the lossless characteristic of the device. The operation principle of this device is shown in figure 1-2 (b). Faraday rotator crystals, quarter-wave plates and polarizing beam splitters are used to achieve light circulation. Note that this device works for randomly polarized light.

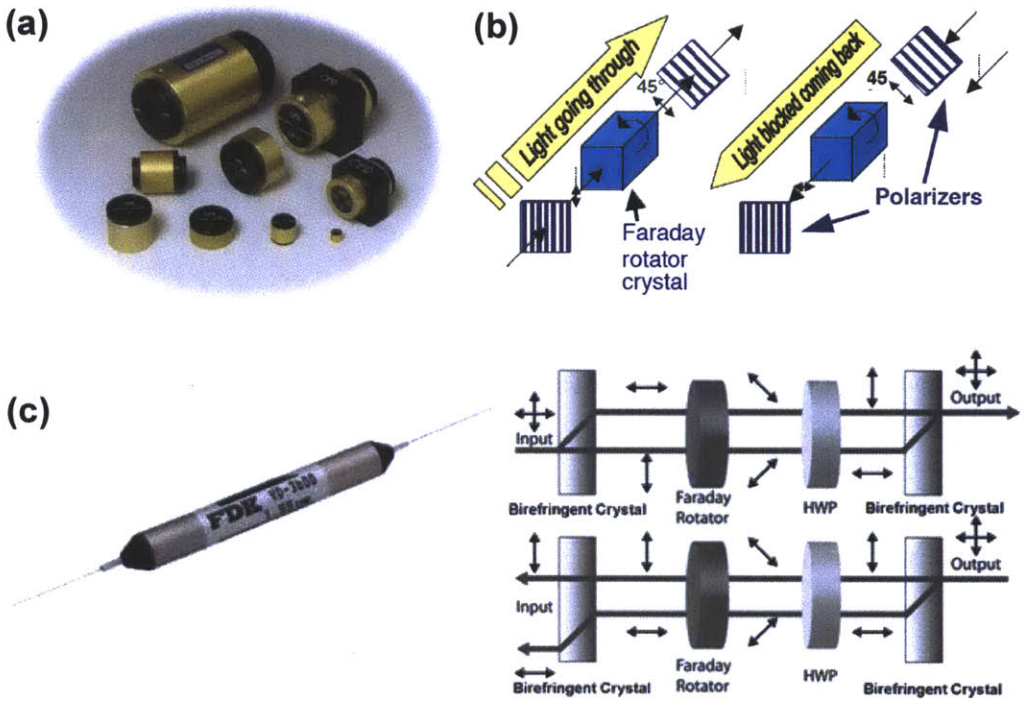

Fig. 1-1 Commercial optical isolators (a) and the principle of operation (b). Also shown is a commercial polarization independent optical isolator with its operation principles in (c) [22]

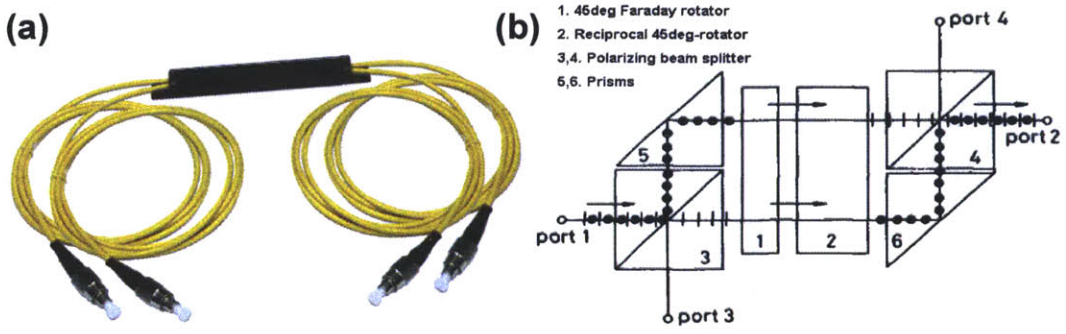

Fig. 1-2 Commercial four-port optical circulators (a) and the principle of operation (b) [23]

Although technologically mature and commercially successful, discrete nonreciprocal photonic devices are incompatible with integrated silicon photonic systems. Firstly the size of discrete devices is large, which is both due to bulky magneto-optical crystals and the complicated device structures using polarizers and wave plates. Secondly, the cost of aligning discrete devices is high and the yield and throughput is low, which is highly undesirable for monolithically integrated lasers. Thirdly, the mechanical stability of discrete devices is poor. Monolithic integration of nonreciprocal photonic devices provides a solution for the above issues. Meanwhile, integration of nonreciprocal photonic components offers a new dimension of functionality to the integrated photonic systems. A variety of functionalities may be achieved based on such devices, as will be discussed in detail in following chapters of this thesis.

1.2 Basic theory of magneto-optical effects

In this section we briefly review the basic underlying physics of magneto-optical effects with a focus on magnetic oxide thin films and integrated planar device structures. We follow the convention of terms and symbols in reference [24]. The underlying material and device physics will serve as a background of study in the following chapters of this thesis.

1.2.1 Microscopic mechanism of magneto-optical effect and material permittivity

Depending on the geometry of the incident wave vector and magnetization direction of the material, there are two different configurations of magneto-optical effects, namely Faraday configuration and Voigt configuration. Shown in figure 1-3, Faraday configuration means that the incident wave vector direction k is parallel to the magnetization direction of the magneto-optical media; and Voigt configuration means that the incident wave vector direction k is perpendicular to the magnetization direction of the magneto-optical media. In the former case, left or right circular polarized light beams show different refractive indices and extinction coefficients, which are called magneto-optical circular birefringence (Faraday

Effect) and magneto-optical circular dichroism (MCD) respectively. In the latter case, linearly polarized light beams with the electric field parallel or perpendicular to the magnetization direction show different refractive indices and extinction coefficient, which are called magneto-optical linear birefringence (Voigt effect) and magneto-optical linear dichroism (MLD) respectively.

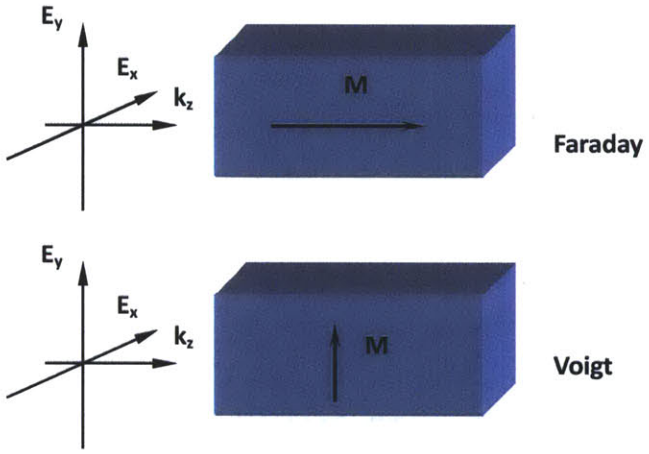

Fig. 1-3 Faraday and Voigt configurations of magneto-optical effects

Generally speaking, all magneto-optical effects are the consequence of splitting of electronic energy levels when a magneto-optical medium is subjected to a magnetic field. In magnetic oxides, these energy levels are the spin-orbital coupling multiplets showing different total angular momentum. Light with different polarization will cause different electron dipole transition between electronic states following the selection rule, which states that only those electric dipole transitions in which the quantum number S is unchanged whereas the quantum numbers L and J change by 0, ±1 are allowed (the transition from J=0 to J=0 is excluded). Meanwhile, only terms with different parity will be allowed for dipole transitions. Macroscopically, this effect results in a difference in refractive indices and absorption coefficients for incident light with different polarizations, which leads to so called magneto-optical birefringence and dichroism.

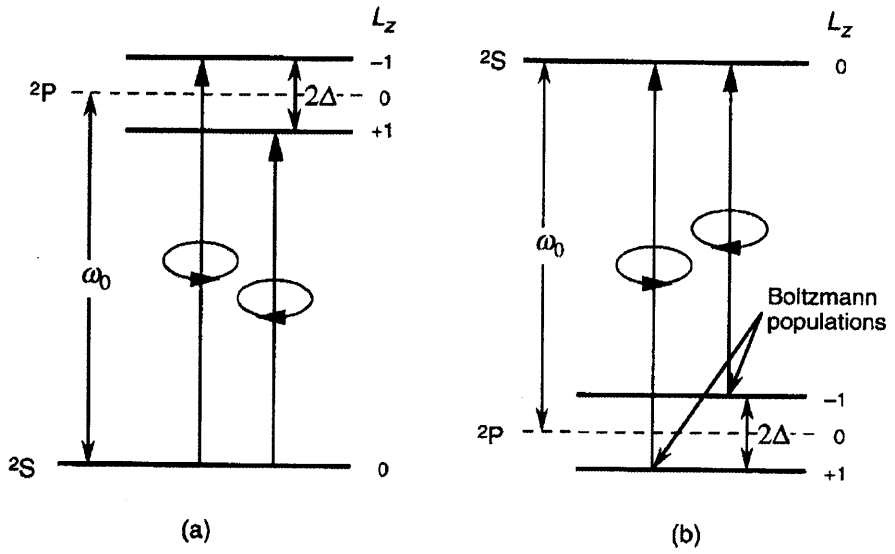

Fig. 1-4 (a) *Diamagnetic* and (b) *paramagnetic* types of electronic transitions

Consider the Faraday Effect for example. When an incident light enters the magneto-optical material along the z axis, the left- (right-) circular polarized photon will have angular momentum and its z-projection to be j=1 and m=+1(-1) respectively. Thus an electronic transition between states with $\Delta J = \pm 1,0$ and $\Delta m_J = +1(-1)$ is introduced. There can be two cases for such transitions to take place, as shown in figure 1-4 (a) and (b), which are called *diamagnetic* and *paramagnetic* transitions respectively. [24] (Note that these names are by convention and should be distinguished from magnetically diamagnetic or paramagnetic materials) The probabilities for left and right polarized light induced transitions are described by oscillator strengthes f_{ab}^{+} and f_{ab}^{-} respectively, where a and b are the ground and excited states, and + and – represents left and right polarized light respectively. In the *diamagnetic* transition, these two oscillator strength are different because the energies for their transitions are different. In the *paramagnetic* transition, these two parameters are different because the two ground state electron populations are different following the Fermi distribution.

Normally, the electric field of incident light can cause the polarization of ions. In a non-magneto-optical medium, the atomic polarizability tensor α_{ij} should be a symmetric tensor. For an ion showing Faraday Effect, the off-diagonal component is no longer 0 due to

$f_{ab}^{+} \neq f_{ab}^{-}$. If most of these ions in the material are macroscopically aligned to an external magnetic field, the permittivity tensor ε_{ij} will also show a non-zero off-diagonal component. The relationship between ε_{ij} and α_{ij} is:

$$\varepsilon_{ij} = \delta_{ij} + 4\pi N\alpha_{ij} \tag{1-1}$$

where $\delta_{ij} = 1$ for i=j and $\delta_{ij} = 1$ for $i \neq j$, N is the number of ions per volume. The off diagonal component $\varepsilon_{ij}(i \neq j)$ is related to the magnetization direction. This nontrivial off diagonal components can be expressed as a perturbation of the non-magneto-optical diagonal permittivity tensor in a lossless isotropic medium [25]:

$$\hat{\varepsilon} = n_f^2 \begin{pmatrix} 1 & 0 & 0 \\ 0 & 1 & 0 \\ 0 & 0 & 1 \end{pmatrix} + \Delta\varepsilon, \text{where } \Delta\varepsilon = iK'' \begin{bmatrix} 0 & M_z & -M_y \\ -M_z & 0 & M_x \\ M_y & -M_x & 0 \end{bmatrix} \tag{1-2}$$

K'' is a parameter proportional to $|f_{ab}^{+} - f_{ab}^{-}|$ [26] and is related to the Faraday rotation by $\theta = -k_0 \frac{K'' M_s}{2n_f}$. M_s is the saturation magnetization. M_x is the material magnetization along the x direction. Based on the non-diagonal and non-symmetric permittivity tensor in (1-2), magneto-optical effects can be derived using Maxwell equations discussed in section 1.2.2 and 1.2.3 below. Note that here we focus on the real part of the off-diagonal tensor. The imaginary part causing magneto-optical dichroism can be derived similarly, and is related to the real part following the Kramers-Kronig relations.

1.2.2 The Faraday Effect

For a magneto-optical medium in Faraday configuration with applied field and incident light along the z axis, the permittivity tensor can be expressed as: [24]

$$\hat{\varepsilon} = \begin{pmatrix} \varepsilon_1 & -ig & 0 \\ ig & \varepsilon_1 & 0 \\ 0 & 0 & \varepsilon_z \end{pmatrix} \tag{1-3}$$

For a planar wave with $E = E_{xy}\exp[-i(wt - kz)]$, Maxwell equations require that: [24]

$$\nabla^2 \overline{E} + \omega^2 \hat{\mu}\hat{\varepsilon}\overline{E} = 0 \tag{1-4}$$

by substituting (1-3) into (1-4) and solving the equation, one obtains the two eigenmodes of a Faraday rotator: [24]

$$e_+ = 1/\sqrt{2}\begin{pmatrix}1\\-i\end{pmatrix}\exp[-i(\omega t - c^{-1}n_+ z)] \tag{1-5}$$

$$e_- = 1/\sqrt{2}\begin{pmatrix}1\\+i\end{pmatrix}\exp[-i(\omega t - c^{-1}n_- z)] \tag{1-6}$$

which are left and right circular polarized light. For linearly polarized incident light, the electric field can be written as a linear combination of these two eigenmodes as: [24]

$$E(0) = \begin{pmatrix}1\\0\end{pmatrix} = \frac{1}{\sqrt{2}}E_0 e_+ + \frac{1}{\sqrt{2}}E_0 e_- \tag{1-7}$$

After propagating for distance z, the electric field is: [24]

$$E(z) = \begin{pmatrix}\cos\theta\\-\sin\theta\end{pmatrix}\exp(-i\phi) = E_0\begin{pmatrix}\cos(c^{-1}\omega\Delta n z)\\-\sin(c^{-1}\omega\Delta n z)\end{pmatrix}\exp[-i\omega(t - c^{-1}n_0 z)] \tag{1-8}$$

Obviously, this is still a linearly polarized light with polarization plane rotated by $-\theta$ with respect to the incident light, provided that ε_1 and $\Delta n = (1/2)n_0 Q$ where $Q = {}^{g}/_{\varepsilon_1}$ are both real. This phenomenon is called the Faraday Effect, and was firstly observed by Michael Faraday in 1845. The Faraday rotation angle can be expressed as: [24]

$$\theta = -c^{-1}\omega\Delta n z = -\frac{\omega n_0}{2c}Qz \tag{1-9}$$

For isolator applications, the figure of merit (FoM) defined by the Faraday rotation devided by the material loss per length is a criterion for material usefulness. Recently, Alex et. al. proved that the figure of merit can be expressed by a first order approximation as [27]:

$$FoM = \frac{\mathrm{Re}(g)}{\mathrm{Im}(g) + \mathrm{Im}(\varepsilon_1)} \tag{1-10}$$

In integrated magneto-optical devices, a slab waveguide or ridge waveguide structure is usually used as shown in figure 1-5. When magnetized along the z direction, the Faraday Effect manifests itself as a mode conversion between TE and TM polarized modes. Optical birefringence arises in such devices, which causes difference between the first and second diagonal component of tensor (1-3) and the Faraday rotation can no longer be expressed in

equation (1-9). The waveguide birefringence comes from several issues including structural birefringence [27], stress [28] or growth induced birefringence [29], which significantly limits the Faraday rotation of the integrated devices. Due to the different modal index of the TE and TM modes, the coupling efficiency is limited. Quantitatively, Tabor and Chen [30] derived the analytical expression of Faraday rotation in a birefringent medium. Using a perturbation method [25], Dötch showed that the mode conversion efficiency of TE and TM modes in a photonic waveguide can be expressed by:

$$\frac{\left|A^{TM}(L)\right|^2}{\left|A^{TE}(L)\right|^2} = \frac{|k|^2}{|k|^2 + \frac{\Delta\beta^2}{4}} \sin^2\left(L\sqrt{|k|^2 + \frac{\Delta\beta^2}{4}}\right) \tag{1-10}$$

where $A^{TM}(z)$ and $A^{TE}(z)$ are the amplitudes of TM and TE polarized light, k is the coupling constant defined by $k = \frac{\omega\varepsilon_0}{4}\iint \vec{E}^{*TE}\Delta\varepsilon\vec{E}^{TM}dxdy$, and $\Delta\beta = \beta^{TM} - \beta^{TE}$ is propagation constant difference caused by the birefringence. Note a complete TE-TM mode conversion can only be achieved when $\Delta\beta = 0$.

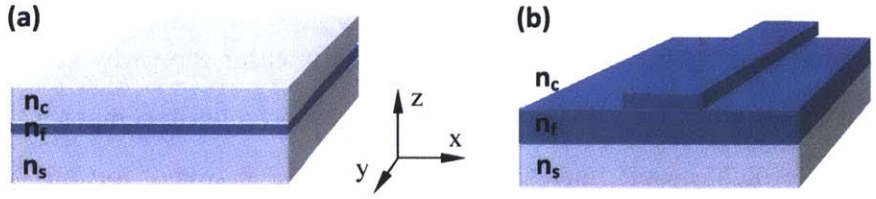

Fig. 1-5 A typical slab waveguide (a) and a ridge waveguide (b) used in integrated photonics. The waveguides are consisted of one substrate layer (index n_s) one film layer (index n_f) and one top cladding layer (index n_c), with $n_f > n_s$ and $n_f > n_c$.

1.2.3 The Voigt/Cotton-Mouton effect

For the Voigt geometry, where the light is propagating along the z direction and the magnetic field is along y direction the permittivity tensor will be: [24]

$$\hat{\varepsilon} = \begin{pmatrix} \varepsilon_{11} & 0 & jg \\ 0 & \varepsilon_{11} & 0 \\ -jg & 0 & \varepsilon_{11} \end{pmatrix} \tag{1-11}$$

Following a similar derivation as the Faraday Effect, the eigenmodes are found to be linearly polarized: [24]

$$\begin{cases} d_{//} = \begin{pmatrix} 0 \\ 1 \end{pmatrix} \exp[-j\omega(t - c^{-1} n_{//} x)] \\ d_{\perp} = \begin{pmatrix} 1 \\ 0 \end{pmatrix} \exp[-j\omega(t - c^{-1} n_{\perp} x)] \end{cases} \quad (1\text{-}12)$$

where $n_{//} = \sqrt{\varepsilon_0}$ and $n_{\perp} = (\varepsilon_1 - g/\varepsilon_0)^{1/2}$. This equation states that the medium is linearly birefringent to light with polarizations parallel or perpendicular to the magnetic field directions.

In integrated magneto-optical devices, a new phenomenon called Nonreciprocal phase shift (NRPS) appears due to the field asymmetry in a magneto-optical material with the Voigt geometry. In waveguide geometries shown in figure 1-5, when the waveguide is magnetized along the x direction, the propagation constants of TM polarized light will be different between forward and backward propagating directions due to the modal asymmetry in the magneto-optical material along the y direction. Similar effect exists for TE polarized light when magnetic field is along the y axis and modal asymmetry exists along x direction. An analytical expression of this effect is described by Mizumoto *et al.* [1] in a slab waveguide structure shown in figure 1-5 (a) with a permittivity tensor shown by equation (1-11), the characteristic equation of the TM modes is found to show a linear component of propagation constant β, which means that β is nondegenerate between forward and backward propagation directions. By applying perturbation theory, Dötch showed that the NRPS in photonic waveguides can be expressed as [25]:

$$\Delta\beta^{TM} = -\frac{2\beta^{TM}}{\omega\varepsilon_0 N} \iint \frac{K'' M_y}{n_0^4} H_y \partial_x H_y \, dx dy \quad (1\text{-}13)$$

This equation shows that the NRPS is proportional to the Faraday rotation and the field gradient in the magneto-optical material. Note that in bulk materials, the term of $\partial_x H_y$ is trivial, and the NRPS effect vanishes. A detailed discussion and simulation of our NRPS devices will be based on this equation in chapter 4, chapter 5 and chapter 6.

1.3 Magneto-Optical materials and semiconductor integration

To evaluate the usefulness of a magneto-optical material, a figure of merit based on Faraday rotation is defined as:

$$FoM = \frac{\Theta}{\alpha} \tag{1-14}$$

where Θ and α are the Faraday rotation and absorption coefficient per length of the material. For semiconductor integration, another criterion is the compatibility with semiconductor substrates and fabrication techniques to achieve high quality magneto-optical materials. A simultaneous satisfaction of both high FoM and semiconductor compatibility is a prerequisite for material applications in high quality semiconductor integrated magneto-optical devices. However, all magneto-optical materials known so far are having either FoM or integration problems. Therefore explorations of new materials or novel integration technologies for conventional materials are highly desired for integrated nonreciprocal photonic device applications.

In this section, we will discuss several magneto-optical material candidates. As we mentioned in 1.2.1, the magneto-optical effect is related to the electronic states with different total angular momenta. To achieve a macroscopic magneto-optical effect, the total angular momentum of magneto-optical ions has to be macroscopically aligned. This is usually done by spin-orbital coupling in a ferromagnetic/ferrimagnetic material under an external magnetic field. Several magneto-optical oxides including iron garnets, orthoferrites and magnetic perovskites show high Faraday rotation as well as low optical absorption coefficient. They are considered to be candidates for nonreciprocal photonic devices such as optical isolators..

- **Iron Garnets (Chemical Formula: $A_3Fe_5O_{12}$)**

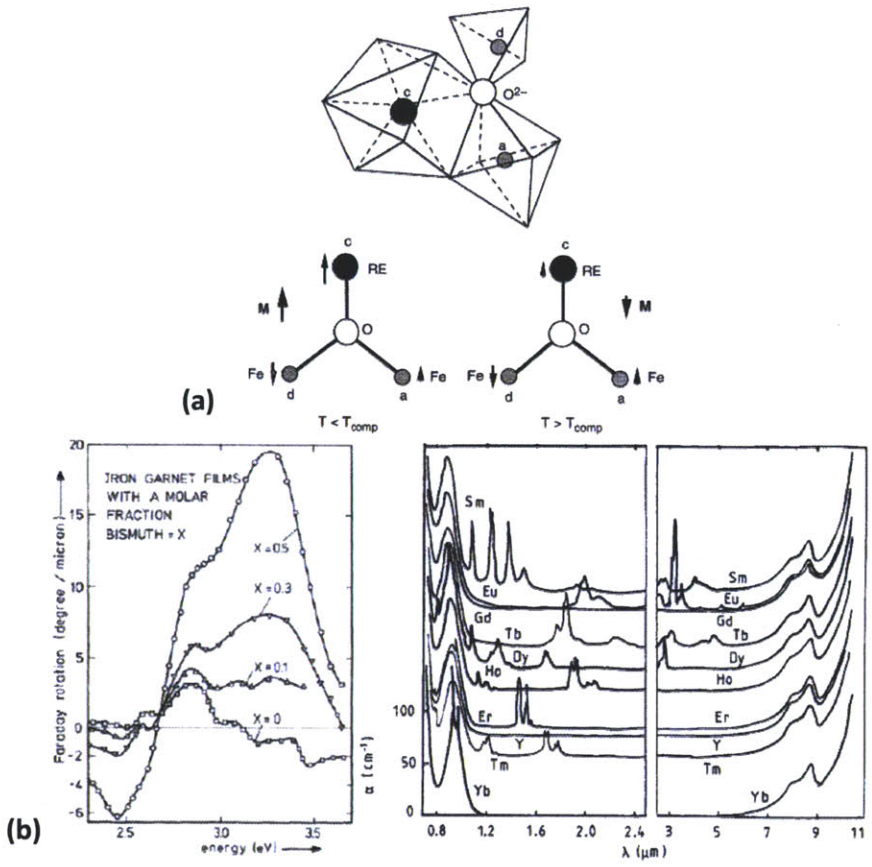

Fig. 1-6 (a) Garnet crystal structure showing the tetrahedral, octahedral and dodecahedral oxygen coordinated sites. [34] (b) The Faraday rotation of $Bi_xY_{3-x}Fe_5O_{12}$ film and the optical transparency of garnet materials in the infrared wavelengths. [35]

Iron garnet materials have a large unit cell which contains 8 formula units. Three kinds of cation sites are present in the garnet lattice with different oxygen coordination numbers as shown in figure 1-6 (a), where sites a, d and c are octahedral, tetrahedral and dodecahedral sites respectively. 24 of the magnetic Fe^{3+} ions occupy the tetrahedral sites and 18 of them occupy the octahedral sites. These ions couple antiferromagnetically between tetrahedral and octahedral sites. The net magnetization is due to the rest of the tetrahedral ions. The dodecahedral sites are usually occupied by large rare earth irons. When this iron has net moment on the 4f shells such as Gd^{3+}, a compensation temperature occurs in the saturation magnetization temperature curve. Examples for iron garnets used in optical isolator and circulators are $Y_3Fe_5O_{12}$ (YIG), $Bi_3Fe_5O_{12}$ (BIG) and $(Ce_1Y_2)Fe_5O_{12}$. Figure 1-6 (b) shows the Faraday rotation spectrum of Bi doped YIG and optical absorption spectrum of some garnet materials. Iron garnets show high transparency (α<0.05 dB/cm at 1550 nm) as well as

strong Faraday rotation in the near infrared wavelengths. For Bi and Ce doped YIG, the Faraday rotation can achieve the order of -10^3 deg/cm at 1550 nm while maintaining low optical absorption. The strong Faraday rotation is due to the enhancement of electronic states splitting of Fe ions by Bi $6s^2$ electron pairs [32] for Bi doped YIG, or due to electronic transitions in Ce^{3+} ions magnetically aligned with Fe^{3+} ions in the garnet lattice for Ce doped YIG [33]. Typical FoM of single crystal garnet materials is larger than 100 deg/dB, making them widely used in commercial optical isolators.

However, this material is hard to integrate to Si platform due several reasons. Firstly, garnets have a complex unit cell structure and much larger lattice parameter compared with semiconductors (YIG:12.376 Å, Si: 5.43 Å, GaAs: 5.65 Å), which excludes the possibility of heteroepitaxial growth of garnet films on a conventional semiconductor substrate; Secondly, the thermal expansion coefficient of YIG (10.4×10^{-6} /°C) is much larger than Si (2.33×10^{-6} /°C), GaAs(5.73×10^{-6} /°C), InP(4.75×10^{-6} /°C) or SiO_2(0.55×10^{-6} /°C). Cracks can easily generate in crystallized YIG films on silicon when the thickness exceeds the critical value of about 100 nm; [36] Thirdly, crystallization of the garnet phase usually requires a high thermal budget. Also impurity phases such as $YFeO_3$, Fe_2O_3 and Bi_2O_3 can precipitate out during the crystallization process [37], which may cause optical scattering loss in integrated photonic devices. These factors make the fabrication of high optical quality magnetic garnet films and also optical isolators on semiconductor substrates very difficult.

Progresses in monolithic integration of garnet materials on silicon has been made in the past decade. Stadler *et al.* demonstrated integration of $Y_3Fe_5O_{12}$ polycrystalline thin films and waveguides on silicon using sputter deposition and rapid thermal annealing. [38][39] Amorphous YIG films were deposited by co-sputtering Y and Fe targets in Ar and O_2. The films were crystallized in pure YIG phase by rapid thermal annealing at 750 °C for 5 s. Köner *et al.* reported the stabilization of $Bi_3Fe_5O_{12}$ phase on a furnace annealed polycrystalline YIG film on SiO_2 [40]. Polycrystalline $Bi_3Fe_5O_{12}$ garnet phases were confirmed by XRD and TEM measurements. Strong Faraday rotation was observed from the $Bi_3Fe_5O_{12}$ layer.

Despite this progress, the optical loss of polycrystalline garnets still needs to be systematically studied before these materials can be considered applicable in a semiconductor integrated magneto-optical device. Integration and loss analysis of photonic devices based on these materials will be carried out in chapter 5 and chapter 6 of this thesis.

- **Orthoferrites (Chemical Formula: $AFeO_3$)**

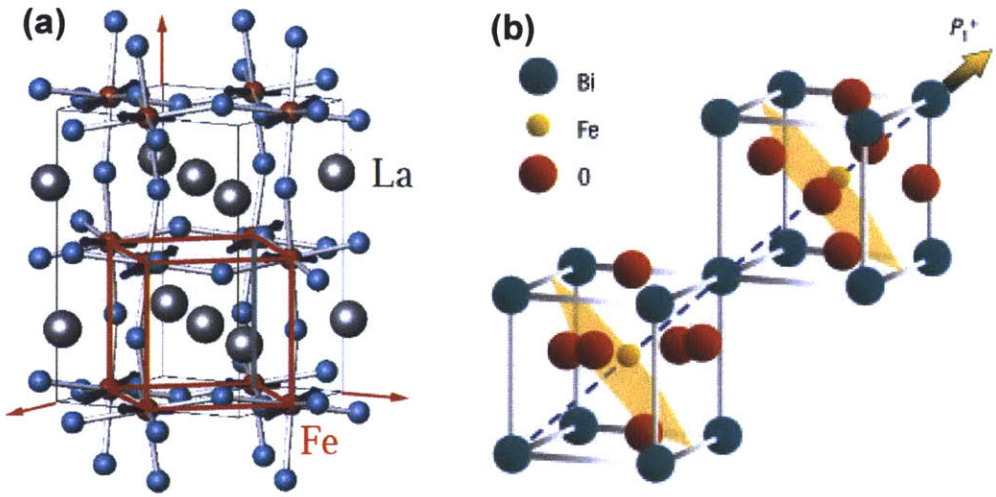

Fig. 1-7 Lattice structure of (a) $LaFeO_3$ [42] and (b) $BiFeO_3$ [43]

The orthoferrites are a class of distorted perovskites having Fe^{3+} ions in the B site and octahedrally coordinated with O^{2-} ions, whereas the A site is occupied by large rare earth ions. As an example, figure 1-7 shows the lattice structure of $LaFeO_3$ and $BiFeO_3$. $BiFeO_3$ and Bi double perovskites may provide high Faraday rotation provided that Bi^{3+} ions show strong covalent interactions with the octahedral complexes as occurs in garnet materials. This process enhances the non-degeneracy of the spin-orbit coupling levels as well as the Faraday rotation of the material as observed in garnets. Due to the distorted cell structure, orthoferrites are weakly ferromagnetic with the spin of Fe^{3+} slightly "canted" at about 0.5° from 180° antiferromagnetic coupling direction, therefore offering not fully cancelled ferromagnetism and Faraday rotation from the Fe sublattices at room temperature. The Faraday rotation and optical absorption of bulk orthoferrites were studied in the 1970's. It has been found that the intrinsic Faraday rotation (Faraday rotation for light propagating along optical axis and not

influenced by material birefringence) is about 3 times that of YIG at a wavelength region from 600 to 1800nm [41], while the optical absorption remains low as $\alpha < 0.5\ cm^{-1}$. [35] These materials seem to be more promising for integrated nonreciprocal photonic devices by appreciating that the orthoferrites are much better lattice matched with silicon compared to garnets, which offers the opportunity of epitaxial growth on silicon.

However, integration of orthoferrites is also challenging due to several factors. Firstly, the magnetization of these materials are small (~5emu/cm^3 compared to 140emu/cm^3 in YIG) and is dependent on the lattice structure such as the canting angle α. [44] Strain and lattice distortion in epitaxial films may influence the material properties significantly. Secondly, the phase purity and thermal budget are issues for fabricating orthoferrite thin films. Schmool *et al.* deposited orthoferrite thin films on quartz substrates by PLD. [45] High temperature furnace annealing up to 860°C for 1hr is required for film crystallization. Impurity phases such as garnets and iron oxides were found in films. Thirdly, multiple crystal orientations may appear in expitaxial non-cubic orthoferrites deposited on cubic semiconductor substrates, which needs to be controlled for low optical scattering in planar photonic devices.

To investigate the properties of integrated orthoferrite films, a study on $BiFeO_3$ and Bi_2FeMnO_6 thin films is described in chapter 3. A structural analysis on the multiple crystal orientations of an epitaxial $LaFeO_3$ film on $SrTiO_3$ substrates is also described in the same chapter.

- **Magnetic Perovskites (Chemical Formula: ABO_3)**

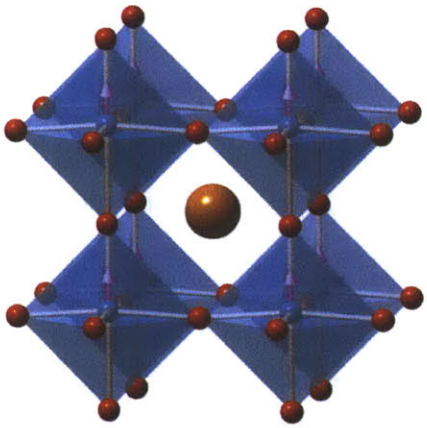

Fig. 1-8 Lattice structure of a $BaTiO_3$ unit cell [46]

Different from orthoferrites, regular perovskite materials show cubic or tetragonal lattices, therefore can be epitaxially grown on semiconductor substrates with a single orientation. Examples include $SrTiO_3$, $BaTiO_3$ and $(LaSr)MnO_3$, and the lattice structure is shown in figure 1-8. Regular perovskites usually show antiferromagnetism when they are doped on the B site with transition metal ions due to the 180° B-O-B bonding angle following the Goodenough-Kanamori theory. When multiple valence states exist on the B site, ferrimagnetism or even ferromagnetism occur due to double exchange, for example $(LaSr)MnO_3$ is room temperature ferromagnetic. Cho et. al [47]. reported a Faraday rotation of -2.6 deg/μm for $La_{0.82}Sr_{0.18}MnO_3$ at 2.9 eV. The FoM of $(LaSr)MnO_3$ is limited by free carrier absorption in the metallic material.

Compared with garnets and orthoferrites, challenges of perovskite materials come from achieving room temperature ferromagnetism with high material FoM. Recently, Fe doped $BaTiO_3$ and $BaZrO_3$ films show room temperature ferromagnetism. Rajamani *et al.* observed a promising Faraday rotation of 330 deg/cm and a FOM of 3.7 deg/dB in $Ba(Ti_{0.8}Fe_{0.2})O_3$ films at room temperature. [48] Systematic studies on the origin of the ferromagnetism of these material systems are required. Controlling the material properties to achieve higher FoM is also needed for practical applications. These issues will be studied in chapter 4.

Other than the materials mentioned above, several other materials not being studied in this

thesis are also under active research. Spinel ferrites, which are room temperature ferrimagnetic materials show significant magneto-optical activity in the communication wavelengths. These materials are limited by high optical absorption and low FoM at such wavelengths. The mechanism of optical absorption is still not clearly understood. But it is found the absorption coefficient is proportional to the multiplication of the octahedral and tetrahedral Fe populations [49], suggesting that the absorption may be due to charge transfer between two sites and directly coupled with the ferrimagnetism. Recently, it has been demonstrated that optical absorption in nanoparticle spinels are significantly lower than its bulk counterpart [50]. Efforts of integrating magneto-optical waveguides based on these nanoparticles have been carried out [51]. However the device figure of merit is still far from application requirements. Transition metal ion doped magnetic semiconductors are also studied in the waveguide geometry for magneto-optical performances [22]. These materials are based on compound semiconductors such as Mn doped GaAs and Fe doped InP due to higher solubility of transition metal ions in the lattice compared to group IV semiconductors, and are paramagnetic at room temperature. High Verdet constant (Faraday rotation per unit length and per unit applied magnetic field) and FoM are achieved in materials with bandgap energies close to the operation wavelength. However, these materials need high field up to 1T for application, which is challenging in integrated devices.

1.4 Integrated nonreciprocal photonic devices

A variety of integrated nonreciprocal photonic devices have been studied based on Faraday or Voigt effects. In this section, a review of these devices will be carried out with a focus on the progresses of semiconductor integration. Three types of optical isolators based on nonreciprocal mode conversion (NRMC), nonreciprocal phase shift (NRPS) and nonreciprocal loss (NRL) will be discussed. Finally several recently proposed semiconductor compatible non-magneto-optical isolators including nonreciprocal Raman amplification, nonreciprocal optical force and nonreciprocal photonic transitions will be introduced.

- **Nonreciprocal mode conversion (NRMC) devices**

A natural way of integrating optical isolators in a planar geometry is using the Faraday Effect, which causes TE and TM mode conversion in a waveguide geometry. Efforts have been carried out on epitaxial garnet films on single crystal garnet substrates since the 1980's. [52] [53] For efficient mode conversion, a buried channel waveguide geometry was fabricated to eliminate the total birefringence. [52] Annealing and etching processes have also been carried out for birefringence elimination and was demonstrated experimentally. [53] An alternative way to cancel out the birefringence effect is called quasi phase matching (QPM), in which the sign of Faraday rotation is periodically reversed along the waveguide direction by annealing or chemical design of the magneto-optical material. [54] An isolation ration of -31 dB and insertion loss of 1.5-3dB was demonstrated in these devices. [53]

In case of semiconductor integration, Yokoi *et al.* proposed optical isolation by wafer bonding of a single crystal Ce:YIG on GaInAsP waveguide on InP substrate. The simulated device size for 45° Faraday rotation is up to hundreds of micron meters due to the small confinement factor in the garnet crystal. [55] Monolithic integration of YIG waveguides on silicon substrates have been carried out by Stadler *et al.* [39] By first etching the sputter deposited amorphous YIG layer followed by a rapid thermal annealing step, crack free polycrystalline YIG waveguides are demonstrated on silicon. The waveguides showed a propagation loss of 15.5dB/cm and the birefringence can be tuned by etching the waveguide geometry. Holmes *et al.* deposited Ce:YIG films on GaAs waveguides on AlGaAs bottom cladding with a QPM geometry and qualitatively demonstrated mode conversion in such structures. [54] Magnetic semiconductor materials of Fe doped InP or InGaAsP were also integrated in a waveguides on InP substrates. [22] A Faraday rotation of 100deg/cm/T and propagation loss of 4.34dB/cm was observed in these waveguides, which may be further optimized by tuning the bandgap of the magnetic semiconductor material.

- **Nonreciprocal phase shift (NRPS) devices**

Because of the difficulty of tuning the device birefringence in magneto-optical waveguides, another magneto-optical effect called nonreciprocal phase shift (NRPS) is used for optical isolation. As we discussed in chapter 1.2.3, the propagation constant of a magneto-optical

waveguide is nonrecriprocal in the Voigt geometry. This effect can be used in interferometers to achieve optical isolation. A schematic plot of a Mach-Zehnder isolator is shown in figure 1-9. When the magneto-optical materials on both arms of the interferometer are magnetized perpendicular to the waveguides and along opposite directions, NRPS with different signs are achieved so that light constructively interferes at the transmission side and destructively interferes when reflected back to the incident side. The first NRPS optical isolator design was demonstrated by Aurature *et al.* back in 1975 [56]. Several groups developed such Mach-Zehnder isolators on epitaxial garnet films on single crystal garnet substrates. [57][58] Isolation ratio up to -19dB and excess loss of 2dB was reported. [58]

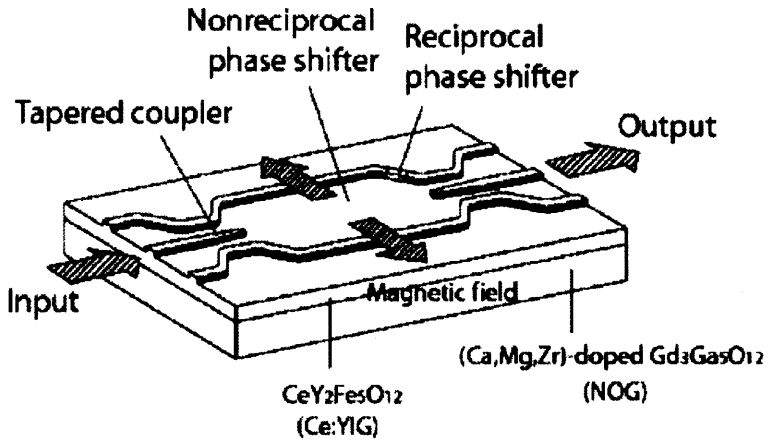

Fig. 1-9 A schematic plot of a Mach-Zehnder interferometer based optical isolator [57]

For semiconductor integration, Mizumoto *et al.* recently demonstrated successful wafer bonding of single crystal Ce:YIG on silicon Mach-Zehnder interferometers. [1] An isolation ration of -21dB and insertion loss of 8dB is observed in this device. Monolithic integration strategies of NRPS devices are limited by the magneto-optical materials on silicon. Several device structures based on monolithic thin film materials and optical resonance have been proposed. Photonic crystals [59], garnet thin film base optical resonators [60] and magneto-optical polymer based optical resonators [61] were simulated. However experimental demonstration is still lacking due to the difficulty of patterning the magneto-optical material, magnetic field, or relying on the modal asymmetry in the bending region of the resonators.

- **Nonreciprocal loss (NRL) devices**

There is a special kind of nonreciprocal photonic devices based on nonreciprocal loss of the device which is achieved by placing an absorptive magnetic metal close to an optical gain medium such as a semiconductor optical amplifier (SOA) in the device. Figure 1-10 shows a schematic plot and the SEM image of such a device. The ferromagnetic metal is magnetized perpendicular to the light propagation direction. The refractive index of the magnetic metal is different between the forward and backward propagating light, therefore the confinement factor and loss in the metal is different, and an optical nonreciprocity is observed in the active device. Isolation ratios of 14.7 dB/mm for TE mode at 1.3 μm wavelength [62] and 9.9 dB/mm at 1.55 μm wavelength [63] have been demonstrated so far. Different from NRMC and NRPS isolators, the isolation ratio in these devices is proportional to the device length. Therefore very high isolation ratio can be achieved provided the device is long enough.

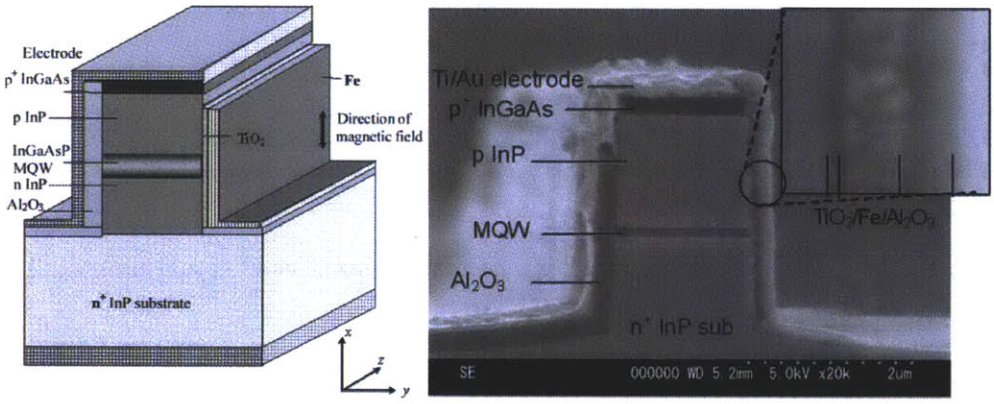

Fig. 1-10. (a)Schematic plot and (b) SEM image of a NRL isolator [62]

Despite the simple design and good isolation ratios, NRL devices shows several drawbacks compared to NRMC and NRPS devices. Firstly, the loss level of these devices is high due to the presence of the metal layer. Propagation loss as high as 7.1 dB/mm is observed [62], which is significantly higher than practical requirements. Secondly, NRL devices are active devices. Power dissipation is needed for device operation which is undesired. Thirdly, amplification of spontaneous emission also takes place in the SOA, which degrades the laser and isolator module performance.

Different from magneto-optical nonreciprocal photonic devices discussed above, non-magneto-optical devices were also proposed recently. Manipatruni *et al.* proposed an optical isolator based on nonreciprocal optomechanical structures. [4] The device uses the different optomechanical forces between forward and backward propagating light on a Fabry-Perot cavity with one movable and one fixed mirror to achieve nonreciprocal optical resonance and isolation, resembling a gas or liquid one-way valve. Krause *et al.* proposed that stimulated Raman emission in silicon waveguides can be used in nonreciprocal photonic devices. [3] This effect is based on different amplitude stimulated Raman emission when the signal light and pump light is propagating in the same or opposite directions. Yu and Fan proposed that by dynamically modulating the index of refraction of a silicon waveguide in a manner of propagating wave, optical nonreciprocity can be achieved. This is due to Nonreciprocal interband photonic transitions between different modes in the waveguide taking place only in one direction of light propagation. [2] Fundamentally, all these novel devices are based on phenomena related to the different signs of wave vector between forward and backward propagating lights. Due to fabrication difficulties, none of these devices have been experimentally realized yet.

From the introductions of materials and devices above, we can summarize the current status of semiconductor integration of nonreciprocal photonic components. For magneto-optical materials, challenges still remain in either monolithically integrating garnet materials or exploring new materials with high figure of merits; for devices, monolithically integrated devices are still lacking. Improving the performance as well as reducing the footprint is critical for the application of such devices in photonic integrated circuits. In the following chapters of this thesis, we will try to resolve these challenges by providing both materials and device solutions both by experimental study and theoretical simulations. By the end of the thesis, we hope to provide improved magneto-optical thin film materials for semiconductor integration, an experimentally demonstrated monolithically integrated on-chip nonreciprocal photonic device, and theories to understand both the material and device performances for future integrated nonreciprocal photonic systems.

References

[1] Y. Shoji, T. Mizumoto, H. Yokoi, I. Hsieh and R. M. Osgood, *Appl. Phys. Lett.*, **92**, 071117 (2008).

[2] Z. Yu and S. Fan, *Nature Photonics*, **3**, 91 (2009).

[3] M. Krause, H. Renner and E. Brinkmeyer, *Electronics Letters*, **44**, 691 (2008)

[4] S. Manipatruni, J. T. Robinson and M. Lipson, *Phys. Rev. Lett.*, **102**, 213903 (2009)

[5] L.C. Kimerling, The economics of science: from photons to products, in: *Optics and Photonics News*, Optical Society of America, Washington, DC, pp. 19–52, October, 1998

[6] L.C. Kimerling, *Appl. Surf. Sci.*, **159-160**, 8 (2000)

[7] M. Paniccia, *Nature Photonics*, **4**, 498 (2010)

[8] W. M. Green, M. J. Rooks, L. Sekaric, and Y. A. Vlasov, Optics Express, **15**, 17106 (2007)

[9] S. Assefa, F. Xia and Y. A. Vlasov, *Nature*, **464**, 80 (2010)

[10] J. F. Liu, J. Michel, W. Giziewicz, D. Pan, K. Wada, D. D. Cannon, S. Jongthammanurak, D. T. Danielson, L. C. Kimerling, J. Chen, F. O. Ilday, F. X. Kartner and J. Yasaitis, *Applied Physics Letters*, **87**, 10 (2005)

[11] R. Sun, J. Cheng, J. Michel and L. Kimerling, *Optics Letters*, **34** 15 (2009)

[12] J. S. Levy, A. Gondarenko, M. A. Foster, A. C. Turner-Foster, A. L. Gaeta and M. Lipson, *Nature Photonics*, **4**, 37 (2010)

[13] Q. Xu, B. Schmidt, S. Pradhan and M. Lipson, *Nature*, **435** 325 (2005)

[14] J. F. Liu, X. C. Sun, R. Camacho-Aguilera, L. C. Kimerling and J. Michel, *Optics Letters*, **35,** 5 (2010)

[15] E. M. Yeatman, M. M. Ahmad, O. McCarthy, A. Vannucci, P. Gastaldo, D. Barbier, D. Mongardien and C. Moronvalle, *Optics Comm.*, **164**, 19 (1999)

[16] E. J. Klein, D. H. Geuzebroek, H. Kelderman, G. Sengo, N. Baker and A. Driessen, *IEEE Photon. Tech. Lett.*, **17**, 2358 (2005)

[17] E. Little, J. S. Foresi, G. Steinmeyer, E. R. Thoen, S. T. Chu, H. A. Haus, E. P. Ippen, L. C. Kimerling and W. Greene, *IEEE Photon. Techn. Lett.*, **10,** 4 (1998)

[18] N. Schunk and K. Petermann, *Electron. Lett.*, **25**,63 (1989)

[19] H. Temkin, N. Olsson, J. Abeles, R. Logan and M. Panish, *IEEE Quant. Electron.*, **22**, 286 (1986)

[20] A. Chraplyvy, D. Marcuse and R. Tkach, *J. Light. Techn.*, **4**, 555 (1986)

[21] M. Levy, *IEEE J. Sel. Topics Quant. Electron.*, **8**, 1300 (2002)

[22] T. R. Zaman, X. Guo, and R. J. Ram, *J. Light. Techn.*, **26**, 291 (2008)

[23] I. Hidetoshi, I. Hiroshi, K. Iwasaki, Y. Kubodera, J. Torii, N. Juichi, *Electron. Lett.*, **15**, 830 (1979)

[24] A. K. Zvezdin and V. A. Kotov, *Modern Magnetooptics and Magnetooptical Materials*, Institute of Physics Publishing, Bristol and Philadelphia, 1997

[25] H. Dötsch, N. Bahlmann, O. Zhuromskyy, M. Hammer, L. Wilkens, R. Gerhardt and P.Hertel, *J. Opt.Soc. Am. B*, **22**, 240,(2005)

[26] C. S. James, *IEEE Trans. Magn.*, **K4G-8,** 95 (1972)

[27] A. Taussig, G. F. Dionne and C. A. Ross, *Phys. Rev. B*, **77**, 021407 (2008)

[27] M. Tateda, and T. Kimura, *IEEE J. Quant. Electron.*, **18**, 1975 (1982)

[28] H. Dammann, E. Pross, G. Rabe, W. Tolksdorf, and M. Zinke, *Appl. Phys. Lett.*, **49**, 1755 (1986)

[29] K. Ando, N. Koshizuka, T. Okuda and Y. Yokoyama, *J. J. Appl. Phys.*, **22**, 618 (1983)

[30] W. J. Tabor and F. S. Chen, *J. Appl. Phys.*, **40**, 2760 (1969)

[31] T. Mizumoto and Y. Naito, *IEEE Trans. on Microwave Theory and Techniques*, **MTT-30**, 922 (1982)
[32] G. F. Dionne and G. A. Allen, *J. Appl. Phys.*, **75**, 6372 (2004)
[33] M. Gomi, H. Furuyama and M. Abe, *J. J. Appl. Phys.*, **29**, L99 (1991)
[34] G. F. Dionne, *Magnetic Oxides*, Springer, 2009
[35] D. L. Wood and J. P. Remeika, *J. Appl. Phys.*, **38**, 3 (1967)
[36] T. Boudiar, B. Payet-Gervy, M. -F. Blanc-Mignon, J. -J. Rousseau, M. Le Berre and H. Joisten, *J. Magn. Magn. Mater.*, **284**, 77 (2004)
[37] N. Kumar, D.S. Misra, N. Venkataramani, Shiva Prasad and R. Krishnan, *J. Magn. Magn. Mater.*, **272 - 276**, e899 (2004)
[38] S. Sung, X. Qi and B. J. H. Stadler, *Appl. Phys. Lett.*, **87**, 12111 (2005)
[39] S. Sung, X. Qi and B. J. H. Stadler, *CLEO* (2007).
[40] T. Körner, A. Heinrich, M. Weckerle, P. Roocks and B. Stritzker, *J. Appl. Phys.*, **103**, 07B337 (2008)
[41] W. J. Tabor, A. W. Anderson, and L. G. Van Uitert, *J. Appl. Phys.*, **41**, 7 (1970)
[42] J. W. Seo, J. Fompeyrine, H. Siegwart and J. Locquet, *Mat. Res. Soc. Symp. Proc.*, **666**, F8.8.1 (2001)
[43] T. Zhao, A. Scholl, F. Zavaliche, K. Lee, M. Barry, A. Doran, M. P. Cruz, Y. H. Chu, C. Ederer, N. A. Spaldin, R. R. Das, D. M. Kim, S. H. Baek, C. B. Eom and R. Ramesh, *Nature Materials*, **5**, 823 (2006)
[44] R. S. Tebble and D. J. Craik, *Magnetic Materials* , Wiley-Interscience,New York, 1969
[45] D. S. Schmool, N. Keller, M. Guyot, R. Krishnan, and M. Tessier, *J. Appl. Phys.*, **86**, 5712 (1999)
[46] The perovskite lattice, *http://www.camsoft.co.kr/CrystalMaker/graphics/resources/hires/perovskite.jpg*, 2008
[47] J. Cho, M. Gomi and M. Abe, J. J. Appl. Phys., **29**, 1686 (1990)
[48] A. Rajamani, G. F. Dionne, D. Bono and C. A. Ross, *J. Appl. Phys.*, **98**, 063907 (2005)
[49] G. B. Andreozzi, U. Halenius, H. Skogby, *Phys. Chem. Minerals*, **28**, 435 (2001)
[50] R. F. Ziolo, E. P. Giannelis, B. A. Weinstein, M. P. O'Horo, Bi. N. Ganguly, V. Mehrotra, M. W. Russell and D. R. Huffman, *Science*, **257**, 219 (1992)
[51] F. Choueikani, F. Royer, D. Jamon, A. Siblini, J. J. Rousseau, S. Neveu and J. Charara, *Appl. Phys. Lett.*, **94**, 051113 (2009)
[52] E. Pross, W. Tolksdorf, and H. Dammann, *Appl. Phys. Lett.*, **52**, 682 (1988)
[53] N. Sugimoto, H. Terui, A. Tate, Y. Katoh, Y. Yamada, A. Sugita, A. Shibukawa and Y. Inoue, *J. Lightwave Technol.*, **14**, 2537 (1996)
[54] B. M. Holmesa and D. C. Hutchings, *Appl. Phys. Lett.*, **88**, 061116 (2006)
[55] H.Yokoi and T.Mizumoto, *Electron. Lett.*, **33**, 1787 (1997)
[56] F. Auracher and H. H. White, *Opt. Commun.*, **13**, 435 (1975)
[57] T. Mizumoto, S. Mashimo, T. Ida, and Y. Naito, *IEEE Trans. Magn.*, **29**, 3417 (1993)
[58] J. Fujita, M. Levy, R.M. Osgood Jr., L.Wilkens, and H. Dotsch, *Appl. Phys. Lett.*, **76**, 2158, (2000)
[59] Z. Wang and S. Fan, *Optics Letters*, **30**, 1989 (2005)
[60] N. Kono, K. Kakihara, K. Saitoh and M. Koshiba, *Optics Express*, **15**, 7737-7751 (2007)
[61] D. Jalas, A. Petrov, M. Krause, J. Hampe and M. Eich, *Optics Letters*, **35**, 3438-3440 (2010)
[62] H. Shimizu and Y. Nakano, *J. Lightwave. Technol.*, **24**, 38 (2006)
[63] W. Van. Parys, B. Moeyersoon, D. Van. Thourhout, R. Baets, M. Vanwolleghem, B. Dagens, J. Decobert, O. L. Gouezigou, D. Make, R. Vanheertum and L. Lagae, *Appl. Phys. Lett.*, **88**, 071115 (2006)

Chapter 2
Experiment and Simulation Methods

In this chapter, the experiment and simulation methods used in this thesis are introduced. All thin film oxide materials studied in this thesis were fabricated by pulsed-laser deposition (PLD), while the optical waveguides and resonators were fabricated by optical lithography, lift-off and e-beam lithography methods. Structural characterization methods including X-ray diffraction (XRD), vibrating sample magnetometry (VSM), superconducting quantum interference device (SQUID) magnetometry, Faraday rotation and ellipsometry were used to analyze the material structures and properties. Optical transmittance measurements were carried out on optical waveguides and resonators. First-principles simulation using density functional theory (DFT) was applied for the Bi-orthoferrite systems. Mode profile simulations of the optical waveguides were achieved by using the film mode matching (FMM) method in the FIMMWAVE software. Based on the mode profiles, magneto-optical nonreciprocal phase shift in the devices were also simulated by numerical methods.

2.1 Thin Film and Photonic Device Fabrication

2.1.1 Pulsed-laser deposition (PLD)

Pulsed-laser deposition is a physical vapor deposition technique, carried out in a vacuum system and sharing some of the characteristics of both evaporation and sputtering. Firstly used in the late 1980s [1], this technique was widely applied in complex oxide deposition and epitaxial growth. Compared to evaporation and sputtering, PLD is advantageous in maintaining good stoichiometry transfer from the target to the film and obtaining non-equilibrium phases in complex material systems. A schematic plot of this technique is shown in figure 2.1a. The film deposition is achieved by focusing a pulsed ultraviolet laser beam on a bulk target material, generating a small portion of the material in a plume form containing the atomic species of the bulk material in vacuum, and depositing on a substrate.

The essential components for the PLD are the laser, the optics, the chamber, the target and the substrate. Ultraviolet pulsed lasers are usually used such as KrF (λ=248nm) and Nd:YAG (λ=355nm). The pulse duration is typically in the range of nanoseconds. Because most materials are highly absorptive in these wavelengths, the laser energy can be effectively absorbed to generate plumes. The laser pulses are guided and focused by high quality quartz optical components to achieve high enough energy density (typically 2~5J/cm^2) on the target. To prevent particulates of melted droplets from the target, high density pellets of ceramics, metals or polymers are usually used for the target material. A high base pressure in the 10^{-6} Torr level or better in the PLD chamber is needed for material purity. Reactive gases such as O_2 are usually required both to maintain stoichiometry in the thin film material and to decrease the kinetic energy of the atoms in the plume. The substrate is usually placed close to the target in the order of several centimeters to allow homogenous deposition from the plume. The substrate is usually heated to achieve crystallization and epitaxial growth of the required phase in the film. The deposition process of PLD can be summarized in figure 2-2 (a) and can be separated into four steps. [2] In initial short periods (0.1~20ns), the laser pulse is absorbed the target material. At t~1μs, plume species (atomic, di-atomic, molecular and ionic) are generated on the target surface. At t~1-4 μs, these species travels towards the substrate in vacuum and finally deposit on the substrate at t~4 μs to form thin films. A typical plume generated in a PLD chamber is shown in figure 2-2 (b).

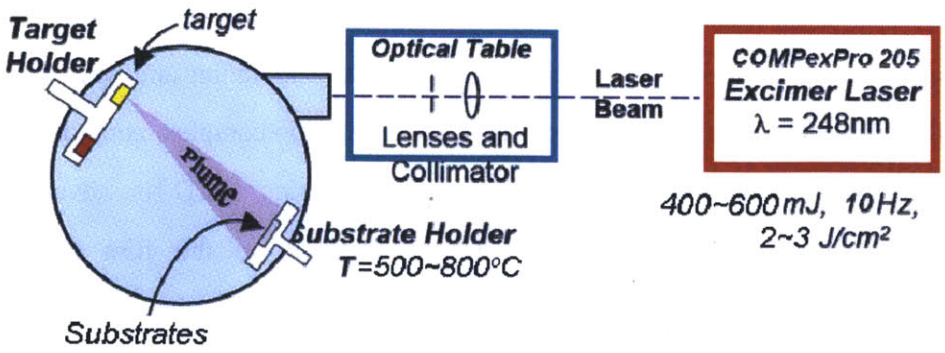

Fig. 2-1 A schematic plot of the pulsed-laser deposition system

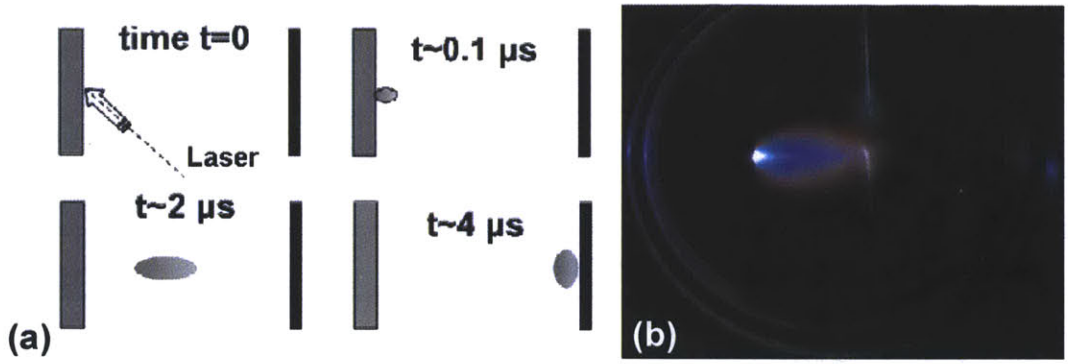

Fig. 2-2 (a) The PLD process [2] (b) A plume generated in a PLD chamber

Except $Bi_{1.2}FeO_3$ and $Bi_{2.4}FeMnO_6$ targets purchased from Plasmaterials Inc., all the targets used in this thesis were fabricated by standard ceramic fabrication methods. Precursor powders with the stoichiometric element ratios of the final target compositions were mixed and ball milled with YSZ (yttrium stabilized zirconia) grinding media for 24 hours in ethanol. The mixture was then dried and calcinated in a tube furnace in air to form the desired phase. Then the calcinated powders were uniaxial and cold isostatic pressed (CIP) at 40,000 psi for 2 min into a 1.1" diameter pellet. Finally, the pellet was transferred to a tube furnace and sintered to form the final target.

Several parameters are critical for PLD. They are the energy density E, the pulse rate h, the target to substrate distance d, the chamber pressure P and the substrate temperature T. Other than these controllable parameters, the laser specs, target and substrate materials are also important. For the experiments discussed in this thesis, we use a Coherent COMPexPro 205 KrF (248 nm) excimer laser. For all systems, the energy density were fixed to 2~3 J/cm^2. Before deposition, the chamber was pumped to a vacuum level of 5×10^{-6} torr. Then the substrate is heated to the desired temperature at a speed of 10 °C/min. Oxygen or vacuum conditions were adjusted after reaching the deposition temperature. After the deposition, the samples are cooled down to room temperature at a speed of 5 °C/min with or without high oxygen pressure for oxygen stoichiometry. The specific fabrication conditions for different materials systems are summarized in table 2-1. It should be noted that these conditions are determined by various factors, such as the material stoichiometry, the valence state of ions,

the kinetic energy of the plume and the strain state of the film etc., which will be discussed specifically in following chapters.

Table 2-1 PLD fabrication conditions for various oxide thin films in this thesis

Materials	*h*(Hz)	*d*(cm)	*P*(mTorr)	*T* (°C)	Target	Substrates*
$BiFeO_3$	10	7	7.5 (O_2)	680	$Bi_{1.2}FeO_{3+\delta}$	MgO(001), STO(001)
Bi_2FeMnO_6	10	7	1.0 (O_2)	680	$Bi_{2.4}FeMnO_{6+\delta}$	MgO(001), STO(001)
$LaFeO_3$	10	7	10-200 (O_2)	700-850	$LaFeO_3$	$SrTiO_3$(001)
$Sr(Ti_{1-x}Fe_x)O_3$ related systems	10	6	2×10^{-6} (Vacuum)	700	$Sr(Ti_{1-x}Fe_x)O_3$	LAO, LSAT, STO, Si(001)
$Sr(Ti_{1-x}Co_x)O_3$	10	5.5	$2.5\text{-}3.5\times10^{-6}$ (Vacuum)	700	$Sr(Ti_{1-x}Co_x)O_3$	LAO, LSAT, STO, Si(001)
$Y_3Fe_5O_{12}$	10	6	10 (O_2)	500	$Y_3Fe_5O_{12}$	SiO_2/Si, SOI
$Bi_xY_{3-x}Fe_5O_{12}$	5	6	50 (O_2)	650	$Bi_{1.2x}Y_{3-x}Fe_5O_{12+\delta}$	SiO_2/Si, SOI
$Ce_1Y_2Fe_5O_{12}$	5	6	10-50 (O_2)	650	$Ce_1Y_2Fe_5O_{12}$	SiO_2/Si, SOI

* STO: $SrTiO_3$, LAO:$LaAlO_3$, LSAT: (La,Sr)(Al,Ta)O_3, SOI: Si(220nm)/SiO_2(3μm)/Si

2.1.2 Photolithography and lift-off

Several waveguide structures were fabricated by photolithography and lift-off methods. The lift-off process is a thin film patterning process in which thin films were deposited on pre-patterned photoresist, followed by the removal of the resist in solvents. Compared to etching, lift-off offers a faster and easier way for device fabrication. This method was introduced by previous studies for waveguide patterning. [3][4] A schematic plot of this process is shown in figure 2-3. Firstly, the magneto-optical films were deposited using PLD on the substrates having a lower index compared to the magneto-optical material and chalcogenide glass (i.e. LSAT (n=2.0 at 1550nm) or SiO_2 buffered Si (n=1.45 at 1550nm)). NR9-1000PY (Futurrex) negative photoresist was spin coated on the MO film with a

thickness of ~1 μm. After exposure by deep UV-aligner and development in CD-26 developer (Shipley), patterns with 2 μm to 8 μm waveguide or optical resonator structures were formed in the resist. A spatial resolution of 1 μm was achieved by the lithography process. Chalcogenide glass films such as As_2S_3 or GeS_2 were then thermally evaporated on the samples which were kept at room temperature. A lift-off process was carried out by ultrasonicating the samples in acetone to form the strip-load waveguide structure. After that, a 2 μm thick SU-8 (n=1.58, MicroChem) photoresist layer was spin-coated onto the waveguide structures and exposed under room light for 10 min as a top-cladding layer.

Fig. 2-3 A schematic plot of the fabrication process using optical lithography and lift-off methods

2.1.3 E-beam lithography

Electron beam (E-beam) lithography is a mask-less resist patterning technique which uses electron beams rather than photons to expose resist patterns. Due to the shorter wavelength of electrons compared to photons, e-beam lithography can achieve much higher spatial resolution. This technique was applied for silicon on insulator optical resonator fabrication in this study to achieve a feature size of ~100 nm. Figure 2-4 shows a schematic plot of the fabrication process. Starting from a Si(220 nm)/SiO_2(3 μm)/Si SOI wafer, a hydrogen silsesquioxane (HSQ) resist (Dow Corning XR-1541 4%) was spin-coated on the wafer for a thickness of 60 nm. 450 nm wide HSQ patterns were defined by electron beams exposure and development in a tetramethylammonium hydroxide (TMAH) developer. The silicon channel waveguides and resonators were formed by reactive ion etching (RIE) the patterns in HBr. The mask HSQ layer on silicon was removed by etching the samples in a 100:1 HF solution for 2 min. Several of the resonators were spin coated with thick HSQ resist up to 1 μm (Dow Corning Fox-25) and annealed to form a top-cladding layer. A second patterning process and etching process was carried out on this layer to expose part of the resonators for nonreciprocal photonic device fabrication, which will be discussed in detail in chapter 6.

After this step, the magneto-optical garnet films were deposited on the silicon photonic devices and rapid thermal annealed for crystallization.

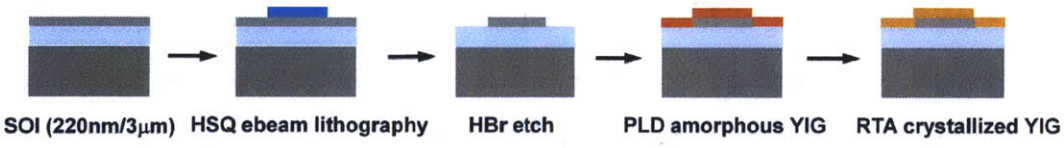

Fig. 2-4 A schematic plot of the fabrication process using e-beam lithography

2.2 Characterization

2.2.1 X-ray diffraction

Phase identification and texture analysis of the magneto-optical films were carried out by X-ray diffraction. These techniques include 1DXRD, 2DXRD, X-ray pole figures and X-ray reciprocal space mapping (RSM).

1DXRD and 2DXRD

The X-ray diffraction from a sample is fully described by the Ewald sphere shown in figure 2-5. Ideally if there is a 3D detector which covers the solid-angle of 4π, all diffraction patterns of the sample can be collected. In practice this is hard to achieve, but depending on the detector size, XRD can be classified as 1DXRD and 2DXRD respectively. Conventional ω-2θ diffraction XRD patterns are collected by 1D detectors. During the ω-2θ scan, it covers a great circle of the Ewald sphere as shown by a red line in fig. 2-5 (a) (if sample normal coincides with the diffraction normal). However 2D detectors with capability of simultaneously detecting large 2θ and γ angles cover an area of the Ewald surface shown by the blue regions for one ω-2θ scan. This technique can observe the spatial distribution of diffraction patterns, which offers opportunity to characterize crystal textures in a single scan.

All of the films in this study were analyzed by 1DXRD (Rigaku RU300). Texture and epitaxial analysis was carried out on 2DXRD (Bruker D8 with General Area Detector Diffraction System (GADDS) [5] for $BiFeO_3$, Bi_2FeMnO_6, $LaFeO_3$, $Sr(Ti_{1-x}Fe_x)O_3$ related

systems and $Sr(Ti_{1-x}Co_x)O_3$ films. Figure 2-5 (b) shows a typical 2DXRD pattern of a $LaFeO_3$ film grown on an STO(001) substrate. The (003) diffraction pattern of the film is localized in a small 2θ and γ range, indicating the film is epitaxial.

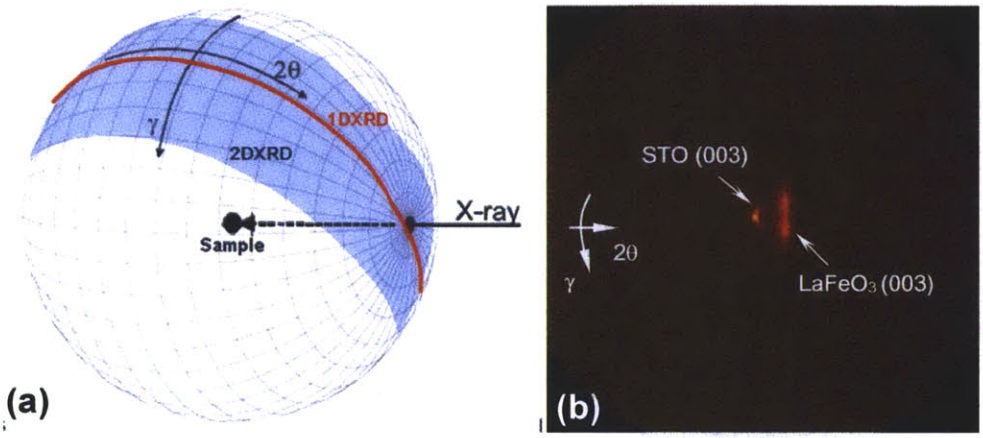

Fig. 2-5 (a) The Ewald sphere of a sample under X-ray diffraction with the detection regions by 1D and 2DXRD during a ω-2θ scan (b) A typical 2DXRD pattern of a $LaFeO_3$ film on $SrTiO_3$ substrate

X-ray pole figures and X-ray reciprocal space mapping

X-ray pole figure is a figure recording the variation of the diffraction intensity with respect to the sample orientations in three dimension. X-ray reciprocal space mapping is a record of the diffraction intensity as a function of the reciprocal space dimensions. These two techniques both characterize the sample texture, while expressed in either real or reciprocal space respectively. Because both the film and substrate diffraction patterns can be simultaneously collected on X-ray RSM, quantitative analysis of the film lattice parameter, strain state or defect density can be carried out by this method.

A typical X-ray pole figure and X-ray RSM is shown in figure 2-6 (a) and (b) respectively. Fig. 2-6 (a) shows the (100) and (110) diffraction pole figures in a $SrTiO_3$ film deposited on CeO2/YSZ (Yttrium stabilized ZrO_2) on silicon. [6] The figure is shown in polar coordinates with the two coordinates of ϕ and κ indicating the sample rotation angles. Epitaxial and fiber textured phases coexist in this film. In the X-ray RSM of figure 2-6 (b) [7], the two coordinates correspond to reciprocal spacing along the in-plane and out-of-plane directions respectively. The film and substrate lattice constants are calculated based on inspecting the

diffraction peak positions in the RSM.

In our study, X-ray pole figures are used to characterize the crystal orientations of $LaFeO_3$ films epitaxially deposited on $SrTiO_3$. The characterization is carried out by measuring the (111) diffraction of $LaFeO_3$ on 2DXRD equipment. X-ray RSM is measured on $Sr(Ti_{1-x}Co_x)O_3$ films deposited on $LaAlO_3$(001) substrates. Both the film (124) and the substrate (224) diffraction are collected on a PANalytical X'Pert Pro Multipurpose Diffractometer. The in-plane lattice parameter as well as the in-plane strain of the film is calculated assuming a tetragonal lattice structure.

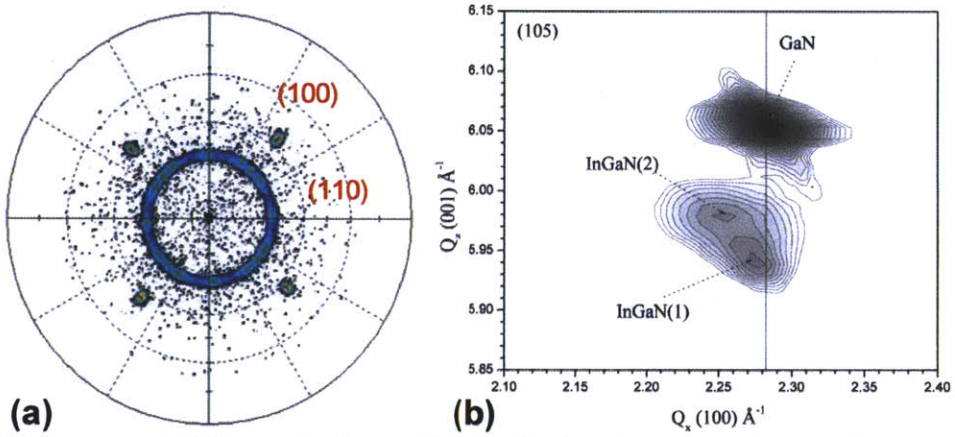

Fig. 2-6 Examples of (a)X-ray pole figure of $SrTiO_3$ film deposited on CeO_2/YSZ buffered Si(001) substrate [6]and (b)X-ray reciprocal space map of InGaN epitaxially deposited on a GaN substrate[7]

2.2.2 Vibrating sample magnetometry (VSM)

The VSM is an inductive method to measure the sample magnetization under applied magnetic field. The working principle is Faraday's law of electromagnetic induction, which states that the electromotive force generated in a pickup coil is proportional to the time variation of the magnetic flux. A schematic plot of this equipment is shown in figure 2-7. The sample is loaded onto a diamagnetic sample holder (pyrex glass or quartz) and vibrated along the z direction. Homogeneous magnetic field up to 1.3 T read by the Gauss meter can be applied along the x direction across the sample. Depending on the magnetization value of the sample, different voltage values can be read from the pickup coils, which are calibrated to a standard sample with known magnetization. Therefore the sample hysteresis can be measured.

A coil heater furnace with flowing inert gas can also be used to heat up the sample and perform magnetization-temperature dependence measurements. By cooling the flowing gas, low temperature measurements can also be carried out.

The VSM used in our study is an ADE Technologies VSM Model 1660. The magnetic field range used for room temperature magnetic hysteresis characterizations is -1 T to +1 T. Curie temperature measurements are also carried out from room temperature to 700 °C, the limit of our coil heater. Several factors are taken care of during our measurements. Because VSM can achieve a magnetization resolution of 10^{-6} emu, samples were cleaned to be free of trace contaminations for accurate measurements. Environmental AC electronic noise was screened during measurements. Also the calibration sample is positioned with a similar geometry as the sample to be measured for quantitative accuracy and minimum shape effect.

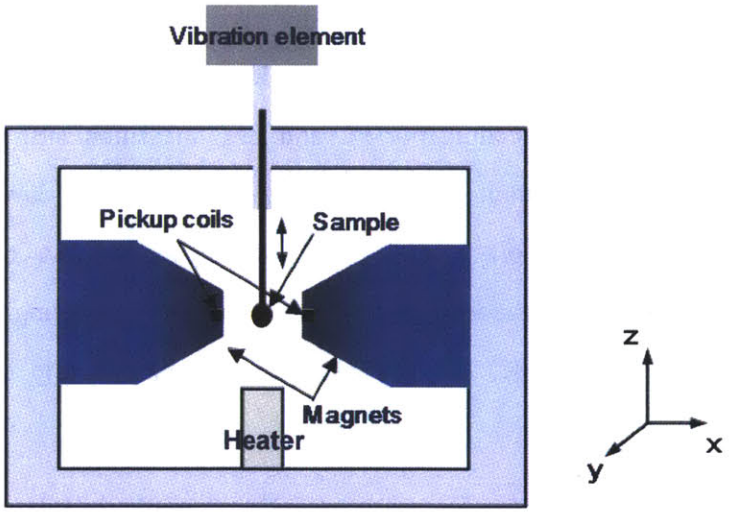

Fig. 2-7 A schematic plot of a vibrating sample magnetometer

2.2.3 Superconducting quantum interference device (SQUID)

SQUID magnetometry is a magnetization measurement method based on measuring the magnetic flux of the sample. It is known as the most sensitive flux measurement method so far, with a field resolution at the 10^{-17} T level demonstrated. The operation mechanism is shown in figure 2-8 (a). [8] The magnetic flux of the sample is measured by a ring of

superconductor interrupted by one or more Josephson junctions (superconductor separated by a thin normal resistor). Below the superconducting transition temperature, the voltage-current curve of this device is shown in figure 2-8 (b). A critical current I_c is observed which separates the normal and superconducting states of the device. When on standby, the device is biased with a current I_b to be sitting between the two states. When a sample with magnetization passes the device causing a flux change, a current is generated in the superconductor due to the Meissner effect, which causes a variation of the voltage across the device according to the I-V curve. This change is quantized as shown in figure 2-8(b). By counting the oscillations of the voltage, the flux and the magnetization of the sample can be measured.

Low temperature (from 5K to 300K) magnetization-temperature (M-T) curves were measured for $Sr(Ti_{1-x}Co_x)O_3$ samples on a Quantum Design SQUID magnetometer. Saturation magnetization M_s-T curve, field cooling (FC) and zero field cooling (ZFC) curves were measured. For Ms-T curve measurements, the samples are saturated at a field of 8000 Oe with in-plane magnetization direction. For FC and ZFC measurements, the samples were firstly cooled to 5 K without applied magnetic field. Then the ZFC curve is collected by warming up the sample at an in-plane field of 1000 Oe. The sample was cooled down to 5 K afterwards under 1000 Oe, and the FC curve was collected during cooling. Low temperature hysteresis of $Sr(Ti_{1-x}Co_x)O_3$ at 5 K, 10 K and 20 K were also measured in a -5 T to +5 T field range.

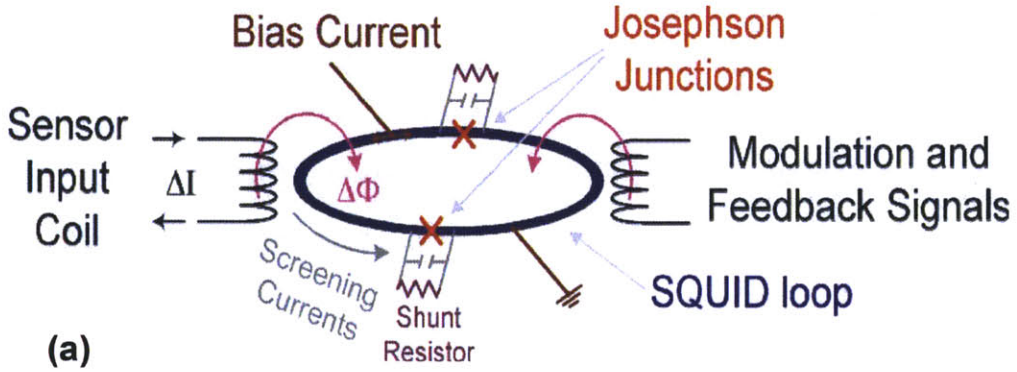

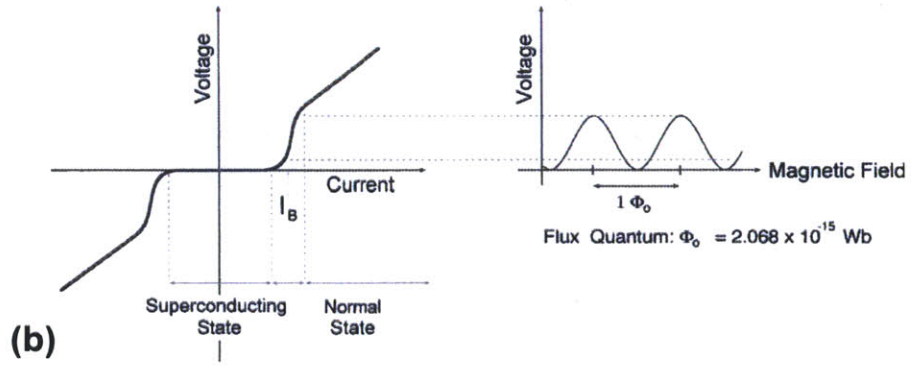

Fig. 2-8 (a) Sketch of a superconductor pickup coil with Josephson Junctions used in SQUID measurements (b) The I-V and V-Φ curve of the device shown in (a) [8]

2.2.4 Faraday rotation

The Faraday rotations of all films were characterized on a custom-built apparatus at 1550 nm wavelength, with the laser light and magnetic field directions perpendicular to the film plane. A sketch of this device is shown in figure 2-9. An infrared laser light with the wavelength range of 1.47 to 1.56 μm was linearly polarized by a polarizer and modulated at 1000 Hz by a Faraday cell modulator controlled with a lock-in amplifier. The light was then aligned through a path bored through pole pieces of an electromagnet, between which the sample was placed. Then it passed through an analyzer set as 1° off from extinction. The transmitted light signal was detected by a Ge detector, filtered by a band path filter and shown on the lock-in amplifier and oscilloscope. By scanning the magnetic field with computer control, the Faraday rotation hysteresis of the sample is collected. The Faraday rotation value is determined by calibration the signal intensity on the lock-in amplifier with 1° off from extinction between the polarizer and the analyzer. The rotation angle is assumed to be linearly proportional to the signal intensity, which is applicable for thin film samples with small rotation angles.

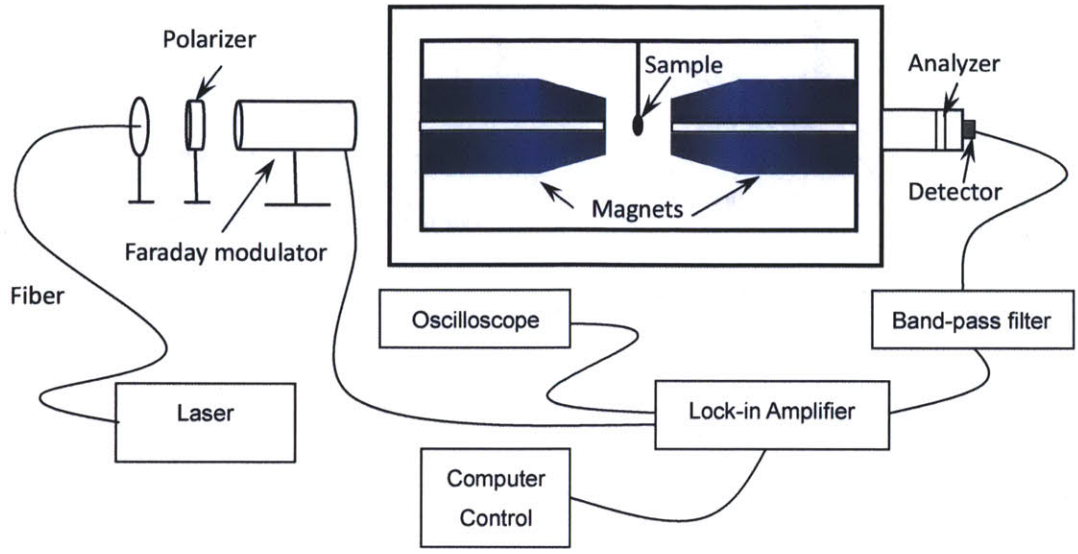

Fig. 2-9 A schematic plot of the thin film Faraday rotation measurement setup

2.2.5 UV-Vis-NIR spectrophotometry

The optical transmittance of the thin film samples were characterized by UV-Vis-NIR spectrophotometry. A deuterium discharge lamp for UV measurements and a tungsten-halogen lamp for visible and NIR measurements were used as the light source. A monochromator scanned the light wavelengths from UV to NIR range, which was then guided by optics to simultaneously pass through a reference and a testing sample. Both transmission intensities are collected and compared to the case of no samples in the optical path (namely the baseline) to determine the transmittance from the testing sample. The UV-Vis-NIR spectrophotometry used in our study is a Cary 500i UV-Vis-NIR Dual-Beam Spectrophotometer with a range from 175 nm to 2000 nm. Thin films samples were compared to air as the standard sample for transmittance measurements. The optical bandgap and absorption were estimated from the measurement spectrum.

2.2.6 Ellipsometry

The optical constants (the refractive index n and extinction coefficient k) of several thin film systems were characterized from 400 nm to 1700 nm wavelengths on a WVASE32 ellipsometer. The ellipsometry method is based on measuring the intensity and polarization state of a linearly polarized light reflected from a sample surface to determine the optical

constants. A schematic plot of the measurement set-up is shown in figure 2-11. [9] Components of linearly polarized light with polarization parallel (*s* polarized) and perpendicular (p polarized) to the sample surface are simultaneously reflected from the sample surface. The reflected light is elliptically polarized, and is related to the incident light by:

$$r_s = \frac{E_{sr}}{E_{si}} = |r_s| \exp(i\delta_s)$$

$$r_p = \frac{E_{pr}}{E_{pi}} = |r_p| \exp(i\delta_p)$$

and described by parameter ρ:

$$\rho = \frac{r_s}{r_p} = \tan\psi \exp(i\Delta)$$

The parameters Ψ and Δ are measured by changing the polarizer and analyzer angles and recorded as a function of wavelength, whereas the optical constants are obtained by fitting the spectrum. For a two layer sample (i.e. air/substrate) the following equation is valid:

$$n + ik = \sin\Phi \sqrt{1 + \frac{(1-\rho)^2}{(1+\rho)^2} \tan^2\Phi}$$

where Φ is the angle of incidence. For multilayer samples the equation will be more complicated.

General oscillator model was used for the fitting process. [10] This model firstly fitted the imaginary part of the material by assuming harmonic oscillator absorption at different wavelengths. The index of refraction was then fitted by Kramers-Kronig relation. A Mean Squared Error (MSE) parameter was used to describe the fitting accuracy by comparing the fitted Ψ and Δ curve to the measured results. MSE<10 was usually required for the final results. In our measurements, MSE<1 was achieved for all samples.

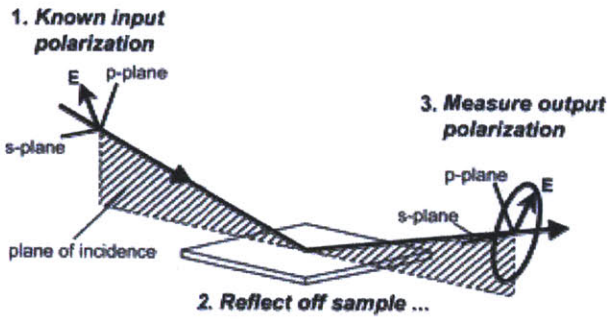

Fig. 2-10 A schematic plot of the ellipsometry measurement setup [9]

2.2.7 Optical waveguide and resonator characterization

The waveguide and resonator transmission measurements were performed on a Newport AutoAlign workstation in combination with a LUNA tunable laser (optical vector analyzer, LUNA Technologies, Inc.). Figure 2-11 (a) shows a photograph of the measurement stage. The samples were cleaved to form end facets and placed on a thermostat stage and kept at 25°C. Lens-tip fibers were used to couple light from the laser into the device from the one of the end facets. An infrared detector was used to align the fiber by imaging the guided mode from the output facet. Then another fiber was aligned to the output facet to collect the transmitted light. Reproducible coupling was achieved via an automatic alignment system with a spatial resolution of 50 nm. By scanning the input wavelength, transmission spectrums in the wavelength range of 1470nm to 1560nm were collected for all devices.

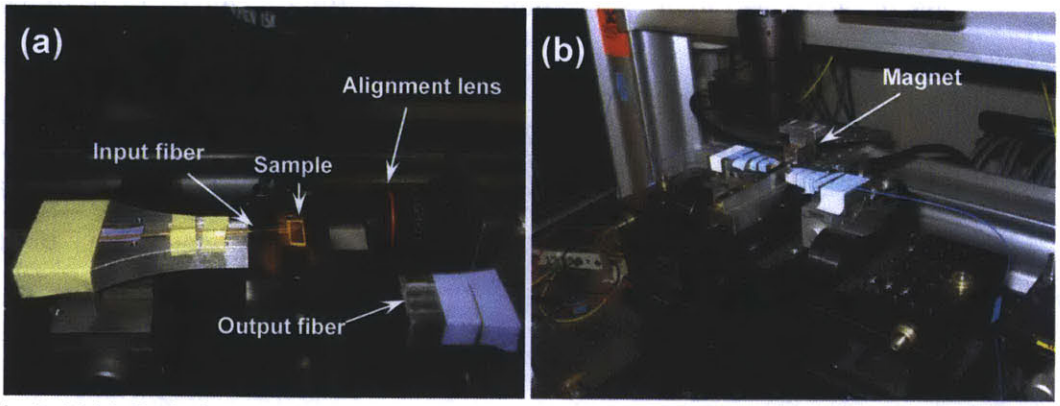

Fig. 2-11 (a) Optical waveguide and resonator transmittance measurement stage (b) The nonreciprocal phase shift measurement setup

Nonreciprocal phase shift (NRPS) measurement for the resonator devices were also carried

out on the same stage. As shown in figure 2-11 (b), a permanent magnet was placed close to the device under test with the magnetic field direction perpendicular to the light wave vector (i.e. the Voigt geometry). The magnetic field across the sample was ~1500Oe. By flipping the magnetic field direction, the device nonreciprocity was measured and calculated by comparing the difference between the transmission spectra.

2.2.8 Other characterization methods

Several other methods were used to support the structure and property characterization. The elemental composition of thin films was measured by wavelength dispersive spectroscopy (WDS). To characterize the distribution of ions, element depth profile of Bi_2FeMnO_6 was analyzed on a Physical Electronics Model 660 scanning Auger microprobe. The ion valence states of $Sr(Ti_{1-x}Co_x)O_{3-\delta}$ and $Sr(Ti_{1-x}Fe_x)O_{3-\delta}$ systems were characterized by X-ray photoelectron spectroscopy (XPS) on a Kratos Axis Ultra spectrometer with a monochromated Al K_α source and a hemispherical analyzer. The high resolution spectrum at the Co *K*-edge was measured with a pass energy of 20 eV and an energy resolution of 0.3 eV. To analyze the Co valence states throughout the film thickness, X-ray absorption near edge spectroscopy (XANES) at the Co *K*-edge was also carried out. The measurement was performed in fluorescence mode at beamline U7C of the National Synchrotron Radiation Facility, China. High resolution planar and cross sectional TEM analysis was performed on $LaFeO_3$ and $Sr(Ti_{1-x}Co_x)O_{3-\delta}$ samples. Waveguide and resonator cross sections were measured on a Zeiss/Leo Gemini 982 SEM. Optical modes and NRPS were simulated based on the measured device geometries.

2.3 Simulation

2.3.1 First-principles simulation using Density Functional Theory (DFT)

We applied density functional theory with spin polarized general gradient approximation (GGA) and GGA+U (Liechtenstein's implementation) [11] methods to calculate the structure and electronic structure of $BiFeO_3$, $BiMnO_3$ and Bi_2FeMnO_6. The density functional theory

was proposed by Hohenberg and Kohn in 1964. The name of this theory comes from the two major statements, i.e. 1) there is a one to one relationship between the ground state electron density and the external potential, and 2) there is a universal functional which relates the ground state energy of an electronic system to the electron density. This functional is later described explicitly in Kohn-Sham theory as a sum of kinetic, Coulomb and exchange energies. The first term is simply the non-interacting electron kinetic energy. The Coulomb energy is a spatial integral of electrostatic interaction energy at a certain electron density level. The last term cannot be accurately determined and is approximated by various methods. The most commonly used nowadays are the LDA and GGA approximations. For LDA, the exchange energy at each point in space is approximated by the exchange-correlation energy of a homogeneous electron gas with the same electron density, while for GGA this is further improved by also considering the electron density gradient.

The Kohn-Sham equation relating the electron density and the electron wavefunction is:

$$\left\{-\frac{\nabla_1^A}{2}-\left(\sum_{A=1}^{M}\frac{Z_A}{r_{1A}}\right)+\int\frac{\rho(\mathbf{r}_2)}{r_{12}}d\mathbf{r}_2+V_{XC}[\mathbf{r}_1]\right\}\varphi_i(\mathbf{r}_1)=\varepsilon_i\varphi_i(\mathbf{r}_1)$$

where the four terms in the parenthesis on the left are the kinetic, ion-electron Coulomb interaction, electron-electron Coulomb interaction and the exchange terms respectively. An obvious non-physical flaw is in the third term, where the electron is Coulomb interacting with itself because every electron contributes to the electron density $\rho(r_2)$. This causes error in simulated wavefunctions and tends to delocalize the electrons, and is particularly significant in highly localized electron systems such as 3d transition metal ions. To account for the highly correlated and localized behavior of these electrons, +U methods are introduced, which adds on-site electron interaction and exchange energy terms to the above formula [11] for more accurate simulation results.

For $BiFeO_3$, $BiMnO_3$ and Bi_2FeMnO_6 simulations, Projected Augmented Wave (PAW) [12] pseudopotentials were implemented in the Vienna *ab initio* Simulation Package (VASP) [13]. The cut-off energy was 500 eV. 5×5×5, 3×3×3 and 3×3×3 k-point meshes were used for $BiFeO_3$, $BiMnO_3$ and Bi_2FeMnO_6 respectively. Full relaxation of the atomic coordinates and

lattice vectors was achieved using both GGA and GGA+U energy functionals until the total ground state energies converged within 3 meV for each unit cell. The screened Coulomb interaction parameter U and exchange parameter J entered the Hamiltonian to account for the on-site electron-electron interactions in the localized 3d orbitals for Fe and Mn. We set U=J=0 eV for GGA calculations. For GGA+U calculations, we fixed J(Fe)=J(Mn)=1 eV, and varied U(Fe) or U(Mn) from 4 to 8 eV. The lattice structures, ground state energies and electronic structures were simulated and analyzed to understand the material properties.

2.3.2 Waveguide mode simulation using Film Mode Matching (FMM) method

The waveguide modes were simulated by film mode matching (FMM) method in the FIMMWAVE software [14]. This is a numerical method to simulate the mode distribution in a 2D waveguide cross section. A graphical illustration of this method is shown in figure 2-11. [15] The waveguide is divided into slices along the y direction. Each slice is a slab waveguide which is homogenous along the x direction. The 2D mode is based on solving the TE and TM modes in each 1D slice and matching the boundary conditions between slices. Ideally if an infinite number of 1D modes are used, the solved 2D mode will be exact. In practice, we used 80 modes in each slice. 1000 slices and 200 layers were used to allow good resolution of the field amplitudes. The field amplitudes were expressed as matrices and were used for NRPS simulations, as will be discussed in detail in chapter 6 and 7.

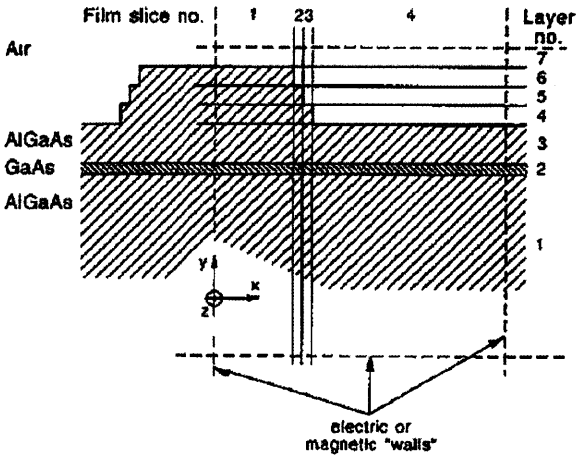

Fig. 2-12 A typical ridge waveguide divided in a series of vertical slices and simulated by FMM method. The sloped side walls are approximated by staircases. [15]

References

[1] A. Inam, M. S. Hedge, X. D. Wu, T. Venkatesan, P. England, P. F. Miceli, E. W. Chase, C. C. Chang, J. M. Tarascon and J. B. Wachtman, *Appl. Phys. Lett.*, **53**, 908 (1988)

[2] R. Eason ed., *Pulsed Laser Deposition*, Wiley-Interscience publication, 2007

[3] J. Frantz, L. Shaw, J. Sanghera and I. Aggarwal, *Opt. Express*, **14**, 1797 (2004)

[4] J. Hu, V. Tarasov, N. Carlie, N. Feng, L. Petit, A. Agarwall, K. Richardson and L. Kimerling, *Optics Express*, **15**, 11798 (2007)

[5] B. B. He, *Powder Diffraction* , **18**, 71 (2003)

[6] H.S. Kim, L. Bi, H. Paik , D. J. Yang, Y. C. Park , G. F. Dionne and C. A. Ross, *Nano Lett.*, **10**, 597 (2010)

[7] M. R. Correia, S. Pereira, and E. Pereira, J. Frandon, I. M. Watson, C. Liu, E. Alves, A. D. Sequeira and N. Franco, *Appl. Phys. Lett.*, **79**, 1432 (2001)

[8] R. L. Fagaly, *Rev. Sci. Instrum.*, **77**, 101101 (2006)

[9] Ellipsometry configuration, *http://www.jawoollam.com/tutorial_4.html*, 2010

[10] X. Gao, H. Feng, J. Ma, Z. Zhang, J. Lu, Y. Chen, S. Yang and J. Gu, *Physica B*, **405**, 1922 (2010)

[11] A. I. Leichtenstein, V. I. Anisimov and J. Zaamen., *Phys. Rev. B*, **52**, R5467 (1995)

[12] G. Kresse and D. Joubert, *Phys. Rev. B*, **59**, 1758 (1999)

[13] G. Kresse and J. Furthmüller, *Phys. Rev. B*, **54**, 11169 (1996)

[14] Integrated Optics Software FIMMWAVE 4.5, Photon Design, Oxford, U.K. [Online]. Available: http://www.photond.com

[15] A. S. Sudbo, *Pure Appl. Opt.*, **2**, 211 (1993)

Chapter 3
Heteroepitaxial Orthoferrite Thin Films

Orthoferrite single crystals with the chemical formula of $LnFeO_3$ (*Ln* stands for rare earths) were studied in the 1970's for bubble memory and magneto-optical applications. Liquid phase epitaxy of orthoferrites on heterogeneous substrates was found to be extremely difficult. [1]Recently, due to the potential of multiferroic applications, heteroepitaxial $BiFeO_3$ thin films fabricated by physical vapor deposition methods have been widely studied [2], whereas $LaFeO_3$ epitaxial films have been studied as a model system to understand antiferromagnetic domain structures [3]. As a promising magneto-optical system, nowadays orthoferrites may find an application in integrated nonreciprocal photonic devices due to better compatibility to semiconductor substrates compared with garnets. In this chapter, our study on $BiFeO_3$, Bi_2FeMnO_6 and $LaFeO_3$ epitaxial thin films on $SrTiO_3(001)$ substrates will be introduced. Experimental characterization of the film structure, magnetic and optical properties will be shown, and theoretical understanding will be discussed based on first-principle simulations and kinetic models.

3.1 $BiFeO_3$ and Bi_2FeMnO_6 films on $SrTiO_3(001)$ substrates

3.1.1 Introduction

Among the orthoferrites, perhaps $BiFeO_3$ is the most systematically studied in recent years. [2][4][5] Due to the canted antiferromagnetic nature of orthoferrites, $BiFeO_3$ is weakly ferrimagnetic (~0.017 emu/cm^3) [6]. Ordered double perovskites, in which two different B-site cations form a superlattice within the ABO_3 perovskite structure, provides a possible way to achieve stronger ferrimagnetism in $BiFeO_3$. In ordered double perovskites with Curie temperature (T_c) above RT, the spins and orbital angular momentum vectors of the two types of B-site ions align along their own macroscopic directions when magnetized. Due to the difference in net moments, the two sublattices provide a net magnetization and Faraday

rotation at certain wavelengths. [7] This Faraday rotation can be further enhanced by A site Bi^{3+} ions, which have strong covalent interactions with the octahedral complexes, therefore enhancing the non-degeneracy of the spin-orbit coupling levels as well as the Faraday rotation of the material. [8][9]

The structure and magnetic properties of bismuth orthoferrites and several other bismuth perovskite systems have been well studied. $BiFeO_3$ bulk crystal belongs to the *R*3*c* space group, as shown in figure 1-7 (b). The unit cell of $BiFeO_3$ can be considered to be a deformed ideal cubic perovskite. By moving Bi and Fe atoms along the pseudocubic [111] direction and O atoms along the pseudocubic <110> directions, the unit cell is elongated with the neighboring octahedrons rotated in different directions about the [111] axis. [10] $BiFeO_3$ is antiferromagnetic with a Néel temperature of $T_N \sim 640K$. [11][12] The Fe spins form a G-type antiferromagnetic (G-AFM) structure, in which the spins are coupled ferromagnetically in the pseudocubic (111) planes and antiferromagnetically between neighboring (111) planes, so that each Fe atom couples antiferromagnetically with its nearest Fe neighbors. [13] Besides $BiFeO_3$, another bismuth perovskite, $BiMnO_3$ is also well studied because of its multiferroic properties at low temperature. [14] Due to the Bi $6s^2$ lone pairs, the unit cell of the $BiMnO_3$ bulk crystal is distorted to *C*2 symmetry at and below room temperature [15]. In contrast to $BiFeO_3$, $BiMnO_3$ is ferromagnetic with $T_c \sim 105$ K [16]. This is because ferromagnetic rather than antiferromagnetic superexchange between the e_g orbitals of neighboring Mn^{3+} ions is favored in the distorted unit cell [16-18]. There are also several experimental studies on $BiFe_{1-x}Mn_xO_3$ bulk crystals and thin films [20][21][23][24]. A general finding is that incorporation of Fe in the Mn-rich side drives the material from ferromagnetic to antiferromagnetic, while adding Mn in the Fe-rich side results in higher saturation magnetization at room temperature.

Despite these previous studies, there are several questions remaining. Firstly, is B-site ordering likely to occur in certain double perovskite systems (specifically $BiFe_{1-x}Mn_xO_3$ in this study)? Previous experimental results indeed show that incorporating Mn into the $BiFeO_3$ lattice enhanced the magnetization [23][24], but whether this is caused by local B site

ordering is unclear. Secondly, for magneto-optical isolator applications, how do the Bi and B-site ions influence the optical and magneto-optical properties of these perovskites? Although $YFeO_3$ and rare earth based orthoferrites show high optical transparency (α<0.5 cm^{-1}) and high Faraday rotation constant at 1550 nm wavelength [25][26], as far as we know, the infrared optical and magneto-optical properties of bismuth perovskites and bismuth double perovskites have not been reported. In order to answer these questions, we apply both experimental and first principles calculation methods to investigate the structural, magnetic and optical properties of $BiFeO_3$ and Bi_2FeMnO_6 epitaxial thin films.

3.1.2 Spin ordering considerations

Based on anticipated effects of local interactions in a generic ABO_3 perovskite lattice, the magnetic moment and Faraday rotation should be dominated by antiferromagnetic spin ordering. In a stoichiometric specimen of $BiFeO_3$ or Bi_2FeMnO_6, the most stable valence for either Fe or Mn is 3+. For $Fe^{3+}(3d^5)$, the five spins are aligned in a half-filled 3d shell ($t_{2g}^3e_g^2$) high-spin configuration as dictated by Hund's rule; for the same reason, $Mn^{3+}(3d^4)$ is in a high-spin $t_{2g}^3e_g^1$ arrangement in octahedral B sites that is further stabilized by a strong Jahn-Teller axial distortion along the *z*-axis.

An important characteristic of the perovskite lattice is the 180-degree cation-anion-cation bonds that involve the e_g orbitals in bonding/antibonding linkages with the oxygen 2p orbitals, while relegating the t_{2g} orbitals to nonbonding roles. According to the Goodenough-Kanamori rules for 180-degree superexchange couplings [17], the expectations for five possible combinations in these compounds are

1. $Fe^{3+} - O^{2-} - Fe^{3+}$ strong AFM
2. $Mn^{3+} - O^{2-} - Mn^{3+}$ vibronic FM/AFM
3. $Fe^{3+} - O^{2-} - Mn^{3+}$ vibronic AFM/FM
4. $Fe^{2+} - O^{2-} - Mn^{4+}$ vibronic AFM
5. $Fe^{4+} - O^{2-} - Mn^{2+}$ vibronic AFM

In case 1, both e_g orbitals are half-filled on both sides and present the classic case of correlated antiferromagnetism by virtual charge transfer. Case 2 is less certain because only one e_g orbital is occupied, thereby producing a weaker AFM. However, if local Jahn-Teller effects become correlated, the AFM ordering can be overcome by a vibronic FM ordering [17-19]. In case 3 for dissimilar cations, a vibronic mechanism is also available, and the most likely result would be a moderate-to-weak antiparallel spin stabilization that is partially offset by delocalization FM exchange between a half-filled and empty pair of overlapping e_g orbital states.

If the Fe and Mn are spatially ordered in the B sites, despite an antiparallel alignment a quasi-ferrimagnetic effect could be observed as a net one Bohr magneton moment from the difference between the opposing Fe^{3+} (S = 5/2) and Mn^{3+} (S = 2) moments. Cases 4 and 5 are less likely ionic states based on ionization potentials and Madelung energy considerations. The meager Faraday rotation data also indicate that Fe^{3+}/Mn^{3+} ferrimagnetic ordering is not likely since some kind of interionic charge transfer would be necessary to satisfy the S = 0 selection rule for allowed electric dipole transitions. [7][26]

If the specimen is nonstoichiometric, polaronic conduction between mixed-valence cations (double exchange) can create FM properties by any of the following mechanisms (listed according to frequency of occurrence), with effectiveness determined by the particular bonding stabilization and activation energy:

1. $Fe^{2+} \leftrightarrow Fe^{3+} + e^-$ frequent in spinels and garnets
2. $Mn^{3+} \leftrightarrow Mn^{4+} + e^-$ basis for magnetoresistance in LaSr manganites
3. $Fe^{3+} \leftrightarrow Fe^{4+} + e^-$ infrequent in spinels and garnets
4. $Mn^{2+} \leftrightarrow Mn^{3+} + e^-$ infrequent in spinels and garnets

Charges can transport by tunneling at low temperatures or by thermal activation (random hopping) where T approaches the Debye temperature. Note also that static as well as dynamic magnetoelastic effects from Fe^{2+}, Mn^{3+}, or Fe^{4+} can be expected in each situation.

3.1.3 The structure of $BiFeO_3$ and Bi_2FeMnO_6 films

Element stoichiometry and phase diagram

Table 3-1 shows the WDS results for $BiFeO_3$ films grown on MgO (001) substrates at various T_s and P_{O_2}. The bismuth versus iron atomic ratio shows a strong dependence on T_s and P_{O_2} during growth. Near-stoichiometric films can only be achieved in a small process window. Note that either high T_s or low P_{O_2} yield iron-rich films, while either low T_s or high P_{O_2} yield bismuth-rich films. The bismuth deficiency is due to the evaporation of bismuth at high T_s or low P_{O_2}, which is consistent with several previous reports [2][4][27], and which is partly offset by the use of Bi-rich targets.

TABLE 3-1 Bi:Fe atomic ratios of $BiFeO_3$ films grown on MgO (001) substrates at various substrate temperatures and oxygen partial pressures

	530°C	580°C	630°C	680°C
Vacuum	-	0.325	0.199	0.230
3 mTorr O_2	0.648	0.850	0.800	0.382
7.5 mTorr O_2	1.477	0.980	0.961	0.670
15 mTorr O_2	-	1.338	1.307	-

The phase diagram of $BiFeO_3$ as a function of P_{O_2} and T_s during growth is shown in fig. 3-1, from data obtained by 2DXRD analysis. For comparison, the results on both STO and MgO substrates are shown. Firstly we notice that either high T_s or low P_{O_2} favors the growth of γ-Fe_2O_3 (maghemite), while either low T_s or high P_{O_2} gives Bi-rich films and favors the growth of Bi_2O_3. Secondly, in most of the intermediate temperature and pressure range, $BiFeO_3$ and $Bi_2Fe_4O_9$ coexist on both substrates. On MgO there is no process window for the growth of single-phase perovskite $BiFeO_3$, while on STO, there is a narrow window favoring single phase $BiFeO_3$ growth, because the $BiFeO_3$ phase is stabilized by epitaxial growth on the STO substrate. [27] Considering the stoichiometry and phase diagram of $BiFeO_3$, it is clear that the atomic ratio of bismuth to iron determines the final phases in the film, and this

compositional stoichiometry shows a stronger dependence on P_{O_2} than on T_s. Single phase $BiFeO_3$ films can only be obtained by pseudomorphic growth on a lattice-matched substrate at a P_{O_2} and T_s chosen to give correct film stoichiometry.

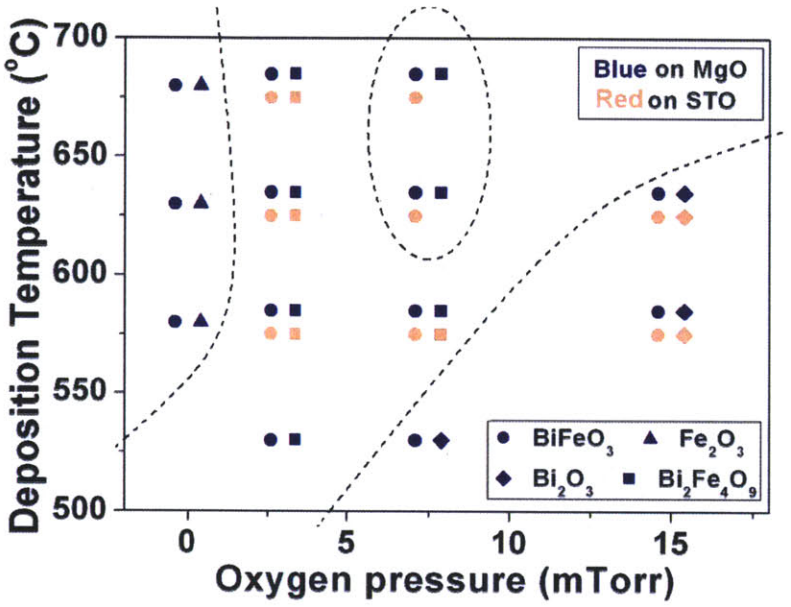

Fig. 3-1 The phases forming during film growth in $BiFeO_3$ deposited on MgO (001) and $SrTiO_3$ (001) substrates as a function of substrate temperature and oxygen partial pressure. The dashed lines separate the conditions under which Fe_2O_3, Bi_2O_3 or $BiFeO_3$ perovskite phases dominate. The single-phase perovskite is formed at intermediate pressures and high temperatures on $SrTiO_3$ substrates.

Table 3-2 shows the phase and compositional analysis of Bi_2FeMnO_6 films grown on STO substrates. In this system, we fixed T_s at 680°C and varied P_{O_2} to obtain epitaxial growth of the perovskite phase. Two samples were annealed *in situ* in the PLD chamber for 2 hours at the growth conditions before cooling down. The general trend of increasing Bi:(Fe+Mn) with P_{O_2} follows that seen in $BiFeO_3$, but *in situ* annealing leads to significant loss of Bi and formation of additional Fe and Mn oxides. A single phase growth window is found around P_{O_2}=1 mTorr for unannealed samples. Compared with $BiFeO_3$ growth, Bi_2FeMnO_6 single phase growth is more sensitive to fluctuations in fabrication conditions. For example an oxygen pressure change of $\pm$0.2 mtorr away from 1 mTorr will lead to formation of significant amounts of secondary phases, indicating that Bi_2FeMnO_6 is even less stable than $BiFeO_3$. The Fe:Mn atomic ratio is close to 1 and independent of oxygen pressure.

Table 3-2 Phases and compositions of Bi_2FeMnO_6 films grown on $SrTiO_3$ (001) substrates at 680°C and various oxygen partial pressures. Two of the samples were in-situ annealed at the fabrication conditions for two hours before characterization

P_{O_2} (mTorr)	Phases	Bi/(Fe+Mn) (at.%)	Fe/Mn (at.%)
0.8	Bi_2FeMnO_6, γ-Fe_2O_3, Mn_3O_4	0.94	0.91
1	Bi_2FeMnO_6	1.07	0.92
3.5	Bi_2FeMnO_6, Bi_2O_3	1.10	0.91
2.5 (*in-situ* annealed)	Bi_2FeMnO_6, Bi_2O_3, γ-Fe_2O_3, Mn_3O_4	0.56	0.95
7.5 (*in-situ* annealed)	Bi_2FeMnO_6, Bi_2O_3, γ-Fe_2O_3, Mn_3O_4	0.65	0.94

Based on these results, optimum conditions were chosen to grow epitaxial $BiFeO_3$ and Bi_2FeMnO_6 films with only trace amounts of impurity phases (mainly α-Bi_2O_3 or β-Bi_2O_3) on STO (001) substrates for further analysis. The thickness of the $BiFeO_3$ and Bi_2FeMnO_6 films was 850 nm and 220 nm respectively as confirmed by profilometer. The 1DXRD and 2DXRD spectra of both films are shown in fig. 3-2(a)-(d). Both $BiFeO_3$ and Bi_2FeMnO_6 show $(00k)_c$ pseudocubic diffraction peaks in the 1DXRD spectrum, while the well-defined spot-like diffraction patterns on 2DXRD spectra indicate both films are epitaxially grown on STO. The 1DXRD spectra show that Bi_2FeMnO_6 has a larger out-of-plane lattice parameter than $BiFeO_3$. The in-plane lattice parameter analysis of the (122), (202) and (112) diffraction peaks of both films were carried out by 2DXRD. By fitting the lattice spacing, we obtained all the lattice parameters for both films. $BiFeO_3$ has a monoclinic unit cell with a = b = 4.037 Å, c = 3.947 Å, and 90°− β= −0.88°, while Bi_2FeMnO_6 has a monoclinic unit cell with a=3.915 Å, b=3.935 Å, c=3.986 Å and 90°− β= −0.5°, where β is the angle between the *a* and *b* directions. Both films are distorted to monoclinic symmetry with *c* axis out-of-plane by their epitaxial relation with the substrate. Bi_2FeMnO_6 shows a smaller unit cell volume (61.40 $Å^3$) compared with $BiFeO_3$ (64.31 $Å^3$). Compared with the $SrTiO_3$ substrate (cubic cell with a=3.905 Å and unit cell volume 59.55 $Å^3$), the largest in-plane lattice mismatch of $BiFeO_3$ and Bi_2FeMnO_6 are 3.4% and 0.8% respectively. Although better lattice matching is achieved

in Bi_2FeMnO_6, the film quality is not as good as for $BiFeO_3$. At a Bi_2FeMnO_6 thickness of 220 nm, a small amount of impurity phase is observed, and this increases with thickness. In contrast, for $BiFeO_3$, epitaxial film growth was achieved at a thickness of 850 nm, and the impurity phase was limited to a trace amount. This observation suggests that the perovskite phase of Bi_2FeMnO_6 is less stable compared with $BiFeO_3$.

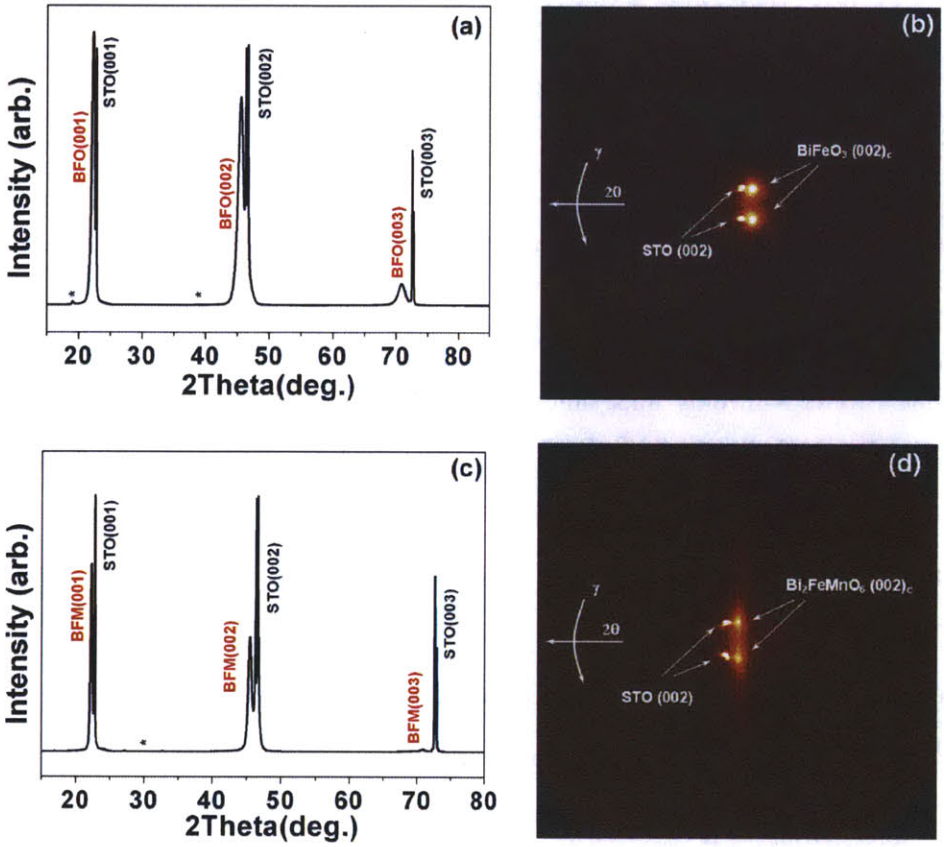

Fig. 3-2 1DXRD diffraction spectra for (a) $BiFeO_3$ and (c) Bi_2FeMnO_6 epitaxial films on $SrTiO_3$ (001) substrates. "*" indicates peaks from a trace amount of Bi_2O_3. Also shown are the 2DXRD pseudocubic $(002)_c$ diffraction patterns of (b) $BiFeO_3$ and (d) Bi_2FeMnO_6 films. Both patterns were taken at an x-ray incident angle of ω=23° and the frame center was 2θ=46°. The data collection region is $31° < \theta < 61°$ and $75° < \gamma < 105°$. The samples were rotated by 360° about the axis normal to the sample surface during the measurement.

Element depth profile and valence states

Auger spectroscopy (AES) was carried out to measure the element depth profile of both samples. Figure 3-3 shows the result on the Bi_2FeMnO_6 film. The Bi:(Fe+Mn) atomic ratio is 4.5 at the film surface but decreases to 1 within 10 nm film thickness, while the Fe:Mn

atomic ratio remains almost constant. There is no change in either ratio for the remaining thickness of the film. This surface bismuth-rich layer is also found in the $BiFeO_3$ film according to AES and XPS surface analysis. However, due to large charging effects in this film, we could not obtain a clear AES depth profile spectrum. The bismuth-rich surface layer was found previously in epitaxial $BiFeO_3$ films and was attributed to strain relaxation along the thickness direction of the film. [27] This effect causes the $BiFeO_3$ phase to have a higher free energy of formation than Bi_2O_3 near the film surface, favoring the growth of the latter.

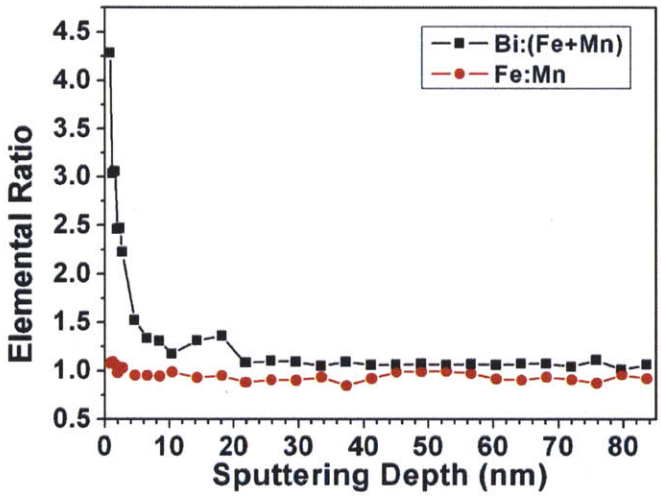

Fig. 3-3 Bi:(Fe+Mn) and Fe:Mn atomic ratios in a Bi_2FeMnO_6 film as a function of depth, from AES

Figure 3-4 (a), (b), and (c) shows the XPS core level spectra of Fe 2p in $BiFeO_3$, and Fe 2p and Mn 2p in Bi_2FeMnO_6 respectively. To assure our analysis was carried out on the perovskite phase, Ar^+ ion milling was performed until the bismuth concentration was stable in survey scans. The XPS spectra of Fe and Mn reveal the usual $2p_{3/2}$ and $2p_{1/2}$ doublet arising from spin-orbital interaction. Comparing both spectra we found that the Fe 2p lines resemble each other in $BiFeO_3$ and Bi_2FeMnO_6 films. The binding energy of the Fe $2p_{3/2}$ level is 710.57 eV in $BiFeO_3$ and 710.61 eV in Bi_2FeMnO_6. No shoulder peak was found around the Fe $2p_{3/2}$ peak in either sample. Moreover, a satellite peak was found about 8.0 eV above the Fe $2p_{3/2}$ principal peak. This satellite peak is considered to be characteristic of the oxidation state of the Fe. [21] Due to different d orbital electron configurations, during relaxation of the metal ions, Fe^{2+} and Fe^{3+} will show a satellite peak at 6 eV or 8 eV above their $2p_{3/2}$ principal peaks respectively. [28] The structure and similarity of the Fe 2p core level spectra in both

$BiFeO_3$ and Bi_2FeMnO_6 films indicate that Fe is mainly in the 3+ valence state in both systems. On the other hand, in Bi_2FeMnO_6 film, the Mn $2p_{3/2}$ principal peak has a binding energy of 642.2 eV. A shoulder peak below this energy originates from Mn^{2+} and indicates the presence of multiple valence states of Mn. In the stoichiometric Bi_2FeMnO_6, the average valence state of the B-site cation is 3+, and since Fe is mainly present as Fe^{3+}, this suggests that Mn must exhibit Mn^{2+}, Mn^{3+} and Mn^{4+} valence states. Previous XPS analysis on 10at.% Mn-doped $BiFeO_3$ indicates that the oxidation state of Fe was primarily 3+. [21] From our analysis this effect seems to persist even with 50at.% Mn present in the B-sites.

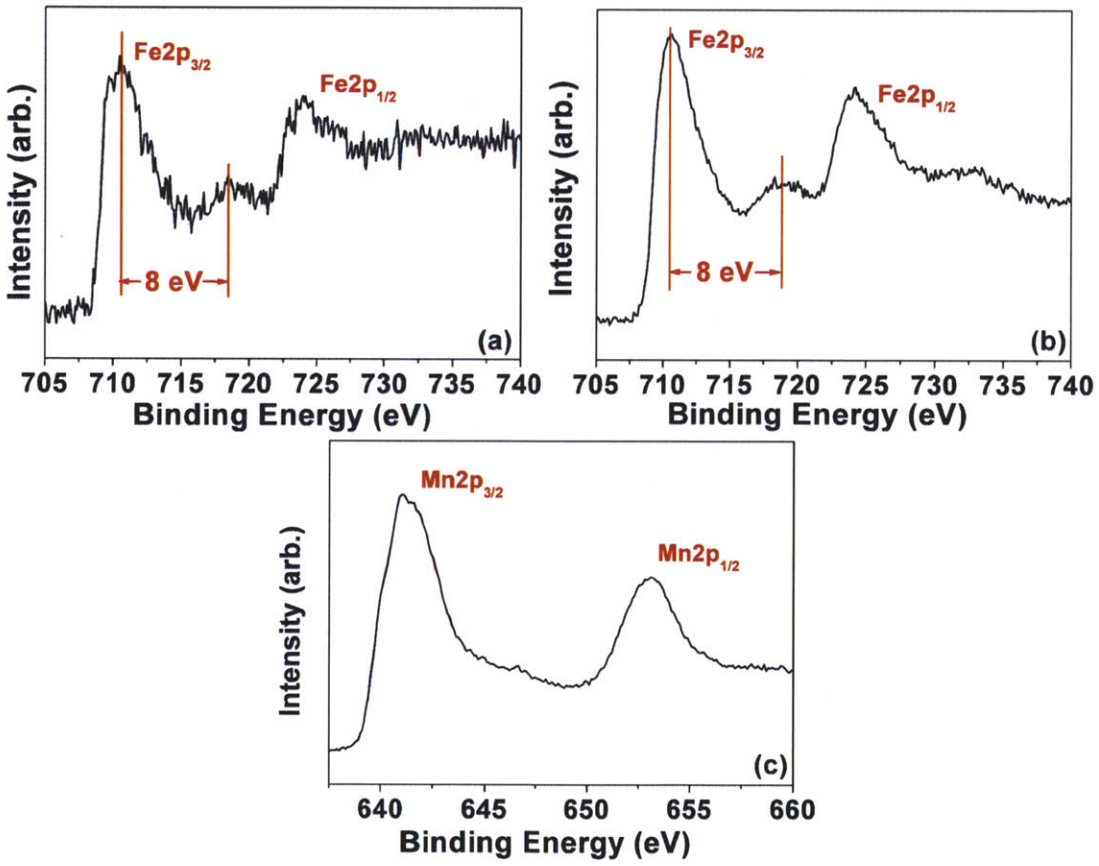

Fig. 3-4 XPS spectra of the Fe 2p peaks for (a) $BiFeO_3$ and (b) Bi_2FeMnO_6 and (c) the Mn 2p peaks for Bi_2FeMnO_6

3.1.4 Magnetic, MO and Optical properties of $BiFeO_3$ and Bi_2FeMnO_6 films

Figure 3-5 (a) shows the out-of-plane magnetic hysteresis loops of $BiFeO_3$ and Bi_2FeMnO_6 films measured at room temperature by VSM. The data were obtained by subtracting the substrate magnetization from the overall hysteresis of the samples. Both samples show low

and non-saturating magnetization for an applied magnetic field up to 10 kOe. $BiFeO_3$ exhibits a magnetization of 1.2 emu/cm^3 at 1 kOe resulting from slight canting of the antiferromagnetically-coupled moments, while Bi_2FeMnO_6 exhibits an even smaller magnetization of 0.8 emu/cm^3. These results suggest that the magnetization in Bi_2FeMnO_6 also originates from canted antiferromagnetism at room temperature. In order to investigate the magnetic ordering of Bi_2FeMnO_6 at low temperatures, we measured the magnetization of Bi_2FeMnO_6 at 5 K using a SQUID magnetometer, as shown in figure 5 (b). Bi_2FeMnO_6 shows non-saturating behavior at this temperature. The magnetization at 9 kOe is estimated at 5.4 emu/cm^3, corresponding to 0.03 μ_B per B-site ion. This value is far from the values expected if the Fe and Mn atoms were ordered in the B-sites (4 μ_B for ferromagnetic or 0.5 μ_B for antiferromagnetic ordering of Fe^{3+} and Mn^{3+}), which indicates most of the B-site cations are disordered in this sample.

Faraday rotation hysteresis loops of both films at a wavelength of 1550 nm at room temperature were also measured on both samples. Due to the very low magnetization of both samples, no clear hysteresis was obtained. By subtracting the Faraday rotation signal from our substrate, we estimated the Verdet constant for both films. $BiFeO_3$ shows a Verdet constant of 18 ± 2°/cm·kOe, while Bi_2FeMnO_6 shows a Verdet constant of 50 ± 3°/cm·kOe, both of which are very small.

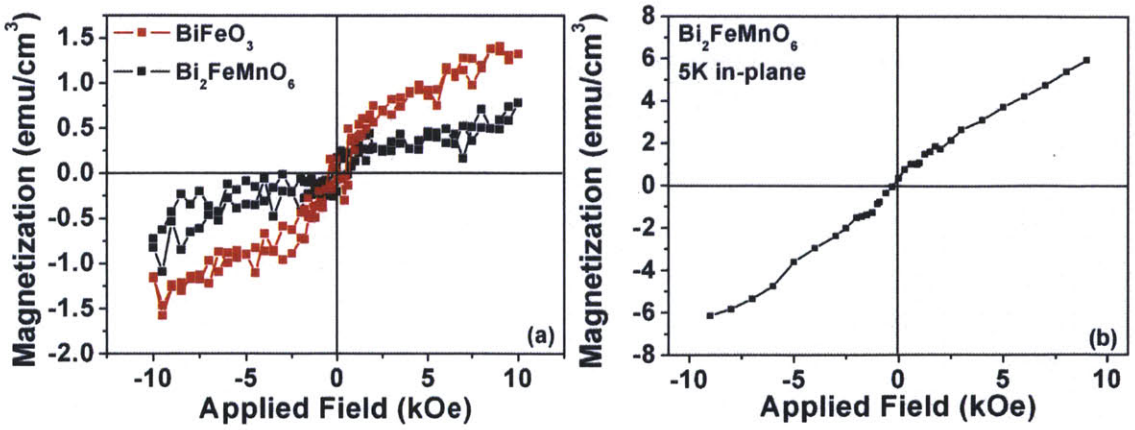

Fig. 3-5 (a) Magnetization as a function of out-of-plane applied field for $BiFeO_3$ and Bi_2FeMnO_6 films at room temperature. (b) In plane magnetization of a Bi_2FeMnO_6 film measured by SQUID magnetometry at 5 K. The plot shows a half loop scanning from -9000 Oe to 9000 Oe.

Figure 3-6 (a) shows the fitted optical constants for the $BiFeO_3$ film as a function of wavelength. At 1550 nm wavelength, the refractive index is n=2.592 and k is smaller than the detection error of the equipment. The small extinction coefficient indicates $BiFeO_3$ is very transparent, similar to yttrium and other rare earth orthoferrites in the infrared wavelength region. [25][26] The validity of our fitting is supported by comparing the n, k data with the spectrophotometry absorption spectra shown in figure 3-6 (b). Firstly, the optical band gaps of $BiFeO_3$ measured by both methods (2.44 eV for ellipsometry and 2.42 eV for spectrophotometry) are very similar. Secondly, using the fitted film thickness, the n, k data and the substrate optical constants, we can obtain a good fit to the experimental absorption spectrum. Note that our fitting did not include the absorption peaks located around 1.0 μm and 0.7 μm caused by Fe^{3+} ${}^6A_1 \rightarrow {}^4T_1$ and ${}^6A_1 \rightarrow {}^4T_2$ crystal field transitions, which will result in under-estimation of the extinction coefficient around these wavelengths. But from both the results of ellipsometry and spectrophotometry, it is clear that $BiFeO_3$ has low optical absorption loss at 1550 nm wavelength.

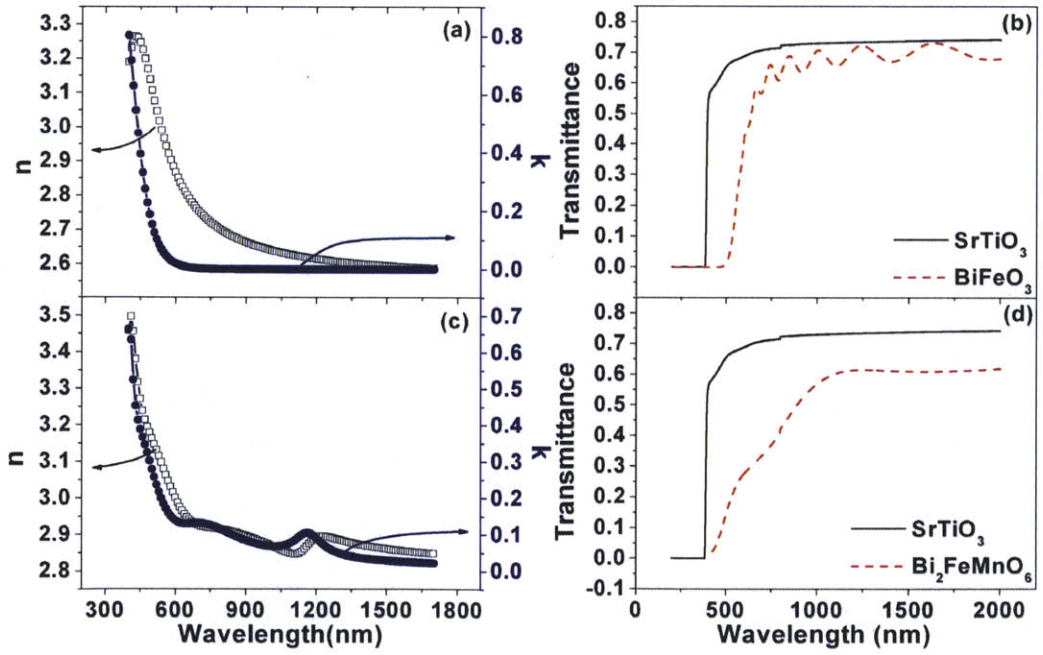

Fig. 3-6 Optical constants as a function of wavelength for (a) $BiFeO_3$ and (c) Bi_2FeMnO_6 films as measured by ellipsometry; Incident light transmittance as a function of wavelength for (b) $BiFeO_3$ and (d) Bi_2FeMnO_6 films as measured by spectrophotometry.

Figure 3-6 (c) shows the fitted optical constants for the Bi_2FeMnO_6 film as a function of wavelength. Quite different from $BiFeO_3$, this film shows a refractive index of n=2.85 and an extinction coefficient of k=0.048 at 1550nm wavelength. We modeled both the surface layer and the underlying Bi_2FeMnO_6 film in this case, because the Bi-rich surface layer thickness is not negligible compared with the overall thickness of this sample. Also, an absorption peak is clear around 1100 nm wavelength. The high extinction coefficient of Bi_2FeMnO_6 film is confirmed by the spectrophotometer results shown in figure 3-6 (d). The Bi_2FeMnO_6 sample has a much lower transmittance in the infrared region compared with the bare STO substrate.

3.1.5 DFT simulation: thermodynamically driven B-site disorder in Bi_2FeMnO_6

Density functional theory with spin polarized general gradient approximation (GGA) and GGA+U (Liechtenstein's implementation) methods were used to calculate the structure and electronic structure of $BiFeO_3$ and Bi_2FeMnO_6. We assumed the space group for $BiFeO_3$ and $BiMnO_3$ to be $R3c$ and $C2$ respectively according to experimental results [2][14], while we varied the space groups for Bi_2FeMnO_6 unit cell to be $Pm\bar{3}m$, $R3$ and $C2$. The magnetic configurations for $BiFeO_3$ and $BiMnO_3$ were set to be G-AFM and FM respectively. For Bi_2FeMnO_6, both FM and G-AFM configurations are presumed for each structural symmetry. In order to investigate how Mn valance state influences the unit cell structure, we also varied Mn to be Mn^{2+}, Mn^{3+} and Mn^{4+} by starting with different spin configurations on the Mn atoms. As a consequence, Fe was set to be Fe^{4+}, Fe^{3+}, Fe^{2+} respectively in these configurations. To estimate the formation enthalpy of Bi_2FeMnO_6, we considered the following reaction at 0 K temperature:

$$BiFeO_3 + BiMnO_3 \rightarrow Bi_2FeMnO_6$$

The formation enthalphy of Bi_2FeMnO_6 was estimated as:

$$\Delta H_f = E(Bi_2FeMnO_6) - E(BiFeO_3) - E(BiMnO_3)$$

where E is the total energy after structure relaxation. By fixing $BiFeO_3$ and $BiMnO_3$ in the $R3c$ and $C2$ space groups respectively, we can compare the formation enthalpy of Bi_2FeMnO_6 with different symmetries. Note that we neglect the small PΔV term. This is

applicable for reactions at atmosphere pressure, but it is not applicable for reactions carried out at high pressures such as several GPa.

Structure and formation enthalpy

Table III shows the structural parameters of $BiFeO_3$, $BiMnO_3$ and Bi_2FeMnO_6 and the formation enthalpy of Bi_2FeMnO_6 after unit cell relaxation. We fixed U(Fe)=7 eV and U(Mn)=6 eV for all related calculations. The calculated $BiFeO_3$ and $BiMnO_3$ lattice parameters show good agreement with experimental data [29][30]. For Bi_2FeMnO_6 there are three noticeable features in the calculation results. First of all, the formation enthalpy of Bi_2FeMnO_6 is always positive for all the structures and magnetic orderings we calculated, suggesting that B-site ordered Bi_2FeMnO_6 is unstable at 0 K. The positive formation enthalpy comes from the Fe and Mn octahedrons as nearest neighbors. Thus, B-site ordering is thermodynamically unfavored, and the pseudo-binary phase diagram of $BiMnO_3$ and $BiFeO_3$ should show complete phase separation at 0 K rather than forming the Bi_2FeMnO_6 compound. Secondly, both the unit cell structure and magnetic ordering affects the formation enthalpy of Bi_2FeMnO_6, with the former having the larger influence. The most stable structure of Bi_2FeMnO_6 is monoclinic with $C2$ space group. This result is not hard to interpret if one compares Bi_2FeMnO_6 with the lattice structure of $BiMnO_3$. In both systems Mn stays at the 3+ valence state, which creates a large lattice distortion due to the Jahn-Teller effect. This distortion is uniaxial, which distorts the unit cell from cubic to tetragonal. Meanwhile, the $6s^2$ lone pair states on Bi^{3+} ions further distort the unit cell to a noncentrosymmetric structure. [31] Note that we cannot obtain stable antiferromagnetic spin ordering during lattice relaxation in Bi_2FeMnO_6 with $R3$ symmetry. Thirdly, by comparing the formation enthalpy of Bi_2FeMnO_6 with FM and AFM magnetic ordering, one finds that AFM ordering is more stable for Bi_2FeMnO_6 with both $Pm\bar{3}m$ and $C2$ symmetries.

In order to verify the effect of cation valence state, we fixed the unit cell of Bi_2FeMnO_6 with $C2$ symmetry and varied the Mn valence states between Mn^{2+}, Mn^{3+} and Mn^{4+}. As a consequence, Fe was set as Fe^{4+}, Fe^{3+} and Fe^{2+} respectively. Fe and Mn were antiferromagnetically coupled in these calculations. However, after lattice relaxation, all three

cases relaxed to a Fe^{3+}/Mn^{3+} configuration, indicating this configuration was thermodynamically most stable. This result is consistent with our XPS measurement that both Fe and Mn ions are mostly in the 3+ valence state. The observation of small amount of Mn^{2+} and Mn^{4+} ions can be interpreted by considering that Mn^{3+}(high spin, *hs*) is a Jahn-Teller ion, which distorts the unit cell to larger sizes. [31] By adopting multiple valence states of Mn, the film can decreases the lattice distortion that would be caused by Mn^{3+} alone, which may result better lattice matching between the film and the substrate.

Table 3-3 Calculated lattice parameters of $BiFeO_3$ (space group R3c), $BiMnO_3$ (space group *C*2) and Bi_2FeMnO_6 (space groups $Pm\bar{3}m$, *R*3 and *C*2) using the GGA+U method, and the formation enthalpy of Bi_2FeMnO_6. G-AFM and FM magnetic ordering was assumed for $BiFeO_3$ and $BiMnO_3$ respectively. Both FM and G-AFM ordering were assumed for Bi_2FeMnO_6. U(Fe)=7 eV, U(Mn)=6 eV and J(Fe, Mn)=1 eV were used for all calculations.

	$BiFeO_3$	$BiMnO_3$	Bi_2FeMnO_6				
Space group	*R*3*c*	*C*2	$Pm\bar{3}m$		*R*3	*C*2	
Magnetic Ordering	G-AFM	FM	FM	G-AFM	FM	FM	G-AFM
a (Å)	5.67	9.71	7.86	7.84	5.71	9.50	9.50
b (Å)	5.67	5.70	7.86	7.84	5.71	5.80	5.77
c (Å)	5.67	10.00	7.86	7.84	5.71	9.78	9.76
α(°)	59.11	90	90	90	59.15	90	90
β(°)	59.11	111.11	90	90	59.15	107.91	107.91
γ(°)	59.11	90	90	90	59.15	90	90
Ω(Å^3)	126.28	516.33	485.83	482.04	129.09	512.74	508.91
Formation enthalpy per Bi basis (eV)	N/A	N/A	1.162	1.155	0.203	0.092	0.057

Electronic structures and effect of U

To investigate the electronic structure of $BiFeO_3$, $BiMnO_3$ and Bi_2FeMnO_6, we also carried out calculations on the density of states (DOS) of these compounds. Figure 3-7 shows the calculated DOS for both spin channels of *R*3*c* $BiFeO_3$ using various U values. In all three calculations, $BiFeO_3$ is predicted to be an insulator. The band gaps are 0.4 eV, 2 eV and 2.4 eV for U=0 eV, 5 eV and 7 eV respectively. Increasing the U value significantly increases the

bandgap, and U=7 eV shows the band gap value closest to our experimental values. Changing the U value also influences the ionicity of the Fe-O bonding. For U=0 eV, Fe 3d and O 2p valence electrons show strong hybridization in the energy range of -6 eV to 0 eV, indicating the Fe-O bonding is highly covalent. This is not reasonable if we consider the electronegativity is quite different between Fe (1.83) and O (3.44). However, as the U value increases, Fe 3d valence electrons are pushed down to lower energy levels, and the $t_{2g} - e_g$ energy split is smaller. This indicates that the Fe-O bonding is more ionic and the electrons are more localized on the Fe and O atoms. Electron spin integration around the Fe site shows that the magnetic moment of Fe is 3.75 μ_B, 4.13 μ_B and 4.25 μ_B for U=0 eV, 5 eV and 7 eV respectively. Interestingly, U=0 eV rather than U=7 eV provides the best prediction of Fe magnetic moment compared with experiments [32]. These calculation results using the GGA+U method are similar to previous results calculated by LSDA and LSDA+U methods. [5] The difference is that for the same U value, GGA predicts slightly larger band gaps and Fe magnetic moments compared with LSDA.

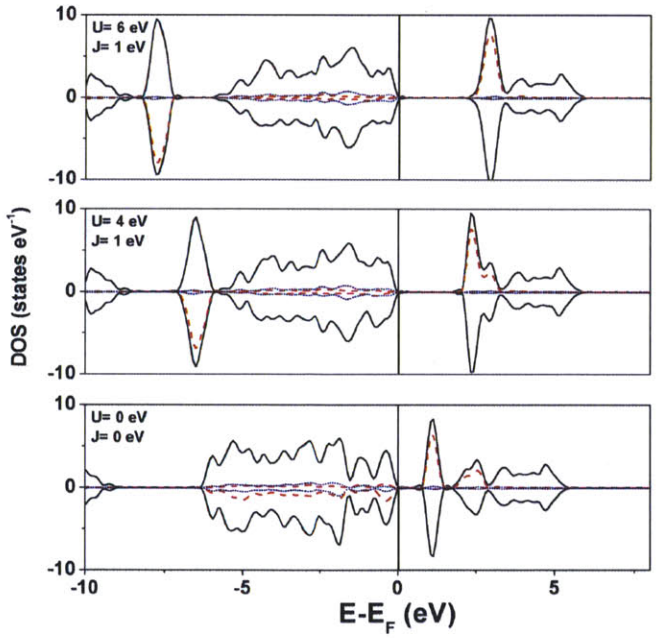

Fig. 3-7 Total, Fe 3d and O 2p density of states (DOS) for *R*3*c*-structured $BiFeO_3$ calculated using GGA method (U=J=0 eV) and GGA+U method (J=1 eV, U=5 eV and J=1 eV U=7 eV). The total DOS is normalized to a formula unit of $Bi_2Fe_2O_6$. As U increases, the calculated band gap energy increases, and the ionicity of Fe-O bonds increases.

Figure 3-8 shows the calculated DOS of $C2$ $BiMnO_3$ for both spin channels using the GGA+U method (U=0 eV, 6 eV and 8 eV). For insulating $BiMnO_3$, it is well known that the LSDA method predicts a half metallic band structure. [31][34][35] This is due to the strong hybridization tendency between Mn 3d and O 2p orbitals in first-principles calculations. Our calculation based on monoclinic $BiMnO_3$ using the GGA method also shows similar behavior. When U=0 eV, Mn 3d and O 2p electrons strongly hybridize and there is no band gap. Applying the GGA+U method enhances the ionicity of the Mn-O bonding and creates a dip in the DOS near the Fermi energy level. A gap of about 0.4 eV opens between the occupied and unoccupied Mn $e_g^{\uparrow}$ states. This effect was observed by Shishidou *et al.* using LDA+U calculations. [35] Different from $BiFeO_3$, as we increase the U value up to 8 eV, this gap does not increase, which still yields large difference between our experimental and calculation results.

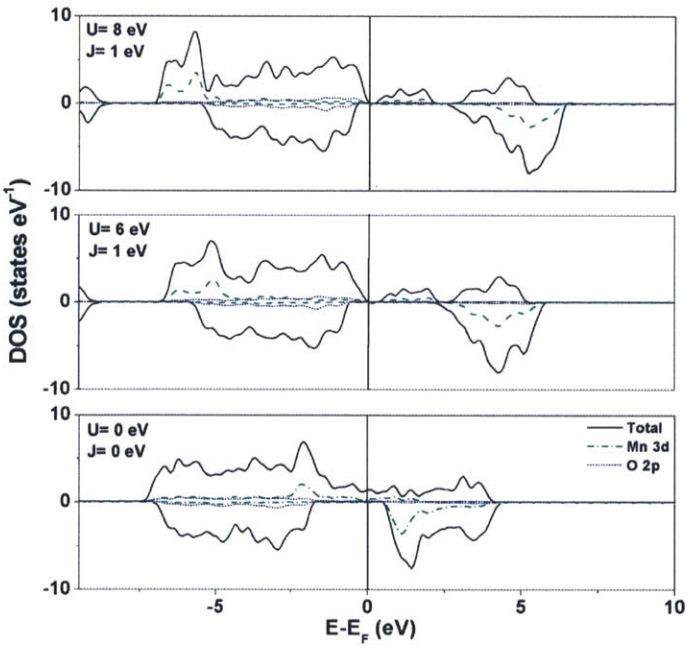

Fig. 3-8. Total, Fe 3d and O 2p density of states (DOS) for $C2$ $BiMnO_3$ calculated using GGA method (U=J=0 eV) and GGA+U method (J=1 eV, U=6 eV and J=1 eV, U=8 eV). The total DOS is normalized to a formula unit of $Bi_2Mn_2O_6$.

However, applying GGA or GGA+U methods to calculate the electronic structure of $C2$

Bi_2FeMnO_6 shows dramatic differences compared with $BiMnO_3$. Figure 3-9 (a) and (b) shows the calculated DOS of monoclinic Bi_2FeMnO_6 with antiferromagnetic spin ordering by applying GGA and GGA+U methods (U(Fe)=7 eV, U(Mn)=6 eV) respectively. The GGA method predicts Bi_2FeMnO_6 to be half metallic, while GGA+U indicates Bi_2FeMnO_6 should be insulating. Compared with our optical measurements, it is clear that the GGA+U method provides a more realistic result. Looking closely into the details of the density of states, the 100% spin polarized structure in the GGA calculation is due to the hybridization of Fe 3d, O 2p and Mn 3d orbitals. The unoccupied Mn $e_g^{\downarrow}$ states hybridize with Fe $t_{2g}^{\downarrow}$ and $e_g^{\downarrow}$ states through oxygen, causing a half metallic structure. In the GGA+U method, the Coulomb repulsion and correlation interaction correction causes lower hybridization between Fe and Mn orbitals, and a gap opens above the Fermi level. Despite this, hybridized states among Fe 3d, Mn 3d and O 2p orbitals can still be found in the valence and conduction bands. This result predicts that Mn-O-Fe type hopping conduction is likely to take place in Bi_2FeMnO_6.

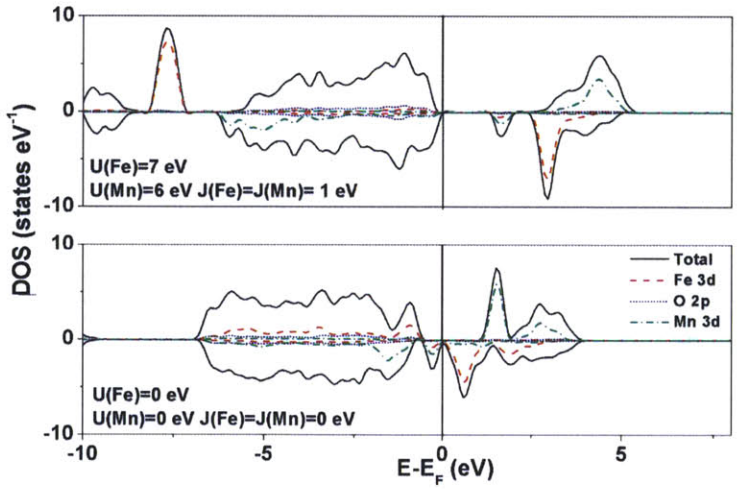

Fig. 3-9 Total, Fe 3d and O 2p density of states (DOS) for *C*2 Bi_2FeMnO_6 calculated using GGA method (J(Fe)=J(Mn)=0 eV, U(Fe)=U(Mn)= 0 eV) and GGA+U method (J(Fe)=1 eV, U(Fe)=7 eV and J(Mn)=1 eV, U(Mn)=6 eV). The total DOS is normalized to a formula unit of Bi_2FeMnO_6. The GGA method predicts a half-metallic band structure while GGA+U indicates this material should be insulating.

It is now useful to compare our experimental results and calculations to understand the properties of Bi_2FeMnO_6. The formation enthalpy for bulk ordered Bi_2FeMnO_6 is predicted to be positive for several crystal symmetries by density functional theory, which assumes

equilibrium phases and atmospheric pressure. This suggests that neighboring Fe and Mn octahedra are not thermodynamically favored in this material; thus it could be difficult to fabricate it as an ordered bulk material. This observation is evident in one previous study by Yang *et al.* [36], who claimed that incorporating Mn>30at.% on the B-site of $BiFeO_3$ is difficult unless high pressure processing is used. Experimentally, the smaller process window for forming Bi_2FeMnO_6 as compared to $BiFeO_3$ (the oxygen pressure window for $BiFeO_3$ growth exceeds 4.5 mTorr while for Bi_2FeMnO_6 it is smaller than 0.4 mTorr) may be indicative of the relative instability of the Bi_2FeMnO_6 perovskite phase, and our films showed no evidence of B-site ordering. In contrast, there are several ordered double perovskites that can be grown by bulk processing, such as La_2MnNiO_6 [27], La_2MnCoO_6 [37] and Sr_2FeMoO_6 [38], and it will be interesting to investigate whether a negative formation enthalpy is predicted in these ordered perovskites following the computational methods used here.

We observed experimentally that Mn tends to adopt multiple valence states in the perovskite film. From the calculation results we infer that Mn^{3+} is thermodynamically the most stable ion in Bi_2FeMnO_6. One possible explanation of the experimental observation is that by adopting multi valence states of Mn, the material can reduce the Jahn-Teller effect from Mn^{3+}. For a thin film material, this process may promote better lattice matching with the substrate, lowering the interface and strain energies. Other factors such as film defects may also have been important in changing the valence states of Mn.

In Bi_2FeMnO_6, the electronic structure calculation predicts a strong tendency for Fe-O-Mn hybridization, and the resulting conductivity due to interatomic hopping is expected to be higher than the conductivity of $BiFeO_3$. The optical absorption spectrum may provide some insight into the conductivity. The large absorption of Bi_2FeMnO_6 in the infrared may be due to free carrier absorption. The absorption peak around 1100 nm does not correspond to any dipole transition energies of Fe or Mn sites, and may therefore be due to interatomic electron hopping, i.e. Verwey conduction. In addition, hopping conduction between Mn with different valence states is possible, as observed for example in $La_{1-x}Sr_xMnO_3$ perovskite [39]. This requires significant amounts of Mn^{2+} and Mn^{4+} to allow percolation to take place.

Quantitative analysis on the amount of Mn^{2+} and Mn^{4+} ions may provide more information on the importance of these two conduction mechanisms. The relatively high conductivity of polycrystalline Bi_2FeMnO_6 was shown in one previous study, although grain boundary conduction and the effects of secondary phases may have been important. [40]

3.2 $LaFeO_3$ films on $SrTiO_3$ (001) substrates

3.2.1 Introduction

$LaFeO_3$ (LFO) is a distorted perovskite-structure antiferromagnet (orthorhombic, a=5.557Å, b=5.5652Å, c=7.8542Å) [41] with high Néel temperature of 740 K in bulk [3], and may be a good candidate for magneto-optics, spin valves and other exchange-bias applications in magnetic memory [41], or for oxygen sensing [43]. The crystal orientation of $LaFeO_3$ strongly influences its antiferromagnetic domain structure and consequently the exchange bias to neighboring ferromagnetic films. [44] Also, due to the non-cubic crystal structure of $LaFeO_3$ optical scattering may occur between crystals with different orientations. The refractive indices along different crystallographic orientations of orthoferrites are significantly different. For example, $YFeO_3$ shows birefringence in the order of 10^{-2} at visible and near infrared wavelengths. [45] The material birefringence causes scattering at domain boundaries and are detrimental to the device transparency. Multiple crystal orientation structure is also widely observed in non-cubic perovskites epitaxially grown on cubic substrates, such as $PbTiO_3$ on $SrTiO_3$. [46] Therefore understanding and controlling the crystal orientation of epitaxial films during growth has general importance for integrating non-cubic oxide materials in photonic devices. When $LaFeO_3$ films are grown on single crystalline cubic substrates with (001) surface orientation, such as $SrTiO_3$(001), MgO(001) and $LaAlO_3$(001), two film orientations, LFO(110)||substrate(100) (the α domain) and LFO(001)||substrate(100) (the β domain) show similar lattice mismatch. Both orientations are observed in epitaxial LFO films on MgO(001) substrates in previous studies [44], while only one orientation (the α domains) has been found in films grown on STO (001) substrates due to the small lattice mismatch between the film and the substrate [42][44][47]. It is highly

desirable the growth mechanism can be understood and the crystal orientations of $LaFeO_3$ can be controlled on a specific substrate.

3.2.2 Crystal orientation control and analysis of $LaFeO_3$ epitaxial films

$LaFeO_3$ epitaixal films on $SrTiO_3(001)$ substrates were fabricated under various conditions shown in table 2-1. Fig. 1 shows the one dimensional X-ray diffraction (XRD) ω-2θ spectra of five LFO films, labeled A-E, fabricated under different conditions of temperature and oxygen pressure. The LFO diffraction peaks originating from the *(l,l,0)* or *(0,0,2l)* planes of the α or β domains respectively overlap due to the similarity in lattice spacings. Therefore, we mark both possibilities in Fig. 3-10(a). The full width at half-maximum (FWHM) of the α(330) or β(006) diffraction peaks for all the samples is around 0.5°, indicating good quality of the films. Considering the α(330)/β(006) diffraction peaks shown in Fig. 3-10(b), a decrease of the out-of-plane (OP) lattice constant (from 4.040 Å to 3.951 Å based on a pseudo-cubic lattice) of the LFO films is found with increasing oxygen pressure, corresponding to a reduced lattice mismatch between the film and the substrate. This trend is attributed to a decrease of oxygen vacancies, which are known to expand the oxide lattice [48], as we increase the oxygen pressure. For samples C and D, broadening and splitting of the diffraction peaks were observed. This may indicate a stress relaxation process in these films as they grow thicker. [49]

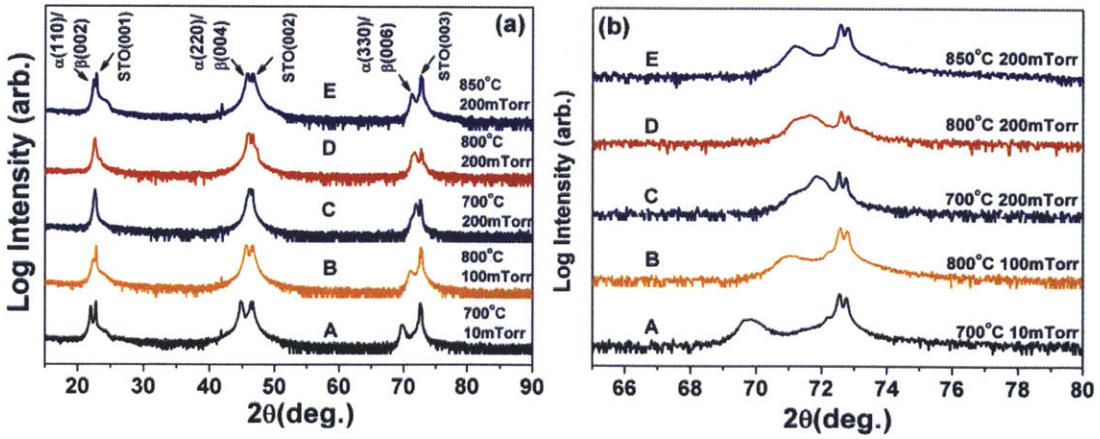

Fig. 3-10 (a) 1 dimensional ω-2θ X-ray diffraction spectra of five $LaFeO_3$ films grown on $SrTiO_3$ (001) substrates (b) Part of the spectra near the $SrTiO_3$ (003) diffraction peak

In order to distinguish the α and β domains, X-ray pole figures of the LFO (111) reflection were measured. As shown in Fig. 2(a), when epitaxially grown on an STO(001) substrate, the surface normals as well as the diffraction peaks of the {111} planes should appear at χ=26.5° and χ =63.5° for the α and β domains respectively. Both α and β domains can have 90° twins (namely α' and β' domains), which yields four-fold symmetry of the diffraction peaks on the ψ axis. Due to the tiny difference between the a and b axes (0.1%) of the LFO unit cell, the diffraction peaks of β and β' domains on the pole figures cannot be differentiated. The X-ray pole figures for three LFO films, A, C and D are shown in Fig. 3-11(b)-(d). The spot-like diffraction patterns indicate epitaxial growth of the films. Only α domains were observed in films grown at high substrate temperature (800°C) or low oxygen pressure (10mTorr) (Fig. 3-11(b) and 3-11(d) which is consistent with previous reports [42][44][47]. However, both α and β domains were observed in films grown at lower substrate temperature (700°C) and high oxygen pressure (200mTorr) as shown in Fig. 3-11(d). The {111} diffraction peaks of the α and β domains appear at the same ψ positions, consistent with the structure shown in Fig. 2(a). The deposition temperature and pressure can therefore be tuned to give films with just the α domains, or with a mixture of α and β domains.

Fig. 3-12 (a) shows a plan view bright field transmission electron microscopy (TEM) image of sample C, which contains α and β domains. A self-assembled mosaic structure with square shaped domains was observed, with an average domain size of about 50 nm. The selected area diffraction pattern of the film is shown in the inset of Fig. 3-12(b). The substrate (100) and (010) diffraction spots are labeled. The circles mark the {001} diffraction spots of the α domains in LFO and the squares mark the {100} diffraction spots of the β domains. This diffraction pattern is different from that of LFO films containing only α domains [44]. By choosing one of the diffraction spots of the β domains, we obtained the plan view dark field TEM image shown in Fig. 3-12(b). The β or β' domains (bright grains) occupy about one third of the sampling area.

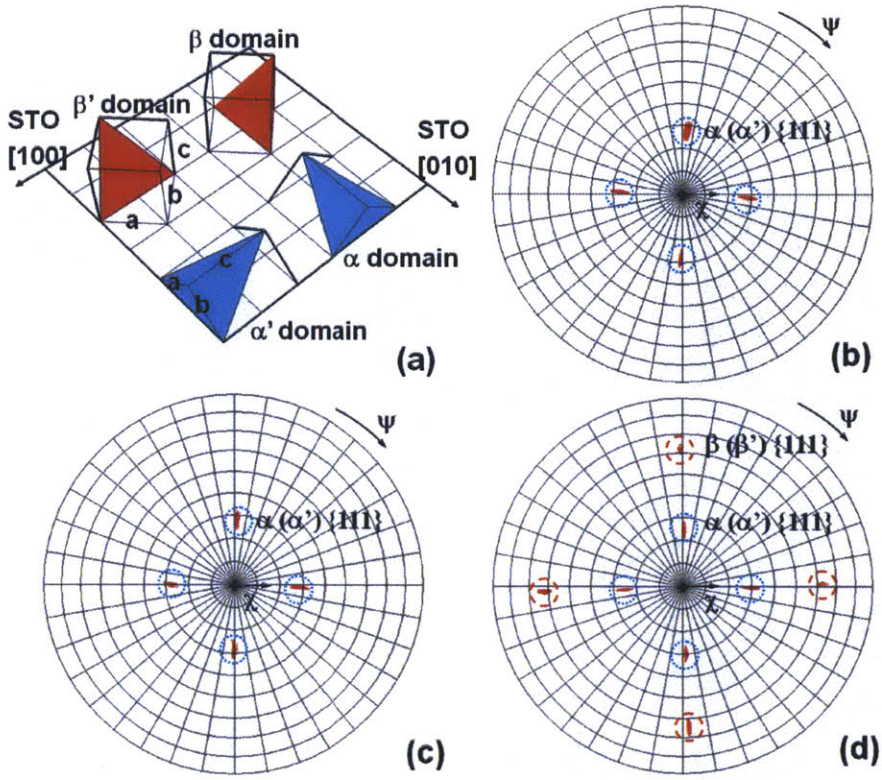

Fig. 3-11 (a) Diagram of the four possible epitaxial orientations of LFO on a STO(001) substrate. The shaded planes represent {111} planes. Also shown are the X-ray pole figures of the (111) reflections for LFO films grown under different conditions: (b) 700°C, 10 mTorr (Sample A), (c) 800°C, 200 mTorr (Sample D) and (d) 700°C, 200 mTorr (Sample C). A fixed 2θ value of 25.3° (corresponding to the LFO(111) planes) was used to collect the data.

A cross-sectional TEM image of sample C is shown in Fig. 3-12(c). Triangular shaped crystal grains were observed throughout the thickness direction of the film. The grain boundaries make similar angles of about 20° to the substrate surface normal. Considering the rectangular shape of the grains in the plain view image, the crystal domains form pyramidal shapes along the film thickness direction. These nano-pyramids initiate at the interface between the film and the substrate. This self-assembled nano-pyramid structure differs from the columnar self-assembled nanostructures reported elsewhere [50][51]. Fig. 3-12(d) is a high resolution transmission electron microscopy (HRTEM) image including several domains with their orientations indicated. The square like pattern in atomic force microscopy image of sample C shown in figure 3-13 agrees well with the plane view TEM image. The root mean square roughness for samples A, C and D is 0.88 nm, 2.22 nm and 1.79 nm respectively.

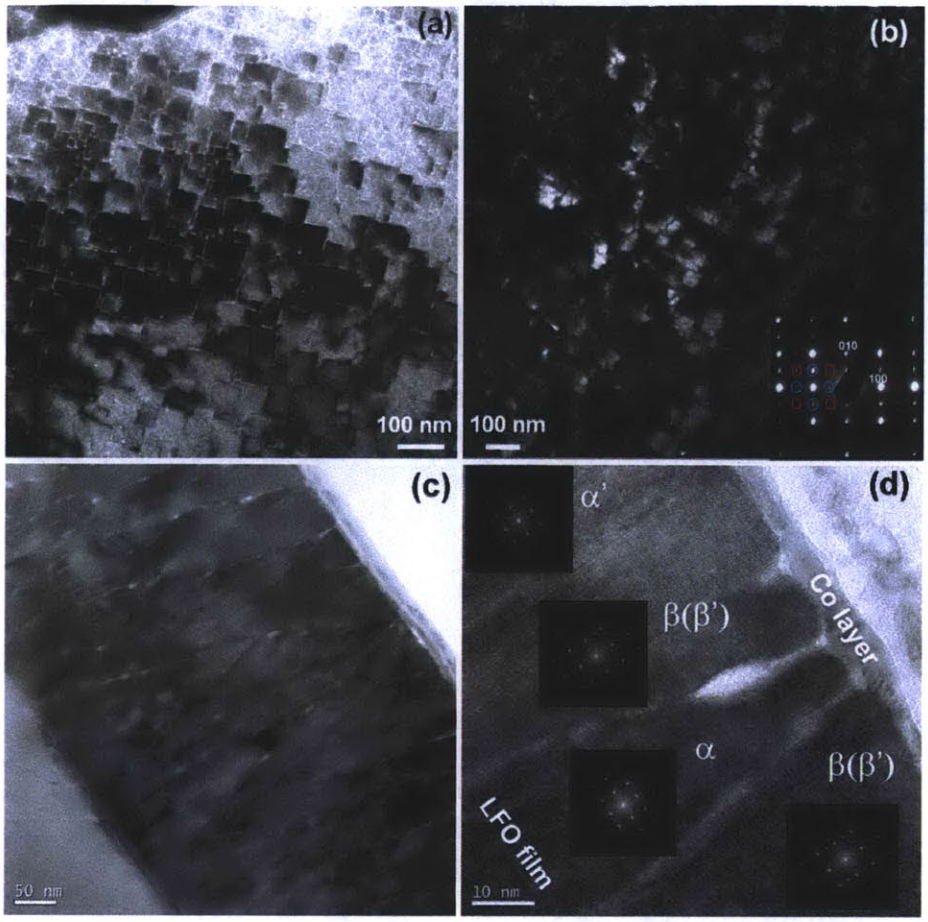

Fig. 3-12 Bright field (a) and dark field (b) plan view TEM images of the LFO film grown on a STO(001) substrate at 700°C substrate temperature and 200 mTorr oxygen partial pressure. (Sample C). The SAED pattern is shown in the inset of (b). The STO(100) and (010) diffraction spots are marked. The circles indicate the diffraction peaks of LFO {001} planes from the α domains while the squares indicate the diffraction peaks of {100} planes from the β domains. One of the β domain diffraction spots was selected to record the dark field TEM image. Also shown are (c) a cross-sectional TEM image and (d) a high resolution cross-sectional TEM lattice image near the LFO film surface, including the FFT patterns.

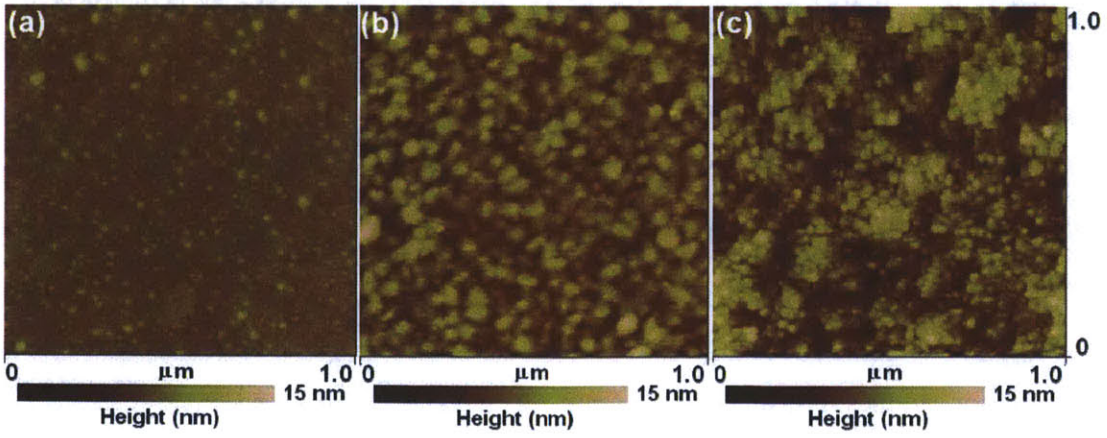

Fig. 3-13 Atomic force microscopy images of $LaFeO_3$ films of (a) sample A (b) sample D and (c) sample C

The different crystallographic structures in sample A, C and D lead to different magnetic exchange bias (EB) on a 5 nm Co overlayer. After field cooling from 500°C, the measured room temperature EB in Co for samples A, C and D is 8±3 Oe, 15±3 Oe and 12±3 Oe respectively. These small absolute EB values are probably due to roughening (see Fig. 3-12(d)) or oxidation of the Co film [44], but they do indicate a higher EB for the double-oriented film (sample C).

The changes in LFO crystal orientation and morphology with the fabrication conditions may be explained by the kinetic model reported in Ref. [52]. According to this model, the lattice mismatch between LFO and STO provides a driving force for add atoms to diffuse away from a nucleated island, and stabilize the islands to a certain size. Either high deposition flux (corresponding to low oxygen pressure [53], sample A) or a high diffusion length of the incoming atoms (corresponding to high substrate temperature, sample D) lead to coalesce of the islands, and prevent the formation of a self-assembled structure. In both cases, the add atoms have sufficient diffusivity to allow the growth of the thermodynamically more stable α domains and suppress the β domains. However, for the LFO film grown under low substrate temperature and high oxygen pressure (sample C), kinetic limitations lead to the coexistence of both α and β orientations within a self-assembled nanostructure. In previous reports [42][44][47], LFO films were deposited on STO at high substrate temperatures and low oxygen partial pressures to improve the film crystallinity. These conditions, and the low lattice mismatch, suppressed the formation of a double-oriented film, in contrast to LFO grown on MgO, which formed a double-oriented film under similar deposition conditions due to the much larger mismatch[42][44]. This result suggests that self-assembled oxide film structures can be promoted by appropriate choice of deposition conditions and substrate material.

3.3 Summary

In this chapter, we studied three heteroepitaxial orthoferrite thin film systems: $BiFeO_3$, Bi_2FeMnO_6 and $LaFeO_3$ on $SrTiO_3(001)$ substrates. For $BiFeO_3$ and Bi_2FeMnO_6, it is found that both films can be epitaxially grown in the perovskite structure within a small window of process parameters. Compared with $BiFeO_3$, Bi_2FeMnO_6 shows a smaller process window, and its magnetic properties imply that the B-site cations are disordered. These observations are attributed to the positive formation enthalpy of ordered Bi_2FeMnO_6 compared with $BiFeO_3$ and $BiMnO_3$ at 0 K. Mn tends to form multiple valence states in Bi_2FeMnO_6 despite the higher stability of the compound only containing Mn^{3+} ions, possibly because the incorporation of Mn^{2+} or Mn^{4+} decreases Jahn-Teller effect of Mn^{3+} in the film. Bi_2FeMnO_6 had a large optical absorption compared to $BiMnO_3$ as a result of electron hopping between Fe and Mn sites as well as between Mn sites with different valence states. For $LaFeO_3$, either single-epitaxial film with only one crystal orientation or double-epitaxial film consisting of nanoscale pyramids of two alternating crystal orientations is fabricated by controlling the pulsed-laser deposition conditions. The double-epitaxial film is promoted by low mobility deposition conditions and by high lattice mismatch strain, and its properties differ from those of a single-epitaxial film, for example double-epitaxial films show higher exchange bias to a Co overlayer. These results provide understanding of thermodynamically driven cation ordering and kinetically driven crystal growth process in heteroepitaxial orthoferrite thin films on cubic substrates, which are can be generally applied to other perovskite material systems for the properties of magnetic and structural ordering in these materials.

References

[1] L. K. Shick and J. W. Nielsen, *J. Appl. Phys.*, **42**, 1554 (1971)

[2] H. Bea, M. Bibes, A. Barthelemy, K. Bouzehouane, E. Jacquet, A. Khodan, *et al., Appl. Phys. Lett.*, **87**, 072508-1 (2005)

[3] A. Scholl, J. Stöhr, J. Lüning, J. W. Seo, J. Fompeyrine, H. Siegwart, J. P. Locquet, F. Nolting, S. Anders, E. E. Fullerton, M. R. Scheinfein and H. A. Padmore, *Science*, **287**, 1041 (2000)

[4] J. Li, J. Wang, M. Wuttig, R. Ramesh, N. Wang, B. Ruette, *et al., Appl. Phys. Lett.*, **84**, 5261 (2004)

[5] J. B. Neaton, C. Ederer, U. V. Waghmare, N. A. Spaldin, K. M. Rabe, *Phys. Rev. B*, **71**, 014113 (2005)

[6] Li. M, MacManus-Driscoll J. L., Appl. Phys. Lett., **87**, 252510 (2005)

[7] G. F. Dionne, A. R. Taussig, M. Bolduc, L. Bi, and C. A. Ross, *J. Appl. Phys.*, **101**, 09C524 (2007)

[8] G.F. Dionne and G.A. Allen, *J. Appl. Phys.*, **73**, 6127 (1993)

[9] G. F. Dionne and G.A. Allen, *J. Appl. Phys.*, **75**, 6372 (1994)

[10] J. Wang. *Deposition and Characterization of Multiferroic BiFeO3 Thin Films. PhD dissertation,* (University of Maryland, Department of Materials Science and Engineering, 2005)

[11] S. V. Kiselev, R. P. Ozerov, and G. S. Zhdanov, *Sov. Phys. Dokl.*, **7**, 742 (1963)

[12] J. R. Teague, R. Gerson, and W. J. James, *Solid State Commun.*, **8**, 1073 (1970)

[13] B. Ruette, S. Zvyagin, A. P. Pyatakov, A. Bush, J. F. Li, V. I. Belotelov, A. K. Zvezdin, and D. Viehland, *Phys. Rev. B*, **69**, 064114–1 (2004)

[14] A. Sharan, J. Lettieri, Y. Jia, W. Tian, X. Pan, D. G. Schlom, and V. Gopalan, *Phys. Rev. B*, **69**, 214109 (2004)

[15] T. Kimura, S. Kawamoto, I. Yamada, M. Azuma, M. Takano, and Y. Tokura, *Phys. Rev. B*, **67**, 180401R (2003)

[16] A. Moreira dos Santos, S. Parashar, A. R. Raju, Y. S. Zhao, A. K. Cheetham, and C. N. R. Rao, *Solid State Commun.*, **122**, 49 (2002)

[17] J.B. Goodenough, *Magnetism and the Chemical Bond* Table XII, Wiley, New York, 1963

[18] J. B. Goodenough, A. Wold, N. Menyuk, and R. J. Arnott, *Phys. Rev.*, **124**, 373 (1961)

[19] G. F. Dionne, *J. Appl. Phys.*, **79**, 5172 (1996)

[20] C. H. Yang, J. H. Song, H. J. Lee, S. Yoon, T. Y. Koo, and Y. H. Jeong, *Phys. Stat. Sol. (b)*, **241**, 1453 (2004)

[21] D. Kothari, V. R. Reddy, A. Gupta, D. M. Phase, N. Lakshmi, S. K. Deshpande and A. M. Awasthi, *J. Phys.: Condens. Matter.*, **19**, 136202 (2007)

[22] J. R. Sahu, C.N.R. Rao, *Solid State Sciences*, **9**, 950 (2007)

[23] V. R. Palkar, D. C. Kundaliya, and S. K. Malik, *J. Appl. Phys.*, **93**, 4337 (2003)

[24] D. L. Wood, J. P. Remeika, and E. D. Kolb, *J. Appl. Phys.*, **41**, 13 (1970)

[25] W. J. Tabor, A. W. Anderson, and L. G. Van Uitert., *J. Appl. Phys.*, **41**, 7 (1970)

[26] G. F. Dionne and G. A. Allen, *J. Appl. Phys.*, **95**, 7333 (2004)

[27] N. S. Rogado, J. Li, A. W. Sleight and M. A. Subramanian, *Adv. Mater.*, **17**, 2225 (2005)

[28] C. Wandelt, *Surf. Sci. Rep.*, **2**, 1 (1982)

[29] F. Kubel and H. Schmid, Acta Crystallogr., *Sect. B: Struct. Sci.*, **46**, 698 (1990)

[30] T. Atou, H. Chiba, K. Ohoyama, Y. Yamaguchi, Y. Syono, *J. of Solid State Chem.*, **145**, 639 (1999)

[31] R. Seshadri and N. A. Hill, *Chem. Mater.*, **13**, 2892 (2001)

[32] I. Sosnowska, W. Schäfer, W. Kockelmann, K. H. Andersen, and I. O. Troyanchuk, *Appl. Phys. A:*

Mater. Sci. Process., **74**, S1040 (2002)
[33] J. B. Neaton, C. Ederer, U. V. Waghmare, N. A. Spaldin, K. M. Rabe, *Phys. Rev. B*, **71**, 014113 (2005)
[34] N. A. Hill, K. M. Rabe, *Phys. Rev. B*, **59**, 8759 (1999)
[35] T. Shishidou, N. Mikamo, Y. Uratani, F. Ishii and T. Oguchi, *J. Phys.: Condens. Matter,* **16,** S5677 (2004)
[36] C. H. Yang, T.Y. Koo and Y.H. Jeong, *Solid State Comm.*, **134**, 299 (2005)
[37] C. L. Bull, D. Gleeson and K. S. Knight, *J. Phys.: Condens. Matter*, **15**, 4927 (2003)
[38] K. I. Kobayashi, T. Kimura, H. Sawada, K. Terakura, Y. Tokura, *Nature*, **395**, 677 (1998)
[39] M. Izumi, T. Manako, Y. Konishi, M. Kawasaki and Y. Tokura, *Phys. Rev. B*, **61**, 12187 (2000)
[40] S. K. Singh, H. Ishiwara and K. Maruyama, *Appl. Phys. Lett.*, **88,** 262908 (2006)
[41] S. E. Dann, D. B. Currie, M. T. Weller, M. F. Thomas and A. D. Al-Rawwas, *J. Solid State Chem.*, **109**, 134 (1994)
[42] A. Scholl, J. Stöhr, J. Lüning, J. W. Seo, J. Fompeyrine, H. Siegwart, J.-P. Locquet, F. Nolting, S. Anders, E. E. Fullerton, M. R. Scheinfein and H. A. Padmore, *Science,* **287**, 1014 (2000)
[43] I. Hole, T. Tybell, J. K. Grepstad, I. Warnhus, T. Grande and K. Wiik, *Solid-State Electr.*, **47**, 2279 (2003)
[44] J. W. Seo, E. E. Fullerton, F. Nolting, A. Scholl, J. Fompeyrine and J-P Locquet, *J. Phys.: Condens. Matter.*, **20**, 264014 (2008)
[45] Jastrzebski L., *Phys. Stat. Sol.*, **21**, 57 (1974)
[46] Bartasyte A., Dkhil B., Kreisel J., Chevreul J., Chaix-Pluchery O., Rapenne-Homand L., Jimenez C., Abrutis A. and Weiss F., *Appl. Phys. Lett.*, **93**, 242907 (2008)
[47] S. Czekaj, F. Nolting, L.J. Heyderman, P. R. Willmott and G. van der Laan, *Phys. Rev. B.*, **73**, 020401(R) (2006)
[48] D. P. Norton, C. Park, J. D. Budai, S. J. Pennycook and C. Prouteau, *Appl. Phys. Lett.*, **74**, 2134 (1999)
[49] J. K. Grepstad, Y. Takamura, A. Scholl, I. Hole, Y. Suzuki and T. Tybell, *Thin Solid Films*, **486**, 108 (2005)
[50] J. Jiang, L. L. Henry, K. I. Gnanasekar, C. Chen and E. I. Meletis, *Nano Lett.*, **4**, 741 (2004)
[51] J. C. Jiang, E. I. Meletis, R. Asuvathraman, K. V. Govindan Kutty, K. I. Gnanasekar and C. L. Chen, *Appl. Phys. Lett.*, **86**, 163110 (2005)
[52] A-L Barabasi, *Appl. Phys. Lett.*, **70**, 2565 (1997)
[53] Y. Z. Yoo, O. Chmaissem, S. Kolesnik, B. Dabrowski, M. Maxwell, C. W. Kimball, L. McAnelly, M. Haji-Sheikh and A. P. Genis, *J. Appl. Phys.*, **97**, 103525 (2005)

Chapter 4
Room Temperature Ferromagnetic Perovskite Thin Films

Perovskite oxides with the chemical formula of ABO_3 have been widely studied due to their unique dielectric and ferroelectric properties. The exploration of ferromagnetism in perovskite structures by doping with ions with uncompensated spins are driven by the interest in room temperature multiferroic materials. Systems such as Fe doped $BaTiO_3$ [1] and Co doped $(La,Sr)TiO_3$ [2] were reported to show room temperature ferromagnetism (RT-FM). Meanwhile, cubic or tetragonal perovskites such as $SrTiO_3$ or $BaTiO_3$ show good lattice match with silicon substrate. A variety of buffer layer mediated epitaxial growth of perovskites on Si was reported.[3][4] Therefore RT-FM perovskites may serve as good candidates for on-chip nonreciprocal photonic device applications if they have good FoM. Rajamani *et al.* demonstrated strong Faraday rotation and good figure of merit in Fe doped $BaTiO_3$ films on MgO substrates. [5] A systematic study on the structure, magnetic and magneto-optical properties of transition metal ion doped perovskites is desired to understand these materials for their future applications.

In principle, orthoferrites discussed in chapter 3 are also perovskites with distorted unit cells. Different from orthoferrites, this chapter is focused on perovskite structures with cubic or tetragonal unit cells. Specifically, we study 3d transition metal ion Fe, Co doped $SrTiO_3$ films. A systematic study on epitaxial $Sr(Ti_{1-x}Co_x)O_{3-\delta}$ films is carried out. By doping $Sr(Ti_{0.6}Fe_{0.4})O_{3-\delta}$ films with donor (Ce) or acceptor (Ga) ions, the magneto-optical, optical properties and figure of merit are controlled and optimized. The fabrication conditions of these films are shown in table 2-1 $Sr(Ti_{0.6}Fe_{0.4})O_{3-\delta}$ and $Sr(Ti_{0.2}Ga_{0.4}Fe_{0.4})O_{3-\delta}$ films were integrated in As_2S_3 glass strip-loaded waveguides. The waveguide transmission loss at near infrared wavelength is characterized. By simulating the mode confinement in the oxide thin film layer, the material loss of the magneto-optical oxides and the device figure of merit are evaluated by numerical methods.

4.1 $Sr(Ti_{1-x}Co_x)O_{3-\delta}$ epitaxial thin films

4.1.1 Introduction

In ordinary perovskites, $SrTiO_3$ shows good silicon compatibility [5] and excellent optical transparency at communication wavelengths [7], making it a promising candidate material for spintronic and integrated magnetooptical applications. Co doped $SrTiO_3$ (STC) is a candidate system for these applications due to the RT-FM observed by different researchers. The mechanism of the RT-FM property of STC is under debate. Zhang *et al.* studied 2 at.% Co-doped Nb:$SrTiO_3$ thin films observing no RT-FM which excludes the mechanism of carrier mediated ferromagnetism in STC. [8] On the other hand, Co-doped (La,Sr)TiO_3 shows RT-FM, [9-11] but the origin of the ferromagnetism is still under debate between intrinsic ferromagnetism from the STC lattice and extrinsic ferromagnetism from impurity nano-clusters. Recently, epitaxial Co-doped $BaTiO_3$ thin films [12] showed intrinsic RT-FM behavior which is dependent on the film thickness. Meanwhile, $Sr(Ti_{1-x}Co_x)O_3$ bulk samples [13][14] show paramagnetic or spin-glass behavior with no RT-FM for any Co concentration. The differences between bulk and thin film materials may be caused by different valence states of Co in bulk compared to thin films. [14] Co valence states can be varied by changing the oxygen partial pressure, and consequently the oxygen stoichiometry, during growth. Lattice strains in epitaxial films can also change the film properties compared to bulk materials. There is therefore a need for a systematic analysis of the film structure and magnetic properties to understand the origin of RT-FM in 3d transition metal ion-doped perovskite structured films such as Co doped $SrTiO_3$.

In this section, we report the RT-FM properties, magnetic anisotropy and magnetooptical properties of $Sr(Ti_{1-x}Co_x)O_{3-\delta}$ films. Epitaxial $Sr(Ti_{1-x}Co_x)O_{3-\delta}$ films were grown on $SrTiO_3$ (cubic, a=3.905 Å at room temperature) and $LaAlO_3$ (rhombohedral below 435°C, a=b=5.365 Å, c=13.11 Å, (expressed in hexagonal geometry) a(pseudo-cubic)=3.79 Å at room temperature) substrates to study the magnetic anisotropy dependence on substrate lattice parameters. It is found that RT-FM and strong magnetic anisotropy can be achieved in

$Sr(Ti_{0.86}Co_{0.14})O_{3-\delta}$ and $Sr(Ti_{0.77}Co_{0.23})O_{3-\delta}$ films fabricated under high vacuum. From our detailed structural and property characterizations, we exclude the possibility of Co metal clusters as a major contributor to the ferromagnetic properties. The magnetoelastic anisotropy in these films may provide evidence for the valence state of the Co ions contributing to the RT-FM properties.

4.1.2 Structure of $Sr(Ti_{1-x}Co_x)O_{3-\delta}$ films

$Sr(Ti_{1-x}Co_x)O_{3-\delta}$ films were epitaxially grown on $LaAlO_3$ (001) (LAO) and $SrTiO_3$ (001) substrates by pulsed laser deposition (PLD) from single phase $Sr(Ti_{1-x}Co_x)O_{3-\delta}$ targets with x=0.05, 0.1, 0.2, 0.3 and 0.5. The films are named STC5, STC10, STC20, STC30 and STC50 respectively. The composition of the STC5, STC20, STC30 and STC50 films was measured by wavelength dispersive x-ray spectrometry (WDS) to be $Sr(Ti_{0.93}Co_{0.07})O_{3-\delta}$, $Sr(Ti_{0.86}Co_{0.14})O_{3-\delta}$, $Sr(Ti_{0.77}Co_{0.23})O_{3-\delta}$ and $Sr(Ti_{0.63}Co_{0.37})O_{3-\delta}$ respectively. Based on the ionic radii (Sr^{2+}: 132pm, Co^{2+}: 84pm, Co^{3+}: 72pm, Co^{4+} high spin: 67pm, Ti^{4+}: 68pm), we expect the Co to be in the B sites.

Figure 4-1(a) shows the 1DXRD ω–2θ scan spectra of the STC films grown on LAO substrates. Except for STC20 which additionally shows weak polycrystalline diffraction peaks from the STC(111) and STC(211) planes (about 2 orders of magnitude weaker than the single-crystal peak), all the other films show STC(00*l*) diffraction peaks only, indicating a "cube-on-cube" orientation relation between the film and the substrate. The broad diffraction features marked by "*" are from twin defects in the LAO substrates. Such features are not observed for films grown on STO substrates under similar fabrication conditions. There are no diffraction peaks from secondary phases observed in any of the films. The calculated out-of-plane (OP) lattice parameter of the STC films based on the (00*l*) diffraction peaks are shown in figure 4-1(b). The OP lattice constant of STC increases from 3.94 Å to 4.02 Å as the Co concentration increases from 7 at.% to 37 at.%, which indicates that the Co incorporated substitutionally into the STC lattice. As a comparison, the OP lattice constant of $SrTiO_3$ fabricated under similar conditions is 3.96 Å. In contrast, in STC bulk samples, the

lattice constant decreases linearly with increasing Co concentration up to 90% Co at the Ti site.[13][14] The inverse trend observed here may suggest that the Co ions in the films are in lower valence states than in bulk samples, so that the lattice expands with increasing Co concentration instead of contracting. This observation will be supported by our XPS characterization results, below. Figure 4-1(c) shows the 2DXRD spectrum of the STC30 film. The well-defined spot-like diffraction pattern of the STC (001) planes suggests epitaxial growth of the STC30 film. The epitaxial growth of STC30 on LAO is further indicated by the spot-like STC30 (124), LAO (244) and LAO (2,2,12) diffraction patterns in the X-ray RSM as shown in figure 4-1(d). Q_x and Q_z correspond to reciprocal spacings along the STC30 [020] in-plane (IP) direction and the STC30 [004] out-of-plane (OP) direction respectively. The difference between the Q_x values of the film and substrate diffraction spots indicate that the lattice mismatch strain is partially relaxed by misfit dislocations during growth. The OP and IP lattice parameters of the film were 3.993 Å and 3.914 Å respectively, both of which are larger than the substrate lattice constant, 3.786 Å. Considering that bulk STC samples show cubic symmetry [13][14], the unit cell of the STC30 film grown on the LAO substrate is rendered tetragonal and the film shows in-plane compressive stress.

A cross-sectional TEM image of an STC30 film on an LAO substrate is shown in figure 4-2(a). The film and the substrate show a semi-coherent interface (a misfit dislocation is visible), and no clusters or secondary phases were found in the film. The inset shows the diffraction pattern at the interface region, which has no evidence of secondary phases. We checked the homogeneity of the STC lattice at various locations in the film. As shown in figure 4-2(b), a uniform perovskite lattice was observed over large areas in the STC film. The two arrows indicate two structural defects in the film which are likely to be misfit dislocations or twin boundaries. This observation is consistent with the partially strain relaxed epitaxial growth scenario as suggested by the X-ray RSM. The inset of figure 4-2(b) shows the EDS mapping of Co within the film cross section. The Co is distributed homogeneously, and there is no Co rich region along the interface.

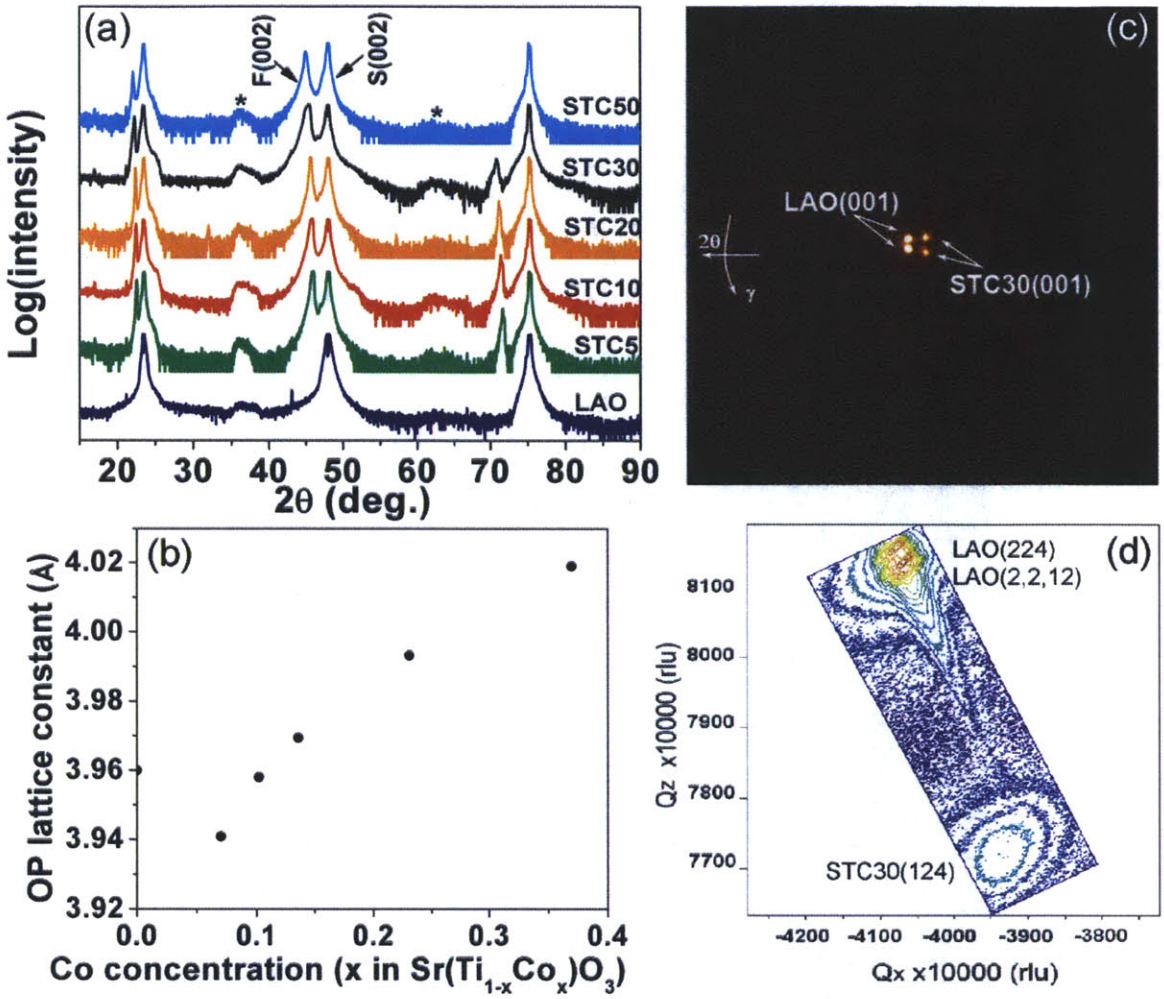

Fig. 4-1 (a) 1DXRD θ-2θ scans for a bare LAO substrate and STC films with various Co concentrations. F(002) and S(002) indicate one of the (00*l*) diffraction peaks of the film and the substrate respectively. The broad diffraction features marked by "*" arise from the twin defects of the LAO substrates. (b) Out-of-plane lattice parameter of STC films as a function of Co concentration determined by the STC(00*l*) diffractions. The measurement error is within the size of the symbols. (The data point around 10 at.% is an interpolation to the measurement data of the other samples) (c) 2DXRD diffraction pattern of STC30 film taken at an x-ray incident angle of ω=11.5°. The frame center was 2θ=23°. The data collection region is $8° < 2\theta < 38°$ and $15° < 2\gamma < 35°$. The sample was rotated by 360° about the axis normal to the sample surface during the measurement. (d) Reciprocal space map (RSM) of the STC30 film (124) and the LAO substrate (244) and (2,2,12) diffraction patterns (both $K_\alpha 1$ and $K_\alpha 2$ peaks). Rlu stands for the reciprocal space unit. 1 rlu = $2/\lambda$, where λ is the wavelength of the Cu $K_\alpha 1$ line, 0.154056nm. The film is epitaxially grown on the substrate at 3.0×10^{-6} torr and is in a state of in-plane compressive stress.

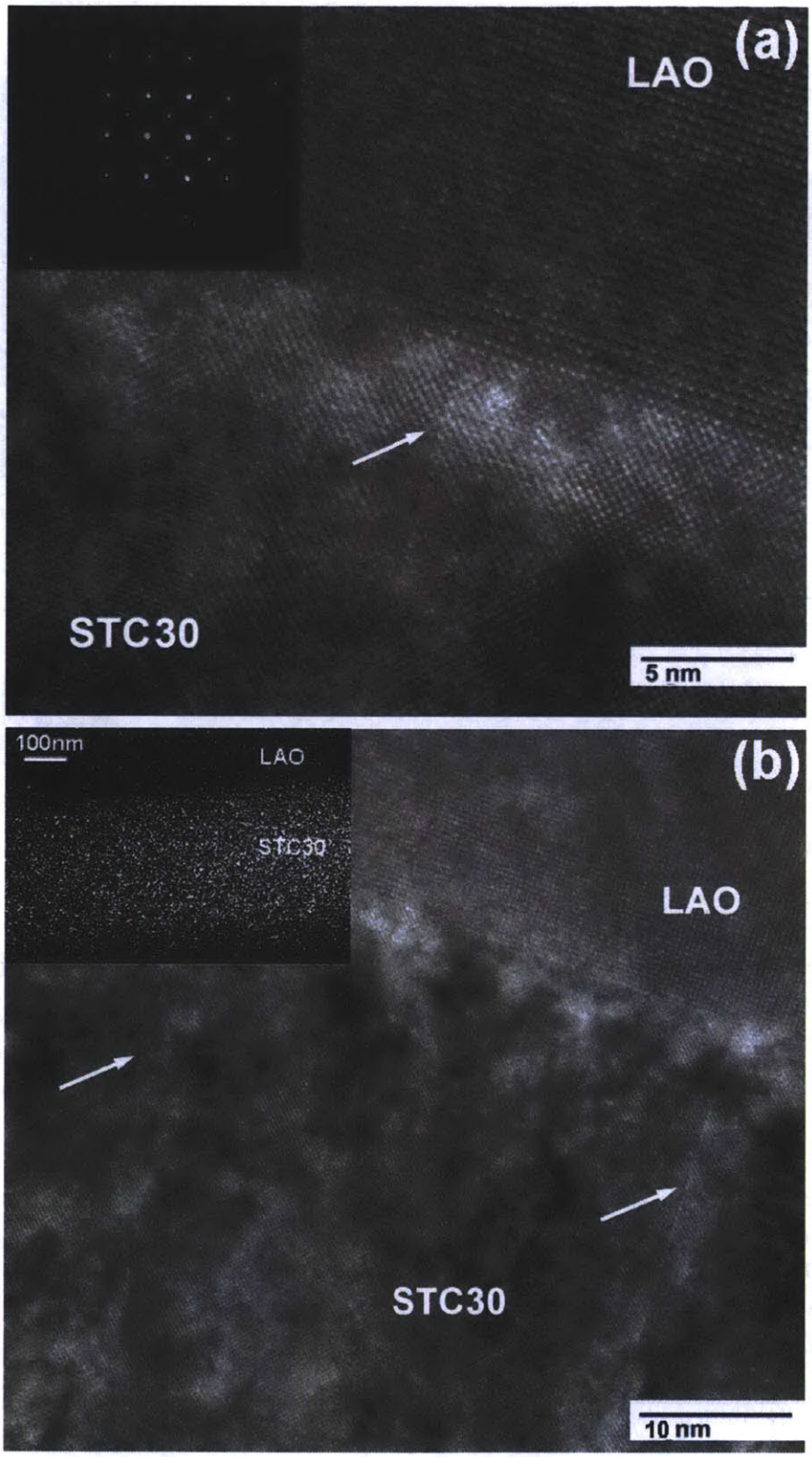

Fig. 4-2 (a) Cross sectional TEM image of the STC30/LAO sample. The inset shows the diffraction pattern at the interface region. (b) Cross sectional TEM image of the same sample showing large area homogeneity of the perovskite lattice with two dislocations marked by arrows. The inset shows the EDS mapping of Co distribution in the film cross section.

The valence state of Co ions in STC30 film was characterized by XPS and XANES. Figure 4-3(a) shows the XPS core level spectra of Co 2p in STC30. The two peaks located at binding energies of 780.4 eV and 796.2 eV are the Co $2p_{3/2}$ and $2p_{1/2}$ doublet arising from spin-orbital interaction. In contrast, Co metal has Co $2p_{3/2}$ and $2p_{1/2}$ at 777.3 eV and 792.4 eV respectively. [15] This difference precludes the existence of Co metal at the STC film surface. Two strong satellite peaks were observed at around 7 eV above the principal peaks. The binding energy separation between the principal and satellite peaks is comparable with that of Co^{2+} or Co^{3+} ions in previous reports.[15-18] The observation of strong satellite peaks is characteristic of high spin Co^{2+} [15], as seen in a Co^{2+}-containing layered perovskite La_2CoO_4 [19], compared to the very weak satellite peaks observed for Co^{3+} and Co^{4+} ions in $La_{1-x}Sr_xCoO_3$ [21] or STC bulk samples[13] fabricated under high oxygen pressure. Therefore the strong satellite peak in our XPS spectrum indicates that Co^{2+} is present in the STC lattice. However, the binding energy of the Co $2p_{3/2}$ peak is smaller than that of pure Co^{2+} perovskites (781.3 eV) [19], suggesting that Co is in a mixed valence state also containing Co^{3+} and Co^{4+}. The amounts of each type of Co ion will be determined by the oxygen stoichiometry, which was not measured here, but in comparison, $SrTiO_3$ films fabricated under a similar high vacuum had a formula of $SrTiO_{2.5}$. [20] A similar oxygen stoichiometry in the STC films would imply significant amounts of Co^{2+} and Co^{3+} to maintain charge balance. Quantitative analysis of the relative concentration of Co is difficult due to the lack of standard XPS spectra. However, based on the measured XPS spectra of Co in $LaCoO_3$, $SrCoO_3$ and La_2CoO_4, we estimate that Co^{2+} and Co^{3+} are the major valence states of Co. The lower valence state of Co ions in the STC film compared with STC bulk samples is attributed to the low oxygen partial pressure used in film deposition. A low valence state yields a larger average diameter of the Co ions, and the STC lattice therefore expands with increasing Co concentration, as illustrated in figure 4-1(b).

Although XPS provides information on the valence states of Co ions, it only measures the surface layer (~5 nm) of the STC film. In order to understand the Co valence states and local environments over a larger sampling depth, fluorescence yield mode XANES at the Co *K*-edge was carried out for the STC30 film, as shown in figure 4-3(b). For comparison, the Co metal absorption spectrum is also shown in the figure. An absorption plateau at $E-E_0=3$

eV is a fingerprint for Co metal clusters. [22] This feature was not observed in the STC30 film. In a previous report by Kasper *et al.* [22], in a dilute Co-doped TiO_2 system, 13% Co atoms in the metallic state produced a clear absorption plateau structure at $E\text{-}E_0$=3 eV. We compared the STC30 spectrum pre-edge feature with calculated spectra based on mixtures of CoO and Co and confirmed that the metallic cobalt atom concentration in the STC30 film, is at most a few percent. There are other notable features in the XANES spectrum. The absorption threshold energy of Co in STC30 is much higher than that of Co metal, indicating that the Co ions are substituting for Ti and located in an oxygen octahedron. The absorption spectrum rises slowly and continuously at E_0 rather than sharply increasing with a plateau structure as found for Co metal. This feature resembles the simulation results of Co-doped TiO_2 containing oxygen vacancies beside the Co_{Ti} sites [23], in which Co ions also occupy an oxygen octahedron. An enhanced absorption tail was also observed in the Cr *K*-edge XANES spectrum of Cr-doped $SrTiO_3$ with a high oxygen vacancy concentration [24], which was explained by the increase of the density of states of the Cr 4p level by nearby oxygen vacancies at the Cr 4p band edge. Comparing with these reports, the XANES spectrum for the STC30 film suggests that the Co ions are substituting for the Ti ions in the STC lattice with oxygen vacancies present at neighboring sites.

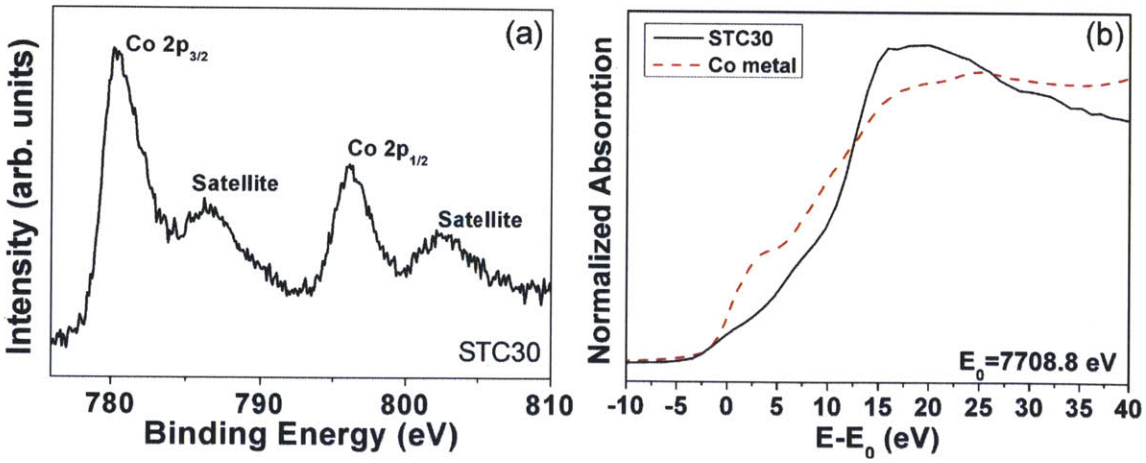

Fig. 4-3 (a) XPS spectrum of the Co 2p peaks in STC30. (b) Co *K*-edge XANES spectrum of the STC30 film with Co metal as a reference sample.

4.1.3 Magnetic, MO and optical properties of $Sr(Ti_{1-x}Co_x)O_{3-\delta}$ films

Figure 4-4 shows the OP magnetic hysteresis loops of STC films grown on LAO substrates at room temperature. The hysteresis loops were obtained by subtracting the diamagnetic signal from the LAO substrates. All the samples were grown at a vacuum level of 3.0×10^{-6} torr. When the Co concentration is low, the films show no significant RT-FM behavior, which is consistent with a previous report. [8] However, with increasing Co concentration, STC20 and STC30 show clear magnetic hysteresis with a saturation magnetization of 0.34 μ_B/Co and 0.55 μ_B/Co (equivalent to 9.30 and 21.60 emu/cm^3 respectively). The OP coercivities of STC20 and STC30 are 32 Oe and 40 Oe respectively. At 5 K, the coercivity of STC30 increases to ~800 Oe and shows a clear ferromagnetic hysteresis as seen in fig. 4-8 (b). Further increasing the Co concentration resulted in a decrease of the magnetic moment. Almost no RT-FM behavior was found for STC50, which may be attributed to increased populations of antiferromagnetic superexchange coupled Co ions in high concentrations.

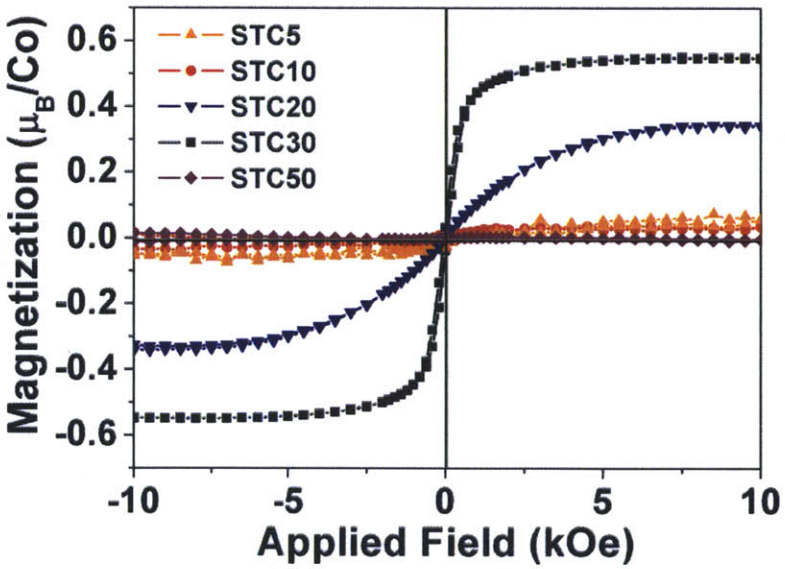

Fig. 4-4 Room temperature out-of-plane magnetic moment of STC samples on LAO substrates. Only STC20 and STC30 samples showed clear RT-FM hysteresis.

The OP saturation magnetization versus temperature curve of the STC30 film on LAO measured at 8000 Oe is shown in fig. 4-5. A Curie temperature higher than 1000 K was found for the film. At T<20 K, a sharp upturn of the M_s with decreasing temperature was observed,

which is believed to be a Brillioun-Weiss curve originating from paramagnetic Co ions. At T>20 K, the M_s decreases almost linearly with increasing T, deviating from both the Curie-Weiss law and the Brillouin-Weiss equation. Such a linear Ms-T curve with similar slope is also observed in another STC30 sample grown at a lower base pressure of 2.5×10^{-6} Torr as shown in fig. 4-5. The inset shows the field cooling (FC) and zero field cooling (ZFC) curves of the sample grown at 3×10^{-6} Torr measured with an in-plane magnetic field of 1000 Oe. The thermomagnetic irreversibility between the FC and ZFC curves indicate a spin glass or superparamagnetic behavior. These findings provide further evidence against the existence of Co metal clusters in the STC films. If the ferromagnetism were from Co metal clusters, the temperature at the maximum magnetization of the ZFC curve (~40 K in this case) would be the blocking temperature T_B. The Co cluster size can be estimated by $K_AV=25k_BT_B$ [25], where K_A is the magnetic anisotropy constant (K_A~4.5×10^6 ergs/cm^3 for Co metal), k_B is the Boltzmann constant and V is the particle volume. Substituting T_B into this equation yields an average Co cluster size of V=31 nm^3 (diameter D~3.85 nm). Co clusters in this size range would have been clearly visible in our cross sectional TEM images. Indeed, considering that Co metal has a saturation magnetization value of 1.7 μ_B/Co, from the saturation magnetization of the sample at 20K (0.68 μ_B/Co), we estimate that sixteen 3.85 nm diameter Co metal clusters on average should show up in the sampling region in fig. 4-2(b) if all the ferromagnetic signal originated from Co metal clusters, assuming the HRTEM sample thickness is only 10 nm. The probability of missing all these nanoclusters in the HRTEM image is 1×10^{-7}. Additionally, the STC30 film magnetization of 0.68 μ_B/Co implies that if the magnetism had come from metallic Co, about 40% of the Co would be metallic, which would have shown up in the XANES spectrum. [22] These results indicate that the RT-FM property observed in the STC30 sample is not likely due to Co metal clusters in the film. Recently, thermomagnetic irreversibility has been reported in structurally homogeneous $Sr(Ti_{1-x}Fe_x)O_3$[9], Co-doped $BaTiO_3$ [10], $BaFe_{1-x}Zr_xO_3$ [26] and Co-doped TiO_2 films [27]. A mixed-state ferromagnetism scenario has been proposed in Co-doped TiO_2 [27], in which Co still resides in the rutile lattice site but exchange-coupling between Co_{Ti}-$Co_{interstitial}$ or neighboring Co_{Ti}-Co_{Ti} pairs leads to ferromagnetism. In STC films, mixed valence is confirmed by XPS, and this may lead to spin-glass behavior (and the associated

thermomagnetic irreversibility) as found in bulk STC. [13]

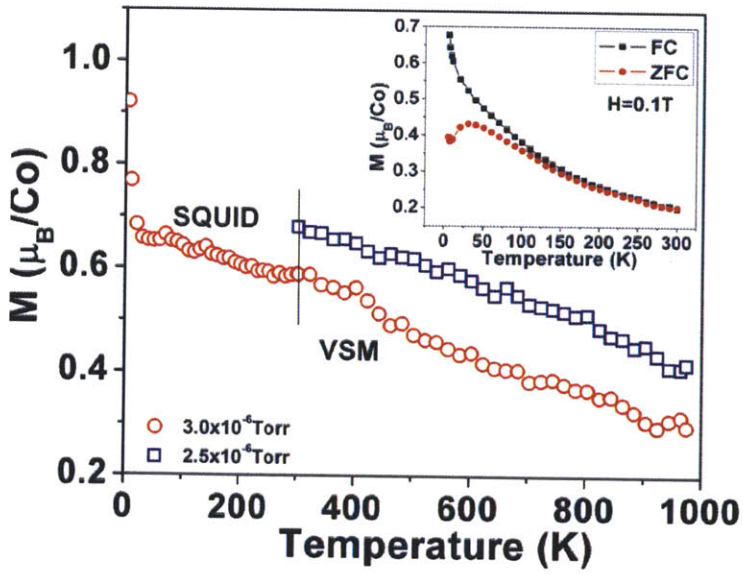

Fig. 4-5 The saturation magnetic moment versus temperature curve of two samples of STC30 measured at 8000 Oe with the magnetic field applied out-of-plane. The inset shows the FC and ZFC magnetic moments of the STC30 film grown at 3×10^{-6} Torr under an in-plane applied field of 1000 Oe

Figure 4-6(a) shows the Faraday rotation of STC films grown on LAO substrates measured at 1550 nm wavelength. The Faraday rotation spectrum resembles the OP magnetic hysteresis shown in figure 4-4, although the Faraday coercivity is larger, 370 Oe for STC30. This result is similar to our previous report in Co-doped CeO_2, and may be related to the excitation state of the electric dipole transitions which cause Faraday rotation. [31] An optical transmission measurement of STC films by UV-Vis-NIR spectrophotometry is shown in figure 4-6(b). The optical band gap for STC30 is 4.15 eV, which is about 0.25 eV higher than pure $SrTiO_3$ fabricated under similar conditions. With increasing Co concentration, the optical transmittance of STC films increases at visible to near infrared wavelength ranges. Such behavior is similar to that of $Sr(Ti_{1-x}Fe_x)O_{3-\delta}$ films [37]. Co^{2+} and Co^{3+} ions at Ti sites behave as acceptors while oxygen vacancies behave as donors. Increasing Co content leads to a decrease of free carrier density and optical absorption in the film. The surface resistivity of STC films measured by the Van der Pauw method is shown in the inset of figure 4-6(b). With increasing Co concentration, the film changes from a semiconductor (STC0) to an insulator (STC30 and STC50), suggesting a non-carrier-mediated mechanism in ferromagnetic STC30.

Hall measurements indicate a negatively charged carrier density of $2.8\times10^{20}cm^3$ in STC0, suggesting a significant concentration of oxygen vacancies in films fabricated under high vacuum. The other films were too resistive to inject sufficient current for Hall measurements. The systematic resistance change of the films supports the defect chemistry model discussed above.

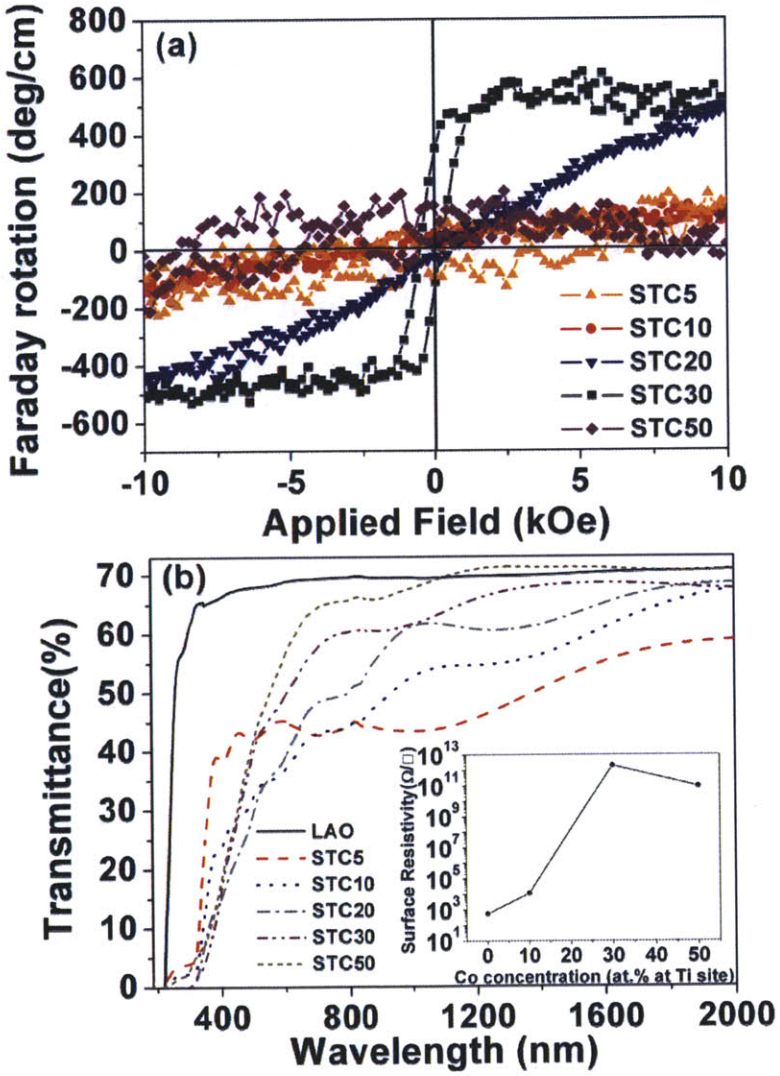

Fig. 4-6 (a) Room temperature Faraday rotation of STC samples at 1550 nm wavelength, measured out-of-plane. (b) The optical transmission spectra of STC films grown on LAO with a bare LAO substrate as a reference sample. The inset shows the surface resistivity as a function of Co concentration for several STC films.

The optical constants of STC30 films were also characterized by ellipsometry. The fitted optical constants are shown in figure 4-7. The film shows an extinction coefficient of low 10^{-3}

level at near infrared wavelengths. A figure of merit (Faraday rotation divided by absorption loss) of 0.57 deg/dB is estimated in STC30 films at 1550 nm wavelength.

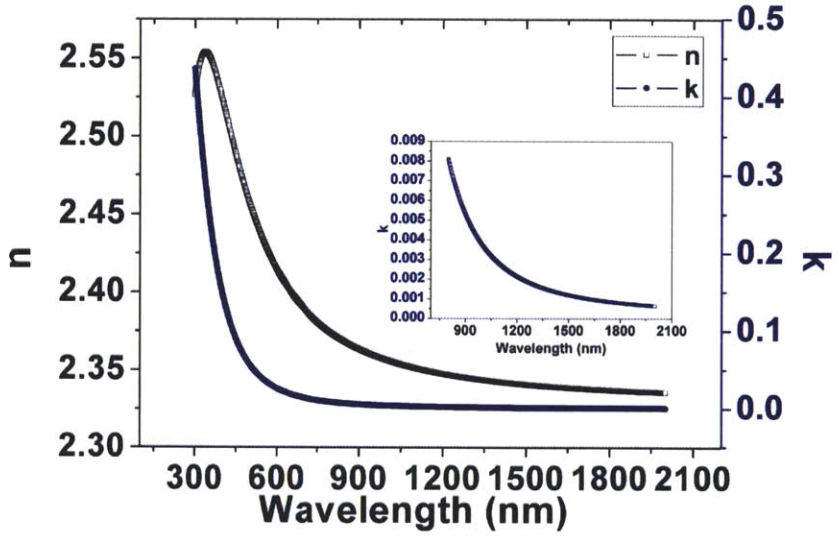

Fig. 4-7 Optical constants of STC30 film characterized by ellipsometry

4.1.4 Magnetic anisotropy and magnetoelastic effect of $Sr(Ti_{1-x}Co_x)O_{3-\delta}$ films

In order to understand the origin of the ferromagnetism in the STC films, we deposited STC30 under various conditions and on both LAO and STO substrates. STC30 grown on LAO substrates show different saturation magnetization, coercivity and magnetic anisotropy depending on the deposition base pressure and growth rate. As shown in Fig. 4-8 (a)-(c), a general finding is that lower deposition pressure yielded higher saturation magnetization (M_s) and coercivity (H_c), which are associated with a stronger OP anisotropy for films grown on LAO substrates. On increasing the base pressure from 2.5 $\times 10^{-6}$ Torr to 3.5×10^{-6} Torr, the M_s decreases from 24.4 emu/cm^3 to 16.5 emu/cm^3, H_c (OP) decreases from 1200 Oe to almost zero, and the film anisotropy changes from highly OP to almost isotropic. These observations suggest that oxygen vacancies play an important role on the valence states of the Co ions and the overall magnetic property of the film. Higher oxygen vacancy concentrations may yield stronger ferromagnetic behavior of the STC films. Measurements (not shown) along different in-plane crystallographic directions indicated no measurable in-plane anisotropy. The magnetic anisotropy in the film is attributed to a magnetoelastic effect with Co ions showing

positive magnetostrictive constant along the [001] (OP) direction. Further evidence for magnetoelastic effects is provided by Fig. 4-8(d), which shows magnetic hysteresis of STC30 deposited on an STO substrate. STO has a larger lattice constant (3.905 Å) than LAO (3.786 Å), resulting in a much smaller compressive stress in the STC30 (lattice mismatch < 1%) and a net IP magnetic anisotropy.

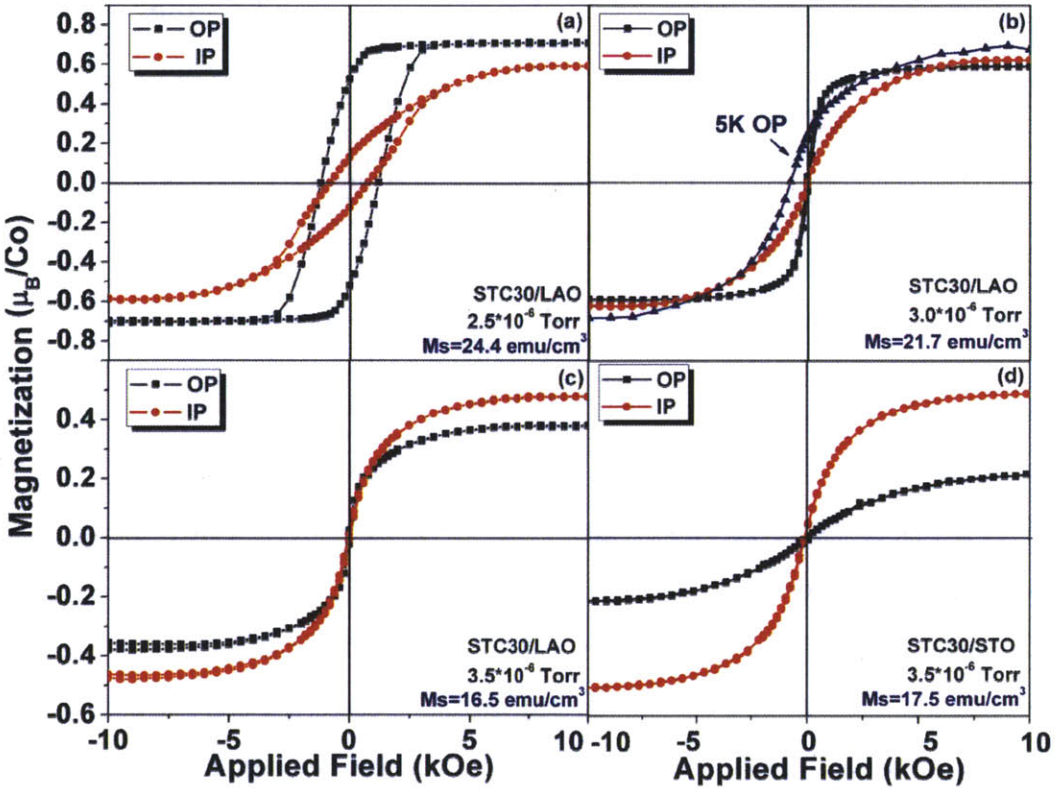

Fig. 4-8 (a)-(c) Magnetic hysteresis showing different saturation magnetization, coercivity and anisotropy for STC30 samples grown on LAO substrates under different conditions noted in the plots. Also shown is the low temperature half hysteresis loop measured from -1T to 1T at 5K for STC30 sample grown at 3.0×10^{-6}Torr, which shows a clear ferromagnetic behavior. (d) Magnetic hysteresis for STC30 grown on an STO substrate.

The observed OP "easy" axis anisotropy in compressively strained films on LAO illustrated dramatically in Fig. 4-8 (a) invites speculation about the valence and spin state of the Co ions that contribute to the anisotropic magnetization properties. Co^0 (Co metal clusters) showed almost no magnetic anisotropy in Co-doped TiO_2. [24] Octahedrally coordinated $Co^{3+}t_{2g}^6$ (low-spin, LS) ions are diamagnetic. Previous studies of $Co^{3+}t_{2g}^4e_g^2$ (high-spin, HS) and $Co^{2+}t_{2g}^5e_g^2$ (HS) both showed negative magnetostriction effects along a <100> axis ($\lambda_{100} < 0$)

that may lead to an "easy" plane anisotropy for a film under IP compressive stress. [25][26] Moreover, the spin state of Co ions in perovskite cobaltates are reported to be sensitive to lattice strain [27], temperature [28] or applied magnetic field [29]. In addition, high-spin, low-spin, and intermediate-spin (IS) states were reported for Co^{3+} and Co^{4+} ions in $La_{1-x}Sr_xCoO_3$ perovskites. [27-30] As a consequence, it is appropriate to consider the various valence/spin-configuration combinations that might favor the OP z-axis distortions observed in Fig. 4-8.

There are two effects namely Jahn-Teller effect (J-T) and spin-orbital stabilization effect (S-O) taking place in 3d transition metal ions, which determines the electron energy configuration. The Jahn-Teller effect lowers the electron system energy level by distorting the lattice to cause lower electron-electron Coulomb interactions between electrons on cations and anions sites, while the spin-orbital stabilization effect lowers the electron system energy by distributing electrons on different orbitals to cause lowest spin-orbital coupling energy. External strain bias on the system changes the relative strength of these two processes. The electron energy level configuration and therefore the magnetoelastic constant of a certain ion may vary depending on the strain status of the lattice. These two stabilization processes take place in several Co ions with different valence and spin states, as shown in table 4-1.

Table 4-1 Magnetoelastic Co ions in an octahedral lattice site

Number of 3d electrons	Ions	S	Occupancy	Comments
5	Co^{4+}(HS)	5/2	$t_{2g}^3e_g^2$	half-filled d shell
	Co^{4+}(LS)	1/2	$t_{2g}^5e_g^0$	J-T or S-O stabilization
6	Co^{3+} (HS)	2	$t_{2g}^4e_g^2$	J-T or S-O stabilization
	Co^{3+} (LS)	0	$t_{2g}^6e_g^0$	filled t_{2g}
7	Co^{2+} (HS)	3/2	$t_{2g}^5e_g^2$	J-T or S-O stabilization
	Co^{2+} (LS)	1/2	$t_{2g}^6e_g^1$	pure J-T stabilization

For our STC30 films deposited on LAO substrates, the CoO_6 octahedron undergoes a highly tetragonal z-axis expansion induced by in-plane compressive stress as confirmed by X-ray

RSM measurements. The e_g doublet and t_{2g} triplet states separated by 10Dq in the main cubic component of the site crystal field then become split further. The J-T stabilization process is dominant. The electron energy level configuration of Co^{4+}(LS) and Co^{2+}(HS) in this case is shown in figure 4-9. Specifically, under biaxial compressive stress in the $x-y$ plane, orbital states of the lower t_{2g} group are split by δ_t into a ground doublet (d_{xz}, d_{yz}) and an excited d_{xy} singlet; the e_g doublet splits by δ_e into lower d_{z^2} and higher $d_{x^2-y^2}$ singlet states. Such configurations correspond to the $Co^{4+}t_{2g}^5e_g^0$(LS) and $Co^{2+}t_{2g}^5e_g^2$(HS) ions that undergo Jahn-Teller z-axis expansions and show $\lambda_{100} > 0$ with an out-of-plane magnetoelastic anisotropy.

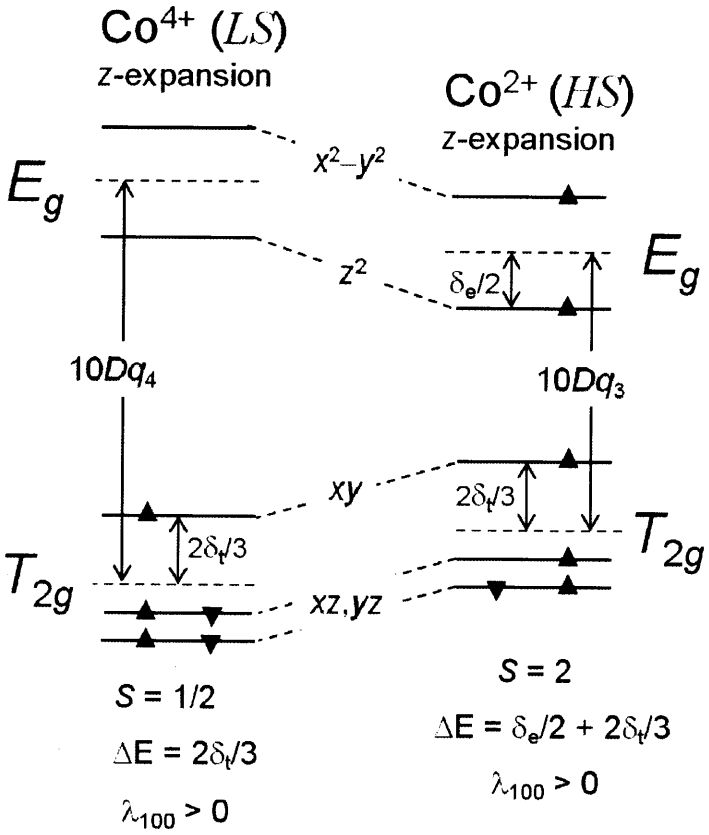

Fig. 4-9 A schematic diagram of the possible 3d electron energy level configuration of the Co^{2+}(HS) and Co^{4+}(LS) ions in STC30 films grown on $LaAlO_3$ substrates.

For films deposited on STO substrates, the much smaller IP compressive stress due to better

match of lattice and thermal expansion coefficients between the film and the substrate leads to much weaker J-T stabilization. Therefore S-O stabilization may become dominant which allows the tetragonal splittings to invert, thereby reversing the signs of δ_t and δ_e to produce a negative λ_{100} and create ground-state t_{2g} single. In fact, the strong spin-orbital-lattice interactions of Co^{2+} ($3d^7$) was reported before which could be used to adjust anisotropy fields or enhance spin-lattice relaxation rates at radio frequencies. [32] The systematic change of the magnetoelastic anisotropy for STC on LAO shown in figure 4-8(a)-(c) may also indicate that the Co valence and spin states are sensitive to fabrication conditions.

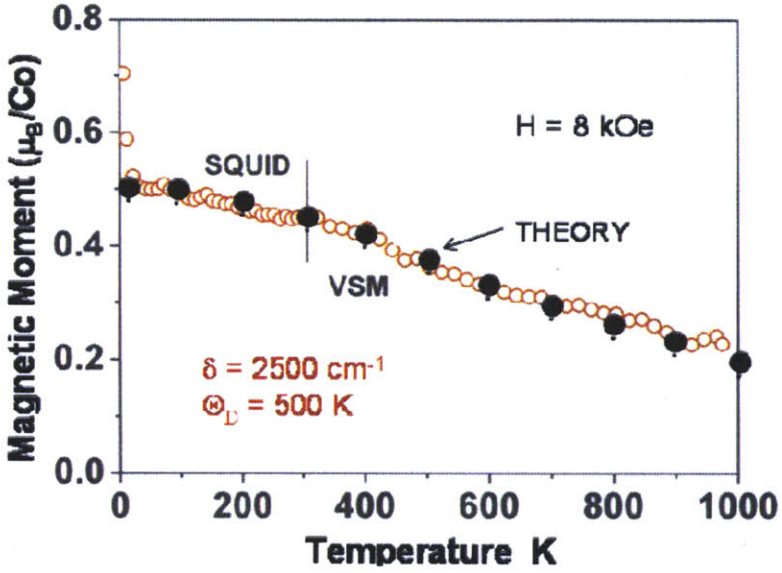

Fig. 4-10 The saturation magnetization versus temperature curve of STC30 on $LaAlO_3$ substrate, measured at applied field of 8000 Oe with out-of-plane configuration. (Red open circles) Also shown is the theoretical fitting to this curve (black full circles).

As shown in figure 4-5, the M-T curve of $Sr(Ti_{0.77}Co_{0.23})O_{3-\delta}$ does not follow the Brillouin function, which may be another evidence of magneto-elastic effects in these systems. The saturation magnetization M_s of both STC samples in figure 4-5 decreases linearly with increasing temperature, which can be fitted using the model of magnetoelastic spin ordering [33]. The M_s is described by $\frac{M_K(T)}{M_K(0)} \approx \tanh[\frac{\delta_t(T)}{2kT}]$ where $\frac{\delta_t(T)}{\delta_t(0)} = \tanh(\frac{\Theta_D}{2T})$. Using a Debye temperature Θ_D~500K [34] and J-T energy $\delta_t(0)$=2500cm^{-1} based on a strain of 3%, the

equation yields a very good fit to the Ms-T curve as shown in figure 4-10. Consistent with magnetic anisotropy analysis above, this result further implies that magnetoelastic effect may be the reason of high temperature ferromagnetism in the STC system.

4.2 Ce and Ga doped $Sr(Ti_{0.6}Fe_{0.4})O_{3-\delta}$ films

Although a magneto-optical figure of merit of 0.56 deg/dB is achieved in STC films, this value is still far from application requirements. Consider a magneto-optical isolator using Faraday Effect, to achieve 45° rotation of the light polarization with 1dB insertion loss, the magneto-optical material needs to have a figure of merit of at least 45 deg/dB. As a comparison, $Sr(Ti_{0.6}Fe_{0.4})O_{3-\delta}$ films fabricated at similar conditions show a figure of merit of 1.1 deg/dB. [37] It is therefore desired to enhance the material figure of merit by controlling the Faraday rotation and optical absorption using chemical doping. In this section, Ce and Ga ions are doped into the $Sr(Ti_{0.6}Fe_{0.4})O_{3-\delta}$ films as donors and acceptors to study the magnetic, magneto-optical and optical properties of the material for higher figure of merit. For Ce doping, it has been demonstrated that Ce^{3+} is soluble over the complete range of $(Ce_xSr_{1-x})TiO_3$ solid solution on the Sr site [35][36]. It is well known that Ce^{3+} doping in the dodecahedral site of $Y_3Fe_5O_{12}$ significantly increases the material's Faraday rotation at near infrared wavelengths. Thus it is expected by doping Ce^{3+} in the $Sr(Ti_{0.6}Fe_{0.4})O_{3-\delta}$ thin film, the Faraday rotation will be enhanced. For Ga doping, it is believed that Ga^{3+} ions (0.62 Å) can substitute for Ti^{4+} ions (0.605 Å) with a stable 3+ valence state and as an acceptor. This may drive Ti and Fe to higher valence, yield different lattice structures and enhance the material figure of merit.

4.2.1 Structure of Ce and Ga doped $Sr(Ti_{0.6}Fe_{0.4})O_{3-\delta}$ films

$(Ce_xSr_{1-x})Ti_{0.6}Fe_{0.4}O_{3-\delta}$ (Ce:STF, x=0, 0.1, 0.2 and 0.3, namely Ce0, Ce10, Ce20 and Ce30 respectively) and $Sr(Ti_{0.6-y}Ga_yFe_{0.4})O_{3-\delta}$ (Ga:STF, y=0, 0.1, 0.2, 0.3, 0.4, 0.5, 0.6, namely Ga0, Ga10, Ga20, Ga30, Ga40, Ga50 and Ga60 respectively) thin films were fabricated using pulsed-laser deposition. Figure 4-11 shows the ω-2θ X-ray diffraction patterns of the Ce:STF

and Ga:STF films. F(00*l*) and S(00*l*) indicate the diffraction peaks from the (00*l*) planes of the film and substrate respectively. All the films crystallized into a perovskite phase and no secondary phase diffraction peaks were observed, suggesting that Ce and Ga are fully soluble in the STF lattice within the concentration range we studied. The films are highly (00*l*) textured, indicating a "cube-on-cube" orientation relationship between the film and the substrate lattices. The insets of fig. 4-11 show the magnified (001) diffraction peaks. With increasing Ce concentration, the film (001) peaks consistently shift to lower 2θ angles, indicating an expansion in the lattice constants; while with increasing Ga concentration, they shift to lower 2θ angles at low Ga concentrations but continues shifting back to higher 2θ angles beyond Ga30. The complicated lattice constant variation with Ga doping is associated with a decrease in epitaxial strain and unit cell tetragonality, which will be discussed later. We notice that all the Ce:STF and part of the Ga:STF film (00*l*) diffraction peaks split into double peaks. This is due to a strain gradient along the thickness direction of the films, which can be understood by X-ray reciprocal space map (RSM) characterizations. As shown in figure 4-12, X-ray RSM was measured on the (103) peak diffractions of both the LSAT substrate and $(Ce_{0.2}Sr_{0.8})(Ti_{0.6}Fe_{0.4})O_{3-\delta}$ film. Both the substrate and the film show spot like diffraction patterns, demonstrating that the film is epitaxial. The film diffraction pattern consists of two spots, one of which shows the same in-plane lattice constant compared with the substrate, and the other shows a broader diffraction spot with a larger in-plane lattice constant. This kind of diffraction pattern indicates that the film consists of two layers with different strain states. During deposition, initially the film grew coherently on the substrate with a fully compressive strained state. When the film thickness exceeded a critical value, misfit dislocations developed and the strain was partially relaxed. The film became more defective and the diffraction pattern became broader. For Ga:STF films, the double peaks feature disappeared at high Ga concentrations. The film shows a homogeneous partially relaxed strain state. The in-plane and out-of-plane lattice parameters of the $(Ce_{0.2}Sr_{0.8})(Ti_{0.6}Fe_{0.4})O_{3-\delta}$ film and substrate can be calculated from the RSM peak positions. The substrate lattice is cubic with a lattice parameter of 3.87 Å. The completely strained film layer shows an out-of-plane lattice parameter of 4.12 Å, while the partially strain relaxed layer shows an in-plane lattice parameter of 3.91 Å and out-of-plane lattice parameter of 4.07

Å. Notice that both layers of the film are highly tetragonalized with a large c/a value.

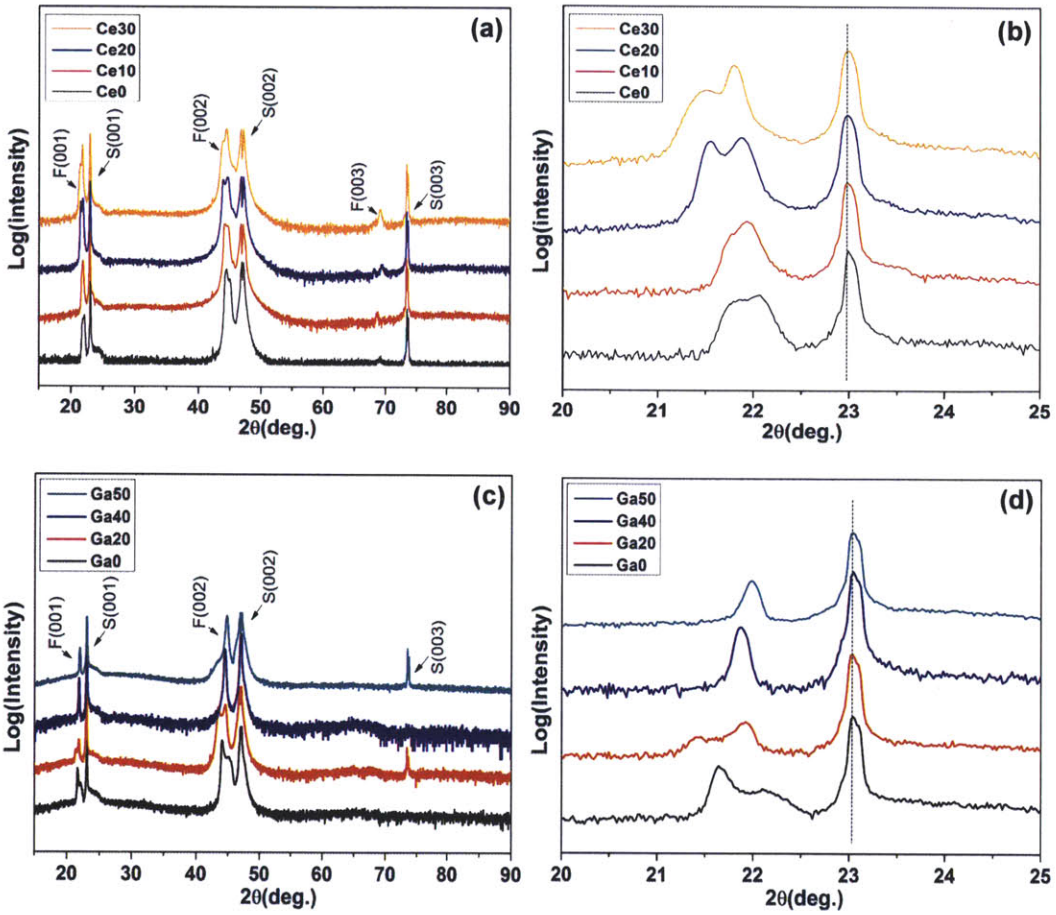

Fig. 4-11 ω-2θ X-ray diffraction patterns of (a) Ce:STF and (c) Ga:STF films with different Ce or Ga concentrations. F(00*l*) and S(00*l*) indicate the (00*l*) diffraction peaks from the film and substrate respectively. Also shown are the magnified (001) diffraction patterns of (b) Ce:STF and (d) Ga:STF films.

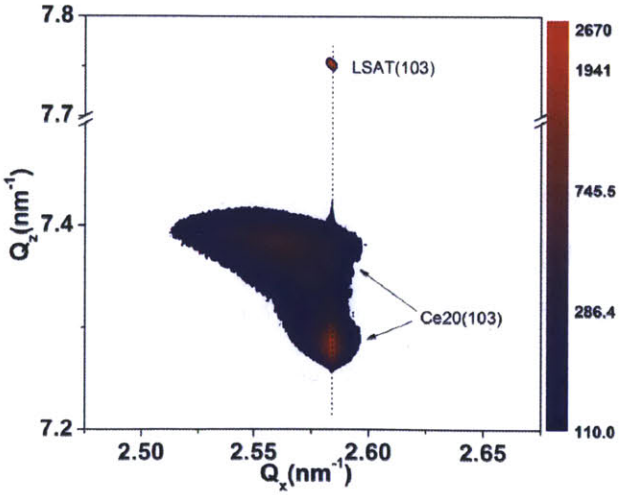

Fig. 4-12 X-ray reciprocal space map of the (103) diffraction peak of the Ce20 film and the LSAT substrate

4.2.2 Magnetic, MO and optical properties of Ce:STF and Ga:STF films

Room temperature ferromagnetic properties were observed in all samples with different Ce or Ga concentrations. Figure 4-13 shows the out-of-plane magnetic hysteresis loops of Ce:STF and Ga:STF films measured by VSM at room temperature. Similar to STF films fabricated in vacuum [37], the Ce doped films show out-of-plane magnetization easy axis with an anisotropy field up to 5000 Oe. The saturation magnetization of the films remains similar for different Ce doping concentrations, with only a slight increase in M_s observed in the Ce30 sample. However the coercivity of the films consistently decreases from 257 Oe in Ce0 to 18.7 Oe in Ce30 with increasing Ce concentrations. The change of saturation magnetization and coercivity of Ce:STF films are shown in the inset of fig. 4-13 (a). This decrease in coercivity indicates that the films become magnetically softer by Ce doping. Meanwhile, the material shows a higher out-of-plane magnetic susceptibility with Ce doping, which can be seen by observing that the Ce30 magnetic hysteresis loop is steeper than Ce0 around the origin. For Ga:STF films, the saturation magnetization decreases nonlinearly with increasing Ga concentration. With increasing Ga concentration up to 30 at.% on the Ti site, the M_s initially slightly decreases from 42 emu/cm^3 to 38 emu/cm^3, then decreases steeply down to 10 emu/cm^3 for Ga50 and Ga60. This trend coincides with the film strain state change from a two layer structure to a single relaxed layer structure beyond Ga30. The coercivity of the films also decreases with increasing the Ga concentration from 500 Oe in Ga0 to ~0Oe in Ga50 and Ga60. Different from Ce:STF, the magnetic anisotropy field also decreases from ~6000 Oe to ~0 Oe. The Ga50 and Ga60 samples are magnetically isotropic between in-plane and out-of-plane directions.

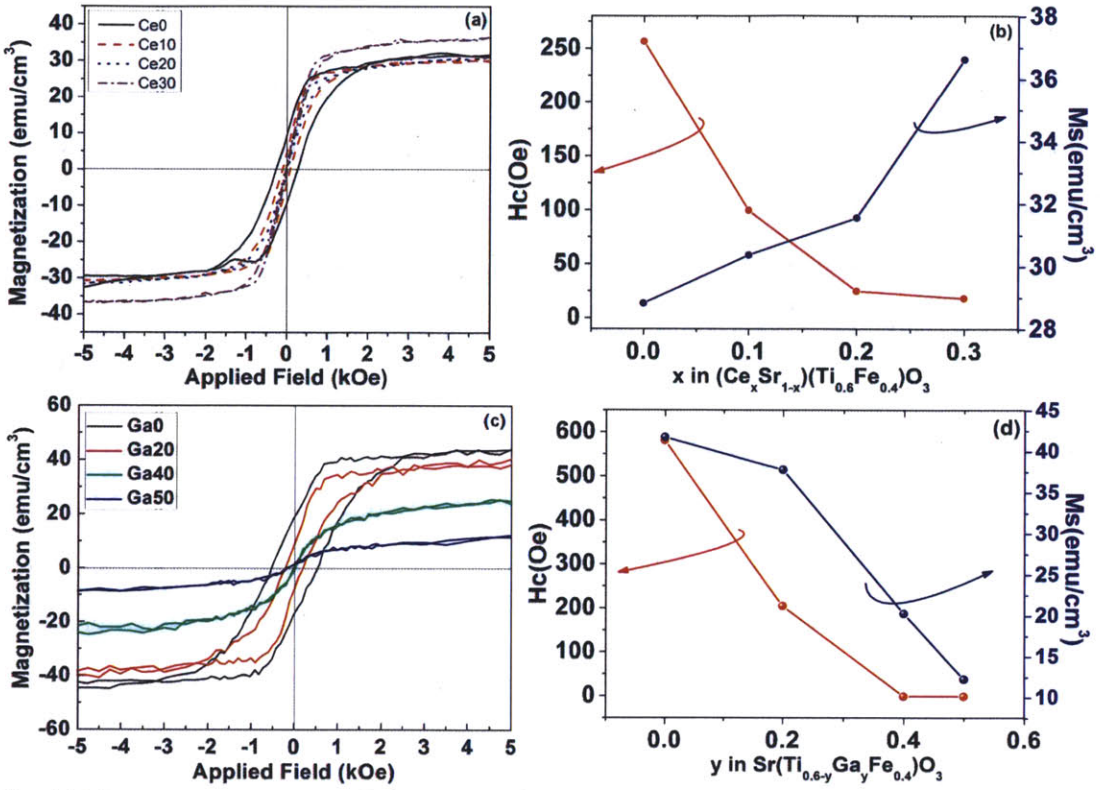

Fig. 4-13 Room temperature out-of-plane magnetic hysteresis loops of (a) Ce:STF and (c) Ga:STF films characterized by VSM. Also shown are the coercivity and remanent magnetization of the out-of-plane magnetic hysteresis loops of (b) Ce:STF and (d) Ga:STF films as a function of Ce or Ga concentration.

Figure 4-14 shows the room temperature Faraday rotation hysteresis loops of the Ce:STF and Ga:STF films at 1550nm wavelength. The magneto-optical hysteresis loops resembles the magnetic ones, although the coercivity is systematically larger in all samples, which is similar to our previous report in the STF system. [37] Interestingly, the saturation Faraday rotation does not show obvious variation between Ce0, Ce10 and Ce20 samples, which seems to faithfully reflect the result that the saturation magnetization of these three samples were comparable to each other; whereas the Ce30 sample shows a 1.5 fold increase in the saturation Faraday rotation, in contrast to only a 1.16 fold increase in the saturation magnetization when compared with other samples. From these results we consider that unlike in magnetic garnets, Ce is not likely to contribute to the magneto-optical properties of this material system at 1550nm wavelength. The Faraday rotation enhancement in Ce doped iron garnets is considered to originate from a Ce^{3+}(4f)-Fe^{3+}(tetrahedral) charge transfer [38]. This mechanism may not take place in Ce:STF because Fe ions are all in the octahedral sites. The

increase of Faraday rotation in the Ce30 sample is possibly due to the higher magnetization in this sample as well as the valence state change in iron ions due to Ce doping. Note that Fe^{2+} in octahedral site of YIG(Si) lattice shows a characteristic transition between electronic levels at 1.20μm wavelength, which leads to higher Faraday rotation compared with Fe^{3+} at near infrared wavelengths. [39] Compared with Ce:STF, Ga:STF films show an almost linear decrease of the Faraday rotation with increasing Ga concentration as shown in figure 4-14 (b). This trend agrees with the decrease of the saturation magnetization with Ga doping but differs in detail, which may also be related to the Fe valence state change with Ga doping.

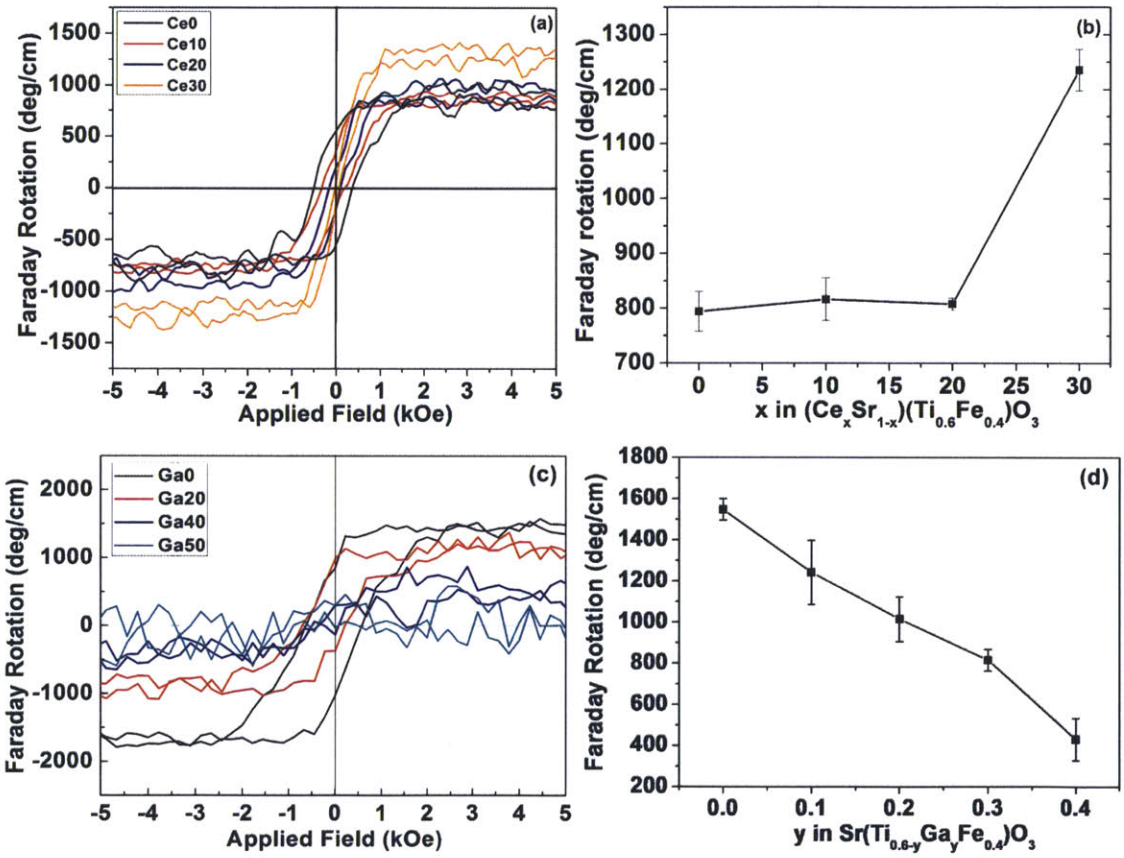

Fig. 4-14 Room temperature Faraday rotation of (a) Ce:STF and (b) Ga:STF films. Also shown are the saturation Faraday rotations of (b) Ce:STF and (d) Ga:STF films as a function of Ce or Ga concentrations.

The optical transmittance spectrum of Ce:STF and Ga:STF films are shown in figure 4-15, where the inset shows the magnified spectrum near the optical band gaps. For Ce:STF samples, as increasing Ce concentration, several variations on the transmission spectrum can be observed. In the ultraviolet region, the optical band gap consistently enlarges with Ce

doping, with the optical band gap of Ce0, Ce10, Ce20 and Ce30 films estimated to be 3.69 eV, 3.73 eV, 3.83 eV and 3.90 eV respectively. In the visible region, the optical transmittance decreases significantly with Ce doping around 600nm wavelength. This absorption peak tails down to the near infrared region, where the optical transmittance consistently decreases with increasing Ce concentration. For Ga:STF samples, a different trend was observed. In the ultraviolet region, Ga doping also opens the optical band gap from 3.67 eV to 3.88 eV. But in the visible region, the optical transmittance increases dramatically with Ga doping. For Ga50 sample, the film is almost transparent at 750nm wavelength and above. The Ga40 film figure of merit reaches 3~4 deg/dB at 1550nm wavelength, which will be discussed in detail in waveguide device characterization of section 4.3.

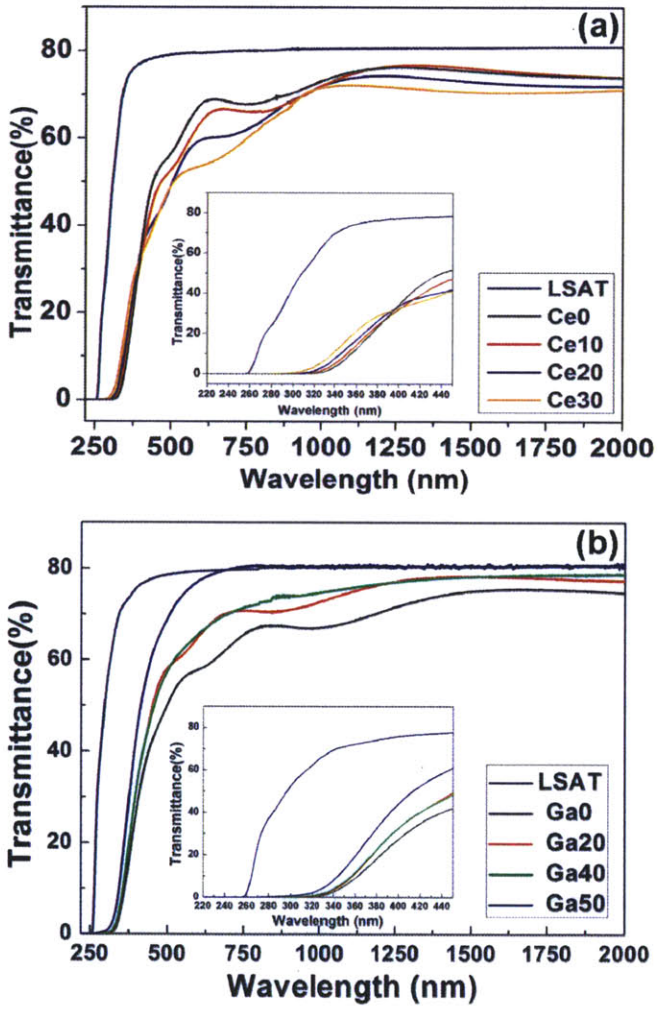

Fig. 4-15 Optical transmittance spectrum of (a) Ce:STF and (b) Ga:STF films measured by UV-Vis-NIR spectrophotometer at room temperature. The inset shows the magnified spectrum near the optical band gap.

4.2.3 Discussion of the influence of Ce and Ga doping on STF thin film properties

The magnetic properties of Ce:STF and Ga:STF films are related to the lattice structures. Table 4-2 shows a study of the in-plane lattice constant and tetragonality of several Ce:STF and Ga:STF films by measuring the X-ray diffraction peak positions of the film (113) peak. It is clearly observed that the saturation magnetization per Fe and the magnetic anisotropy value increases and decreases respectively with the lattice tetragonality. We do not have a clear quantitative correlation between the lattice distortion and the magnetic properties because several samples show both fully strained and relaxed layers. For partially relaxed Ga30, Ga40 and Ga50 samples, the saturation magnetization decreased almost linearly with decreasing lattice tetragonality. These observations are consistent with our theory of magnetoelastic effects discussed in section 4.1.4. The energy level splition of the e_g orbitals is proportional to the tetragonality of the oxygen octahedron. Therefore the higher tetragonality the lattice is, the stronger the Jahn-Teller effect will be. Two consequences of this process are the stronger lattice-spin alignment yielding larger M_s and the higher out-of-plane magnetic anisotropy. This is also consistant with films deposited on substrates with larger lattice mismatch, for example STC deposited on LAO rather than STO. The lattice tetragonality will be higher due to larger lattice strain in the film which favors the out-of-plane magnetic anisotropy observed in figure 4-8 (c) and (d). Similar effects of lattice strain induced spin alignment have also been observed in other transition metal ion doped oxide systems such as TiO_2, SnO_2, In_2O_3 and ZnO. [33] Several films such as Ce30 and Ga20 are highly tetragonal which invites the speculation that these films were tetragonallized following a spontaneous Jahn-Teller distortion process. Fe^{2+}(HS), Fe^{4+}(HS, LS) or even Ti^{3+} may contribute to this process. Doping STF with Ce or Ga increases or decreases the lattice tetragonality respectively. Further study on a systematic investigation of the oxygen vacancy concentrations in these films may help to correlate these observations to a certain ion valence or spin state in the perovskite lattice.

Table 4-2 Lattice constant, tetragonality, saturation magnetization and anisotropy field of several Ce:STF and Ga:STF films

	Ce10	Ce20	Ce30	Ga20	Ga30	Ga40	Ga50
c(strained)(Å)	4.10	4.12	4.13	4.12	N/A	N/A	N/A
c(relaxed)(Å)	4.05	4.06	4.07	4.09	4.07	4.07	4.06
a(strained)(Å)	3.86	3.86	3.86	3.86	N/A	N/A	N/A
a(relaxed)(Å)	3.93	3.88	3.89	3.88	3.86	3.91	3.96
c/a(strained)	1.055	1.065	1.067	1.067	N/A	N/A	N/A
c/a(relaxed)	1.030	1.048	1.046	1.054	1.054	1.041	1.025
$M_s(\mu_B/Fe)$	0.517	0.520	0.600	0.677	0.643	0.435	0.201
H_a(Oe) (Approx.)	5500	6000	7000	6500	3250	2250	0

The optical transmittance of the STF films at visible and near infrared wavelengths decreases or increases with Ce or Ga doping respectively, which can be explained by creation or elimination of electron intervalence charge transfer (IVCT) absorption bands. Doping STF with Ce introduces an absorption band at ~600 nm wavelength. This absorption band has been studied in Ce^{3+} doped $SrTiO_3$ and was attributed to an inter-atomic electronic transition between Ce^{3+} and Ti^{4+} ions. [40] In contrast, doping STF with Ga decreases the Ti concentration and eliminates the electron transition absorption between Ti and Fe ions. The Ti^{4+}/Fe^{2+} IVCT absorption band was observed to be centered at ~500 nm and extends through the full visible spectrum. [41]

4.3 Chalcogenide glass/perovskite based strip-loaded waveguides

Several RT-FM perovskite thin films including $Sr(Ti_{0.6}Fe_{0.4})O_{3-\delta}$ (STF) and $Sr(Ti_{0.2}Ga_{0.4}Fe_{0.4})O_{3-\delta}$ (Ga:STF) on LSAT substrates were integrated into an As_2S_3 chalcogenide glass strip-loaded waveguide structure. The fabrication process is shown in

figure 2-3. Figure 4-11 shows the cross-section SEM image of a 4 μm wide As_2S_3/STF strip-loaded waveguide. The waveguide consists of a LSAT substrate, 100 nm STF film, an As_2S_3 layer with 500 nm thick slab and 400 nm thick rib layers, and a 2.5 μm thick SU-8 top-cladding layer. The interface between the As_2S_3 and STF film maintained its integrity during processing. The As_2S_3 rib shows slanted edges and round corners due to the lift-off process. [42][43] The sidewall angle measured from the SEM image is 55°~60°, which is slightly smaller than that of ChG waveguides fabricated on silicon substrates by lift-off processing. [42][43] The transmission loss of As_2S_3 ridge waveguides, with similar dimensions but without the STF, on LSAT substrates were characterized, and the coupling loss and transmission loss of the As_2S_3 waveguide were estimated from these measurements. Using the measured total transmission loss of the strip-loaded waveguide and simulated confinement factor of the STF film layer, the optical absorption coefficient of the STF film can be estimated.

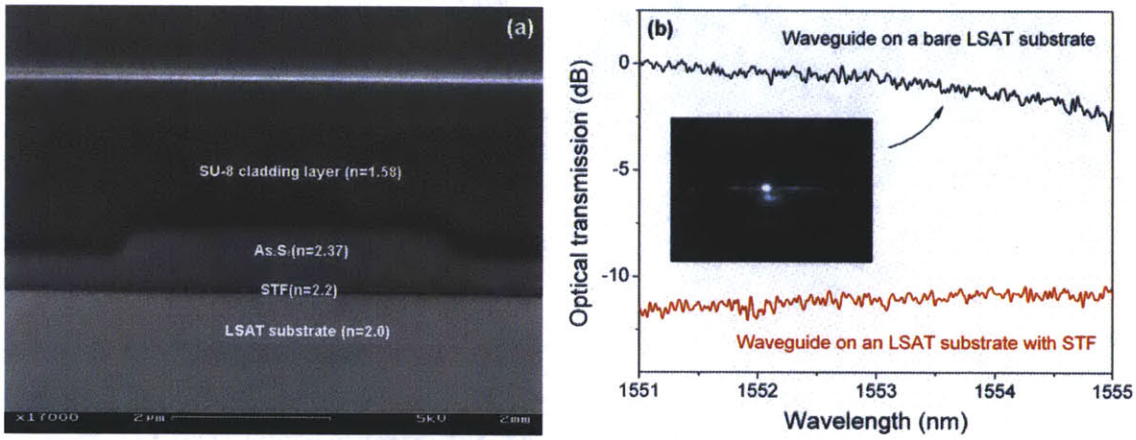

Fig. 4-16 (a) Cross-sectional SEM image of an As_2S_3/STF strip-loaded waveguide with an SU-8 top-cladding layer fabricated on an LSAT(001) substrate. (b) Transmission spectra of an As_2S_3 ridge waveguide and an As_2S_3/STF strip-loaded waveguide with the same dimensions of the As_2S_3 layer on LSAT substrates. The inset shows the measured mode profile of the As_2S_3 ridge waveguide.

Optical transmission was observed in the As_2S_3/STF waveguides at 1550 nm wavelength. The transmission spectra of both waveguides are shown in figure 4-16(b). The optical absorption coefficient of the STF film at 1550 nm wavelength is estimated to be $(5.0 \pm 1.6) \times 10^2 cm^{-1}$. ($\alpha = 4\pi k/\lambda$) Multi-mode beating effects in As_2S_3 ridge waveguides on bare LSAT substrates

and the consequent uncertainty in insertion loss estimation leads to the measurement error bar. These absorption values are higher but in the same order compared to our ellipsometry measurement results on the STF film reported before. [37]

As a comparison, As_2S_3/Ga:STF waveguide shows higher optical transmittance at near infrared wavelengths due to the lower loss of the Ga:STF film. Figure 4-12 shows the cross-sectional SEM image and the transmission spectrum of a 5μm wide As_2S_3/Ga:STF waveguide. The TM mode optical transmittance is higher compared with the TE mode, which may originate from the waveguide side wall scattering. An optical absorption coefficient of 23~27 cm^{-1} was estimated from the Ga:STF layer by simulating the confinement factor of the TM polarized light. Considering the Faraday rotation of this film is ~400 deg/cm, the figure of merit can be calculated to be 3~4 dB/cm.

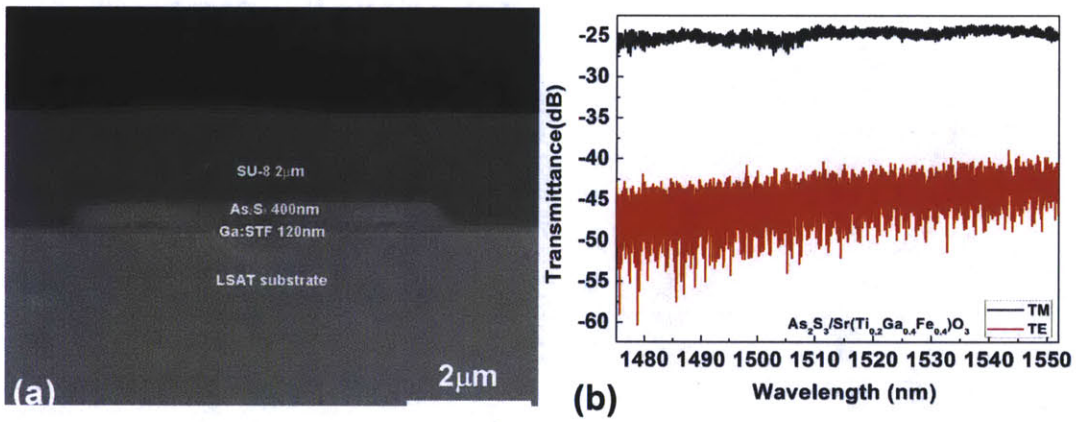

Fig. 4-17 (a) Cross-sectional SEM image of an As_2S_3/Ga:STF strip-loaded waveguide with an SU-8 top-cladding layer fabricated on an LSAT(001) substrate. (b) Transmission spectra of the As_2S_3/Ga:STF waveguide at near infrared wavelengths

The magneto-optical performance, specifically the Nonreciprocal Phase Shift (NRPS) of the strip-loaded waveguides, is simulated based on ChG/STF strip-loaded waveguides. The NRPS in a magneto-optical waveguide structure shown in the inset of figure 4-13(a) can be calculated by perturbation theory, which yields an expression for NRPS to be: [44]

$$\Delta\beta^{TM} = -\frac{2\beta^{TM}}{\omega\varepsilon_0 N}\iint\frac{K''M_y}{n_0^4}H_y\partial_x H_y dxdy$$

where β^{TM} is the propagation constant of a TM mode wave, $\Delta\beta_{TM} = \beta^{forward} - \beta^{backward}$ is the difference between forward and backward propagation constants (NRPS), ω is the frequency, ε_0 is the vacuum dielectric constant, $N = (\iint E \times H^* + E^* \times H)_z dxdy$ is the power flow along the z direction, $K''M_y$ is the off-diagonal component of the dielectric constant matrix under an applied field M_y along the y direction and H_y is the magnetic field component of the electromagnetic wave along the y direction. The integral is over all the magneto-optically active regions in the waveguide. To calculate the NRPS in our strip-loaded waveguide, the TM mode profile is firstly simulated by FIMMWAVE software using a film mode matching method (FMM). [45] From the mode profile the NRPS can be calculated using the equation above. The insertion loss of the waveguide can be also simulated by considering the confinement factor and optical absorption in the STF layer. The results are shown in figure 4-12(a), (b) and (c).

Firstly we note that for a MZ interferometer isolator using NRPS, $\pm 90°$ NRPS has to be achieved in its either arm. The result in fig. 4-13(a) indicates that isolator device within millimeter to low centimeter scales can be fabricated based on most of the proposed WG structures. Secondly, in figure 4-13(a) and (b) the NRPS and insertion loss of the waveguides both decrease with increasing ChG layer thickness. This can be easily understood because the confinement factor in the magneto-optical film decreases with increasing ChG layer thickness. For the same reason, the NRPS and insertion loss also decrease with increasing refractive index of the ChG layer. However in figure 4-13(c), the figure of merit (FOM, defined as NRPS divided by insertion loss) shows a maximum value for a ChG layer thickness of 1.2 μm. This is due to the design trade-off between maximizing the mode asymmetry (NRPS) and minimizing the optical confinement factor (absorption loss) in the STF layer. Meanwhile, waveguides with an As_2Se_3 top layer show the highest FoM in all waveguide dimensions. This result can be interpreted as due to the $\partial_x H_y$ term in equation (1). Higher index contrast between the top and bottom cladding yields higher field gradient and NRPS in the STF layer, therefore the FoM is also enhanced.

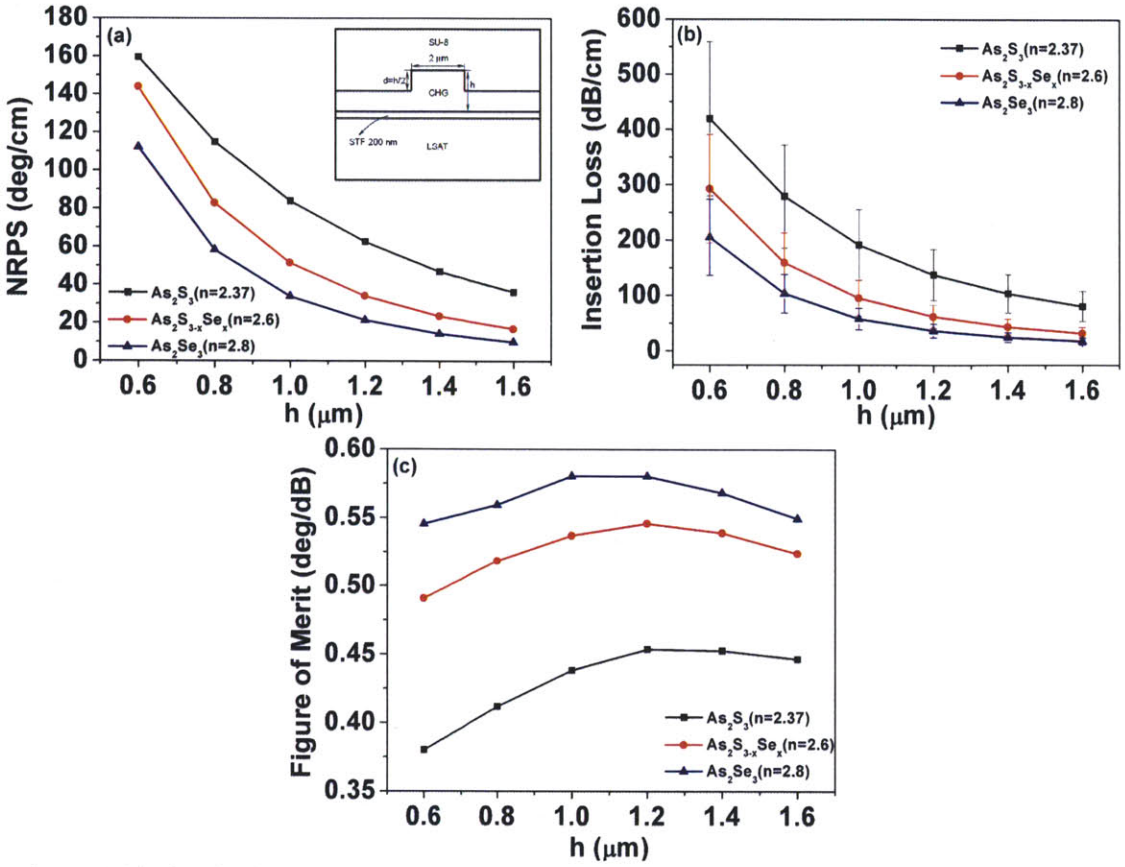

Fig. 4-18 (a) Simulated Nonreciprocal Phase Shift (NRPS) in ChG/STF strip-loaded waveguides. The inset shows the waveguide dimensions used for mode profile simulation. (b) Simulated waveguide insertion loss of ChG/STF strip-loaded waveguides. (c) Figure of merit (FoM) defined as NRPS divided by insertion loss in ChG/STF strip-loaded waveguides.

From the waveguide characterization and simulation results above, we can conclude that the high index of ChG glass is beneficial to the performance of magneto-optical waveguides, and the lift-off method allows non-composition-specific rapid prototyping and prevents etching-induced waveguide sidewall roughness. These analyses indicate that high index ChG is an ideal material for magneto-optical waveguide fabrication. However the FoM of current strip-loaded waveguides is still too low for optical isolator fabrication. Improvement of the FOM may be achieved by either decreasing the Fe^{2+}, Fe^{4+} or Co^{2+} concentration in the STF or STC films to decrease the optical absorption, or doping Ce^{3+} or Bi^{3+} into the STF or STC lattice to enhance the magneto-optical properties, as is done in garnets.

4.4 Summary

In this chapter, we studied several room temperature ferromagnetic perovskite epitaxial thin films including $Sr(Ti_{1-x}Co_x)O_{3-\delta}$, $(Ce_xSr_{1-x})Ti_{0.6}Fe_{0.4}O_{3-\delta}$ and $Sr(Ti_{0.6-y}Ga_yFe_{0.4})O_{3-\delta}$. Epitaxial perovskite thin films were deposited on $LaAlO_3(001)$, $SrTiO_3(001)$ and LSAT(001) substrates using PLD. RT-FM with high Curie temperatures and strong magnetic anisotropy were observed in these films. Secondary ferromagnetic phases such as Co metal clusters were not observed from our structural analysis. Significant magnetic anisotropy is observed in the highly tetragonallized epitaxial perovskite thin films. The magnetic anisotropy varies depending on fabrication conditions, substrate type and ion substitution, which is attributed to magnetoelastic effects in the strained films, and is related to the valence and spin states of the Co or Fe ions contributing to the RT-FM property. As_2S_3/perovskite strip-loaded waveguides were fabricated and characterized. Magneto-optical and waveguide transmission characterization of $Sr(Ti_{0.6-y}Ga_yFe_{0.4})O_{3-\delta}$ film shows a material figure of merit of 3~4 deg/dB at 1550 nm wavelength. Consider nonreciprocal mode conversion isolators, to achieve isolation 45 deg polarization rotationis required. Accounting for 3 dB or 1dB insertion loss, the material should show a figure of merit larger than 15 deg/dB or 45 deg/dB respectively. The Ga:STF films show a figure of merit lower than but close to application requirements, which can be optimized in further studies by better valence state control of the transition metal ions. A summary of material properties of RTFM perovskites and other materials studied in this thesis as well as literature reports will be carried out by the end of chapter 5.

References

[1] R. Maier and J. L. Cohn, *J. Appl. Phys.*, **92,** 5429 (2002)

[2] G. Herranz, R. Ranchal, M. Bibes, H. Jaffres, E. Jacquet, J. L. Maurice, K. Bouzehouane, F. Wyczisk, E. Tafra, M. Basletic, A. Hamzic, C. Colliex, J. P. Contour, A. Barthelemy and A. Fert, *Phys. Rev. Lett.*, **96**, 027207 (2006)

[3] M. B. Lee, M. Kawasaki, M. Yoshimoto and H. Koinuma, *Jpn. J. Appl. Phys.*, **35**, L574 (1996)

[4] F. Sanchez, R. Aguiar, V. Trtik, C. Guerrero, C. Ferrater and M. Varela, *J. Mater. Res.*, **13**, 1422 (1998)

[5] A. Rajamani, G. F. Dionne, D. Bono and C. A. Ross, *J. Appl. Phys.*, **98**, 063907 (2005)

[6] R. A. McKee, F. J. Walker, and M. F. Chisholm, *Phys. Rev. Lett.*, **81**, 3014 (1998).

[7] M. Gaidi, L. Stafford, J. Margot, M. Chaker, R. Morandotti, M. Kulishov, *Appl. Phys. Lett.*, **86**, 221106 (2005)

[8] S. X. Zhang, S. B. Ogale, Darshan C. Kundaliya, L. F. Fu, N. D. Browning, S. Dhar, W. Ramadan, J. S. Higgins, R. L. Greene, and T. Venkatesan, *Appl. Phys. Lett.*, **89**, 012501 (2006)

[9] G. Herranz, R. Ranchal, M. Bibes, H. Jaffres, E. Jacquet, J. L. Maurice, K. Bouzehouane, F. Wyczisk, E. Tafra, M. Basletic, A. Hamzic, C. Colliex, J. P. Contour, A. Barthelemy and A. Fert, *Phys. Rev. Lett.*, **96**, 027207 (2006)

[10] S. X. Zhang, W. Yu, S. B. Ogale, S. R. Shinde, D. C. Kundaliya, Wang-Kong Tse, S. Y. Young, J. S. Higgins, L. G. Salamanca-Riba, M. Herrera, L. F. Fu, N. D. Browning, R. L. Greene, and T. Venkatesan, *Phys. Rev. B*, **76**, 085323 (2007)

[11] Y. G. Zhao, S. R. Shinde, S. B. Ogale, J. Higgins, R. J. Choudhary, V. N. Kulkarni, R. L. Greene, T. Venkatesan, S. E. Lofland, C. Lanci, J. P. Buban, and N. D. Browning, *Appl. Phys. Lett.*, **83**, 2199 (2003)

[12] Y. H. Lin, S. Y. Zhang, C. Y. Deng, Y. Zhang, X.H. Wang and C. W. Nan, *Appl. Phys. Lett.*, **92**, 112501 (2008)

[13] S. Malo and A. Maignan, *Inorg. Chem.*, **43**, 8169 (2004)

[14] C. Pascanuta, N. Dragoeb, P. Bertheta, *J. Magn. Magn. Mat.*, **305,** 6 (2006)

[15] B. J. Tan, K. J. Klabonde and P. M. A. Sherwood, *J. Am. Chem. Soc.*, **113**, 855 (1991)

[16] T. Saitoh, T. Mizokawa, A. Fujimori, M. Abbate, Y. Takeda and M. Takano, *Phys. Rev. B*, **56**, 1290 (1997)

[17] T. Nitadori, M. Muramatsu and M. Misono, *Chem. Mater.*, **1**, 215 (1989)

[18]T. C. Kaspar, T. Droubay, C. M. Wang, S. M. Heald, A. S. Lea, and S. A. Chambers, *J. Appl. Phys.*, **97**, 073511 (2005)

[19] W. Yan, Z. Sun, Z. Pan, Q. Liu, T. Yao, Z. Wu, C. Song, F. Zeng, Y. Xie, T. Hu and S. Wei, *Appl. Phys. Lett.*, **94**, 042508 (2009)

[20] M. Janousch, G. I. Meijer, U. Staub, B. Delley, S. F. Karg and B. P. Andreasson, *Adv. Mater.*, **19**, 2232 (2007)

[21] B. D. Cullity, *Introduction to Magnetic Materials* (Addison-Wesley, Reading, MA, 1972)

[22] T. Matsui, R. Sato and H. Tsuda, *J. Appl. Phys.*, **103**, 07E304 (2008)

[23] S. Ogale, D. Kundaliya, S. Mehraeen, L. Fu, S. Zhang, A. Lussier, J. Dvorak, N. Browning, Y. Idzerda and T. Venkatesan, *Chem. Mater.*, **20**, 1344 (2008)

[24] J. Y. Kim, J. H. Park, B. G. Park, H. J. Noh, S. J. Oh, J. S.Yang, D. H. Kim, S. D. Bu, T. W. Noh, H. J. Lin, H. H. Hsieh and C. T. Chen, *Phys. Rev. Lett.*, **90**, 017401 (2003)

[25] G. F. Dionne and H-S. Kim, *J. Appl. Phys.*, **103**, 07B333 (2008)
[26] G.F. Dionne, *IEEE Trans. Magn,*. **5**, 596 (1969)
[27] D. Fushs, E. Arac, C. Pinta, S. Schuppler, R. Schneider and H. v.Löhneysen, *Phys. Rev. B.*, **77**, 014434 (2008)
[28] C. Zobel, M. Kriener, D. Bruns, J. Baier, M. Grüninger, T. Lorenz, P. Reutler and A. Revcolevschi, *Phys. Rev. B*, **66**, 020402(R) (2002)
[29] M. R. Ibarra, R. Mahendiran, C. Marquina, B. Garcia-Landa and J. Blasco, *Phys. Rev. B*, **57**, **R**3217 (1998)
[30] F. Fauth, E. Suard and V. Caignaert, *Phys. Rev. B*, **65**, 060401(R) (2001)
[31] L. Bi, H. S. Kim, G. F. Dionne, S. A. Speakman, D. Bono, and C. A. Ross, *J. Appl. Phys.*, **103**, 07D138 (2008)
[32] G.F. Dionne, *IEEE Trans. Magn.* (in press).
[33] G. F. Dionne, *J. Appl. Phys.*, **101**, 09C509 (2007)
[34] C. Pascanuta, N. Dragoeb, and P. Bertheta, *J. Magn. Magn. Mater.*, **6,** 305, (2006)
[35] M. Onoda, and M. Yasumoto, *J. Phys.: Condens. Matter*, **9**, 5623 (1997)
[36] Y. F. Yamada, A. Ohtomo, and M. Kawasaki, *Appl. Surf. Sci,*. **254**, 768 (2007)
[37] H. S. Kim, L. Bi, G. F. Dionne, and C. A. Ross, *Appl. Phys. Lett.*, **93**, 092506 (2008)
[38] Gomi M., Furuyama H. and Abe M., *J. Appl. Phys.*, **70**, 7065 (1991)
[39] F. Lucari, E. Terrenzio, and G. Tomassetti, *J. Appl. Phys.*, **52**, 2303 (1981)
[40] G. Blasse, and G. J. Dirksen, *J. Sol. State Chem.* **37**, 390 (1981)
[41] M. N. Taran, M. K. Müller, *Phys. Chem. Min.*, online first, (2010)
[42] J. Hu, V. Tarasov, N. Carlie, L. Petit, A. Agarwal, K. Richardson and L. Kimerling, *Opt. Express*, **15**, 2307, (2007)
[43] J. Hu, V. Tarasov, N. Carlie, L. Petit, A. Agarwal, K. Richardson and L. Kimerling, *Opt. Mater.*, **30**, 1560 (2007)
[44] H. Dotsch, N. Bahlmann, O. Zhuromskyy, M. Hammer, L. Wilkens, R. Gerhardt and P. Hertel, *J. Opt. Soc. Am. B*, **22**, 240 (2005)
[45] Integrated Optics Software FIMMWAVE 4.5, Photon Design, Oxford, U.K. [Online]. Available: http://www.photond.com

Chapter 5
Polycrystalline Iron Garnet Films and Waveguides on Silicon

Due to wide application in commercial optical isolators, iron garnets are the most widely studied materials compared to other magneto-optical material candidates. Because garnets show cubic lattice structure, the dielectric tensor can be expressed as a scalar and is therefore homogeneous along different crystallographic orientations. This unique property suggests that polycrystalline garnet films may also be used for nonreciprocal photonic applications. As introduced in chapter 1, integration of iron garnet films on silicon is challenged by the large lattice and thermal mismatch between the film and the substrate, impurity phases, as well as the high fabrication thermal budget for crystalline garnet films. Although polycrystalline $Y_3Fe_5O_{12}$ films, $Bi_3Fe_5O_{12}$ films and $Y_3Fe_5O_{12}$ waveguides have been fabricated on silicon, several issues have to be investigated before fabricating a practical optical isolator. Firstly, the microstructure, magnetic and magneto-optical property of polycrystalline garnet has to be studied and compared to their single crystal counterparts. Secondly, the optical loss needs to be determined in a waveguide configuration at NIR wavelengths. Thirdly, simple and low cost integration strategies of nonreciprocal photonic waveguides need to be developed.

In this chapter, we demonstrate the integration of $Y_3Fe_5O_{12}$ (YIG), $(Bi,Y)_3Fe_5O_{12}$ (Bi:YIG) and $(Ce,Y)_3Fe_5O_{12}$ (Ce:YIG) polycrystalline films on silicon platforms. Using a two-step deposition strategy, we monolithically integrated phase pure polycrystalline Bi:YIG and Ce:YIG films on silicon. The film structure and magneto-optical properties were studied as a function of the fabrication conditions. Chalcogenide Glass (ChG)/Garnet, Garnet/SOI strip-loaded waveguides and planar optical resonators were monolithically integrated on silicon. The optical transmission loss of the waveguide structures were measured using cut-back and "paperclip" methods. The optical transmission loss of polycrystalline YIG, $(Bi_{0.8}Y_{2.2})Fe_5O_{12}$ (Bi0.8YIG), $Bi_{1.8}Y_{1.2}Fe_5O_{12}$ and $(CeY_2)Fe_5O_{12}$ (CeYIG) films were determined by simulating the confinement factor of waveguide modes in these layers. The

nonreciprocal phase shift (NRPS) and device figure of merit (FoM) of As_2S_3/YIG and As_2S_3/CeYIG as a function of the waveguide geometry is simulated using numerical methods. Possible applications of these devices are discussed based on the simulation results.

5.1 Monolithic integration of iron garnet films on silicon

5.1.1 Integration of polycrystalline YIG films

YIG films with the thickness of 20~80nm were fabricated by PLD using the conditions described in table 2.1. The as deposited amorphous films were crystallized into the YIG phase by rapid thermal annealing at 850°C for 5 min. Figure 5-1 (a) shows the 1D ω–2θ XRD spectrum of an 80nm yttrium iron oxide film deposited on an oxidized silicon wafer after rapid thermal annealing. The diffraction pattern consists of a broad diffraction feature from the amorphous SiO_2 layer and well defined diffraction peaks from crystallized YIG. No secondary phase peaks were observed in the XRD spectrum. From the peak positions, the lattice constant of the YIG film is calculated to be 12.38 Å. Using Scherrer's equation [1], we can estimate the average YIG crystal size is about 22 nm. Similar XRD patterns were also observed on YIG films deposited on SOI substrates. Figure 5-1 (b) shows the atomic force microscope (AFM) image of a 1 μm by 1 μm area on the crystallized YIG film. The film shows a smooth surface with RMS roughness of 0.36 nm. The polycrystal grain size is comparable with the value calculated from the XRD spectrum. The room temperature magnetic hysteresis of a crystallized YIG film is shown in figure 5-1 (b). The YIG film shows a saturation magnetization of 130 emu/cm^3 with an in-plane magnetic easy axis due to magnetic shape anisotropy. Comparing with the bulk magnetization value of 139 emu/cm^3, we estimated that ~95 vol.% of the film has crystallized into the YIG phase. (Note that the 9 emu/cm^3 difference is within the measurement error range and may be due to measurement erros.) This film shows a very low in-plane saturation magnetic field of 100 Oe, which is beneficial for fabricating integrated isolators. We also noticed that the PLD temperature is critical for the final phase purity of the YIG film after RTA. For YIG films deposited at higher substrate temperature of 650°C, iron oxide impurity phases formed in the as deposited

film demonstrated by observing a magnetic hysteresis loop. Although not observed in XRD spectrum, such impurity phases may act as scattering centers and are undesired for integrated photonic devices. Figure 5-1 (c) shows the room temperature Faraday rotation spectrum of a 500 nm polycrystalline YIG film grown on an MgO substrate. A Faraday rotation value of ~100 deg/cm is observed, smaller than the value of 160 deg/cm of YIG single crystals at this wavelength. [2] This is possibly due to the inferior crystal quality of RTA YIG films compared with single crystals and due to the measurement error for small rotation values. Notice that the saturation magnetic field of the Faraday rotation hysteresis is around 1600 Oe, which coincides with the out-of-plane saturation field value determined by VSM.

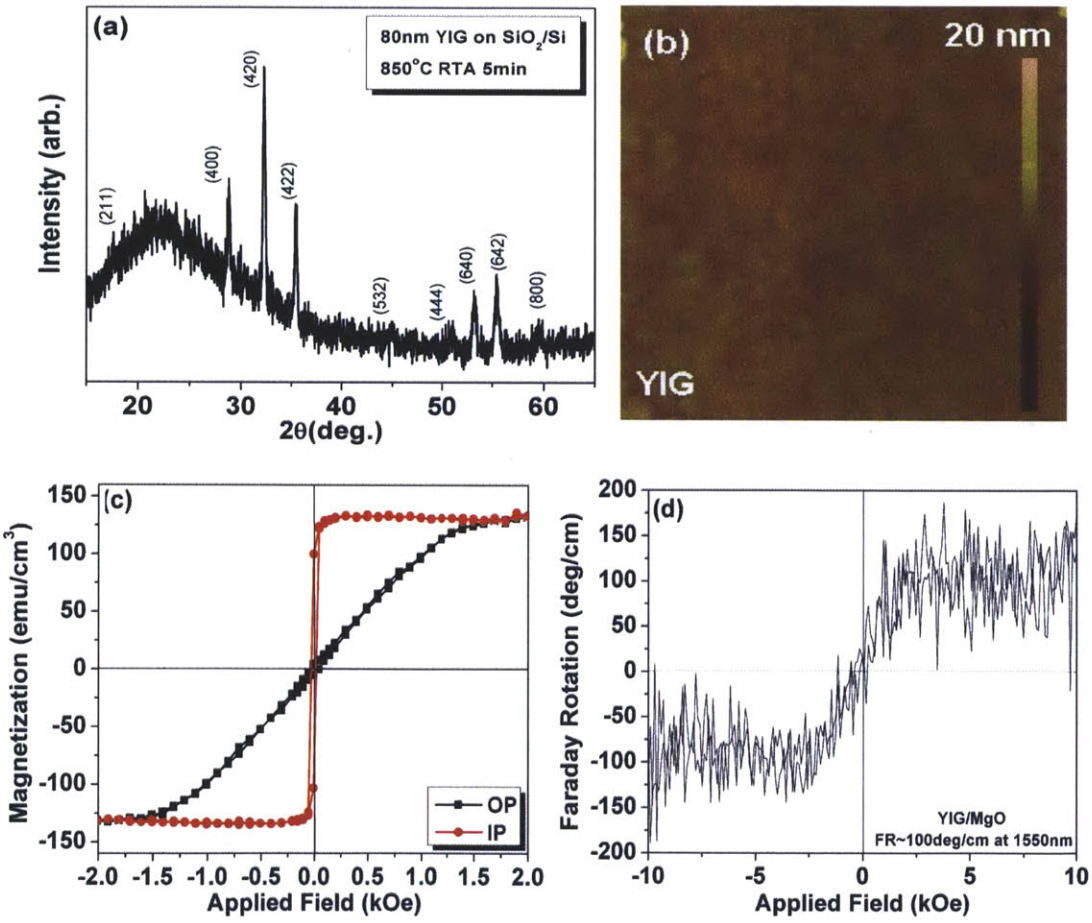

Fig. 5-1 (a) 1D ω–2θ XRD spectrum of an 80 nm YIG film deposited on a SiO_2/Si wafer followed by rapid thermal annealing at 850°C for 5 min. (b) AFM image of 1 μm by 1 μm area on the crystallized YIG film (c) Room temperature in-plane (IP) and out-of-plane (OP) magnetization hysteresis loops of a crystallized YIG film on SiO_2/Si substrate. (d) Room temperature Faraday rotation hysteresis of a 500 nm YIG film on MgO substrate

5.1.2 Two-step integration of Bi:YIG and Ce:YIG films on silicon

To stabilize the garnet phase and reduce the fabrication thermal budget, a two-step integration method was carried out for Bi:YIG and Ce:YIG films integration on silicon. A thin YIG film was firstly deposited by PLD and rapid thermal annealed to crystallize, then the Bi:YIG and Ce:YIG films were deposited by PLD on the YIG buffer layer. The deposition conditions are described in table 2-1. Figure 5-2 (a), (b) and (c) show the ω–2θ X-ray diffraction spectrum of Bi0.8YIG, Bi1.8YIG and CeYIG on oxidized silicon substrate fabricated using the two-step method respectively. For comparison, XRD spectra of films deposited without the YIG buffer layer are also shown. It is clear that two-step grown films show polycrystalline garnet phases while the reference samples without YIG buffer layers show only amorphous diffraction patterns at $2\theta=30^{\circ}$. For the first time we demonstrated that both Bi:YIG and Ce:YIG films can be stabilized by an ultra thin YIG layer using RTA crystallization. The Bi:YIG and Ce:YIG films can crystallize at lower temperatures and require low fabrication thermal budget which is important for photonic device design and fabrication. We calculated the lattice parameter of the garnet films from the XRD patterns. Bi0.8YIG, Bi1.8YIG and CeYIG show lattice constants of 12.40 Å, 12.46 Å and 12.46 Å, which are comparable to bulk samples [3][4] following the Vegard's Law. The crystal sizes are calculated by applying Scherrer's equation. The buffering YIG layer, Bi0.8YIG, Bi1.8YIG and CeYIG films show crystal sizes of 36 nm, 30 nm, 37 nm and 46 nm respectively. It is observed that the film lattice parameter is highly dependent on fabrication conditions. A decrease of the deposition oxygen partial pressure yields smaller or larger lattice parameters of BiYIG or CeYIG films respectively, which are possibly due to desorption of Bi atoms or reduction of Ce ions from 4+ to 3+ with lower oxygen partial pressure. Meanwhile, oxygen vacancies formed at lower deposition pressures may also expand the lattice. Such processes significantly influence the magneto-optical properties of the garnet films, which will be discussed below. Figure 5-2 (d), (e) and (f) shows the AFM image of Bi0.8YIG, Bi1.8YIG and CeYIG films respectively. The surface roughness of the BiYIG films varies significantly depending on the Bi concentrations. Bi0.8YIG, Bi1.8YIG and CeYIG films show surface RMS roughness of 1.81 nm, 4.50 nm

and 0.92 nm respectively, compared with a bare YIG polycrystalline film of 0.36 nm shown in figure 5-1 (b).

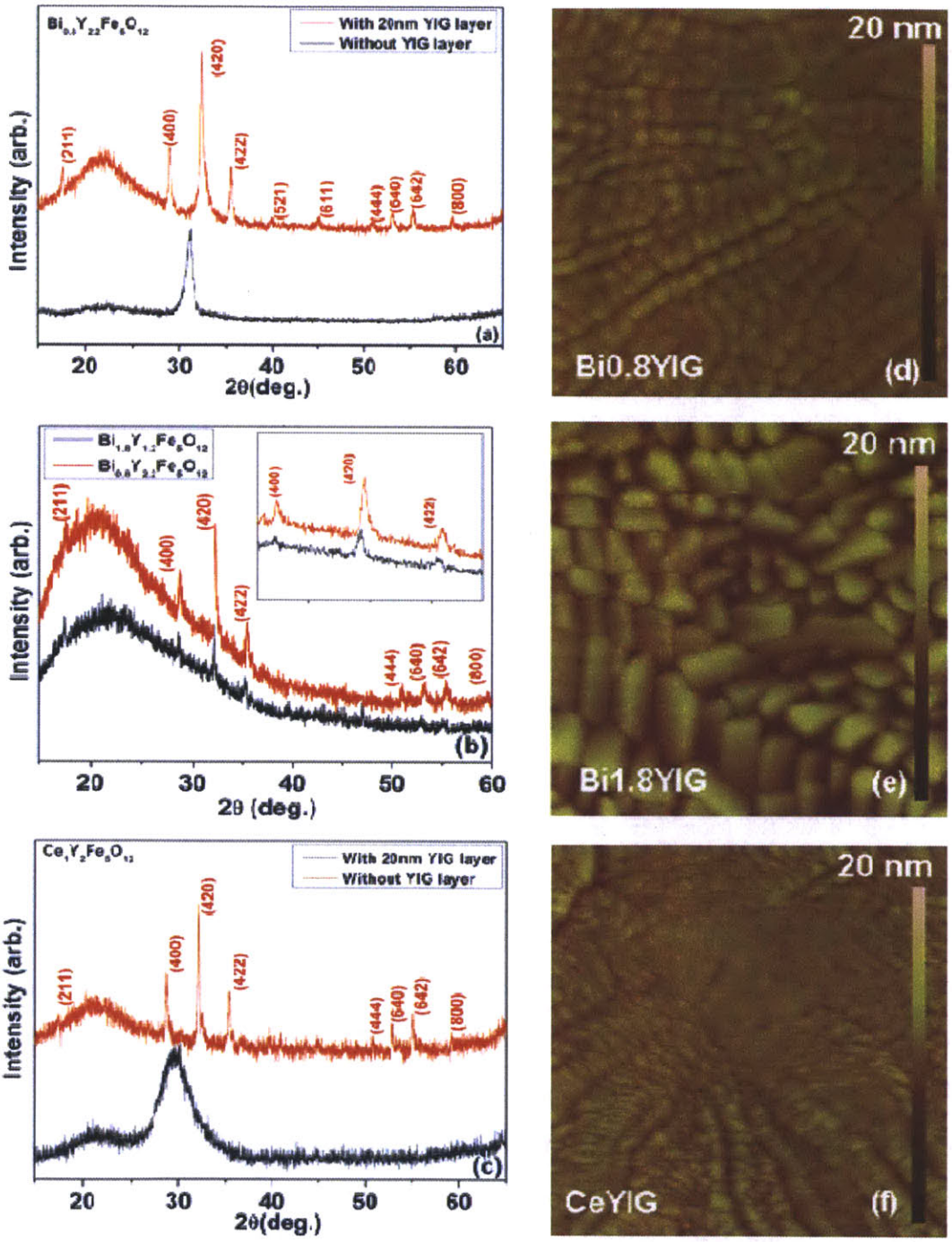

Fig. 5-2 XRD spectrum of (a)Bi0.8YIG, (b)CeYIG and (c)Bi1.8YIG polycrystalline films on oxidized silicon substrates using two-step deposition. Films deposited without the YIG buffer layer is also shown for comparison. AFM images of 1μm by 1μm area of (a)Bi0.8YIG, (b)CeYIG and (c)Bi1.8YIG films are also shown

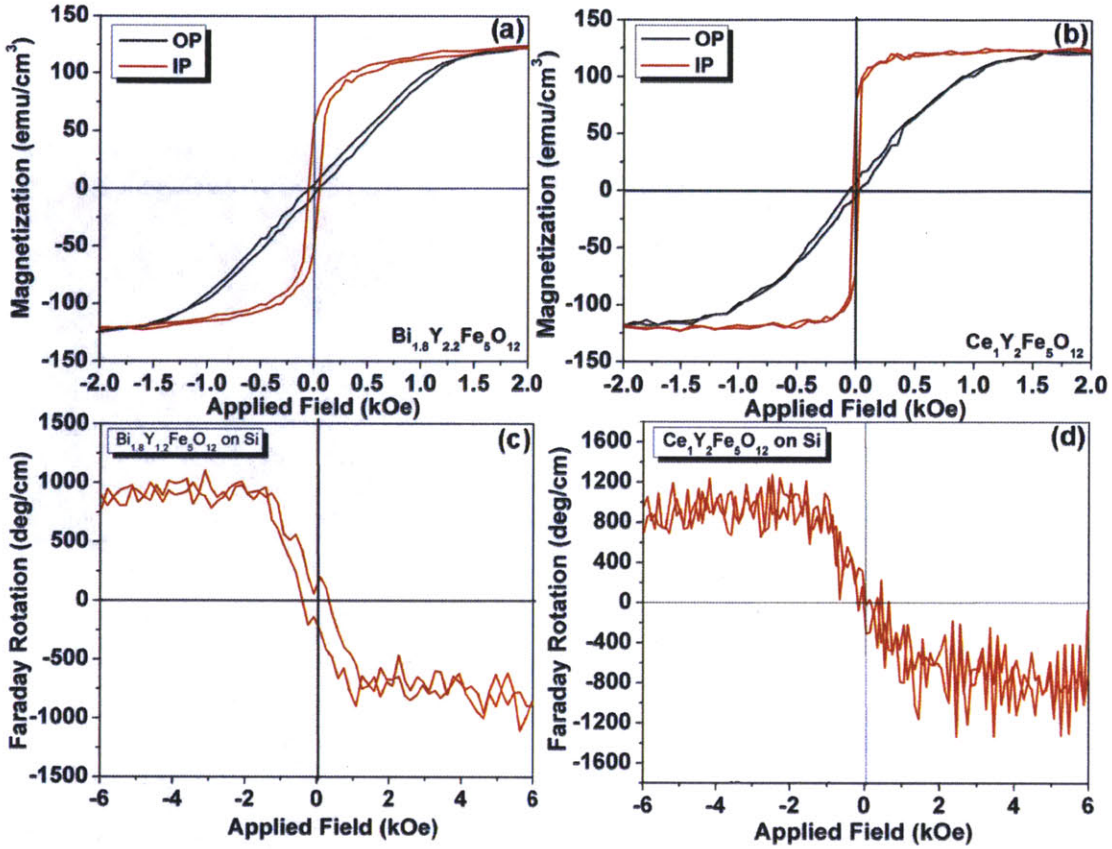

Fig. 5-3 Room temperature magnetization hysteresis and Faraday rotation at 1550nm wavelength of (a),(c) Bi1.8YIG films and (b),(d) CeYIG films. The inset of (d) shows Faraday rotation as a function of fabrication oxygen partial pressure

Figure 5-3 shows the room temperature magnetic and 1550 nm Faraday rotation hysteresis loops of Bi1.8YIG and CeYIG films. Both films show in-plane magnetization easy axis due to magnetic shape anisotropy. Bi1.8YIG shows a higher in-plane saturation field of ~500 Oe compared to ~200 Oe of the CeYIG film, which may be correlated with the different microstructure of these films shown in the AFM images. The saturation magnetization of Bi1.8YIG and CeYIG films are 125 emu/cm^3 and 120 emu/cm^3 respectively. By comparing with the bulk materials, the volume fraction of crystallized garnet phase in Bi1.8YIG and CeYIG films are estimated to be 91 vol.% and 87 vol.% respectively. Although most of the film volume crystallized into garnet phase and show comparable lattice constant to their bulk counterparts, the Faraday rotation of polycrystalline BiYIG and CeYIG films are considerably lower. Bi1.8YIG and CeYIG show saturation Farday rotations of -838 deg/cm

and -830 deg/cm respectively, compared to >-3000 deg/cm and -3300 deg/cm in sputter deposited epitaxial films on garnet substrates. [5][6]

The Faraday rotation of CeYIG samples is also strongly dependent on the deposition oxygen partial pressure. As shown in figure 5-4, the saturation Faraday rotation of CeYIG is maximized at intermediate oxygen pressure, which is consistent with previous reports on epitaxial CeYIG films. [7] Higher oxygen partial pressure leads to higher Ce^{4+} ion population compared with Ce^{3+}, which decreases the Faraday rotation. This explanation is also consistent with the observation of an increase of the lattice constant as decreasing the fabrication oxygen partial pressure of the CeYIG films.

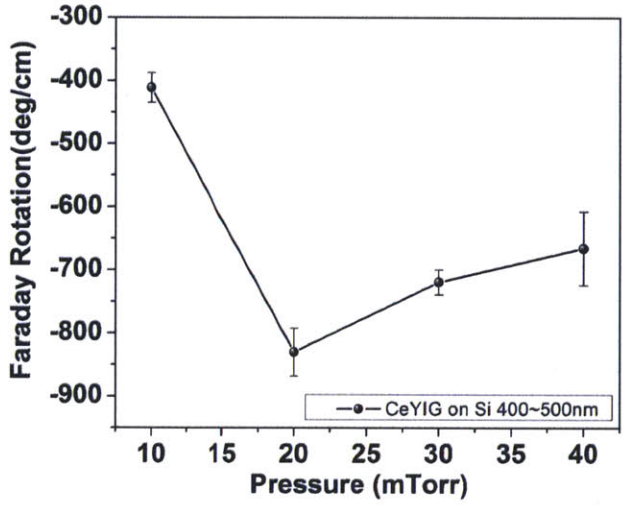

Fig. 5-4 Faraday rotation of polycrystalline CeYIG films on silicon substrates as a function of oxygen partial pressure

5.2 Garnet film based strip-loaded waveguides and resonators

5.2.1 Chalcogenide glass/garnet waveguides and resonators

As_2S_3/YIG, As_2S_3/Bi:YIG and As_2S_3/Ce:YIG were fabricated on oxidized silicon substrate using the strategies described in section 2.1.2. Figure 5-5 (a) shows the top view optical microscope image of the waveguides. The cross-sectional SEM image of a 2 μm wide As_2S_3/YIG strip-loaded waveguide is shown in figure 5-5 (b). The waveguide consists of a 3 μm SiO_2 bottom cladding layer (n=1.44), an 80 nm YIG slab (n=2.2), a 360 nm thick As_2S_3

(n=2.37) channel and a 2 μm thick SU-8 top cladding layer (n=1.58). Notice that the sidewalls of the As_2S_3 layer are slanted to 60°, which is due to the lift-off fabrication process. [8][9] The TM mode optical transmission spectrum of a 13 mm long waveguide with this structure is shown in figure 5-5 (c), also shown for comparison is the transmission spectrum of a 19 mm long bare As_2S_3 channel waveguide on SiO_2/Si substrate with the same As_2S_3 channel thickness. Although shorter in length, the strip-loaded waveguide showed higher insertion loss compared with the bare As_2S_3 channel waveguide, which is due to the incorporation of the YIG slab. A small insertion loss variation versus wavelength is observed in both waveguides, which is due to the multimode beating effect.

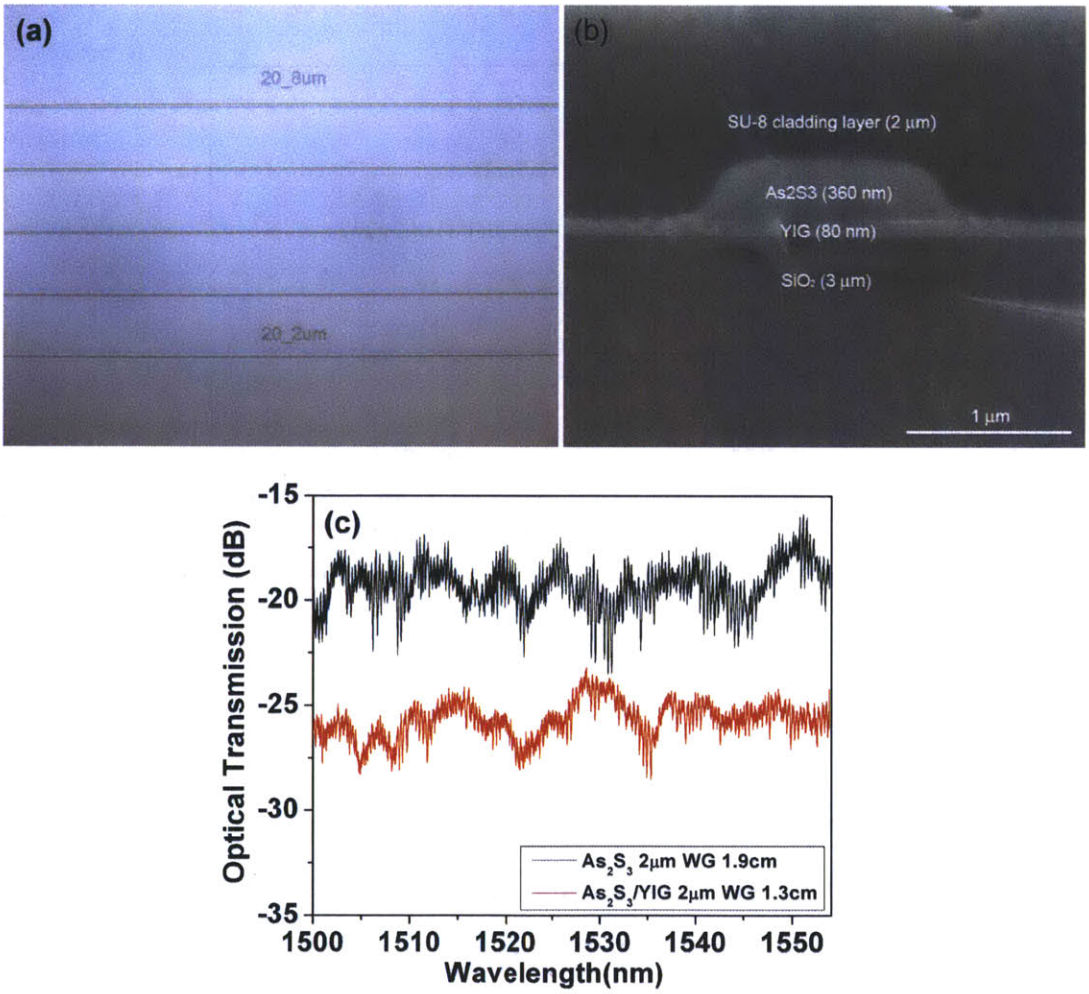

Fig. 5-5 (a) Cross-sectional SEM image of a 2 μm wide As_2S_3/YIG strip-loaded waveguide. (b) TM polarization optical transmission versus wavelength of a 2 μm wide bare As_2S_3 channel waveguide and a 2 μm wide As_2S_3/YIG strip-loaded waveguide

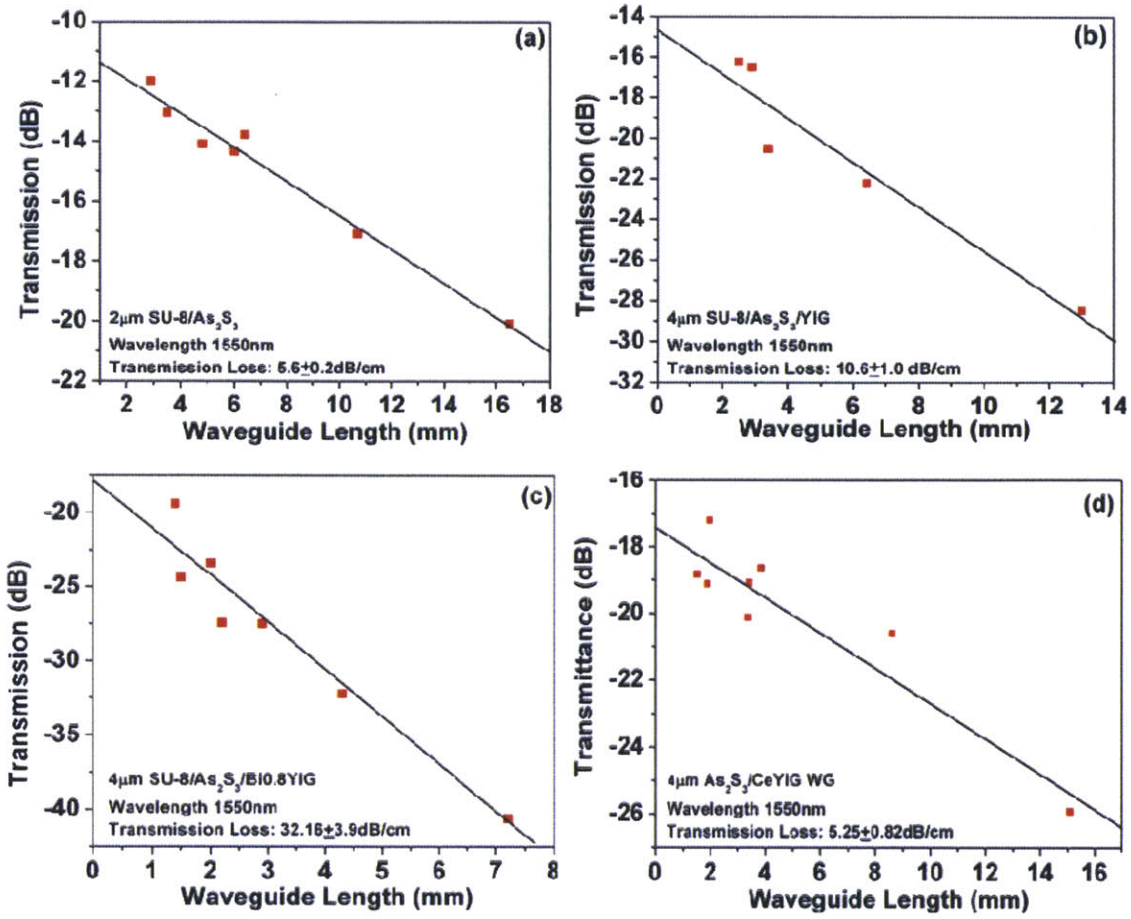

Fig. 5-6 Optical propagation loss of the TM mode incident light at 1550nm for (a) a 2 μm wide As_2S_3 channel waveguide (b) a 2 μm wide As_2S_3/YIG waveguide and (c) a 4 μm wide As_2S_3/YIG waveguide determined by cut-back method

In order to accurately determine the optical loss of the strip-loaded waveguides and the garnet films, cut-back method was carried out to measure the insertion loss of a 2 μm wide As_2S_3 channel waveguide, a 4 μm wide As_2S_3/YIG strip-loaded waveguide, a 4 μm wide As_2S_3/Bi0.8YIG waveguide and a 4 μm wide As_2S_3/CeYIG waveguide. We did not characterize the propagation loss of wider waveguides due to the stronger multi-mode beating effect. The results are shown in figure 5-6. The full square dots are the experimental data and the lines are linear fit to these values. The bare As_2S_3 channel waveguide showed optical loss of 5.6 ± 0.2 dB/cm at 1550nm wavelength, which is slightly larger but consistent with the optical loss of waveguides fabricated by this method.[8][9] The 4 μm wide As_2S_3/YIG, As_2S_3/Bi0.8YIG and As_2S_3/CeYIG waveguides showed transmission loss at 1550 nm

wavelength of 9.7 ± 0.4 dB/cm, 32.15 ± 3.9 dB/cm and 5.25 ± 0.82 dB/cm respectively. The transmission loss of As_2S_3/Bi1.8YIG waveguides are even higher than As_2S_3/Bi0.8YIG waveguides which cannot be accurately measured using this method. We note that the As_2S_3/CeYIG waveguide shows similar loss level compared to the 2 μm wide As_2S_3 waveguides fabricated under similar conditions, indicating the CeYIG layer showing low transmission loss at near infrared wavelengths; whereas As_2S_3/Bi0.8YIG waveguides showed much higher loss originated from the garnet layer. Considering the confinement factor in the YIG layer and the Bi0.8YIG layer are about 11% and 10% respectively, the optical transmission loss is estimated to be ~50 dB/cm (α=11.5 cm^{-1}) for polycrystalline YIG and ~150 dB/cm (α=34.5 cm^{-1}) for polycrystalline Bi0.8YIG respectively. These values are higher than the YIG or Bi:YIG single crystals. In single crystal YIG and BiYb:YIG materials, the propagation loss was reported to be 25.8 dB/cm and 15.4 dB/cm respectively, corresponding to figure of merits of 9.1 deg/dB and 25.8 deg/dB respectively. [10] It is considered that although not observed in X-ray diffraction patterns, a small amount of amorphous or secondary phases may cause scattering in the polycrystalline YIG film, therefore increase the material loss at near infrared wavelengths. Compared to literature reported loss value of 15.5 dB/cm of YIG polycrystalline film on SiO_2 buffered silicon [12], our YIG films shows higher but same order of loss values. For Bi0.8YIG, the optical loss may be partially related to the large film roughness. Also different from epitaxial BiYIG films, in polycrystalline BiYIG, Bi may segregate at grain boundaries which causes index variation and leads to much stronger scattering loss. [11]

In order to determine the transmission loss of polycrystalline CeYIG films, "paperclip" type As_2S_3/CeYIG waveguides were fabricated. As a control sample, bare As_2S_3 channel waveguides with the same structures are fabricated at the same time. Figure 5-7 (a) shows the optical microscope image of one of such waveguides. By measuring paperclip pattern with different straight part length, we were able to measure the transmission loss as a function of waveguide length. As shown in figure 5-7 (b) and 5-7 (c), the transmission loss of a 4 μm wide As_2S_3 and As_2S_3/CeYIG waveguide are determined as 2.99 ± 1.88 dB/cm and 6.67 ± 2.26 dB/cm respectively. Therefore the optical transmission loss of the CeYIG layer is

estimated to be ~40 dB/cm by considering the confinement factor of the waveguide structure. For comparision, CeYIG single crystals show loss values of 2.7 dB/cm and Faraday rotation value of 1250 deg/cm. [13] CeYIG epitaxial film based waveguides on garnet substrates show propagation loss value of 5~10 dB/cm for TM modes and Faraday rotation value of -3300~-3800 deg/cm at 1550 nm wavelength.[5][6] The loss value of our polycrystalline CeYIG is higher than epitaxial CeYIG films and comparable to the polycrystalline YIG films.

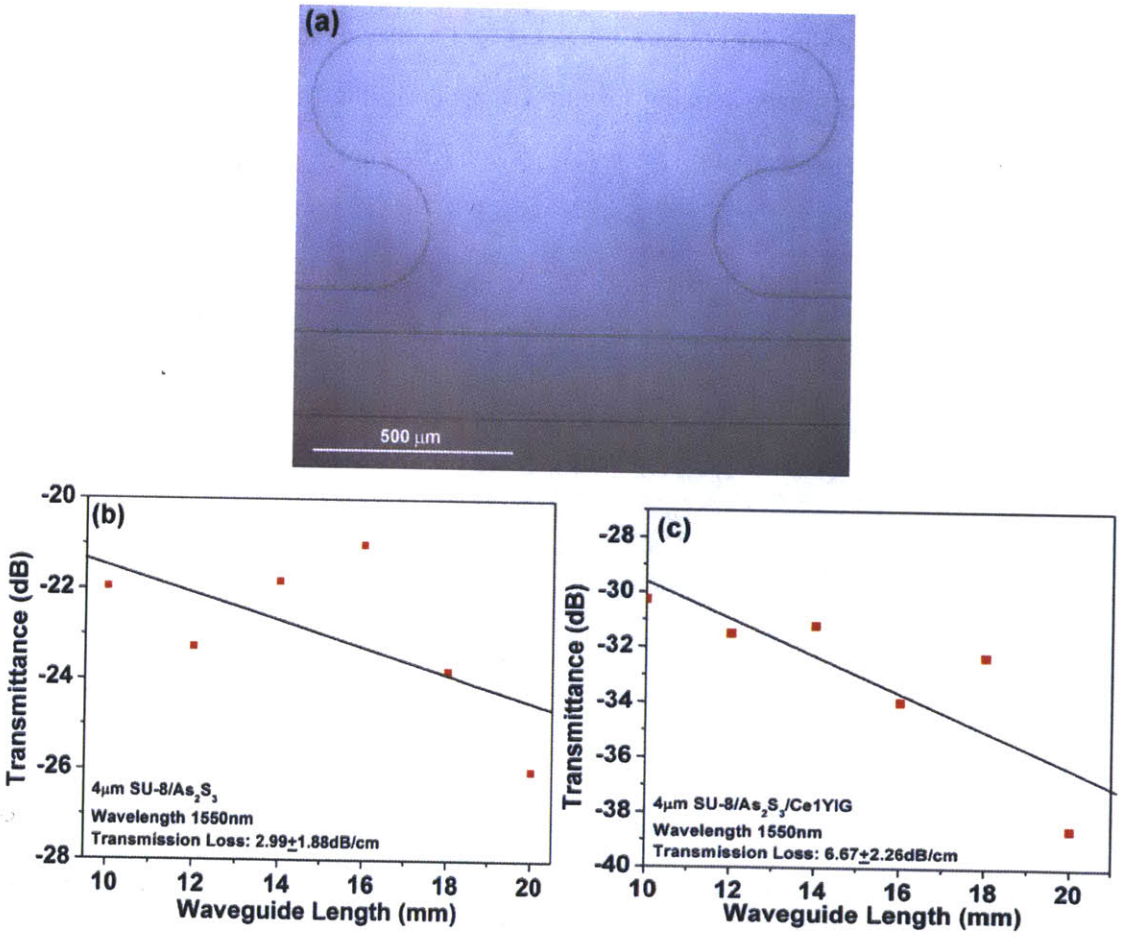

Fig. 5-7 (a) Top view of an As_2S_3/CeYIG paperclip waveguide. The transmission loss measured by paperclip method of a 4 μm wide bare As_2S_3 waveguide and As_2S_3/CeYIG waveguide are shown in (b) and (c) respectively

GeS_2/garnet optical resonators were also fabricated using the waveguide fabrication strategies. Figure 5-8 (a) shows a top view image of a GeS_2/Bi0.8YIG racetrack resonator. The waveguides are 2 μm wide, and the gap size between the bus waveguide and the racetrack resonator is 1 μm. In order to have good coupling between the resonator and the bus

waveguide, we deposit a ridge structured GeS_2 layer on the Bi0.8YIG film. The overall GeS_2 layer thickness is 400 nm with a ridge height of 286 nm, while the Bi0.8YIG layer is 127 nm thick as measured by SEM. The transmission spectrum of such a resonator is shown in figure 5-8 (b). Well defined resonance peak with free spectral range (FSR) of 0.33 nm is observed in the TE mode transmission. The resonance spectrum behaves from under-coupling to over-coupling in a spectrum range of 1529 nm to 1537 nm. The quality factor Q is around 17,000 at critical coupling wavelength, which is calculated by applying a Lorentzian fitting to the resonant peaks. We did not observe resonance in the TM mode transmission spectrum. This is possibly due to higher bending loss of TM mode in the ridge waveguide structure, which leads to under-coupling within the tested wavelength range.

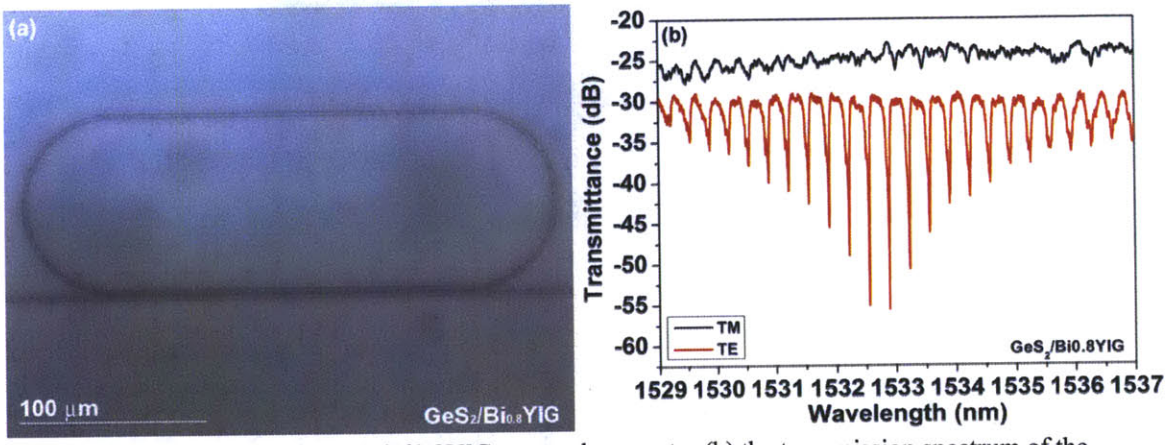

Fig. 5-8 (a)Top view of a GeS_2/Bi0.8YIG racetrack resonator (b) the transmission spectrum of the GeS_2/Bi0.8YIG resonator at NIR

5.2.2 Garnet/SOI waveguides and resonators

We also integrated polycrystalline YIG films in YIG/SOI waveguide and resonator structures using the strategies described in figure 2-4. The top-view SEM image of a 450 nm wide YIG/SOI waveguide is shown in figure 5-9 (a). One can notice that a crack generated even in an 80 nm YIG film after crystallization. However the crack did not propagate through the YIG/SOI waveguide, which can be explained by the reduced surface area of the YIG film on the SOI waveguide compared to a continuous film. The small film area leads to small expansion area and less cracks. [14] The TM mode transmission spectra of a 6 mm long SOI and a 6 mm long YIG/SOI waveguide are shown in figure 5-9 (b). Both waveguides show

single mode propagation characteristics, while the strip-loaded waveguide shows much higher insertion loss due to the incorporation of the YIG layer.

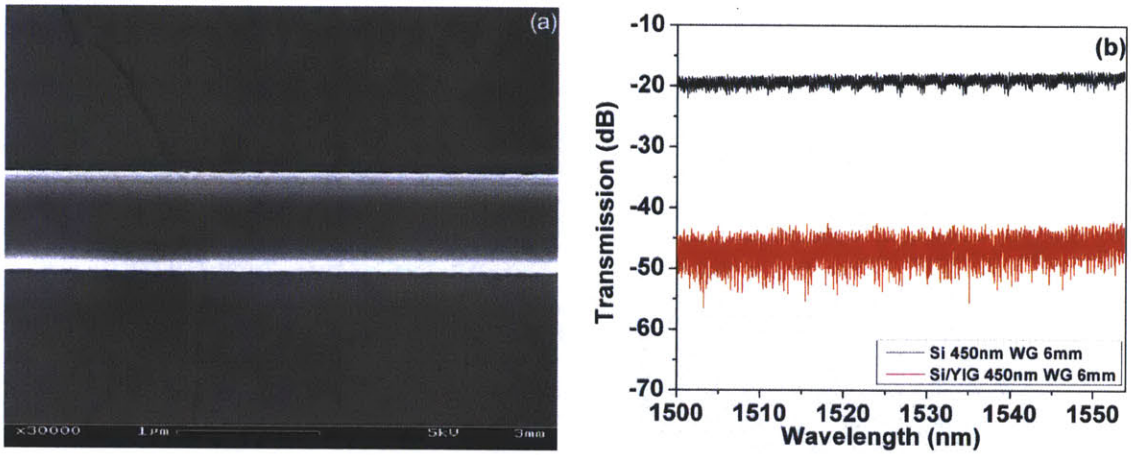

Fig. 5-9 (a) Plane-view SEM image of a 450nm wide YIG/SOI waveguide. (b) TM polarization transmission spectrum of a bare SOI channel waveguide and a YIG/SOI waveguide

To characterize the propagation loss of the YIG/SOI waveguides, a pulley-type silicon ring resonator with a diameter of 40 μm is fabricated as shown in figure 5-10 (a). A 450 nm wide bus waveguide was designed to surround half of the circumference of the ring resonator, which provides stronger coupling between the waveguide and the resonator. The gap between the bus waveguide and the ring resonator was 300 nm. After coating the device with an 80 nm YIG layer, the transmission spectrum was measured as shown in figure 5-10 (b). Evenly spaced resonant peaks were observed in the TM polarization transmission spectrum, while the TE mode signals are too lossy to be measured. The resonator showed a under coupling to over coupling transition with increasing incident light wavelength, and near critical coupling was achieved around 1515 nm. The quality factor Q of this resonator was calculated to be ~10,000. We can calculate the propagation loss of the YIG/SOI waveguide from the following formula [15].

$$\alpha = \frac{2\pi\lambda_r}{FSR \cdot Q_{in} \cdot L} \tag{5-1}$$

where λ_p is the resonance wavelength, FSR is the free spectrum range of the resonance, Q_{in} is the intrinsic quality factor of the resonator (Q_{in}~$2Q_{tot}$ at critical coupling wavelength), L is the cavity length and α is the optical absorption coefficient. The effective index of the YIG/SOI

waveguide is simulated to be 1.98 at 1515 nm wavelength, therefore the optical loss of the waveguide is calculated to be 34 dB/cm. Comparing with the optical transmission spectrum of the straight waveguides shown in figure 5-10 (b) and considering a simulated confinement factor of 28% in the YIG films, the optical loss of the YIG film is estimated to be 60~70 dB/cm. This value is larger than the As_2S_3/YIG case, which is possibly due to increased silicon waveguide side wall roughness during deposition and crystallization of the YIG layer.

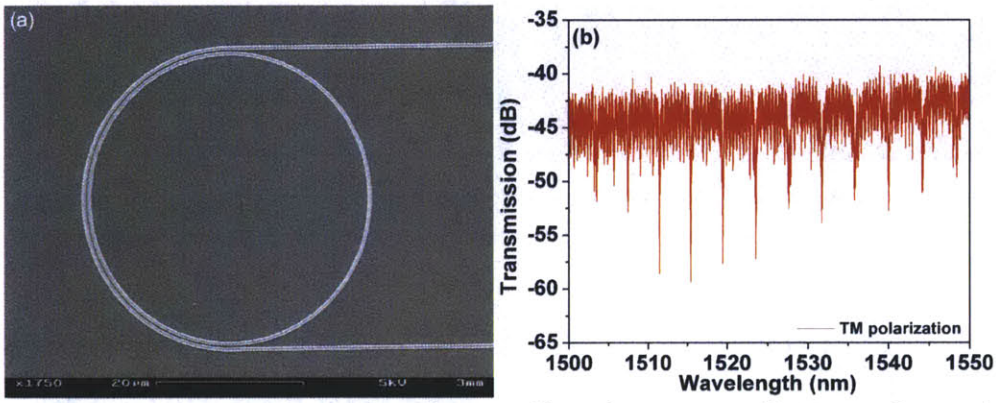

Fig. 5-10 (a) Plane view SEM image of a pulley-type silicon ring resonator. (b) Measured transmission spectrum of TM polarized light in a YIG/SOI pulley type resonator

5.3 NRPS and figure of merit simulation of garnet based waveguides

The magneto-optical performance, specifically the NRPS of these waveguides can be simulated by perturbation theory using the following equation as we discussed in chapter 4.

$$\Delta\beta^{TM} = -\frac{2\beta^{TM}}{\omega\varepsilon_0 N}\iint\frac{K''M_y}{n_0^4}H_y\partial_x H_y dxdy$$

We firstly simulated the fundamental TM mode profile in the As_2S_3/YIG and YIG/SOI waveguides by FIMMWAVE software using a film mode matching method (FMM) [16]. From the mode profile and the experimentally measured Faraday rotation of the YIG film, we calculated the NRPS of both waveguide structures as a function of the As_2S_3 and SOI layer thickness. Also from the measured waveguide propagation loss, we calculated the device figure of merit as a function of the As_2S_3 and SOI layer thickness, which is defined as NRPS divided by optical loss per length. The results are shown in figure 5-11 (a) and (b) for

As_2S_3/YIG and YIG/SOI waveguides respectively. The insets are the schematic plot of the waveguide structures used in the simulations. First of all, we notice that the highest NRPS can be achieved at a certain thickness of the As_2S_3 or the SOI layer. This can be explained as follows: when the As_2S_3 or SOI layer is thin, the guided mode is highly confined in the YIG layer. The $\partial_x H_y$ term can be positive or negative and cancels out when integrated, which yields low NRPS; when the As_2S_3 or SOI layer is thick, the guided mode is weakly confined in the YIG layer. The H_y term is small, which also yields low NRPS. In the As_2S_3/YIG waveguide structure, the highest FoM of 3.12 can be achieved at an As_2S_3 layer thickness of 320 nm. Whereas in the YIG/SOI structure, the FoM shows smaller values and more complex variation with SOI layer thickness. This is because the propagation loss of this waveguide is higher as measured by experiments, and part of the NRPS is canceled by the YIG film on the SiO_2 surface in this structure. An improved device design may be achieved by etching into the SiO_2 cladding layer to decrease the optical confinement in the YIG films on the SiO_2 surface, which may lead to higher device NRPS and FoM.

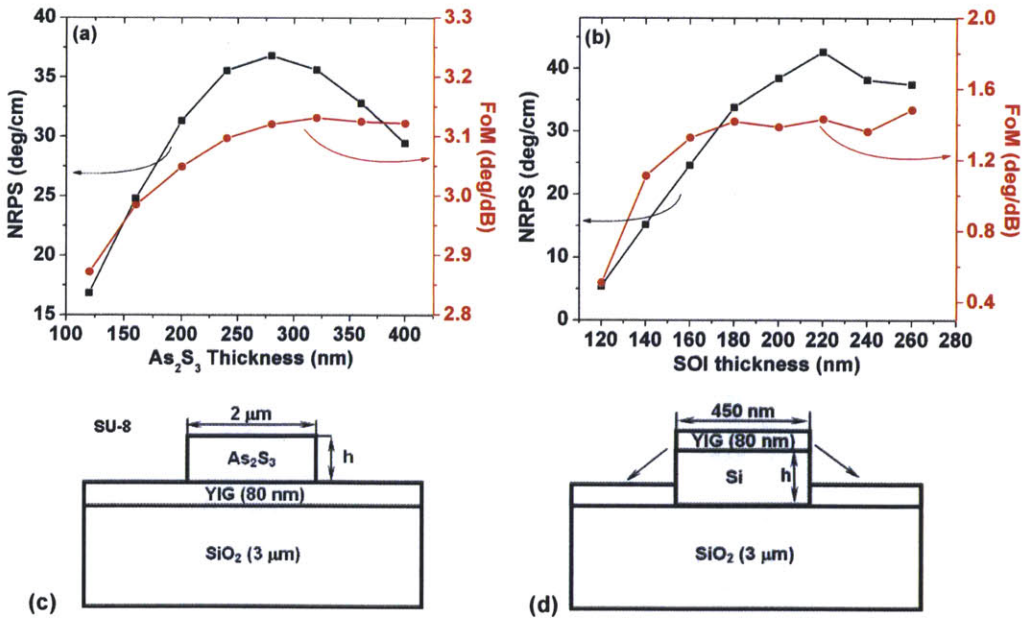

Fig. 5-11 Simulated Nonreciprocal Phase Shift (NRPS) and Figure of Merit (FoM) (NRPS divided by transmission loss per length of the waveguide) in (a) As_2S_3/YIG and (b) YIG/SOI strip-loaded waveguides. Also shown are the waveguide dimensions used for mode profile simulation in (c) As_2S_3/YIG and (d) YIG/SOI strip-loaded waveguides.

The NRPS and FoM of As_2S_3/CeYIG waveguides were also simulated using the same strategies. The results are shown in figure 5-12. The NRPS and FoM maximize at similar As_2S_3 layer thickness compared to As_2S_3/YIG waveguides, suggesting that both properties are mainly controlled by the confinement factor in the garnet layers. Comparing with As_2S_3/YIG waveguides, As_2S_3/CeYIG waveguides show a much higher FOM up to 32.6 deg/dB by simulation, which is due to higher Faraday rotation in the CeYIG films. Considering using such waveguides in a Mach-Zehnder structure which requires 90° NRPS to achieve optical isolation, the device size should be at least 5 mm long and the excess loss due to the garnet layer will be 3 dB. These values are promising, but further improvements on materials and devices are necessary to reduce the excess loss for optical isolation applications. The device footprint is another important issue. A 5 mm long device with Mach-Zehnder interferometer structure is too large compared to other integrated photonic devices, and is also incompatible for high density monolithic integration. We consider that rather than creating a π phase difference using NRPS, integrating such waveguides in a resonator structure such as shown in figure 5-8 will significantly reduce the device footprint. The nonreciprocity can be achieved by different TM mode propagation constants between clockwise and counter-clockwise resonance modes, leading to a non-degeneracy of the resonance frequency of forward and backward propagating light. With the material and waveguide studies in this chapter, we have a platform to realize the nonreciprocal optical resonator devices on silicon, which will be discussed in detail in chapter 6.

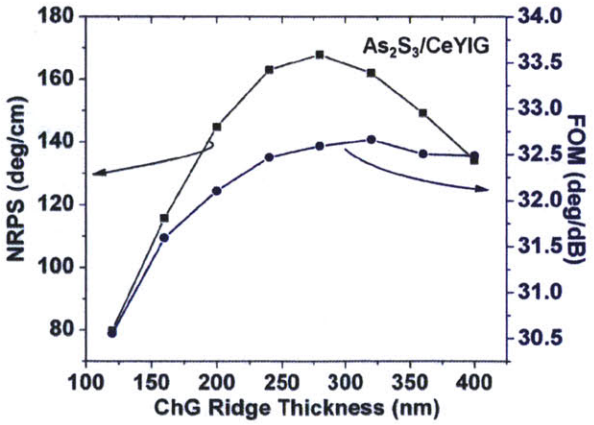

Fig. 5-12 Simulation of NRPS and device FoM (NRPS divided by transmission loss per length of the waveguide) of As_2S_3/CeYIG waveguides on oxidized Si

5.4 Summary

In this chapter, we studied the integration of polycrystalline YIG, Bi:YIG and Ce:YIG on silicon. YIG films were deposited on oxidized silicon substrates and RTA to form the garnet phase. Using a two-step deposition strategy, we integrated phase pure Bi0.8YIG, Bi1.8YIG and CeYIG films on silicon. The structure, magnetic and magneto-optical properties of the polycrystalline films were characterized. Waveguide and resonator devices based on ChG/Garnet and Garnet/SOI structures were demonstrated and characterized. For the first time we measured the optical transmission loss of polycrystalline Bi and Ce doped YIG films by cutback, paperclip and optical resonator methods. Using the measured Faraday rotation and optical loss of the garnet films, we simulated the NRPS and figure of merit these waveguides at 1550 nm wavelength. CeYIG films show a material FoM of ~20 deg/dB, while As_2S_3/CeYIG waveguides show a simulated FoM up to 32.5 deg/dB (NRPS), which are promising for integrated optical isolator applications.

In chapter 4 and 5, we discussed several material candidates for integrated nonreciprocal photonic devices. Here we summarize these materials' performance in table 5-1. Ga:STF and polycrystalline Ce:YIG shows the highest figure of merits among the materials we studied.

Table 5-1 Faraday rotation, optical absorption and figure of merit of several magneto-optical materials studied in this thesis and in literature

Materials	FR (deg/dB)	Loss (dB/cm)	FoM (deg/dB)
$Sr(Ti_{0.77}Co_{0.23})O_{3-\delta}$	-200~-500	300~400	0.57
$Sr(Ti_{0.6}Fe_{0.4})O_{3-\delta}$	-780	700	1.1
$Sr(Ti_{0.2}Ga_{0.4}Fe_{0.4})O_{3-\delta}$	-400	100~120	3~4
$Y_3Fe_5O_{12}$ (polycrystal)	+100	~50	~2
$Ce_1Y_2Fe_5O_{12}$ (polycrystal)	-830	~40	~21
$Y_3Fe_5O_{12}$ (single crystal) [10]	216	23.8	9.1
$Ce_1Y_2Fe_5O_{12}$ (epi. film) [6]	-3300	5.8 (TM mode)	569

References

[1] B.D. Cullity and S.R. Stock, *Elements of X-Ray Diffraction (third ed.),* Prentice-Hall, New Jersey, 2001

[2] J. F. Dillon, *J. Appl. Phys.*, **39**, 922 (1968)

[3] T. Kim, S. Nasu and M. Shima, *J. Nanoparicle Res.*, **9**, 737 (2007)

[4] T. Sekijima, T. Fujii, K. Wakino and M. Okada, *IEEE Trans. Microwave Theory Tech.*, **47**, 2294 (1999)

[5] P. Hansen and J. P. Krumme, *Thin Solid Films*, **114**, 69 (1984)

[6] T. Shintaku, A. Tate and S. Mino, *Appl. Phys. Lett.*, **71**, 1640 (1997)

[7] H. Kim, A. M. Grishin and K. V. Rao, *IEEE Trans. Magn.*, **35**, 3163 (1999)

[8] J. Hu, V. Tarasov, N. Carlie, L. Petit, A. Agarwal, K. Richardson, and L. Kimerling, *Opt. Express* **15**, 2307 (2007)

[9] J. Hu, V. Tarasov, N. Carlie, L. Petit, A. Agarwal, K. Richardson, and L. Kimerling, *Opt. Mater.* **30**, 1560 (2007)

[10] W. Zhao, *Sensors and Actuators A*, **89**, 250 (2001)

[11] H. Zhao, J. Zhou, B. Li, Z. Gui and L. Li, *J. Electroceram.*, **21**, 802 (2008)

[12] S. Sung, X. Qi and B. J. H. Stadler,CThM4 *CLEO* (2008)

[13] T. Sekijima, T. Fujii, K. Wakino and Okada M., *IEEE Trans. Micro. Theo. and Tech.*, **47**, 2294 (1999)

[14] L. Bi, H. S. Kim, G. F. Dionne, S. A. Speakman, D. Bono, and C. A. Ross, *J. Appl. Phys.*, **103**, 07D138 (2008)

[15] B. E. A. Saleh and M. C. Teich, *Fundamentals of photonics,Wiley series in pure and applied optics*, John Wiley & Sons, New York, 1991

[16] Integrated Optics Software FIMMWAVE 4.5, Photon Design, Oxford, U.K. [Online]. Available: http://www.photond.com

Chapter 6
An On-chip Nonreciprocal Optical Resonator

In the previous chapters, we focused on monolithic integration of magneto-optical materials and waveguide devices on silicon. These studies provide thin film materials and basic waveguide device structures for nonreciprocal photonic device integration. As we discussed in chapter 1, monolithic integration and small footprints of nonreciprocal photonic devices are critical for its application. Integrated semiconductor photonic devices such as lasers [1], modulators [2] and detectors [3] were reported with device footprint of tens or hundreds of μm. Although optical isolators based on mode conversion waveguides [4] or Mach-Zehnder interferometers [5] were demonstrated experimentally on garnet substrates, these device structures show large footprint in the scale level of millimeters to centimeters, which is incompatible with other semiconductor devices. Fundamentally the large device footprint is caused by the relatively weak magneto-optical effect of most materials. For example, considering our polycrystalline CeYIG film described in chapter 6 with a saturation Faraday rotation of -830deg/cm, to achieve optical isolation in Mach-Zehnder structures the device need to be at least 5mm long by simulation. Using mode conversion between TE and TM modes, the device need to achieve 45 deg polarization rotation, which corresponds to a 542 μm long waveguide. Taking account of birefringence and integrated polarizer components, the optical isolator can easily scale up to millimeter level.

Optical ring, disk and racetrack resonators are a class of travelling wave resonator devices, in which light couples from the guided modes in a bus waveguide to the circulating modes in the resonators. Due to the strong optical field enhancement and long optical path in the resonators, these devices are used in optical filters [6], an all optical switch [7], nonlinear photonics [8] and biochemical sensor applications [9]. We consider that by incorporating the nonreciprocal photonic component in such resonator structures, the device footprint will be significantly reduced. Although optical resonance based nonreciprocal photonic devices including photonic crystals and optical disk resonators have been proposed very recently, due

to the difficulty of patterning the magneto-optical materials, magnetic domain structures or nonhomogenous magnetic fields, there are no experimental devices demonstrated so far. In this chapter, we demonstrate a monolithically integrated ultra compact nonreciprocal optical racetrack resonator on silicon. Using a "patterned resonator" structure, we experimentally observed the device nonreciprocity of TM polarized mode using a homogenous applied magnetic field. To the best of our knowledge, this device is the world's first monolithically integrated optical isolator on silicon. The device structure, operation principle, fabrication process, simulated and experimental performance are discussed in this chapter. As a basic component of nonreciprocal photonic devices, nonreciprocal optical resonators can be used in a variety of photonic devices including full optical isolators, optical circulators, optical switchs and optical modulators, therefore opening a new dimension of functionalities for integrated photonics.

6.1 Operation principle, device design, and fabrication process

Simply put, the operation principle of a magneto-optical nonreciprocal optical resonator is to lift the degeneracy of the resonance frequencies between forward and backward propagating light in an optical resonator using magneto-optical effect. In a common optical resonator with no magneto-optical effects, the resonant frequencies are identical between forward and backward propagating light. However when magneto-optical effect, specifically, the nonreciprocal phase shift (NRPS) effect is incorporated in the resonator, the resonance wavelengths are nonreciprocal. To understand this, consider figure 6-1 (a). A straight optical waveguide comprised with magneto-optical materials will see NRPS in the TM polarized modes when an external magnetic field is applied perpendicular to the light propagation direction. This effect is proportional to the Faraday rotation of the magneto-optical material and the field gradient across the magneto-optical layer described by equation (1-12). The NRPS effect leads to non-degenerate effective indices for forward and backward propagating TM polarized modes. If this effect takes place in a ring resonator structure shown in figure 6-1 (b), the resonant wavelengths will be non-degenerate between clockwise (CW)

(corresponding to forward propagating light, denoted by +) and counter-clockwise (CCW) (corresponding to backward propagating light, denoted by -) TM resonating modes, which are related to the effective indices by:

$$\lambda_{TM}(\pm) = \frac{Ln_{eff,TM}(\pm)}{N} \tag{6-1}$$

where L is the resonator cavity length and N is an integer. This resonance non-degeneracy serves as the fundamental device characteristics for the functionalities such as optical isolation and circulation that we discuss hereafter.

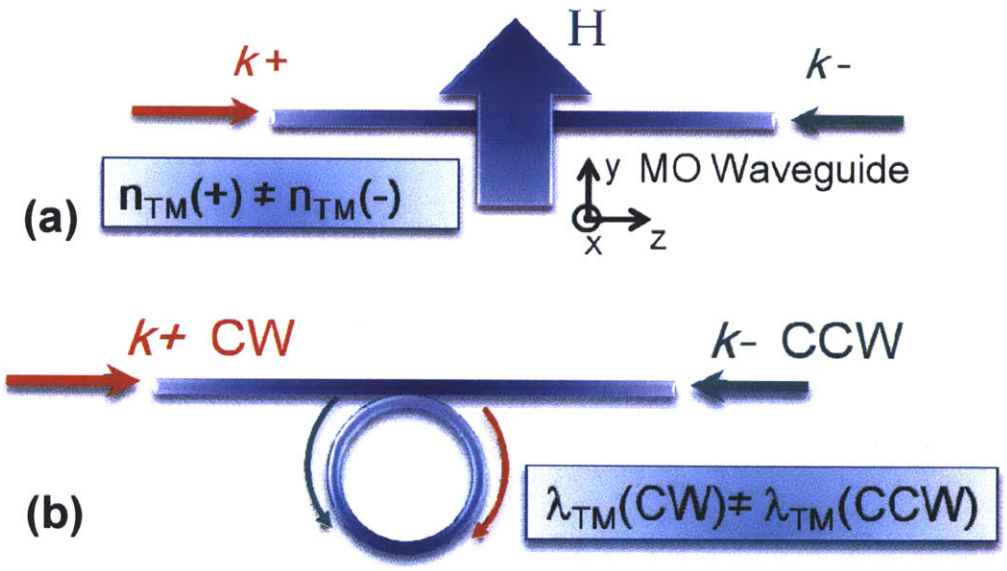

Fig. 6-1 Schematic plot of (a) a nonreciprocal magneto-optical waveguide showing non-degenerate effective indices between forward and backward propagating TM polarized light (b) a nonreciprocal magneto-optical resonator showing non-degenerate resonant frequencies between clockwise and counter-clockwise resonating wavelengths of TM polarized light

The transmission spectrum of a nonreciprocal optical resonator near resonance is shown in figure 6-2. The red and green curves correspond to forward and backward transmittance spectrum respectively. Optical transmission nonreciprocity is achieved for wavelengths near resonance. Consider incident light with the wavelength denoted by the perpendicular line. The forward propagating light is far from resonance and is weakly coupled to the resonator. The transmittance determined by the red curve is high. The backward propagating light is on

resonance and is critically coupled to the resonator. The transmittance determined by the green curve is low. When this device functions as an optical isolator, the maximum isolation ratio and the corresponding insertion loss is determined by the transmittance levels shown by the blue line and red line respectively. Strong optical isolation can be achieved in a wavelength range as shown by shaded regions in the figure.

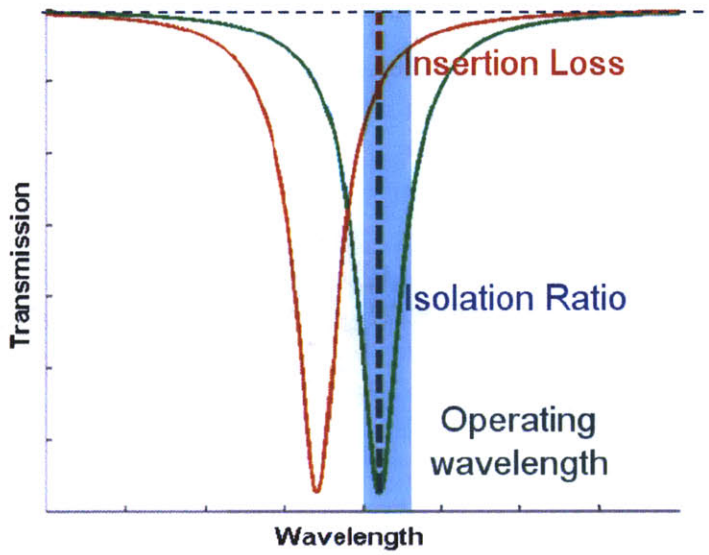

Fig. 6-2 Theoretical transmission spectrum of a nonreciprocal optical resonator. Red and green curves correspond to forward and backward propagating light respectively. The shaded regions show the wavelength range in which high optical isolation ratio can be achieved for the forward propagating light

Although the operation principles are theoretically sound, careful device design is required for experimental realization of device performance. In traveling wave optical resonators, light is circulating in the resonator structure. For a ring resonator consisting of magneto-optical waveguides with TM mode NRPS shown in figure 6-1 (b), if a homogenous external magnetic field is applied across the device, the overall magneto-optical effect will be trivial due to the circulating propagation of the resonant modes. To overcome this issue, recently proposed resonance based integrated nonreciprocal photonic devices require either patterning of the magneto-optical material, or controlling the magnetic domain structure or designing a non-homogenous magnetic field across the resonator, which are not simple to fabricate and hard to realize. Instead of using non-homogenous magneto-optical films or magnetic field, we use a device design shown in figure 6-3. A silicon racetrack resonator is patterned by optical

lithography so that only part of the resonator is covered by magneto-optical thin films. The lengths of the resonator in the covered and uncovered regions are L_1 and L_0 respectively. A homogenous magnetic field H is applied across the device. Because the resonance mode only couples to the magneto-optical material in the L_1 region, the NRPS shows the same sign when light circulates in the resonator, and a macroscopic nonreciprocal effect is observed.

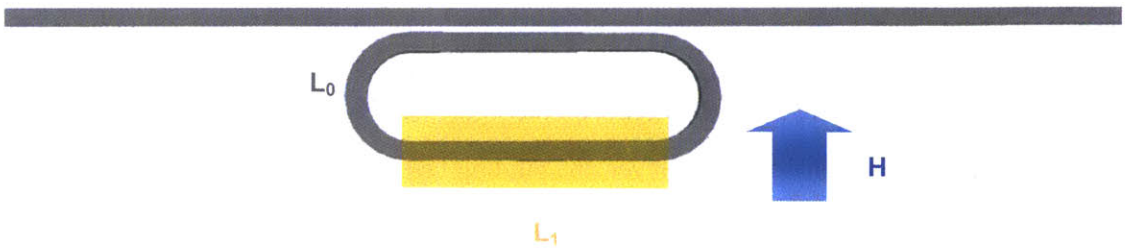

Fig. 6-3 A schematic layout of the nonreciprocal optical resonator using a homogeneous applied magnetic field and a patterned racetrack resonator structure

6.2 Theory of the patterned nonreciprocal optical resonator

To evaluate the performance of the patterned nonreciprocal optical resonator, we consider the resonator structure shown in figure 6-3. Here we focus on the figure of merit (FoM) and the operation bandwidth of the device. For FoM analysis, we introduce three FoMs, the *material FoM* ($F_{mat.}$), the *waveguide FoM* ($F_{wav.}$) and the *resonator FoM* ($F_{res.}$) in the following discussions.

Material FoM ($F_{mat.}$)

The material FoM is simply defined by $FoM = \frac{\Theta}{\alpha_{mat.}}$ as we discussed in chapter 1. Note that the material optical loss $\alpha_{mat.}$ corresponds to the integrated thin film materials rather than their bulk counterparts.

Waveguide FoM($F_{wav.}$)

We define the waveguide FoM as the NRPS divided by the optical loss per length of light propagation in the waveguide. As we discussed in chapter 4 and 5, the NRPS is dependent on the waveguide structure and can be expressed by:

$$\Delta\beta^{TM} = -\frac{2\beta^{TM}}{\omega\varepsilon_0 N}\iint\frac{\Theta}{n_0^4}H_y\partial_x H_y dxdy \tag{6-2}$$

The optical loss can be expressed by:

$$\alpha_{tot} = \Gamma_{MO}\alpha_{MO} + \Gamma_{Guide}\alpha_{Guide} + \Gamma_{clad}\alpha_{clad} + \alpha_{surface} + \alpha_{sidewall} + \alpha_{substrate} \tag{6-3}$$

where Γ stands for the confinement factor in each layer and α is the optical loss coefficient with the units of cm^{-1}. The first three terms on the right side of the equation describes the loss contributions of the magneto-optical layer, the guiding layer (silicon or chalcogenide glasses) and the cladding layer (SiO_2, air or SU-8 resist) respectively. $\alpha_{surface}$ is the absorption and scattering loss of light propagating at the surface of the waveguides, $\alpha_{sidewall}$ is the sidewall scattering loss and $\alpha_{substrate}$ is the optical leakage loss into the substrate. Considering the high index contrast of the waveguide structure, leakage loss $\alpha_{substrate}$ is small. For waveguides we characterized, the TE mode always show lower transmittance than the TM modes, therefore $\alpha_{surface}$ is comparatively small as well, because the TM mode has a much stronger modal intensity at the waveguide surface according to boundary conditions. The cladding materials show much lower loss compared to other terms. Therefore the optical loss can be simplified as:

$$\alpha_{tot} = \Gamma_{MO}\alpha_{MO} + \Gamma_{Guide}\alpha_{Guide} + \alpha_{sidewall} \tag{6-4}$$

For SOI waveguides, the guiding layer material is single crystalline silicon, so the second term on the right may also be neglected.

The waveguide FoM can be expressed by:

$$F_{wav.} = \frac{\Delta\beta^{TM}}{\alpha_{tot}} = -\frac{\Theta}{\Gamma_{MO}\alpha_{MO} + \Gamma_{Guide}\alpha_{Guide} + \alpha_{sidewall}}\cdot\frac{2\beta^{TM}}{\omega\varepsilon_0 N}\iint\frac{1}{n_0^4}H_y\partial_x H_y dxdy \tag{6-5}$$

If the loss from the magneto-optical material is dominating, the equation is simplified as:

$$F_{wav.} = -\frac{\Theta}{\alpha_{MO}}\cdot\frac{2\beta^{TM}}{\omega\varepsilon_0 N\Gamma_{MO}}\iint\frac{1}{n_0^4}H_y\partial_x H_y dxdy = -F_{mat.}\cdot\frac{2\beta^{TM}}{\omega\varepsilon_0 N\Gamma_{MO}}\iint\frac{1}{n_0^4}H_y\partial_x H_y dxdy \tag{6-6}$$

Note that the integral term on the right side of the equation is solely determined by the index of refraction of the different layers in the waveguide, which has a determined maximum value for a certain waveguide structure, achieved by designing the thickness of each layer. For instance, this maxium value is shown in the simulation results of figure 4-13, 5-10 and 5-11. Therefore in the magneto-optical material loss dominant regime $F_{wav.}$ is simply linearly proportional to the $F_{mat.}$.

If the loss from the guiding material or the sidewall scattering is comparable to the magneto-optical materials, $F_{wav.}$ will be smaller than the value in equation (6-6). In this case equation (6-6) can be considered as a maximum possible waveguide FoM for a certain magneto-optical material used in NRPS waveguides if device fabrication is optimized.

Resonator FoM ($F_{res.}$)

The resonator FoM may be defined from figure 6-2 as the ratio between optical isolation ratio and insertion loss. However this term is not well defined because the extinction ratio of an optical resonator is highly dependent on the fabrication process. Ideally, the extinction ratio is infinite if critical coupling condition is exactly met. In practical devices the light can only be close to critical coupling, and the resonator extinction ratio can reach 30 dB or higher. Rather than using this definition, we use the following equation to define resonator FoM.

$$F_{res.} = \frac{2\Delta\lambda}{w} = \frac{\Delta\lambda}{\lambda_r} \cdot Q_{in} \tag{6-7}$$

where $\Delta\lambda$ is the nonreciprocal resonant wavelength shift between forward and backward propagating light, w is the full width at half maximum (FWHM) of the resonance peak, Q_{in} is the intrinsic quality factor of the resonator and λ_r is the resonance wavelength.

We first consider $\Delta\lambda$, the resonance wavelength of forward (λ_f) and backward (λ_b) propagating light satisfies:

$$\frac{L_0 n_{eff\,0}}{\lambda_f} + \frac{L_1 n_{eff\,1}}{\lambda_f} = N \tag{6-8}$$

$$\frac{L_0(n_{eff0}+\frac{\partial n_{eff0}}{\partial\lambda}\cdot\Delta\lambda)}{\lambda_b}+\frac{L_1(n_{eff1}+\frac{\partial n_{eff1}}{\partial\lambda}\cdot\Delta\lambda+\Delta n)}{\lambda_b}=N \tag{6-9}$$

$$\Delta n=\frac{\lambda_b\Delta\beta_{TM}}{2\pi} \tag{6-10}$$

where N is an integer, n_{eff0} and n_{eff1} are the effective refractive index of TM polarized light corresponding to resonator section L_0 and L_1 respectively. Δn and $\Delta\beta_{TM}$ are the TM mode effective index and propagation constant difference between forward and backward propagation light respectively. Using equation (6-8) and (6-10) to substitute N and Δn in equation (6-9), consider $\lambda_f\sim\lambda_b\sim\lambda_r$, we obtain:

$$\Delta\lambda=\frac{\lambda_r^{\,2}L_1\Delta\beta_{TM}}{2\pi(L_0n_{g0}+L_1n_{g1})} \tag{6-11}$$

where n_{g0} and n_{g1} are the group index of resonator section L_0 and L_1 respectively, which are defined as:

$$n_g=n_{eff}-\frac{\partial n_{eff}}{\partial\lambda}\cdot\lambda \tag{6-12}$$

We can also express $\Delta\lambda$ as a function of the free spectral range (FSR) near the resonance wavelength. The FSR is defined as the wavelength difference between neighboring resonances:

$$FSR=\lambda_{r,2}-\lambda_{r,1}=\frac{n_{eff0,2}L_0+n_{eff1,2}L_1}{N_2}-\frac{n_{eff0,1}L_0+n_{eff1,1}L_1}{N_1},\ \text{where } N_1=N_2+1 \tag{6-13}$$

Using the group index definition in equation (6-12) and considering $N_1\sim N_2\sim N\gg1$, we have:

$$FSR=\frac{\lambda_r^{\,2}}{L_0n_{g0}+L_1n_{g1}} \tag{6-14}$$

Therefore we have:

$$\Delta\lambda=\frac{FSR\cdot L_1\Delta\beta_{TM}}{2\pi} \tag{6-15}$$

The quality factor Q of the resonator is defined as the resonance wavelength divided by the

full width of half maximum (FWHM) of the resonant peak. It can be derived using a phasor summation of the electric field circulating in the cavity. Following a similar derivation of Ref. [10], we obtain the following equation for the quality factor Q at critical coupling condition:

$$Q = \frac{\pi(L_0 n_{g0} + L_1 n_{g1})}{\lambda_r \alpha L} \tag{6-16}$$

where α is the loss per unit length of the resonator including light coupling back to transmission in the bus waveguide. At critical coupling wavelength, the loss coefficient can be expressed by:

$$\alpha = (\alpha_0 L_0 + \alpha_1 L_1 + 2\alpha_{junction}) / L \tag{6-17}$$

where the 3 terms on the right are the loss from L_0 region, L_1 region and junctions between L_0 and L_1 regions respectively.

From equations (6-11), (6-16) and (6-17) we can obtain the expression of resonator FoM:

$$F_{res.} = \frac{2\Delta\lambda}{w} = \frac{\Delta\lambda}{\lambda_r} \cdot Q_{in} = \frac{L_1 \Delta\beta_{1M}}{\alpha L} \tag{6-18}$$

This simple expression suggests that the resonator FoM is linearly proportional to the magneto-optical nonreciprocal phase shift, the length of the magneto-optical waveguide section and inversely proportional to the roundtrip loss of the resonator. From equation (6-17), we speculate that the loss factors α_0 and $\alpha_{juction}$ can both be minimized by fabrication optimization and index design between the L_0 and L_1 regions, whereas α_1 is related to the intrinsic loss of the magneto-optical material. When the $\alpha_1 L_1$ term is dominant in equation (6-17), the resonator FoM can be expressed as:

$$F_{res.} = \frac{L_1 \Delta\beta_{1M}}{\alpha_1 L_1} = \frac{\Delta\beta_{1M}}{\alpha_1} \tag{6-19}$$

This is exactly the same equation as (6-5), and is a maximum resonator FoM value by using a magneto-optical waveguide with loss coefficient of α_1. Other loss contributions from α_0 or $\alpha_{juction}$ can both lower the FoM in (6-19). Note that equation (6-19) is independent of the magneto-optical waveguide length L_1, therefore the patterned resonator structure maintains the maximum possible $F_{res.}$ the same as the $F_{wav.}$. This FoM is further related to $F_{mat.}$ by

equation (6-6) and can be maximized by proper design of the guiding layers.

After understanding the resonator parameters as a function of the physical properties of the magneto-optical material and waveguides, we can evaluate the device performance as an optical isolator by approximating the resonant peaks using Lorentzian equations:

$$y = 1 - \frac{a}{1 + (2\delta\lambda / r)^2} \tag{6-20}$$

where $0 < a \leq 1$ is related to the extinction ratio of the resonance. a=1 corresponding to the critical coupling condition where the extinction ratio is infinity. $\delta\lambda$ is the wavelength detuning from the resonance, r is the FWHM of the resonance peak, which is related to the quality factor Q. Equation (6-20) describes the insertion loss due to the resonator structure when the detuning is far from the resonance. The isolation ratio can be expressed as:

$$y = 1 - \frac{a}{1 + 4(\Delta\lambda - \delta\lambda)^2 / r^2} \tag{6-21}$$

where $\Delta\lambda$ is the resonance nondegeneracy due to magneto-optical effect, which is expressed in equation (6-11). Assuming the critical coupling wavelength is at 1550nm, we can investigate the influence of a, Q and $\Delta\lambda$ on the device performance, as shown in figure 6-5 below.

Figure 6-5 (a), (b) show the influence of extinction ratio on the isolation ratio and insertion loss of the device as a function of frequency detuning from resonance. We set the extinction ratios as infinity and -30 dB to -20 dB in 2 dB intervals. Q and $\Delta\lambda$ are fixed to be 20,000 and 40 pm respectively. From the figure it is noted that the extinction ratio mainly influences the isolation ratio, and also shows a slight influence on the isolation bandwidth and insertion loss. For extinction ratio increasing from -20 dB to infinity, the 10 dB isolation bandwidth increases from 2.1 GHz to 2.3 GHz and the critical coupling wavelength insertion loss changes less than 0.1 dB. This result shows that the operation bandwidth and insertion loss are stable to the variation of fabrication sensitive extinction ratio. Figure 6-5 (c), (d) show the influence of quality factor Q on the isolation ratio and insertion loss. We fixed the extinction ratio and $\Delta\lambda$ to be -30 dB and 40 pm respectively and varied Q from 5,000 to 50,000 in

increments of 5,000. It is observed that the quality factor influences the isolation ratio, isolation bandwidth and insertion loss significantly. Increasing Q from 5000 to 50,000 increases the peak isolation ratio from 18 dB to ~30 dB, decreases the 10 dB isolation bandwidth from 3.1 GHz to 1.1 GHz and decreases the insertion loss from 12 dB to 0.7 dB at the critical coupling wavelength. This is reasonable by considering narrowing of the resonance peaks as increasing the value of Q. Finally the influence of $\Delta\lambda$ on the isolation ratio and insertion loss is shown in figure 6-5 (e) and (f). We fixed the extinction ratio and Q to be -30 dB and 20,000 respectively and varied $\Delta\lambda$ from 20 pm to 120 pm by an interval of 10 pm. Similar to the effect of increasing Q, the insertion loss of the device decreases monotonically with increasing $\Delta\lambda$, whereas different from increasing Q both the isolation bandwidth and the peak isolation ratio increases with increasing $\Delta\lambda$. The 10 dB isolation bandwidth increases from 1.5 GHz to larger than 3 GHz by increasing $\Delta\lambda$ from 20 pm to 70 pm and is saturated to the FWHM of the resonance peak by further increasing $\Delta\lambda$.

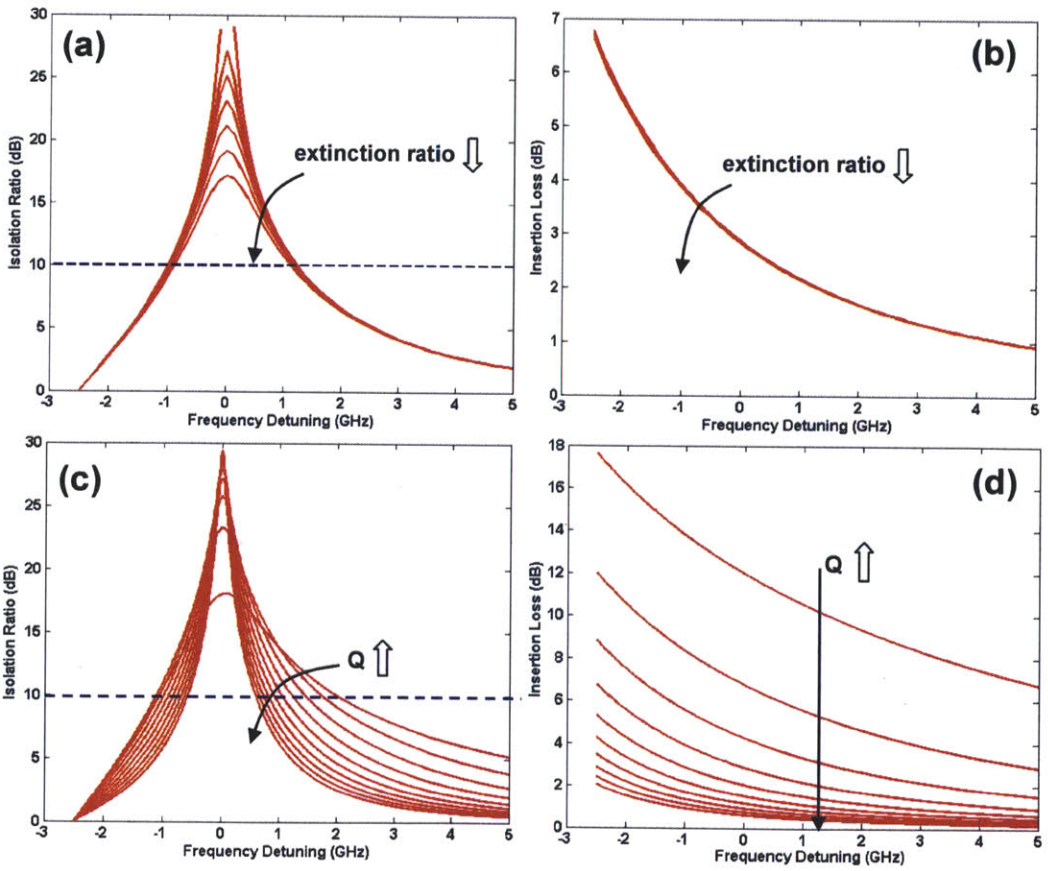

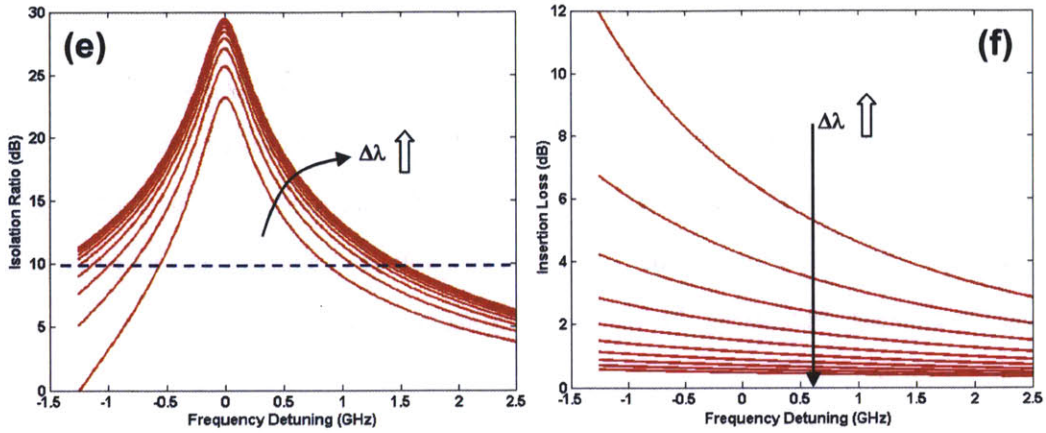

Fig. 6-4 Influence of the extinction ratio on the isolation ratio and insertion loss as a function of frequency detuning from resonance

From the discussions above, we can conclude that to obtain an optical resonator based isolator with high isolation ratio, relatively large operation bandwidth and low insertion loss, we need a resonator device shown in figure 6-3 with large extinction ratio, high nonreciprocity $\Delta\lambda$ and high quality factor Q. (Although the influence of Q is complicated, considering decreasing Q both lowers the peak isolation ratio and the increases the insertion loss, a high Q resonator is still desired for such devices.) Considering equation (6-11) and (6-16), these conclusions point to a device with long magneto-optical section L_1, high NRPS waveguide, high group velocity, low waveguide loss, junction loss and operating at critical coupling conditions. The fabrication sensitive extinction ratio is not important to the device performance as long as the extinction ratio is much higher than the desired isolation ratio. From figure 6-5 (a), with an extinction ratio ~10 dB higher than the desired isolation ratio, the operation bandwidth and insertion loss will not be sensitive to the extinction ratios.

6.3 Garnet/SOI resonator based nonreciprocal optical resonator

To demonstrate the performance of the device structure shown in figure 6-3, we fabricated polycrystalline garnet/SOI patterned optical resonators. The fabrication process flow of the nonreciprocal racetrack resonator on an SOI substrate is shown in figure 6-5. The bare silicon racetrack resonator was firstly fabricated using the process shown in figure 2-4. The bus waveguide and the racetrack consisted of 450 nm wide and 220 nm thick silicon channel

waveguides. The radius of the ring region of the racetrack was 45 μm and the length for the straight region was 200 μm. The overall cavity length was 682.7 μm. The gap between the resonator and the bus waveguide was 200 nm. A 1 μm thick flowable oxide (Fox-25, Dow Corning) was spin-coated on the resonator and rapid thermal annealed to form a SiO_2 top cladding layer. [11] Optical lithography was then carried out on an OAI mask aligner to define the window region on the racetrack resonator using the NR9-1000PY photoresist (Futurrex). An RIE step was carried out using CHF_3 to etch the SiO_2 layer for 600 nm in the window region, which is followed by an HF (1:100) etch process. After the HF etch, AFM measurements were carried out to confirm the exposure of the silicon resonator surface. The devices were then transferred to the PLD chamber for magneto-optical thin film deposition. We used polycrystalline garnet films discussed in chapter 5 to demonstrate the device performance. Bi:YIG or Ce:YIG films were deposited on the device using two-step deposition methods. The crystal phases were then confirmed by XRD analysis. The devices were cleaved on both sides of the bus waveguide to form end facets. Infrared incident light was end-coupled into the device using lens tipped fibers. The transmission spectra in the near infrared wavelengths were measured for magnetic field applied along opposite directions.

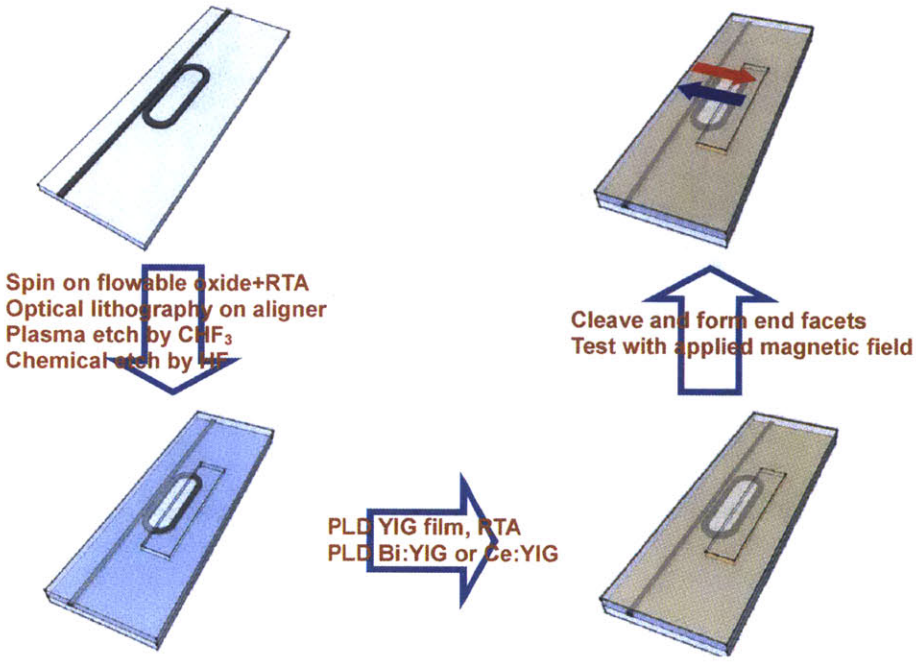

Fig. 6-5 Fabrication process flow of a nonreciprocal racetrack resonator on SOI

A schematic plot of the final device layout is shown in figure 6-6. In order to obtain a clean silicon waveguide surface after RIE and HF etch at the window region, we measured the waveguide surface profile using AFM for different etch period shown in figure 6-7. It is observed that RIE reduced the surface height difference but HF etch increased both the surface height difference and the surface roughness. After exposing the silicon waveguide surface, trenches also formed on both sides of the waveguide and the waveguide sidewalls were also exposed. The surface of the silicon waveguide also became rougher with an RMS roughness of ~1 nm. SiO_2 residues were found to scatter on the silicon waveguide, as shown in the phase contrast image of figure 6-7 (e). These residues were effectively removed after ultrasonicating the sample in IPA for 5 min shown in figure 6-7 (f). The silicon surface also seemed to form a surface oxide layer during this process.

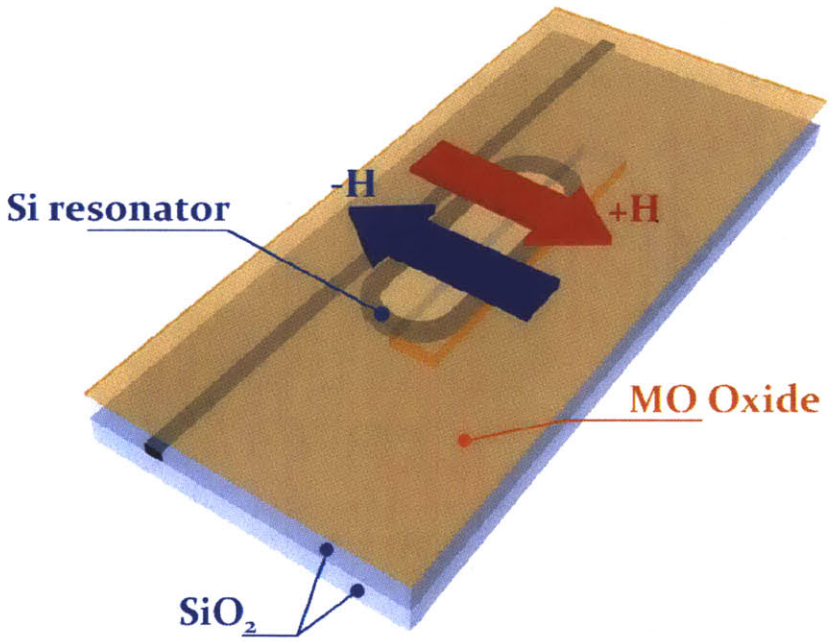

Fig. 6-6 A schematic plot of the patterned nonreciprocal racetrack resonator

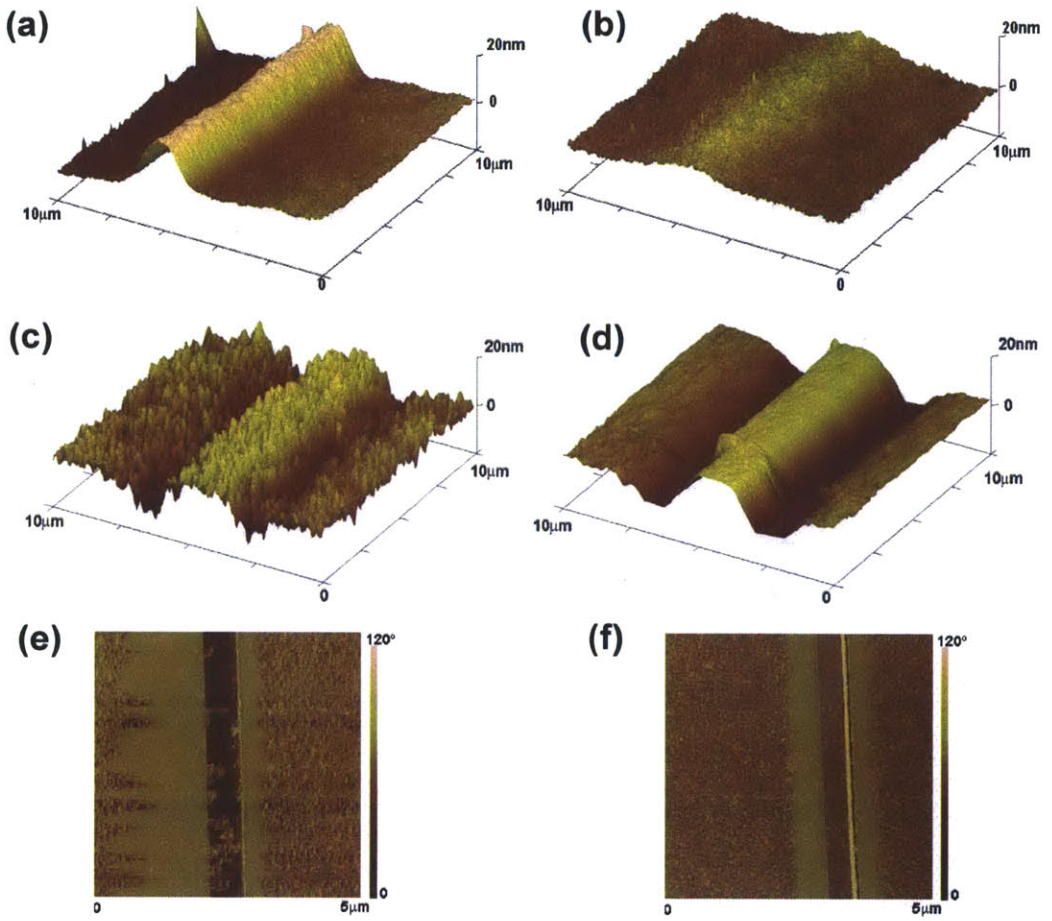

Fig. 6-7 AFM image of the Si waveguides (a) before etch (b) after CHF_3 etch for 15 min (c) after CHF_3 etch for 15 min and HF(100:1) etch for 5 min and (d) after CHF_3 etch for 15min and HF(100:1) etch for 12 min. Also shown are the phase contrast image (e) before and (f) after ultrasonicating in IPA for 5 min

Figure 6-8 shows the transmission spectrum of a reference bare silicon racetrack resonator with SiO_2 top cladding layers. Several resonance bands were observed for both TM and TE polarized light. The quality factor for TM and TE polarizations were Q_{TM}~120,000 and Q_{TE}~5,3000. Following equation (5-1) in chapter 5, we calculated the propagation losses of the bare silicon resonator to be 2.52 dB/cm and 7.29 dB/cm respectively at ~1530 nm wavelength. The higher propagation loss of the TE mode was considered to be due to the scattering loss at the silicon waveguide sidewalls. Note that multiple resonating bands were observed due to the long coupling length between the bus waveguide and the racetrack resonator.

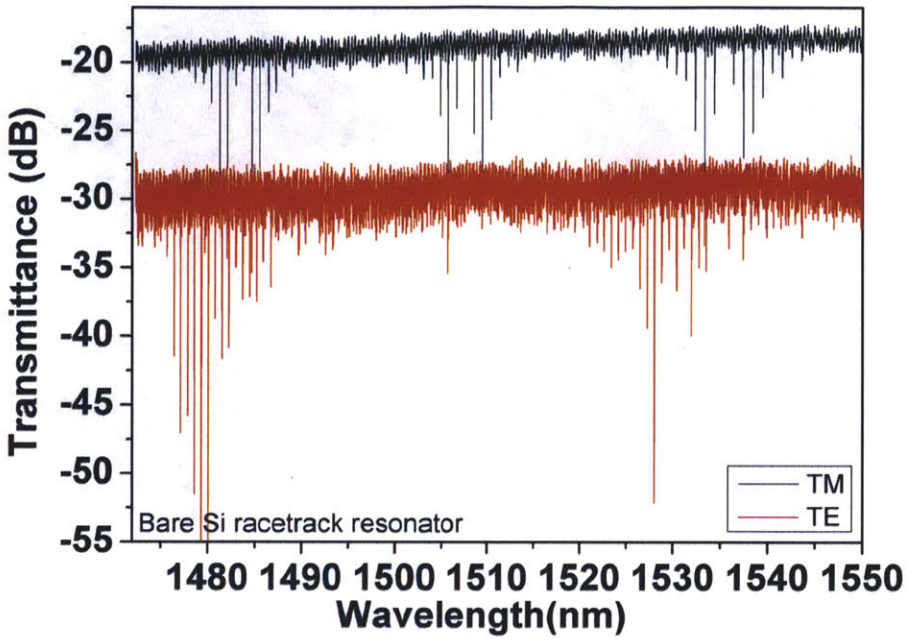

Fig. 6-8 Transmission spectrum of a bare silicon racetrack resonator

Figure 6-9 (a) and (b) show the transmission spectrum of a silicon racetrack resonator coated with Bi1.8YIG(80 nm)/YIG(20 nm) (namely BiYIG sample) and CeYIG(80 nm)/YIG(20 nm) thin films (namely CeYIG sample) respectively. The resonance peak became broader due to the higher loss of the resonator structure. The BiYIG and CeYIG samples show TM mode quality factors of Q~4,200 at 1549 nm wavelength and Q~5,500 at 1541 nm wavelength respectively. The CeYIG sample also shows TE mode resonance with a quality factor of Q~4,800 at 1515 nm wavelength, whereas the TE mode transmittance of the BiYIG sample is close to the detectable signal floor level and no resonance was observed. The optical loss α of BiYIG and CeYIG coated racetrack resonators defined by equation (6-17) can be calculated using equation (5-1) to be 83 dB/cm and 58 dB/cm respectively. The CeYIG sample showed lower loss compared to the BiYIG sample, but both values were much larger than the bare silicon waveguides.

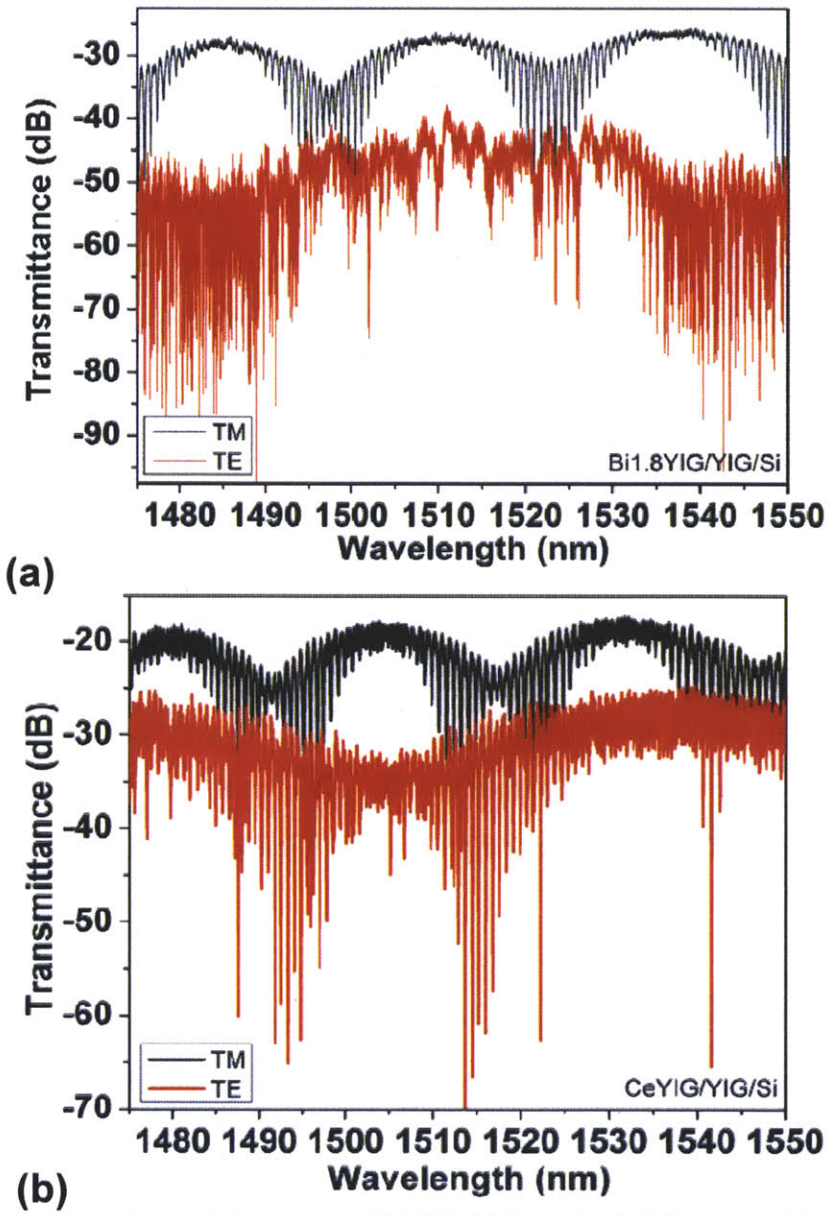

Fig. 6-9 Near infrared transmission spectra of (a) Bi1.8YIG and (b) CeYIG coated silicon racetrack resonators

An in-plane magnetic field of ±1500 Oe was applied perpendicular to the light propagation direction over the garnet coated resonators as shown in figure 2-10 (b). Rather than fixing the applied magnetic field direction and changing the light propagation direction, we fixed the light propagation direction and changed the applied magnetic field direction to detect the device nonreciprocity. These two processes are equivalent because they both change the permittivity tensor of the magneto-optical material from $\hat{\varepsilon}$ to $\hat{\varepsilon}^T$ defined by equation

(1-11). Figure 6-10 (a) (c) shows the TM mode transmission spectra of the BiYIG and CeYIG sample near resonance with opposite applied magnetic field directions respectively. A clear resonance peak shift with respect to the applied magnetic field direction was observed for both samples. The resonant peak positions were plotted as a function of measurement times in figure 6-10 (b) (d) for the BiYIG and CeYIG samples respectively, which indicate that the resonance shift was due to magneto-optical NRPS of the garnet/Si waveguide sections and could be reversibly measured. (The time interval between measurements is about 30 sec.) The drift of the resonant peak positions was considered to be due to the thermo-optical effect of the silicon waveguide. To confirm these conclusions, the TE mode resonance spectrum was also measured for the CeYIG sample as shown in figure 6-10 (e) and (f). There was hardly any nonreciprocal resonance peak shift observed for the TE mode, which agreed with the theoretical expectation of no TE mode magneto-optical NRPS taking place in our device structure; whereas the TE mode resonance peak drifted for almost the same amount compared to the TM mode. These results confirmed that the TM mode resonance peak shift was due to magneto-optical NRPS, and the peak drift was due to the thermo-optical effect of the silicon waveguide.

From figure 6-10, we can estimate the isolation ratio and insertion loss of both resonator devices using the definition of figure 6-2. The BiYIG sample showed a resonance peak shift of 14.8±4.6 pm, a small isolation ration of only ~1.7 dB and insertion loss larger than 20 dB, while the CeYIG sample showed a resonance peak shift of 18.2±1.6 pm, maximum isolation ratio of 19.5±2.9 dB with an insertion loss of 18.8±1.1 dB and a 10 dB isolation bandwidth of 1.6 GHz. Following our theoretical analysis above, this is mainly due to the higher quality factor and extinction ratio of the CeYIG sample compared with the BiYIG sample. Considering our waveguide measurement results in chapter 5, the lower material loss of the polycrystalline CeYIG film compared to Bi1.8YIG is an important factor for higher device quality factor and better optical isolation performance.

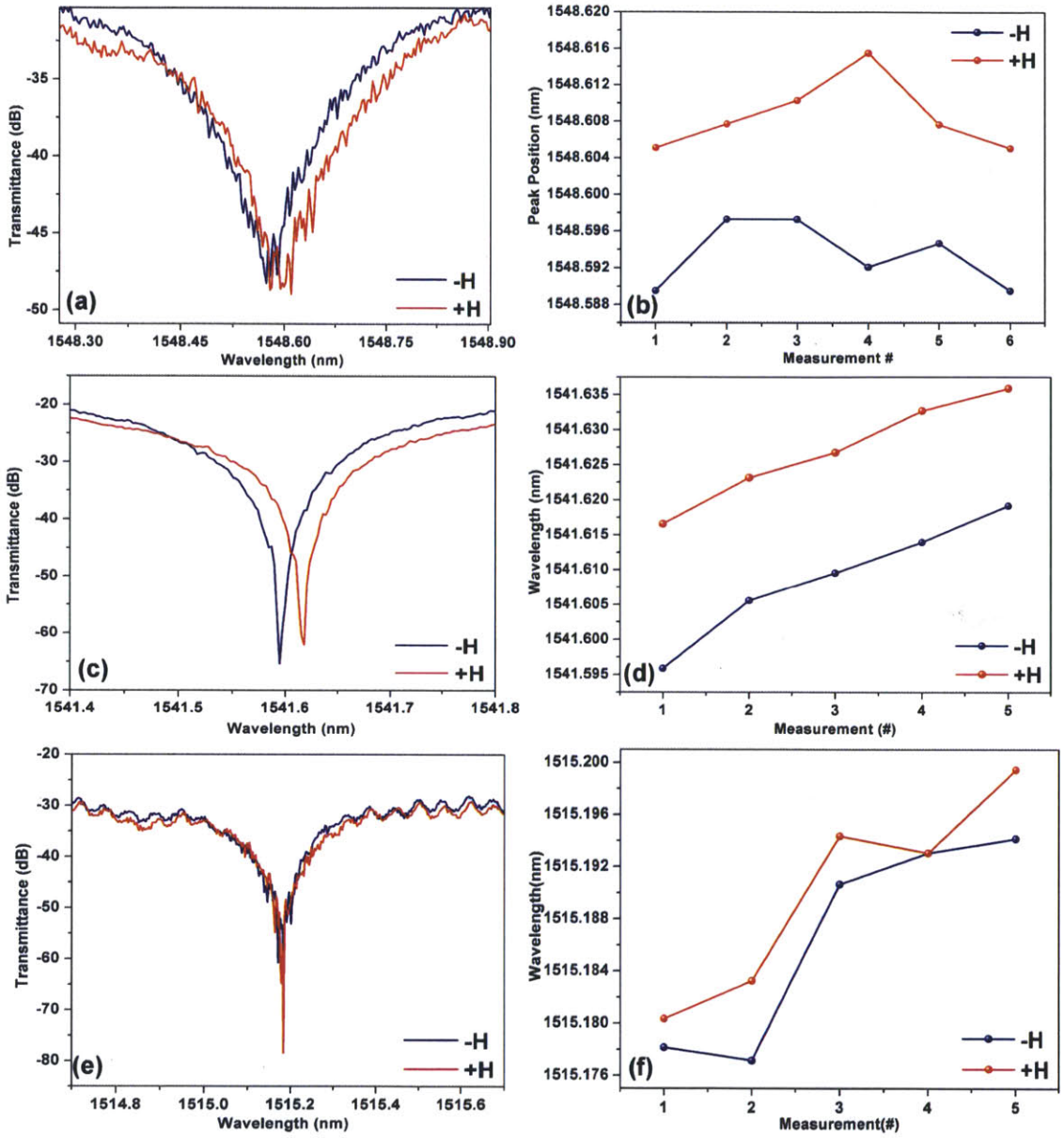

Fig. 6-10 The transmission spectra near resonance wavelengths as a function of applied magnetic field for (a) TM mode of the BiYIG sample (c) TM mode of the CeYIG sample and (e) TE mode of the CeYIG sample. Also shown are the reproducibility of the measured resonance peak shift for (b) TM mode of the BiYIG sample (d) TM mode of the CeYIG sample and (f) TE mode of the CeYIG sample

6.4 Discussion

To evaluate the device performance with the theory discussed in section 6.2, we simulated the magneto-optical resonance shift and the transmission spectrum of the CeYIG sample to compare with the experimental results. We first investigated the resonator device structure. The optical microscope image of figure 6-11 (a) shows that the CeYIG film covers part of the

ring regions of the resonator. Because NRPS only takes place in waveguide sections with magnetic field perpendicular to the waveguide direction, we use an effective magneto-optical section length L_1' instead of L_1 to calculate $\Delta\lambda$ in equation (6-15). The cross-sectional SEM image at the patterned region is shown in figure 6-11 (b). The garnet layer was observed to cover around the silicon waveguide, consistent with our AFM observations in figure 6-8. A similar waveguide cross-section structure was constructed using FIMMWAVE simulation tool and the TM mode profile was obtained shown in figure 6-12. Similar to our discussions in chapter 4 and 5, using equation (6-2) the NRPS of this waveguide at 1541 nm wavelength was simulated to be -231.97 deg/cm from the measured material Faraday rotation value (-1263 deg/cm). Substituting the NRPS value in (6-15) and using the experimentally measured FSR of 0.9009 nm near the resonance wavelength, we obtained a wavelength shift $\Delta\lambda$ of 15.9 pm. This value is comparable but smaller than our experimentally measured value of 18.2±1.6 pm. The error may be originated from several reasons, such as using a rectangular rather than slanted waveguide cross section for simulation, error in the magneto-optical film thicknesses etc.. For instance, taking a value for the thickness of the the YIG buffer layer of 10 nm instead of 20 nm thick, we obtained a simulated $\Delta\lambda$ value of 19.4 pm, due to stronger mode overlap into the CeYIG layer.

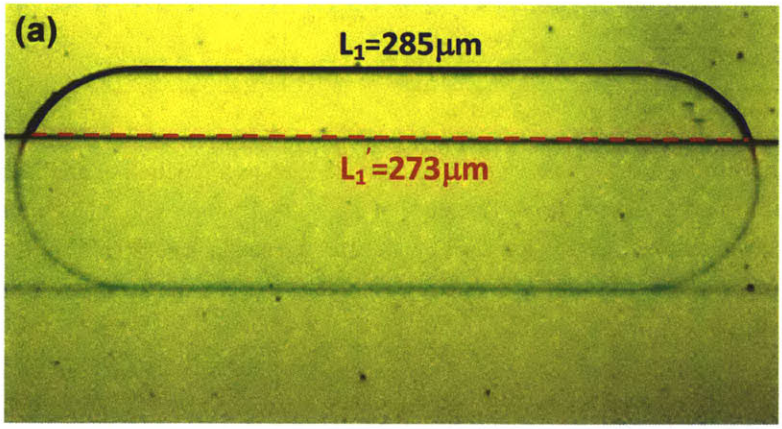

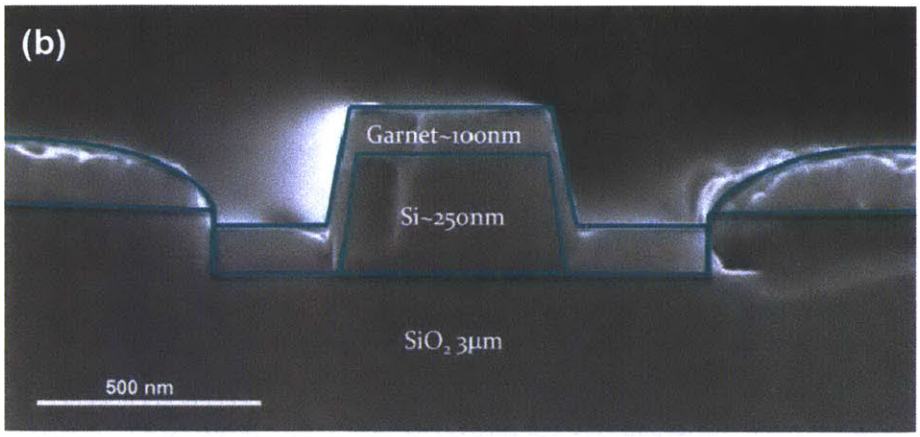

Fig. 6-11 (a) The optical microscope image of the CeYIG sample (b) The cross-sectional SEM image of this sample at the patterned resonator regions.

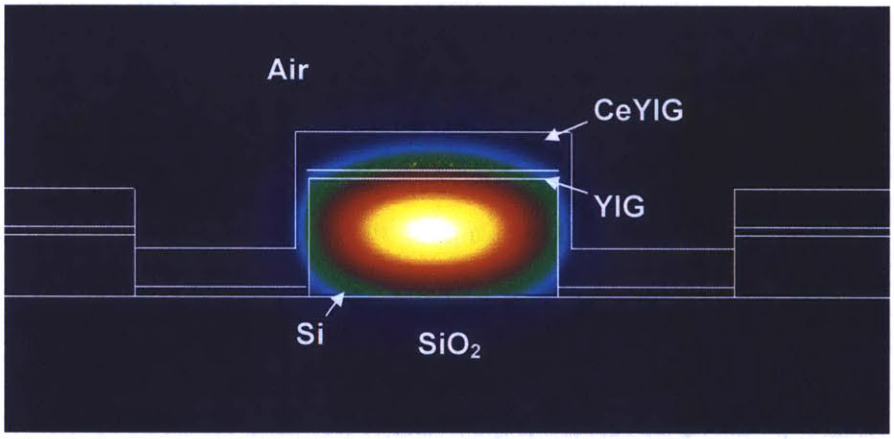

Fig. 6-12 The simulated TM mode intensity profile in a garnet coated silicon waveguide

We also simulated the resonance spectrum by applying a Lorentzian line shape approximation to equation (6-21). Using an experimentally measured quality factor Q of 5500, extinction ratio of 42.5 dB and $\Delta\lambda$ of 19.6 pm in figure 6-8 (c), we compared the simulated and experimentally measured spectrum shown in figure 6-13. A very good match between the Lorentzian line shape approximation and the measured spectrum is observed, with a transmittance difference within 3 dB for all wavelengths between experimental and theoretical spectra.

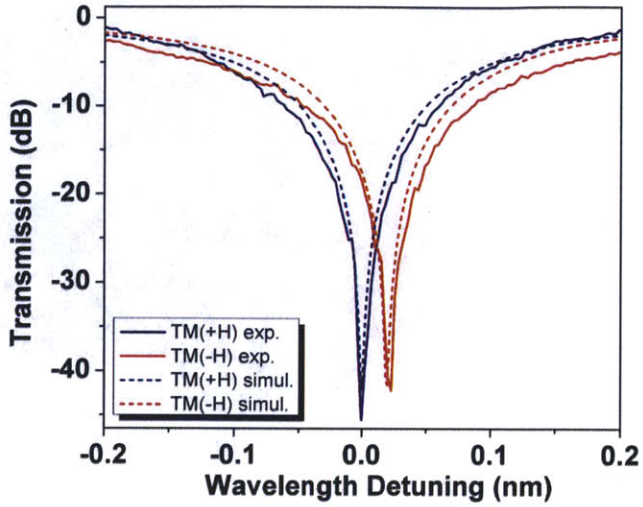

Fig. 6-13 The experimentally measured and simulated TM mode resonance spectrum using Lorentzian line shape approximation of the CeYIG sample

Finally we would like to investigate the origin of losses in the resonator structure. From the simulation results shown in figure 6-4, the major reason for high insertion loss in the current isolator device is the low quality factor value in the resonator. According to equation (6-16) and (6-17), at critical coupling, the quality factor is dominated by three loss terms. Loss from the silicon waveguide was low as demonstrated in bare silicon resonators shown in figure 6-6. We estimated the junction loss by eigenmode expansion method using FIMMPROP software to be 0.15 dB/junction. [12] Using equation (6-17), we calculated the junction loss contribution to the overall loss due to both facets to be 4.4 dB/cm. Comparing with the measured CeYIG sample overall loss coefficient of 58 dB/cm, the CeYIG/SOI waveguide showed ~52.6 dB/cm loss contribution to the total loss, corresponding to ~126 dB/cm of the CeYIG/SOI waveguide. These results show that both the junction loss and the magneto-optical waveguide loss contribute significantly to the overall loss. Therefore the waveguide and the magneto-optical material optimization processes are required for better isolation performances. The future optimization process may include magneto-optical material exploration for higher figure of merit and magneto-optical waveguide fabrication optimization for better waveguide structure *etc.*.

Comparing our isolator device with conventional integrated optical isolators using Faraday or Mach-Zehnder configurations, significant device footprint reduction is achieved.

Conventional optical isolators reported in literatures show device length of 4.1 mm [13], 3.5 mm [14], 7.5 mm (estimated for 90° NRPS) [15] and 4 mm [16] respectively. Therefore our current device shows at least one order of magnitude of footprint reduction, which may be further reduced by reducing the resonator cavity size. The isolation ratio achieve up to -19.5 dB at resonance, which is comparable to most of the other reported optical isolators. This high isolation ratio is due to the design of using a resonator cavity to achieve optical isolation. In mode conversion or Mach-Zehnder isolators, fabrication error can significantly deteriorate the extinction ratio due to either polarization off from ideal or power imbalance between Mach-Zehnder arms. In resonator based optical isolator, the extinction ratio of the backward propagation light is only determined by the extinction ratio of the resonator, therefore relaxes the fabrication requirement. Our current device showed about 2 times of the insertion loss compared to single crystal garnet or epitaxial garnet film based devices on garnet substrates [15][16] due to the higher loss of the magneto-optical waveguide, the loss value can be significantly reduced by optimizing the magneto-optical material and fabricated device structure. Note that the As_2S_3/CeYIG waveguides in chapter 5 shows much lower loss compared to the CeYIG/SOI waveguides. The comparison of the device performance between the resonator based optical isolator and other devices reported in literature is summaried in table 6-1. Note that the coupling loss at the device end facets is excluded.

Table 6-1 Comparison of the isolator performance between resonator based optical isolator and epitaxial garnet film based isolators reported in literature

Devices	Isolation Ratio (dB)	Insertion Loss (dB)	Device Length (μm)
NRMC [13]	27	8~11	4100
NRMC [14]	24	4.6	3150
NRMC [17]	13.3	6.3~8.1	4500
Mach-Zehnder NRPS [15]	19	13	8000
Mach-Zehnder NRPS [16]	21	8	4000
Resonator NRPS	19.5	18.2	290

6.5 Summary

In this chapter, we studied a nonreciprocal optical resonator on silicon. Using a patterned racetrack resonator structure with magneto-optical waveguides showing nonreciprocal phase shift, we demonstrate optical nonreciprocity and optical isolation in this device structure. A rigorous derivation of the resonator performance and isolation behavior as a function of the magneto-optical material properties are derived in analytical expressions. BiYIG/SOI and CeYIG/SOI waveguides based nonreciprocal racetrack optical resonator were monolithically integrated on an SOI platform. As the world's first prototype monolithic integrated ultra-compact optical isolator on silicon, the CeYIG sample shows an isolation ratio of 19.5±2.9 dB, an insertion loss of 18.8±1.1 dB and a 10 dB isolation bandwidth of 1.6 GHz at 1541 nm wavelength for TM polarized light. The simulated resonance spectrum using Lorentzian line shape approximation agrees with experimental results very well. The relatively high insertion loss of the current device was caused by the low quality factor of the resonator structure. The high loss value was attributed to the magneto-optical material losses and the non-ideal CeYIG/SOI waveguide structure of the current sample. Further optimization of the device structure and exploration of better magneto-optical materials will lead to improved device performance for a variety of on-chip nonreciprocal photonic applications.

References:

[1] E. J. Skogen, C. S. Wang, J. W. Raring, G. B. Morrison and L. A. Coldren, *Proc. Integrated Photonics Research Conf.*, IThD2, San Francisco, CA, 2004

[2] W. M. J. Green, M. J. Rooks, L. Sekaric and Y. A. Vlasov, Optics Express, **15**, 17106 (2007)

[3] S. Assefa, F. Xia, Y. A. Vlasov, *Nature*, **464**, 80, (2010)

[4] T. Shintaku, *Appl. Phys. Lett.*, **66**, 2789, (1995)

[5] J. Fujita, M. Levy, R.M. Osgood Jr., L.Wilkens, and H. Dotsch, *Appl. Phys. Lett.,* **76**, 2158, (2000)

[6] S. Xiao, M. H. Khan, H. Shen, and M. Qi, *Optics Express*, **15**, 14765 (2007)

[7] V. Almeida, C. Barrios, R. Panepucci and M. Lipson, *Nature*, **431**, 1081 (2004)

[8] Q. Xu, V. Almeida and M. Lipson, *Optics Letters*, **30**, 2733 (2005)

[9] J. Hu, X. Sun, A. Agarwal and L. C. Kimerling, *J. Opt. Soc. Am. B.*, **26**, 1032 (2009)

[10] J. Hu, *Planar Chalcogenide Glass Materials and Devices*, PhD. Thesis, Massachusetts Institute of Technology (2009)

[11] C. W. Holzwarth, T. Barwicz and H. I. Smith, *J. Vac. Sci. Technol. B*, **25**, 2658 (2007)

[12] Integrated Optics Software FIMMWAVE 4.5, Photon Design, Oxford, U.K. [Online]. Available: http://www.photond.com

[13] T. Shintaku, *Appl. Phys. Lett.*, **73**, 1946 (1998)

[14] T. Shintaku, *Appl. Phys. Lett.*, **66**, 2789 (1995)

[15] J. Fujita, M. Levy, R.M. Osgood Jr., L.Wilkens, and H. Dotsch, *Appl. Phys. Lett.,* **76**, 2158, (2000)

[16] Y. Shoji, T. Mizumoto, H. Yokoi, I. Hsieh and R. M. Osgood, *Appl. Phys. Lett.*, **92**, 071117 (2008).

[17] T. Shinkatu and T. Uno, *J. Appl. Phys.*, **76**, 8155 (1994)

Chapter 7
Conclusions and Future Work

7.1 Conclusions

Integration of nonreciprocal optical components in planar photonic circuits on a semiconductor platform has been challenging for long time. To engage in this quest, this thesis focuses on the exploration of novel magneto-optical thin film materials and on-chip nonreciprocal photonic device structures. The two major contributions of this work are: 1) Discovery of a novel room temperature ferromagnetic perovskite system with high magneto-optical figure of merit. 2) Demonstration of a monolithic integrated ultra-compact optical isolator on silicon. This work provides both material and device candidates for future planar nonreciprocal photonic devices, and also opens new territories for fundamental and applied material and device research based on these new materials and device structures.

1) Room temperature ferromagnetic perovskite thin films

We demonstrated room temperature ferromagnetism in a perovskite thin film material system including Fe or Co doped $SrTiO_3$. By further doping these materials with Ce or Ga, we systematically controlled the saturation magnetization, magnetic anisotropy, Faraday rotation and optical absorption of the films. A high figure of merit of 3~4 deg/dB at 1550nm wavelength was measured in the Ga and Fe co-doped $SrTiO_3$ film. Significant magnetic anisotropy and non-Brillouin-shape thermal magnetization curve was observed in these materials systems, which is considered to originate from magneto-elastic effects of Fe and Co ions under lattice distortion. Experimental demonstration of magneto-optical strip-loaded waveguides with chalcogenide glass/ferromagnetic perovskite structures were successfully carried out on single crystal perovskite substrates.

2) A monolithically integrated nonreciprocal optical resonator on silicon

We proposed, simulated and experimentally demonstrated a monolithically integrated nonreciprocal optical resonator on silicon. As a fundamental component, this ultra-compact, non-material-selective device structure offers opportunities to develop a variety of planar nonreciprocal photonic devices including optical isolators and circulators. Using a patterned resonator structure, we experimentally demonstrated optical isolation up to 19.5±2.9 dB with 10 dB isolation bandwidth of 1.6 GHz in a CeYIG/SOI racetrack resonator with 0.018 mm^2 device footprint. The resonator properties and nonreciprocal performance were analytically expressed in material parameters. Magneto-optical waveguide loss and waveguide junction scattering loss are both considered to be important factors for performance optimization.

During the exploration of novel magneto-optical material and devices, we also contributed to the material understanding for several oxide thin film systems. These contributions included experimental and theoretical investigation of the B-site disorder behavior of Bi_2FeMnO_6 films, experimental control and characterization of self-assembled nanostructures in epitaxial $LaFeO_3$ films, and phase stabilization, characterization and waveguide integration of polycrystalline iron garnet films on silicon. These systematic studies on ferrite thin films provide material structure and property insights for not only magneto-optical but also other applications, such as materials used in integrated multiferroic, exchange biasing and microwave frequency devices.

7.2 Future Work

There are several interesting future works that could be carried out on the ferromagnetic perovskite materials and the planar nonreciprocal photonic devices. I summarize them as following:

1) In-depth understanding of the RTFM properties in peroskite thin films

An in-depth understanding of the RTFM properties of perovskite thin films using more detailed experimental characterization methods and first-principle simulations is required. Although a variety of characterization processes have been made on these thin film materials, a systematic experimental study on the local atomic structure, influence of defects, valence states and oxygen vacancies in these films has not been carried out. Characterization methods including high resolution TEM analysis, Rutherford back scattering spectrum, and extended X-ray absorption fine structure spectrum are needed for detailed structure analysis for transition metal ions in the perovskite lattice. We established a theory to correlate the magneto-elastic effect to the RTFM properties. This theory needs to be more systematically and quantitatively studied based on samples with different cations, valence states and strain states. First principles simulation on the material electronic structures may also provide insight on the influence of strain, valence states and oxygen vacancies of the magnetic properties.

2) Exploration of multiferroic applications using transition metal ion doped perovskites

Another application of the transition metal ion doped perovskites is in multiferroic devices. Due to the RTFM property, tetragonalized lattice structure and high resistivity of the Fe and Co doped $SrTiO_3$ films, these materials are very promising as intrinsic ferromagnetic and ferroelectric multiferroic material candidates. Preliminary piezoelectric force microscopy measurements already showed that these films had room temperature ferroelectric domains. [1] Polarization-voltage hysteresis curve measurements need to be carried out to verify the ferroelectric properties in these materials. Another interesting property of these materials is the electrocoloration process under applied voltage due to oxygen vacancy diffusion. [2] This process may also influence the ferromagnetic property of these materials due to valence state change of the transition metal ions after redistribution of oxygen vacancies under applied voltages. The possibility of oxygen vacancy population control may also be used to tune the ferromagnetic property of an adjacent ferromagnetic oxide material, such as $La(Co,Mn)O_3$ [3], therefore resulting in a voltage controlled room temperature ferromagnetic material. Thanks to their compatibility with silicon substrates, these perovskite materials can also be

easily integrated for on-chip device applications.

3) Controlling of the self-assembled nanostructures in epitaxial oxide films

Several interesting self-assembled nanostructures have been discovered in our studies. We introduced the nano-pyramid structure of epitaxial $LaFeO_3$ films in chapter 3. Another structure is a [110] cone in [100] matrix structure of Fe doped $SrTiO_3$ epitaxial films. [4] These structures enable possibility of tuning the crystal orientation dependent properties in the thin film oxides. Therefore controlling the self-assembled nanostructures to be long range ordered will be interesting for such applications. Long range ordering may be achieved by using patterned substrates during the film growth process. Novel nanoscale ferromagnetic or ferroelectric devices can be developed based on these ordered nanostructures.

4) Exploration of planar nonreciprocal photonic devices

The study of a planar nonreciprocal optical resonator in chapter 6 provides us the possibility of introducing optical nonreciprocity in planar integrated optical circuits. Using the nonreciprocal optical resonator as a basic device structure, we can develop a variety of novel planar nonreciprocal photonic devices. Figure 7-1 summarizes several of the proposed devices. Figure 7-1 (a) shows the design of a complete optical isolator. Different from the isolator structure discussed in chapter 6, this device uses a drop port waveguide for laser output. Due to the nonreciprocity of the resonator, back reflected light will have a different resonant wavelength. Using a frequency dependent filter on the input bus waveguide, back reflected light with any wavelength will be isolated by the device, therefore achieving complete optical isolation in the frequency space. Figure 7-1 (b) shows the design of a four port optical circulator. This device can be simply constructed using two bus waveguides coupling to the nonreciprocal resonator. Light near resonant wavelengths undergoes a circulating path of A-B-C-D-A with the magnetic field configuration shown in the figure. By flipping the in-plane magnetic field by 180°, the circulating path will be reversed as A-D-C-B-A. Figure 7-1 (c) shows the schematic plot of a magneto-optical switch. By

applying magnetic field in different directions, light near resonant wavelengths may travel through the through port or the drop port, therefore the device acts as a two port optical switch. A multiport switch can be achieved by cascading of these devices. Figure 7-1 (d) shows the schematic plot of a magneto-optical modulator, using an AC magnetic field which may be generated by an AC current, the output light can be modulated from the through port or the drop port of the nonreciprocal resonator, therefore achieving an ultra-compact optical modulator structure.

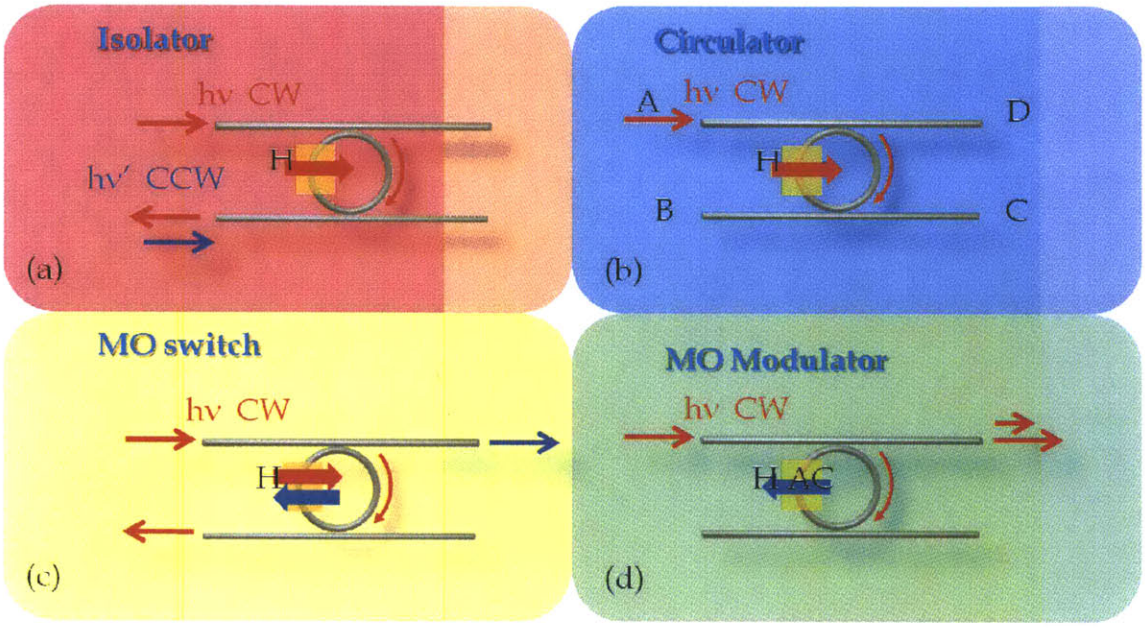

Fig. 7-1 Schematic plot of planar nonreciprocal photonic devices using nonreciprocal optical resonators

To realize these devices, optimization on the resonator performance is required with a focus on reducing the resonator cavity loss, which can be achieved by better material and device design as discussed in chapter 6. Temperature stability of these devices is also required for stable performance, which can be achieved by using athermal resonator designs [5][6] or using microheaters to control the resonant frequency [7]. Another strategy is incorporating the light source in the same resonator with the isolator structure, and therefore no frequency alignment is needed. To allow polarization independent performance, exploration of TE mode nonreciprocal optical structures is also desired for future studies. These devices may be realized by similar strategies used for TM mode resonators with different mode profile

distribution designs in the magneto-optical resonator structure.

References

[1] H. S. Kim, H. J. Paik, D. J. Yang, L. Bi, Y. J. Choi, J. W. Lee, J. K. Kang, Y. C. Park, Y. Kim, M. Alexe, G. F. Dionne and C. A. Ross, *in preparation*, (2011)

[2] J. Blanc and D. L. Staebler, *Phys. Rev. B*, **4** 3548, (1971)

[3] H. Z. Guo, A. Gupta, J. Zhang, M. Varela and S. J. Pennycook, *Appl. Phys. Lett.*, **91** 202509, (2007)

[4] H. S. Kim, L. Bi, H. Paik, D. J. Yang, Y. C. Park, G. F. Dionne and C. A. Ross, *Nano. Lett.*, **10** 597, (2010)

[5] B. Guhua, B. B. C. Kyotoku and M. Lipson, *Optics Express*, **18** 3487, (2010)

[6] V. Raghunathan, W. N. Ye, J. Hu, T. Izuhara, J. Michel and L. Kimerling, *Optics Express*, **16** 17631, (2010)

[7] P. Dong, W. Qian, H. Liang, R. Shafiiha, N. Feng, D. Feng, X. Zheng, A. V. Krishnamoorthy and M. Asghari, Optics Express, **18** 9852, (2010)